



VCU

Virginia Commonwealth University
VCU Scholars Compass

Theses and Dissertations


Graduate School

2019

Material Interactions and Self-Assembly in Inkjet Printing

Karam Nashwan Al-Milaji

Follow this and additional works at: <https://scholarscompass.vcu.edu/etd>

 Part of the [Industrial Engineering Commons](#), [Industrial Technology Commons](#), [Manufacturing Commons](#), and the [Other Operations Research, Systems Engineering and Industrial Engineering Commons](#)

© The Author

Downloaded from

<https://scholarscompass.vcu.edu/etd/6053>

This Dissertation is brought to you for free and open access by the Graduate School at VCU Scholars Compass. It has been accepted for inclusion in Theses and Dissertations by an authorized administrator of VCU Scholars Compass. For more information, please contact libcompass@vcu.edu.

Copyright © 2019 Karam N. Al-Milaji. All Rights Reserved

Material Interactions and Self-Assembly in Inkjet Printing

A dissertation submitted in partial fulfillment of the requirements for the degree of Doctor of
Philosophy at Virginia Commonwealth University

By

Karam Nashwan Al-Milaji

M.Sc. Mechanical and Nuclear Engineering, Virginia Commonwealth University, Richmond,

Virginia, 2016

Director:

Dr. Hong Zhao

Assistant professor

Department of Mechanical and Nuclear Engineering

Virginia Commonwealth University

Richmond, Virginia

August 2019

Acknowledgments

In the name of Allah, the most Merciful and Beneficent

First and Foremost, all praises and thanks are due to Allah, Almighty, the greatest of all, on whom we ultimately depend for sustenance and guidance. I would like to thank and praise Allah Almighty for giving me the opportunity, determination, and the strength to finish this journey. His continuous grace and mercy were with me throughout my life and ever more during the tenure of my research. I would like to thank God Almighty for enabling me to undertake this research study and to persevere to complete it satisfactorily. Without his blessings, this achievement would not have been possible.

No words can adequately express my sincere gratitude to my advisor Dr. Hong Zhao for her continuous support, guidance, and encouragement. Besides my Advisor, I would like to thank my committee members Dr. Daren Chen, Dr. Hooman Tafreshi, Dr. Christina Tang, and Dr. Nga Ng Tse for their insightful comments and informative discussions that motivated me to widen my research area from various perspectives.

I am deeply indebted to Dr. Ravi Hadimani and Dr. Dmitry Pestov for their useful guidance, precious instructions, and valuable trainings, which I needed to pursue my degree.

More importantly, special thanks to the Higher Committee of Educational Development in Iraq (HCED) for their financial support and cooperation that assisted me during this endeavor.

Finally, none of this would have been to succeed without the constant source of love, patience, support, and motivation of my wonderful parents, wife, and daughters.

Table of contents

Acknowledgments	ii
Tables of Figures	ix
Abstract	xxiii
CHAPTER 1 Introduction	26
1.1 Introduction	26
1.2 Physics of Inkjet Printing	27
1.2.1 Droplet Formation	27
1.2.2 Ink Requirements	29
1.2.3 Droplet-Droplet and Droplet-Substrate Interactions	31
1.2.4 Solvent Evaporation	34
1.3 Motivation and Objectives	35
1.4 Outline	37
CHAPTER 2 Literature Review	39
2.1 Motivation for Investigating the Coffee-Ring Effect	39
2.2 Multibody Interactions in an Evaporating Particle-Laden Droplet	41
2.3 Particles Assembly at the Air-Liquid Interface	45
2.3.1 Particles Pushed to and Adsorbed at the Interface	47
2.3.2 Particles Captured by the Descending Air-Liquid Interface	50

CHAPTER 3 Interfacial Self-Assembly of Colloidal Nanoparticles in Dual-Droplet Inkjet

Printing	54
3.1 Introduction	54
3.2 Experimental section	57
3.2.1 Materials	57
3.2.2 Substrate Treatment	58
3.2.3 Ink Preparation	58
3.2.4 Dual-Droplet Inkjet Printing Process	58
3.2.5 In Situ Observation of Droplet Impact and Solvent Evaporation.....	59
3.2.6 Morphology Characterization.....	59
3.2.7 Optical Spectrum Characterization.....	59
3.2.8 Image Analysis	60
3.2.9 COMSOL Simulation.....	60
3.3 Results and Discussion.....	61
3.3.1 Dual-Droplet Inkjet Printing.....	61
3.3.2 Effect of Solvent Composition on the PS Nanoparticle Deposition.....	63
3.3.3 Effect of Functional Groups on the PS Nanoparticle Deposition.....	69
3.3.4 Effect of Substrate on the PS Nanoparticle Deposition.....	73
3.3.5 Discussion.....	75
3.3.6 Implication in Printed Optical Devices	76

3.4 Conclusion.....	79
CHAPTER 4 pH-Modulated Self-Assembly of Colloidal Nanoparticles in a Dual-Droplet Inkjet Printing Process	81
4.1 Introduction.....	81
4.2 Materials and Methods.....	83
4.2.1 Materials.....	83
4.2.2 Substrate Treatment.....	83
4.2.3 Ink Preparation	84
4.2.4 Dual-Droplet Inkjet Printing Process	84
4.2.5 Morphology Characterization.....	84
4.2.6 Surface Profilometry.....	85
4.2.7 Zeta Potential Characterization of Colloidal Nanoparticles and Dopamine-Coated Substrates.....	85
4.3 Results and Discussion.....	85
4.3.1 Self-Assembly of Nanoparticles at Different pH Values	85
4.3.2 Effect of pH on Deposit Morphology of Carboxyl-PS Nanoparticles.....	89
4.3.3 Effect of pH on Deposit Morphology of Sulfate-PS Nanoparticles	95
4.3.4 Discussion.....	100
4.4 Conclusion.....	104
CHAPTER 5 Probing the Colloidal Particle Dynamics in Drying Sessile Droplets	107

5.1	Introduction	107
5.2	Materials and Methods	109
5.2.1	Materials	109
5.2.2	Confocal Microscopy Characterization	109
5.2.3	Ink Preparation	110
5.2.4	Dual-Droplet Inkjet Printing Process	110
5.2.5	Morphology Characterization	111
5.2.6	Analytical Analysis.....	111
5.3	Results and Discussion.....	116
5.3.1	Particle Pinning and Assembly in Conventional and Dual-Droplet Inkjet Printing	116
5.3.2	Confocal Imaging of Particle Pinning at the Contact Line.....	122
5.3.3	Binary Particle Deposition in Dual-Droplet Printing	124
5.3.4	Discussion.....	127
5.4	Conclusion.....	134
 CHAPTER 6 Inkjet Printing of Magnetic Particles Toward Anisotropic Magnetic		
Properties..... 136		
6.1	Introduction	136
6.2	Methods.....	138
6.2.1	Inkjet Printing of Magnetic Particles.....	138
6.2.2	Morphology Characterization.....	139

6.2.3	Magnetic Characterization.....	139
6.2.4	Numerical Simulation of Magnetic Field and Particle Motion	139
6.3	Results and Discussion.....	142
6.3.1	Implication in Printed Anisotropic Magnetic Films	155
6.4	Conclusion.....	157
CHAPTER 7 Direct Embedment of Silver Nanowires by Inkjet Printing for Stretchable		
Conductors.....		
7.1	Introduction	159
7.2	Experimental Section	161
7.2.1	Materials	161
7.2.2	Preparation of the Liquid PDMS Layer.....	161
7.2.3	Preparation of the AgNW Ink.....	161
7.2.4	Fabrication of Embedded AgNW Lines	162
7.2.5	Characterization.....	162
7.2.6	Electrical Characterization of the Embedded AgNW Lines.....	163
7.2.7	Viscosity Characterization.....	163
7.3	Results and Discussion.....	163
7.3.1	Direct Inkjet Printing and Embedding of AgNWs into an Elastomer Substrate	163
7.3.2	Alignment Process of the Embedded AgNWs	172
7.3.3	Electrical Characterization of the Embedded AgNWs	174

7.3.4 Discussion.....	176
7.4 Conclusion.....	177
CHAPTER 8 Concluding Remarks.....	179
8.1 Review of the Results and Conclusions	179
8.2 Key Differences Between Conventional and Dual-Droplet Inkjet Printing.....	181
8.3 Future Works.....	182
References	184
Appendix A: Supporting Information	210
Curriculum Vitae	211

Tables of Figures

Figure 1.1: Illustration of (a) continuous inkjet printing and (b) drop-on-demand inkjet printing.....	28
Figure 1.2: Dynamics of the jetted droplets. ²²	30
Figure 1.3: Droplet spacing effect on the coalescence behavior, (a) individual drops, (b) scalloped, (c) uniform, (d) bulging, and (e) stacked coins. Drop spacing decreases from left to right. ³¹	33
Figure 1.4: Droplet coalescence scenarios, induced by different dynamic wettabilities of ink droplets on substrates. The difference among (A1, B1, and C1) is the surface tension and nanoparticle concentration, which resulted in different dynamic wettabilities of ink droplets on the substrates. This, in turn, have led to (A2, A3) spherical cap deposition, (B2, B3) continuous line deposition, and (C2, C3) dumbbell structure after coalescing and drying. ³²	33
Figure 2.1: Illustration of the coffee-ring formation.....	40
Figure 2.2: (a) Assembly of negatively charged colloidal particles and (b) positively charged colloidal particles at the edge of the sessile droplet on a negatively charged glass substrate, which demonstrated the order to disorder assembly structures at the contact line. ⁷⁵ (c) Schematic illustration of the impact of DLVO force on the particle deposition, where a system lacking the DLVO interaction results in a ring formation, while having such attractive DLVO force renders more uniform particle depositions and (d) particles deposition change with respect to pH value. ⁷⁶ (e) Illustration of the influence of protein adsorption on the particle deposition. Manipulating the surface charge of the colloidal particles resulted in different particle-particle and particle-substrate electrostatic and	

hydrophobic interactions as indicated by the four routes.⁷⁷ (f) Flow field pattern representations observed in a drying Whisky droplet, and (g) schematics of solutal and surfactant Marangoni flows. The ethanol/water and surfactant mixtures do not produce uniform particle deposition unless they are combined with a polymer to enhance the particle adhesion to the substrate.⁴³ 42

Figure 2.3: (a) Illustration of the particle self-assembly at the air-liquid interface during solvent evaporation (the top row). The second row is the optical images showing monolayer islands formation of dodecanethiol-passivated gold nanocrystals at the interface during the evaporation process. Scale bars are 50 μm .⁸⁹ (b) Optical images showing the self-assembly of thiol-capped Ga-In nanoparticles at the air-liquid interface in a cosolvent system (water/ethanol mixture), presented at different stages of solvent evaporation.⁹⁰ (c) Schematic illustration of the surfactant-mediated electrostatic and hydrophobic interactions among the particles, the air-liquid, and liquid-substrate interfaces. For a system with like-charged particle/surfactant mixtures, a ring-like particle deposition was obtained after solvent evaporation. However, uniform particle deposits were obtained when utilizing oppositely charged systems.⁹¹ 48

Figure 2.4: (a) Ring formation of colloidal droplets dried at room temperature versus uniform particle deposition of evaporating the same colloidal system in an environmental chamber at an elevated temperature. The colloidal particles were captured by the fast descending interface, forming uniform particle deposition. Scale bars are 0.5 mm.⁹⁵ (b) Effect of particle shape on the particle deposition.³⁷ The ellipsoidal particles tend to adsorb at the air-liquid interface during the evaporation, resulting in uniform depositions as opposed to the ring-like depositions of spherical particles. The confocal microscope

images shown on the right demonstrate adsorption of ellipsoidal particles at the air-liquid interface and accumulation of the spherical particles at the contact line..... 51

Figure 3.1: Schematic of the dual-droplet printing process. Blue represents the supporting droplet; red is the wetting droplet; and gold represents the PS nanoparticles. 55

Figure 3.2: Schematics of (a) dual-droplet printing (this work); and (b) conventional inkjet printing, causing either coffee-ring formation or not well controlled deposition morphology..... 56

Figure 3.3: (a) Wetting droplet impact onto a supporting droplet by high-speed imaging (time interval of 0.2 ms between each image). (b) Images of PS nanoparticle film floating on the interface during the evaporation process ($t = 0, 51.5, 69.9, 78.3, 80.3,$ and 80.6 s). The suspension of sulfate-functionalized PS nanoparticles prepared with 100% ethanol was used for the wetting droplets, three of which were deposited onto the supporting droplet. The PS nanoparticle size is 100 nm in diameter. 62

Figure 3.4: Optical images of aldehyde/sulfate-functionalized PS nanoparticle deposition at (a) 100% ethanol; (b) 80 wt%/20 wt% ethanol/water; and (c) 50 wt%/50 wt% ethanol/water-diluted inks in the wetting droplets. The four columns represent various nanoparticle amounts of one, three, five, and ten wetting droplets (WDs), respectively. The scale bar is 100 μm . A dopamine-treated substrate was used, and the PS nanoparticle size is 100 nm in diameter..... 65

Figure 3.5: SEM images of Aldehyde/sulfate-functionalized PS nanoparticle deposition at (a) 100% ethanol; the scale bar is 5 μm ; and (b) 50wt⁰/50wt% ethanol/water diluted inks in the wetting droplets; the scale bar is 10 μm . The four columns represent various

nanoparticle amounts of one, three, five and ten wetting droplets (WDs), respectively. A dopamine-treated substrate was used. The PS nanoparticle size is 100 nm in diameter. 66

Figure 3.6: Normalized BCC from the center to the periphery of the nanoparticle depositions shown in Figure 3.4 using (a) 100% ethanol-diluted inks, (b) 80 wt%/20 wt% ethanol/water-diluted inks, and (c) 50 wt%/50 wt% ethanol/water-diluted inks for the wetting droplets. WD: wetting droplet..... 67

Figure 3.7: Schematics of two regimes of self-assembly through (a) particle-interface interaction; and (b) combination of particle-interface, particle-substrate, and particle-flow field interactions..... 68

Figure 3.8: SEM images of sulfate-functionalized PS nanoparticles deposition at various locations of the circular depositions of (a) one wetting droplet and (b) five wetting droplets. The wetting droplet ink is prepared with 100% ethanol and the PS nanoparticle size is 100 nm in diameter. 70

Figure 3.9: Optical images of sulfate-functionalized PS nanoparticle deposition at (a) 100% ethanol; (b) 80 wt%/20 wt% ethanol/water; and (c) 50 wt%/50 wt% ethanol/water-diluted inks of the wetting droplets. The four columns represent various nanoparticle amounts of one, three, five, and ten wetting droplets, respectively. The scale bar is 100 μ m. A dopamine-treated substrate was used, and the PS nanoparticle size is 100 nm in diameter..... 71

Figure 3.10: Optical images of carboxyl-functionalized PS nanoparticle deposition at (a) 100% ethanol; (b) 80wt%/20wt% ethanol/water; and (c) 50wt%/50wt% ethanol/water diluted inks of the wetting droplets. The four columns represent various nanoparticle amounts of one, three, five and ten wetting droplets (WDs), respectively. The scale bar is

100 μm . A dopamine-treated substrate was used, and the PS nanoparticle size is 100 nm in diameter..... 72

Figure 3.11: Optical images of sulfate-functionalized PS nanoparticle deposition on a PET substrate at (a) 100% ethanol and (b) 50 wt%/50 wt% ethanol/ water-diluted inks in the wetting droplets. The four columns represent the four conditions of one, three, five, and ten wetting droplets, respectively. The scale bar is 100 μm and the PS nanoparticle size is 100 nm in diameter. 74

Figure 3.12: Optical images of PS nanoparticle assembly with diameters of (a) 100 nm, (b) 200 nm, and (c) 300 nm. The scale bar is 50 μm . (d–f) SEM images of these assembly of (a–c). The scale bar is 2 μm . g) UV–vis reflection spectra; (h) comparison of the full-field simulation, the Braggs calculations (pink solid line), the Mie calculations (black dotted line), and the measured reflection peak locations (circles). 78

Figure 4.1: Schematic of the dual-droplet inkjet printing, where different interparticle and particle-substrate interactions are initiated at the interface and in the bulk of the supporting droplet. As the solvent evaporates, different deposition patterns are obtained depending on the type of the nanoparticles utilized and the pH value of the supporting droplet. 86

Figure 4.2: The measured zeta potentials of carboxyl- and sulfate-PS particles in water and surface zeta potential of the dopamine-coated glass slide with respect to different pH values. The standard deviations for the colloidal particles and the dopamine-coated substrates are ~ 1 mV and ~ 3 mV, respectively. 88

Figure 4.3: Deposit patterns obtained from jetting one wetting droplet with carboxyl-PS particles on supporting droplets with different pH values. The scale bar is 100 μm 90

Figure 4.4: Illustration of the multibody interactions at different pH values for (a) carboxyl-PS particles, and (b) sulfate-PS particles. The positive and negative signs represent ions available in the supporting droplet at various pH values..... 91

Figure 4.5: Deposit pattern evolution obtained from jetting one wetting droplet (WD) and 3WDs with carboxyl-PS particles on the supporting droplets with different pH values. More particles tend to diffuse into the supporting droplet as the pH value increases. The scale bar is 100 μm 92

Figure 4.6: SEM images of deposits with carboxyl-PS particles at various pH values. The scale bar in the optical images is 100 μm 95

Figure 4.7: SEM images of deposits with sulfate-PS particles at various pH values. The scale bar in the optical images is 100 μm 96

Figure 4.8: Deposit patterns obtained from jetting one wetting droplet with sulfate-PS particles on the supporting droplets with different pH values. The scale bar is 100 μm 97

Figure 4.9: Deposit pattern evolution obtained from jetting one WD and 3WDs with sulfate-PS particles on the supporting droplets with different pH values. Sulfate-PS particles are more robust toward pH change, where the nearly monolayer of PS particles is always present. The scale bar is 100 μm 98

Figure 4.10: SEM images showing the deposit edges at different pH values; (a) deposition of one WD of carboxyl-PS particles at pH 1.5, (b) deposition of one WD of sulfate-PS particles at pH 1.5, (c) deposition of one WD of carboxyl-PS particles at pH 11.5, and (d) deposition of one WD of sulfate-PS particles at pH 7. 101

Figure 4.11: Height profiles near the deposit edges obtained from dual-droplet printing of (a) carboxyl-PS particles, and (b) sulfate-PS particles at different pH values. The red dash

lines represent the ring region while the inset shows the z-height of each individual peak with its corresponding pH value. (For interpretation of the references to color in this figure legend, the reader is referred to the web version of this article. 103

Figure 5.1: Schematics of the particles at the contact line (a) in the bulk of the supporting droplet; (b) at the interface of the supporting droplet. 115

Figure 5.2: Conventional inkjet printing of particle-laden droplets on the PET substrates with different particle concentrations. (a) 20 nm carboxyl-PS particles, (b) 100 nm carboxyl-PS particles, and (c) 1 μm carboxyl-PS particles. The scale bar is 100 μm 117

Figure 5.3: Schematics of conventional inkjet printing and dual-droplet inkjet printing of particle-laden droplets. (a) Conventional inkjet printing of sessile droplet with low particle loading that depicts the depinning/pinning behaviors of the contact line. (b) Conventional inkjet printing of particle laden-droplets with high particle loading. The particles migrate and concentrate at the contact line by virtue of the evaporation-induced flow, causing the contact line pinning. (c) Dual-droplet printing process, where the contact lines remain pinned during solvent evaporation. The middle of the deposit is composed of nearly closely-packed monolayer of nanoparticles. 120

Figure 5.4: Optical images of particle depositions of the dual-droplet printing various numbers of wetting droplets (WDs): (a) one WD, (b) three WDs, (c) eight WDs, and (d) nine WDs. 300 nm sulfate-PS particles were used in the wetting droplet(s), and no particles were in the bulk of the supporting droplet. The scale bar is 100 μm 121

Figure 5.5: Confocal microscope images of (a) a supporting droplet of DI water on a coverslip glass slide with no particles in the bulk and at the air-liquid interface, (b) and (c) 200 nm sulfate-PS particles self-assembled at the interface of the supporting droplet and

particle pinning at the contact line, (d) 20 nm carboxyl-PS particle transporting to the contact line of the supporting droplet. 123

Figure 5.6: Schematic of dual-droplet inkjet printing that demonstrates the monolayer formation of nanoparticles at the interface (300 nm sulfate-PS) and different particle assembly obtained near the three-phase contact line depending on the particle size in the supporting droplet, (a) 20 nm carboxyl-PS particles forming stratified ring structure, (b) 100 nm carboxyl-PS particles resulting in blended ring structure, and (c) 1 μm carboxyl-PS particles leading to scattered particle deposition among the particle assembly from the interface..... 125

Figure 5.7: Optical images of the particle depositions generated by dual-droplet printing of nine wetting droplets with 300 nm sulfate-PS particles and different sizes and concentrations of carboxyl-PS particles in the supporting droplet. (a) 20 nm carboxyl-PS particles, (b) 100 nm carboxyl-PS particles, and (c) 1 μm carboxyl-PS particles. The scale bar is 100 μm 126

Figure 5.8: SEM images of the particle deposits shown in Figure 5.7, demonstrating the versatile particle assembly obtained in vicinity of the contact line region. (a) Stratified ring (20 nm carboxyl-PS particles), (b) blended ring (100 nm carboxyl-PS particles), and (c) ring of 300 nm sulfate-PS particles decorated with a few 1 μm carboxyl-PS particles. Carboxyl-PS nanoparticles of 0.2 mg/mL were used in the supporting droplet. 127

Figure 5.9: SEM images of the binary particle depositions shown in Figure 5.7, demonstrating the versatile particle configuration obtained in vicinity of the contact line region. (a) Stratified ring (20 nm carboxyl-PS particles/300 nm sulfate-PS particles), (b) blended ring (100 nm carboxyl-PS particles/300 nm sulfate-PS particles), and (c) ring of

300 nm sulfate-PS particles decorated with a few 1 μm carboxyl-PS particles. Particle concentration in the supporting droplet was 0.5 mg/mL. 128

Figure 5.10: (a)-(c) Calculated advection and diffusion velocities of the 20 nm, 100 nm, and 1 μm carboxyl-PS particles in the bulk of the supporting droplet, respectively. The dashed lines represent 0.2 mg/mL and 0.5 mg/mL particle concentrations used in the experimental study. (d) Calculated advection and diffusion velocities of the 300 nm sulfate-PS particles at the interface of the supporting droplet. The dashed lines represent the range of particle concentrations obtained from jetting one to nine wetting droplets..... 129

Figure 5.11: Phase diagram of the deposition morphology showing its dependence on the particle size and concentration in the supporting droplet. Diamond dots indicate the experimental data. Different dot colors correspond to different ring structures..... 130

Figure 5.12: (a) Further illustration of the formation of stratified ring structure; (b) SEM image showing that the 20 nm PS particles can pass the 300 nm PS particles and deposit closer to the leading edge of the supporting droplet. The local concave shape of the particle pinning line has kept the 20 nm particles from completely going under the 300 nm PS particles. (c) SEM image of the stratified ring structure..... 132

Figure 5.13: Stratified ring structure formed by 20 nm carboxyl-PS particles (0.001 mg/mL) in the supporting droplet and 300 nm sulfate-PS particles in the wetting droplets. The 20 nm particles could migrate to the contact line via infiltration through the interstices of the 300 nm particles..... 133

Figure 6.1: Spatial representation of two magnetic dipoles in a uniform magnetic field..... 142

Figure 6.2: Illustration of the solvent imbibition process and the contact line pinning. The droplet size is 30 nL. Particle concentration is 25 mg/mL. 143

Figure 6.3: Evaporation-induced radial and diffusion velocities of the magnetic particles in terpineol oil. The mean particle size is 5 μm . The blue and red dash lines represent the particle concentrations of 10 mg/mL and 25 mg/mL, respectively. Please refer to chapter five for the calculation of radial and diffusion velocities in an evaporating sessile droplet..... 144

Figure 6.4: Optical images of particle depositions of different droplet volumes, printed with 25 mg/mL ink concentration. “Random” refers to samples printed without applying external magnetic field and “Aligned” refers to samples with one-dimensional chains of particles when the magnetic field is applied during the printing process. 144

Figure 6.5: Optical microscope images of particle depositions of different droplet volumes, printed with 10 mg/mL particle concentration. “Random” refers to samples printed without applying external magnetic field and “Aligned” refers to samples with one-dimensional chains of particles when the magnetic field is applied during the printing process..... 145

Figure 6.6: Illustration of solvent infiltration mechanism into the photopaper for droplets bigger than 30 nL. Dashed arrows indicate the solvent infiltration. When no magnetic field is applied, the particles follow the direction of the flow as the solvent seeps into the porous substrate beyond the three-phase contact line, resulting in a ring-like particle deposition. 147

Figure 6.7: SEM images demonstrating the difference in particle accumulation at the TCL region with and without applying magnetic field for droplet volumes of 30 nL and 50 nL. The images present a clear evidence of the reduced number of particles deposited at the TCL when the magnetic field was applied. Ink concentration is 25 mg/mL..... 148

Figure 6.8: Schematic illustration of the magnetic field effect on ferromagnetic particle deposition. Ring-like depositions are produced when no magnetic field is applied, whereas,

aligned chain-like patterns with much suppressed CRE are formed when a magnetic field is applied..... 149

Figure 6.9: (a-f) Demonstration of chaining process of two magnetic dipoles in the presence of magnetic field at the angle $\alpha = 30^\circ$. The magnetic field is in the positive y-axis. The elapsed time for the two dipoles to collide is 446 μs . In this case, the dipoles travel in elliptical path until they align and collide..... 150

Figure 6.10: Distance between the two dipoles during the chaining process. The characteristic time for the two dipoles to collide is obtained when this distance reaches 10 μm , which is two times of the particle radius. The characteristic times for chaining t_{ch} are 328 μs , 446 μs , 692 μs , and 1.5 ms, for the orientation angles of zero, 30° , 45° , and 60° , respectively. 151

Figure 6.11: Interaction forces acting between the two dipoles in the simulation domain. Positive forces represent attractive forces between the two particle dipoles; and the negative forces are repulsive forces..... 151

Figure 6.12: (a) and (b) Magnetic field simulation, which illustrate the magnetic field in XY and YZ planes. One droplet is placed on the top center of the permanent magnet. (c) Illustration of the magnetic field gradient inside the sessile droplet. 152

Figure 6.13: (a) Two particles released in the simulation domain with an initial velocity of zero; (b) particle migration in the z-direction toward the substrate under the influence of the magnetophoretic force and drag force. The particles are positioned at a vertical distance (L_m) away from the substrate, to calculate the characteristic time (t_{pz}) for the magnetic particles to reach the substrate. 153

Figure 6.14: (a) Magnetization curves of the films with chains of particles and the films with random particle deposition. “Random” refers to the magnetization curve of the films fabricated without external magnetic field (i.e., random particle deposition). “Parallel” and “Normal” refers to the magnetization curves of films with magnetic particle chains, when the testing magnetic field is parallel to the chain direction and perpendicular to the chain direction, respectively. (b) Optical and SEM images of the printed films with magnetic field (left) and without magnetic field (right). Clear chain formation is observed on the films fabricated with external magnetic field. The scale bar is 100 μm 155

Figure 6.15: Magnetization curves of the printed “Random” films at different orientation angles with respect to the testing magnetic field. “Random” refers to films printed without applying magnetic field with random particle deposition..... 156

Figure 6.16: Magnetization curve of the photopaper..... 157

Figure 7.1: Illustration of the direct embedment of AgNWs into an elastomer layer by inkjet printing..... 164

Figure 7.2: (a) Histograms of AgNWs length distribution. (b) Optical image of the as-synthesized AgNWs. (c) and (d) SEM images of the as-synthesized AgNWs, where the AgNW diameter is $\sim 100 \text{ nm} \pm 20 \text{ nm}$ 165

Figure 7.3: Demonstration of the penetration depth of AgNW lines with respect to the number of printing passes and PDMS layer thickness. Different penetration depths of AgNW lines were obtained for various printing passes when utilizing a thick PDMS layer (i.e., 1.5 mm). However, the AgNW lines were found to deposit in the vicinity of the supporting PET substrate when using PDMS layer thickness less than 250 μm . The yellow circles highlight the location of printed AgNW lines. 166

Figure 7.4: Illustration of the fabrication process of embedded AgNW lines. (a) Represents printing on a liquid PDMS layer with 1.5 mm thickness. (b) Represents printing on a liquid PDMS layer with a 100 μm thickness. (c) Represents the case of printing on a liquid PDMS layer with a 40 μm thickness. 167

Figure 7.5: Optical images of the printed AgNW lines with respect to the number of printed passes and PDMS layer thickness. The top row represents lines produced when printing into a 100 μm layer thickness, while the bottom row represents lines printed into a 40 μm layer thickness. Bulging and waviness were observed when printing more than three passes for PDMS layer thicknesses that are less than 100 μm 168

Figure 7.6: (a) and (b) show the top and the cross-sectional views of AgNW lines, printed with five passes on a PDMS layer with 100 μm thickness on a PET substrate. The printed line was deposited in vicinity of the supporting substrate. (d) and (e) are the top and cross-sectional views of AgNW lines, printed with five passes on a PDMS layer with 100 μm thickness that was spin-coated on a cured PDMS supporting substrate. (c) and (f) present the contact angles of the AgNW ink on PET and PDMS substrates when submerged into liquid PDMS, indicating the strong droplet-substrate interactions on the PET substrate..... 170

Figure 7.7: Penetration depth of AgNW line with respect to curing temperature. (a) Shows the lifted AgNW line to the surface of the PDMS when the sample was directly cured after printing. (b) and (c) present embedded AgNW lines when the samples were left to rest for 30 min then cured at 90 $^{\circ}\text{C}$ for 10 min, and samples cured at the room temperature for 24 h., respectively. Five printing passes were used and the PDMS thickness is $\sim 100 \mu\text{m}$ 171

Figure 7.8: (a) Schematic illustration of the formation mechanism of aligned AgNWs and FIB-SEM cross-sectional image of an AgNW line printed with a single pass. (b) and (c) are SEM images of AgNW lines printed with one and five passes, respectively. 173

Figure 7.9: (a) Bending test of a sample with two AgNW lines printed with 5 printing passes. The line length is ~25 mm with initial resistance (R_0) of 0.88 k Ω . The bending radius is ~7 mm. (b) Resistance change of embedded AgNW lines during the first 100 stretching/releasing cycles, tested at 10% strain, and (c) is resistance change between 100 to 200 stretching/releasing cycles. The samples were composed of two AgNW lines printed with five passes. 174

Abstract

Material Interactions and Self-Assembly in Inkjet Printing

By: Karam Nashwan Al-Milaji, Ph.D.

A dissertation submitted in partial fulfillment of the requirements for the degree of Doctor of Philosophy at Virginia Commonwealth University.

Virginia Commonwealth University, 2019

Major Director: Hong Zhao, Assistant Professor, Department of Mechanical and Nuclear Engineering

Inkjet printing has attracted much attention in recent years as a versatile manufacturing tool, suitable for printing functional materials. This facile, low-cost printing technique with high throughput and accuracy is considered promising for a wide range of applications including but not limited to optical and electronic devices, sensors, solar cells, biochips, and displays. The performance of such functional devices is significantly influenced by the deposit morphology and printing resolution. Therefore, fabrication functional devices with precise footprints by inkjet printing requires deep understanding of ink properties, material interactions, and material self-assembly.

In conventional inkjet printing process, where sessile droplets are directly printed on substrates, particle depositions are usually associated with the well-known, undesirable coffee-ring effect due to the high solvent evaporation rate at the edges of the printed droplets. Such particle accumulation phenomenon in vicinity of the three-phase contact lines of sessile droplets is considered detrimental to inkjet printing applications. This study investigates the material interactions and

self-assembly of colloidal inks in inkjet printing applications at different length scales. The potential of inkjet printing has been exploited through employing the dual-droplet inkjet printing of colloidal particles to investigate the self-assembly of colloidal nanoparticles at the air-liquid interface and at the three-phase contact line of sessile droplets, which provide better understanding of the particle deposition morphologies after solvent evaporation. Different from conventional inkjet printing, the dual-droplet printing involves jetting wetting droplets, containing colloidal nanoparticles dispersed in solvents with high vapor pressure, over supporting droplets composed of water only. By tuning the surface tensions and controlling the jetting parameters of the jetted droplets, monolayers with closely-packed deposition of colloidal nanoparticles are demonstrated. Various solutions are proposed to totally suppress or mitigate the coffee-ring effect in inkjet printing applications through tuning the pH value of the supporting droplets in the dual-droplet inkjet printing to control the multibody interactions (i.e., particle-particle, particle-interface, and particle-substrate interactions) or by applying magnetic field to direct the self-assembly of colloidal particles in conventional inkjet printing. In addition, the influence of various forces such as drag force, van der Waals force, electrotactic force, and capillary force on the particle deposition and assembly in vicinity of the three-phase contact line area were investigated for both the conventional and dual-droplet inkjet printing techniques.

Finally, fabrication of functional devices such as stretchable conductors have also been demonstrated by inkjet printing of silver nanowires into elastomer substrate, where the viscous liquid elastomer layer shaped the printed silver wire lines into tens of micrometers in diameter. The silver nanowires align along the printing direction during solvent evaporation, resulting in wires with good mechanical stability and electrical performance. The printing techniques and the outcomes presented in this study can be harnessed in engineering and manufacturing a wide range

of technological applications ranging from high-performance optical and electronic devices to stretchable conductors and sensors.

CHAPTER 1 Introduction

1.1 Introduction

The potential of inkjet printing technology is widely recognized as a personal printing tool and commonly utilized for commercial applications, mainly in graphics and other conventional printing applications.¹ The inkjet is a direct printing technique that utilizes liquid phase materials, where small droplets could be jetted through a small orifice on designated areas with high precision.² Recently, there has been an immense interest in employing the inkjet printing in fabricating functional devices such as electronic displays,³ sensors,⁴ solar cells,⁵ thin-film transistors,⁶ organic semiconductors,⁷ etc. Unlike the conventional printing and patterning processes (e.g., photolithography, screen printing, imprinting, etc.), where time consumption and multistep printing approach are inevitable, inkjet printing is simple, non-contact printing technique, where the printhead doesn't come in contact with the substrate.⁸ The significance of inkjet printing stems from its low material waste, few printing steps, low temperature working environment, scalability, and compatibility with various inks and substrates.⁹ As the revolution of the high-resolution patterns generation continues to rise, it is expected that such printing process will become a standard fabrication tool that can be harnessed in wide range of technological applications.¹⁰

There are number of physical processes and constrains involved in this printing technique. These are: i) droplet formation, ii) ink requirements, iii) droplet-droplet and droplet-substrate interactions, iv) solvent drying mechanism. When the jetted colloidal droplets impinge on substrates, their final deposition morphologies are dictated by many factors such as substrate temperature and wettability,^{11,12} surface roughness,^{13,14} humidity,¹⁵ particle size and concentration,^{16,17} etc. Such factors could significantly influence the resolution and performance

of the printed patterns. A plethora of research effort have been diligently dedicated to improve our understanding of droplet formatting, impact, and droplet evaporation in inkjet printing process and their effect on the printing resolution and device functionality. However, a little is known about the potential of the dual-droplet inkjet printing of particle-laden droplets to fabricate functional devices. The influence of the self-assembly of colloidal particles at air-liquid interface, multibody interactions (i.e., particle-particle, particle-substrate, and particle-interface interactions), and deposition and assembly of colloidal particles near the three-phase contact line (TCL) on producing functional devices will be the focal point of this study. In addition, fabrication functional devices such as stretchable sensors through direct embedment and alignment of silver nanowires into elastomer substrates is also demonstrated.

1.2 Physics of Inkjet Printing

1.2.1 Droplet Formation

There are two different droplet formation mechanisms in the inkjet printing process, these are continuous and drop-on-demand inkjet printing as illustrated in Figure 1.1. In continuous inkjet printing, droplets are generated by virtue of Rayleigh instability of the liquid column, ejected from a small nozzle via piezoelectric membrane. The directionality of the jetted droplets is controlled by applying electrical potential to the nozzle, where these droplets could be steered by charged deflectors. The generated droplets are slightly larger than the diameter of the jetting nozzle. When no jet is needed, the charged droplets could be guided to the gutter by the charged deflectors to recycle the unused ink. This printing method is mainly used for high-speed graphical applications

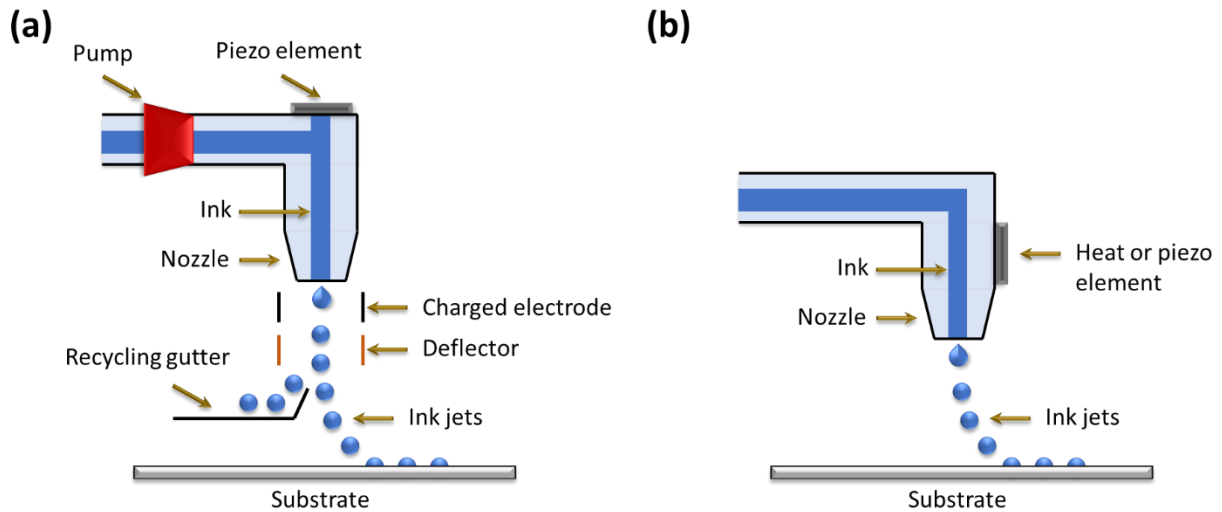


Figure 1.1: Illustration of (a) continuous inkjet printing and (b) drop-on-demand inkjet printing.

and labeling, where the drop generation rate is in range of 20-60 kHz and the droplet velocity is typically > 10 m/s.¹ However, this raises a concern about ink contamination since the ink is exposed the environment during the recirculation process.

On the other hand, in drop-on-demand inkjet printing, the droplet is generated by a pulse either thermally or piezoelectrically. Droplet positioning is achieved by locating the printhead over the desired printing spot before ejecting the ink droplet. The ink is driven by pressure propagation in the fluid chamber or by gravity. When the exerted pressure exceeds the threshold of surface tension force and the applied backpressure, which is usually used in gravity driven inkjet devices to hold the meniscus at the nozzle's tip, an ink droplet can be ejected. In a thermal drop-on-demand inkjet printing, mainly used by Canon and Hewlett-Packard,¹⁸ the ink is in direct contact with the heating element, where a bubble is generated once the ink temperature reaches the boiling point. This bubble collapses when the heating element is turned off, generating a strong pressure pulse to push the ink out of the nozzle. Therefore, the thermal drop-on-demand inkjet printing imposes restrictions on a number of polymers and inks contain volatile solvents if printed using this

approach.¹⁰ The piezoelectric drop-on-demand printing, on the other hand, relies on pressure pulses generated by an actuator, made of a piezoelectric material. In this case, droplet size and velocity could be readily tuned by controlling the actuation pulse (i.e., shape and magnitude of the pulse). For this reason, the piezoelectric drop-on-demand inkjet printing is heavily used in research and industrial applications.

In this study, two piezoelectric printheads driven by sine and trapezoidal waveforms are utilized to jet picoliter particle-laden droplets. Each nozzle consists of a micro-glass dispenser on which a piezoelectric actuator is attached. The capillary glass is connected to fluid supply tube at one end and to an orifice, in the range of 30 μm to 80 μm , at the other end. By applying a voltage to the actuator, the inner diameter of the capillary glass tube increases/decreases accordingly, producing pressure variation responsible for ejecting ink droplets. Based on the ink requirements, the waveform and other jetting parameters were tuned to optimize the jetting performance.

1.2.2 Ink Requirements

Droplet generation in inkjet printing requires specific ink physical properties based on the jetting mechanism and the diameter of the nozzle. These are: surface tension, viscosity, and density.¹⁹ Such parameters are not only crucial for droplet formation but also critical to droplet spreading and deposit morphology after solvent drying. Grouping of the abovementioned ink properties into dimensionless formulas such as Reynolds (Re),²⁰ Weber (We),²⁰ and Ohnesorge (Oh)²⁰ provides a useful tool for understanding the ink behavior.²¹

$$Re = \frac{\rho u a}{\eta}, \quad 1.1$$

$$We = \frac{\rho u^2 a}{\sigma}, \quad 1.2$$

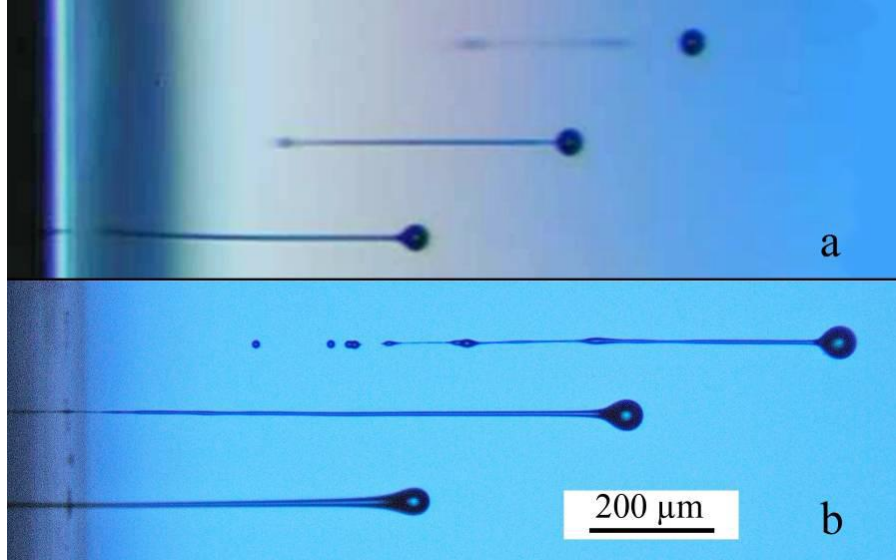


Figure 1.2: Dynamics of the jetted droplets.²²

$$Oh = \frac{\sqrt{We}}{Re} = \frac{\eta}{(\sigma\rho a)^{1/2}}, \quad 1.3$$

where ρ is the fluid density, u is droplet velocity, a is a characteristic length, σ is the surface tension of the ink, and η is the dynamic viscosity of the ink.

In inkjet printing, the ink viscosity is typically lower than 20 mPa.s.¹⁰ Otherwise, the viscous dissipation of the ink is high, and thus, no droplet could be formed. Therefore, liquids with lower viscosities are preferred in inkjet printing. Usually, the ejected droplet emerges with a long tail or a ligament that is still connect to the ink at the nozzle tip. At the final rupture of the ligament, some of the ink returns to nozzle and the rest will either catch up and emerge with the ejected droplet in flight or break up to smaller satellites that adversely affect the printing resolution (Figure 1.2).²² Satellite formation is undesirable in printing applications and could be controlled by tuning the Z number, $Z = 1/Oh$. Even though the range of the Z number is not well defined,^{23,24} the general consensus is that $(1 < Z < 14)$.²¹

Additionally, the nozzle diameter with respect to colloidal particle size should be considered to prevent jetting instability and nozzle clogging.²⁵ The rule of thumb is to keep the particle size to nozzle diameter ratio close to 1/50. However, different particle to nozzle ratios have been demonstrated (i.e., larger than 50% of the nozzle diameter) by printing large graphene oxide flakes.²⁶

1.2.3 Droplet-Droplet and Droplet-Substrate Interactions

1.2.3.1 Droplet Impact and Spreading

Inertial forces, capillary forces, and gravitational forces have a great influence on droplet impact and spreading on substrates. The dimensionless numbers used to predict and analyze the impact and spreading of colloidal droplets on surfaces are Reynolds (Re), Weber (We'), Capillary (Ca), and bond (Bo) numbers. The capillary and bond numbers are expressed in eq. 1.4 and eq. 1.5 below.

$$Ca = \frac{\eta u}{\sigma} \quad 1.4$$

$$Bo = \frac{\rho g a^2}{\sigma} \quad 1.5$$

where g is the gravitational acceleration. From the definition of Weber number (We'), the increase in droplet's inertia with respect to surface tension leads to splashing phenomenon upon the droplet impact on a substrate. Similarly, high Reynolds number (Re) suggests that such increase in droplet inertia enhances the spreading on substrates, where the spreading velocity is governed by the Capillary number (Ca). Droplet spreading on smooth surfaces have been intensively investigated by many research groups both theoretical and experimentally. In a moment when the jetted droplet first touches the substrate, its dynamic contact angle is assumed at its maximum value (180°). The

liquid then starts to wet and spread over the surface with a certain advancing contact line velocity at a dynamic contact angle. Both the advancing contact line velocity and the dynamic contact angle decrease gradually as the kinetic energy dissipates as a result of the friction between the liquid and the surface in addition to the liquid viscosity.^{27,28} The final static contact angle is attained if all the kinetic energy is dissipated and the TCL become pinned.²⁸ It should be noted that the pinning effect of the TCL is not only dependent on the kinetic energy of the jetted droplet and the energy of the solid, liquid, and solid-liquid interfaces but also on the surface roughness of the substrate.²⁹ Finally, in inkjet printing process, Bond number (Bo) must be considered to evaluate the effect of gravitational force on the jetted droplets. Depending on the ink physical properties and the jetting parameters, the influence of the gravitational force on the jetted droplets could be neglected and the shape of the jetted droplets on substrates is assumed to be spherical cap if the $Bo \ll 1$. This assumption doesn't hold if the TCL is not pinned.

1.2.3.2 Droplet Coalescence

Graphics printing necessitates deposition of isolated drops to generate pixelated images. However, printing continuous features such as lines for different applications requires droplet overlapping. Therefore, the key parameters for forming continuous patterns are the droplet spreading and substrate wettability, where uniform lines can be printed if there are significant low advancing and receding contact angles.³⁰ Figure 1.3 illustrates the effect of droplet spacings, delay periods, and substrate temperatures on the morphology of the printed lines.³¹ Large droplet spacing, more than twice the droplet's radius, results in isolated footprints after solvent drying. If the droplet spacing is decreased, then the isolated droplets could overlap and merge to form a scalloped pattern. The

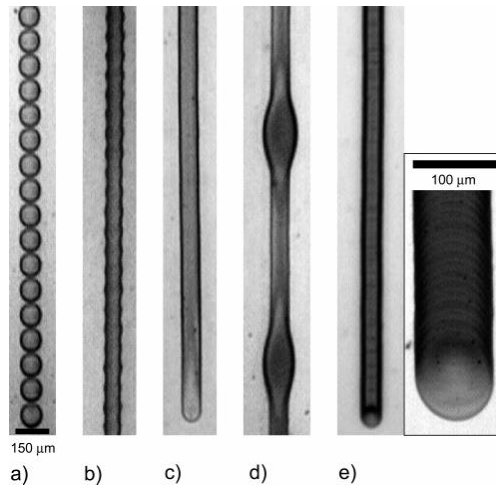


Figure 1.3: Droplet spacing effect on the coalescence behavior, (a) individual drops, (b) scalloped, (c) uniform, (d) bulging, and (e) stacked coins. Drop spacing decreases from left to right.³¹

scalloped lines are usually narrower than isolated printed droplets as fluid expansion is partially arrested. Further decrease in droplet spacing may eliminate the scalloping effect and lead to a smooth, straight uniform and narrow printed line. Printing droplets even closer could result in discrete bulging along the printed line, separated by regions of uniform narrow lines. These bulges tend to form periodically in the middle and at the leading edges of the printed lines. The dynamic

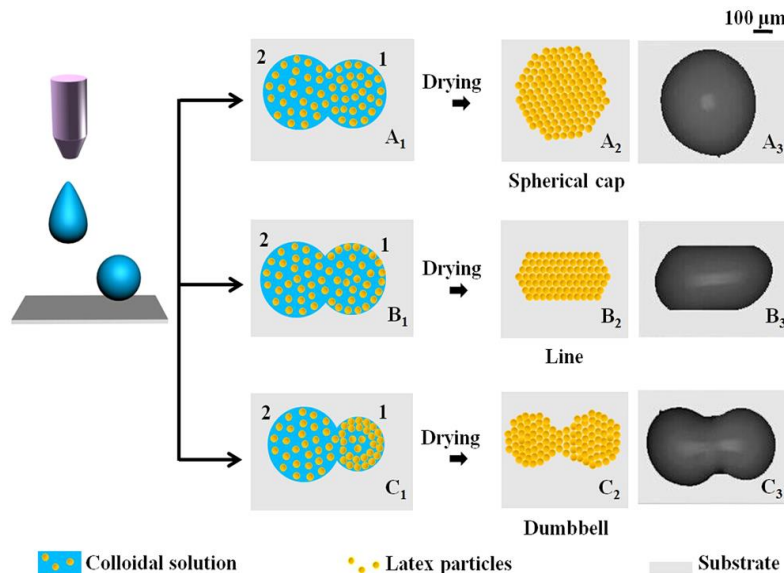


Figure 1.4: Droplet coalescence scenarios, induced by different dynamic wettabilities of ink droplets on substrates. The difference among (A1, B1, and C1) is the surface tension and nanoparticle concentration, which resulted in different dynamic wettabilities of ink droplets on the substrates. This, in turn, have led to (A2, A3) spherical cap deposition, (B2, B3) continuous line deposition, and (C2, C3) dumbbell structure after coalescing and drying.³²

wettability on substrates via controlling the surface tension of the printed droplets have been reported to influence the coalescence of sessile droplets. Figure 1.4 displays different droplet coalescence scenarios, which resulted in spherical, straight line and dumbbell particle depositions.³² The surface tension of the printed droplets could be manipulated by varying the delay time introduced between the consecutive printed droplets that affected the nanoparticle concentration and solvent composition.

1.2.4 Solvent Evaporation

Solvent evaporation is of great importance in a number of technological applications such as inkjet printing, where the deposit morphology is significantly influenced by the solute distribution after solvent drying. Commonly, when a particle-laden droplet is deposited on a solid surface, its solute tends to aggregate at the TCL region. Two decades ago, Deegan et al. were the pioneers in explaining the phenomenon of the coffee-ring effect (CRE), where they observed that the solvent evaporation rate is the highest near the edge of the droplet.^{33,34} If the droplet has pinned contact lines, the excess solvent loss through the edge must be replenished by a fluid from the bulk so that the droplet retains its equilibrium state. This, in turn, initiates a lateral evaporative-induced convective flow that drives the suspended colloidal particles to the TCL region, forming a ring-like deposit. The CRE is considered detrimental in printing applications. Recently, significant research efforts have been devoted to suppress or mitigate the coffee-ring formation by means of, controlling the drying conditions of solvents (e.g., substrate temperature,¹¹ relative humidity,¹⁵ and volatile solvents³⁵), modifying particle shapes,^{36,37} adjusting substrate wettability,^{12,38} and intentionally inducing Marangoni flow due to surface tension gradient that is generated by temperature difference across the interface, surfactant, or cosolvent,³⁹⁻⁴³ etc. Therefore,

understanding these different mechanisms is of significant importance for controlling the particle depositions, which is proven to be advantageous in a wide range of technological applications such as inkjet printing of electronic,^{10,44–48} optical,^{49,50} and biomedical devices,^{51–53} to name a few. More details are presented in the following chapters to provide a solid understanding of the drying mechanism and pattern formation upon the evaporation of particle-laden sessile droplets.

1.3 Motivation and Objectives

Undoubtedly, inkjet printing will become an indispensable tool for fabricating functional devices in the near future. So far, it has been demonstrated that such printing process is a viable method for fabricating optic/electro devices, sensors, biochips, displays, and other devices. The potential that the inkjet printing has such as low-cost, speediness, convenience, flexibility made it a strong rival for other conventional printing processes (i.e., photolithography, screen printing, etc.). However, as briefly mentioned in the previous section, inkjet printing of functional materials is usually associated with the so-called coffee-ring effect (CRE), especially when the solute migrates to the contact line region by virtue of the evaporative-induced convective flow. Even though, the feasibility of exploiting the CRE in some applications has been demonstrated, it is considered detrimental in inkjet printing applications, where the performance of the printed patterns is significantly affected by the deposit morphology and printing resolution. Therefore, deep understanding of ink properties, material interactions, and material self-assembly is crucial for fabrication functional devices with precise footprints.

To date, a plethora of research have been dedicated to provide a better understanding of solvent evaporation and particle migration to the edge of the sessile droplets in addition to ways to mitigate or totally suppress the coffee-ring formation. Yet, a little is known about the self-assembly and the

multibody interactions of colloidal particles at the air-liquid interface of sessile droplets and their contribution to the TCL pinning and the CRE suppression.

In conventional inkjet printing, sessile droplets are directly printed on substrates. Upon solvent evaporation, the particle deposition may be either ring-like or uniform with no closely-packed, monolayer of particles. Different techniques were examined in this study in order to provide preventative solutions to the coffee-ring formation. We employed the dual-droplet inkjet printing to investigate the self-assembly of colloidal particles in sessile droplets and its impact on particle deposition. The dual-droplet printing method is used to transform the Langmuir–Blodgett (LB) concept to picoliter droplets, generated by inkjet. Deposition of monolayer nanoparticle films is achieved by consecutive dual-droplet printing of supporting droplets and wetting droplets. The supporting droplet acts as the LB trough, and the wetting droplet contains colloidal nanoparticles. The colloidal particles spread and assemble over the air-liquid interface of the supporting droplet as the solvent dries to produce a uniform, nearly monolayer, closely-packed deposition of nanoparticles with no particle accumulation at the TCL. Additionally, the self-assembly of colloidal particles in sessile droplets printed on porous substrates through exerting external magnetic field to tune the magnetic anisotropic properties and suppress the CRE was also investigated.

The second goal of this study is to emphasize and further elucidate the potential of inkjet printing in fabricating functional devices such as stretchable conductors. Stretchable conductors have attracted great attention owing to their potential applications as electrodes for wearable electronic devices. However, conventional stretchable conductors, made by depositing conductive materials on the surface of stretchable substrates, often show mechanical instability between the substrate and the conductive materials, posing a significant hurdle for stretchable electronics. Recently,

silver nanowire based stretchable conductors have been demonstrated by different approaches. Yet, direct embedment of silver nanowires into a liquid elastomer remains a critical challenge. In this study, we developed one-step inkjet printing and embedment of silver nanowires in elastomer substrates for stretchable conductors, which significantly enhanced the mechanical stability and electrical performance of the printed patterns. This study uncovers facile techniques to control the assembly and deposition of colloidal inks through liquid process, which is of huge interest in enormous industrial and research applications, especially for inkjet printing of functional devices.

1.4 Outline

The material interactions and self-assembly of colloidal inks in inkjet printing applications at different length scales were investigated in this study. The potential of inkjet printing has been harnessed through employing different printing techniques such as the dual-droplet inkjet printing of colloidal particles to investigate the self-assembly of colloidal nanoparticles at the air-liquid interface of sessile droplets, and direct printing of functional materials on various types of substrates (i.e., porous substrates and elastomer substrates) to provide better understanding of the deposition morphologies and their functionalities after solvent evaporation. The chapters of this dissertation are organized as follows: Chapter 2 is a literature review of the recent advances in the self-assembly of colloidal inks affected by the multibody interactions (i.e., particle-particle, particle-substrate, particle-interface interactions) of colloidal nanoparticles in sessile droplets. Chapter 3 introduces the dual-droplet inkjet printing mechanism for generating monolayers, closely-packed deposition of colloidal nanoparticles, where nanoparticle networks were generated by jetting multiple wetting droplets with different particle sizes. Chapter 4 investigates the pH modulating in dual-droplet inkjet printing and its effect on the multibody interactions to suppress

the CRE. Chapter 5 is probing of the colloidal particle dynamics in evaporating sessile droplets, where the particle assembly and deposition in vicinity of the TCL in both the conventional and dual-droplet inkjet printing were examined. Chapter 6 studies the effect of applying external magnetic field on the magnetic particle assembly on porous substrates. The printed features exhibited one-dimensional (1D) patterns with anisotropic magnetic properties, which mitigated coffee-ring formation. Chapter 7 explores the ability to utilize the inkjet to fabricate stretchable conductors by embedding colloidal droplets of silver nanowires into elastomer layer. The last chapter is overall conclusions and recommendations for future work.

CHAPTER 2 Literature Review

The importance of inkjet printing and the associated printing physics were introduced in chapter one. The present chapter provides an overview of the literature concerning controlling the deposition morphologies of inkjet printing, including suppressing the CRE by means of manipulating the flow field and adjusting the multibody interactions (i.e., particle-particle, particle-interface, and particle-substrate interactions).

2.1 Motivation for Investigating the Coffee-Ring Effect

Drying of particle-laden droplets on a substrate usually leaves ring-like deposits that is known as the coffee-ring effect (CRE).⁵⁴⁻⁵⁶ This ubiquitous phenomenon is familiar to everyone who has observed drying of coffee spills. Deegan et al. were the pioneers who first investigated this remarkable observation two decades ago.^{33,34,57} The driving force behind such an omnipresent process is the non-uniform evaporation flux taking place at the air-liquid interface of the sessile droplet, where it is found to be higher in vicinity of the TCL.^{9,34} The greater liquid loss at the edges must be replenished from the bulk liquid of the sessile droplet. This, in turn, initiates an outward flow referred to as evaporation-induced flow that drives the particles to the contact line.^{34,58} As a result, a ring-like shape pattern is evolved as the solvent completely evaporates. Figure 2.1 illustrates the colloidal particle migration to the TCL during solvent evaporation process.

Following the seminal work of Deegan and coworkers, particle deposition and assembly structure, obtained from evaporating particle-laden droplets, have been subjected to a plethora of theoretical and experimental studies for scientific and industrial applications. The research endeavors to

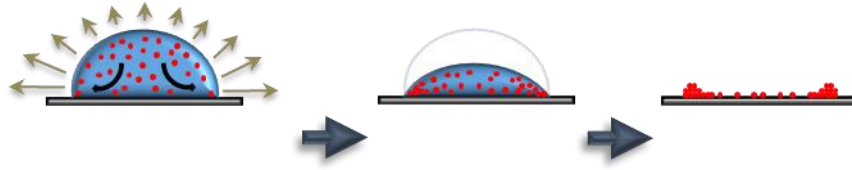


Figure 2.1: Illustration of the coffee-ring formation.

understand the drying mechanisms of colloidal droplets revealed some crucial factors affecting the coffee-ring formation, particularly, surface wettability and contact line dynamics, solvent evaporation, and properties of the colloidal particles (e.g., particle size and shape, functional groups, hydrophobicity, charge density of the particles, etc.).⁵⁹ To date, considerable efforts have been devoted to counteract the colloidal particles' migration to the contact lines by means of, controlling the drying conditions of solvents (e.g., substrate temperature,¹¹ relative humidity,¹⁵ and volatile solvents³⁵), modifying particle shapes,^{36,37} changing solvent density and viscosity,⁶⁰ adjusting substrate wettability,^{12,38} initiating acoustic field,⁶¹ and exerting electrowetting.⁶² Although the CRE has been demonstrated as a potential tool to be implemented in some disciplines such as particle separation^{63–65} and disease detection.^{66,67} This phenomenon is deemed detrimental and must be avoided in many technological applications such as producing coatings and patterns,^{31,68,69} fabricating functional microarrays,^{70–72} and detecting biomolecules by various spectroscopy techniques.^{73,74} Therefore, understanding these different mechanisms of suppressing or mitigating the CRE is of significant importance for controlling the particle depositions, which has proven to be advantageous in a wide range of inkjet-printed functional devices such as electronic,^{10,44–48} optical,^{49,50} and biomedical devices,^{51–53} to name a few.

2.2 Multibody Interactions in an Evaporating Particle-Laden Droplet

In an evaporating particle-laden droplet on a solid substrate, multiple bodies (e.g., colloidal particles with various functional groups and charge levels, solvent(s), substrates with different surface chemistry and heterogeneities, and ambient gas phase) interact with each other during solvent evaporation. Such intricate interactions affect droplet wetting and contact line pinning behavior (solvent-substrate interaction), evaporation-induced flow (air-liquid interaction), and ultimately particle deposition that is influenced by particle-particle, particle-flow, particle-substrate, and particle-interface interactions. It is beneficial to introduce how the multibody interactions affect and direct the particle assembly and deposition, because similar interactions could be utilized to enable particle assembly at the air-liquid interface.

Yan et al. studied the assembly of charged colloidal particles on charged glass substrates near the contact line of an evaporating sessile droplet.⁷⁵ The colloidal particle mobility and ordering in vicinity of the contact line were highly impacted by the particle-substrate interactions. For colloidal particles possessing the same surface charge as the substrate, they were readily transported to the edge of the sessile droplet by virtue of the convective flow resulting in ordered, self-assembled ring-like depositions. Conversely, opposite charges of colloidal particles and substrates led to a decrease in particle mobility and poor particle packing at the contact line region. The lack of particle orderliness was attributed to the strong Coulombic attraction forces between the spherical particles and the substrate, whereas no such Coulombic adhesion was present in systems with alike surface charges of particles and substrates (Figure 2.2a and 2.2b). Similar particle-substrate interactions were observed when ionic and nonionic surfactants were introduced to the system, affecting the final particle deposition. The authors also commented on the role of

hydrophobic interactions between surfactant coated particles and substrate, causing the particles to strongly adhere to the substrate.

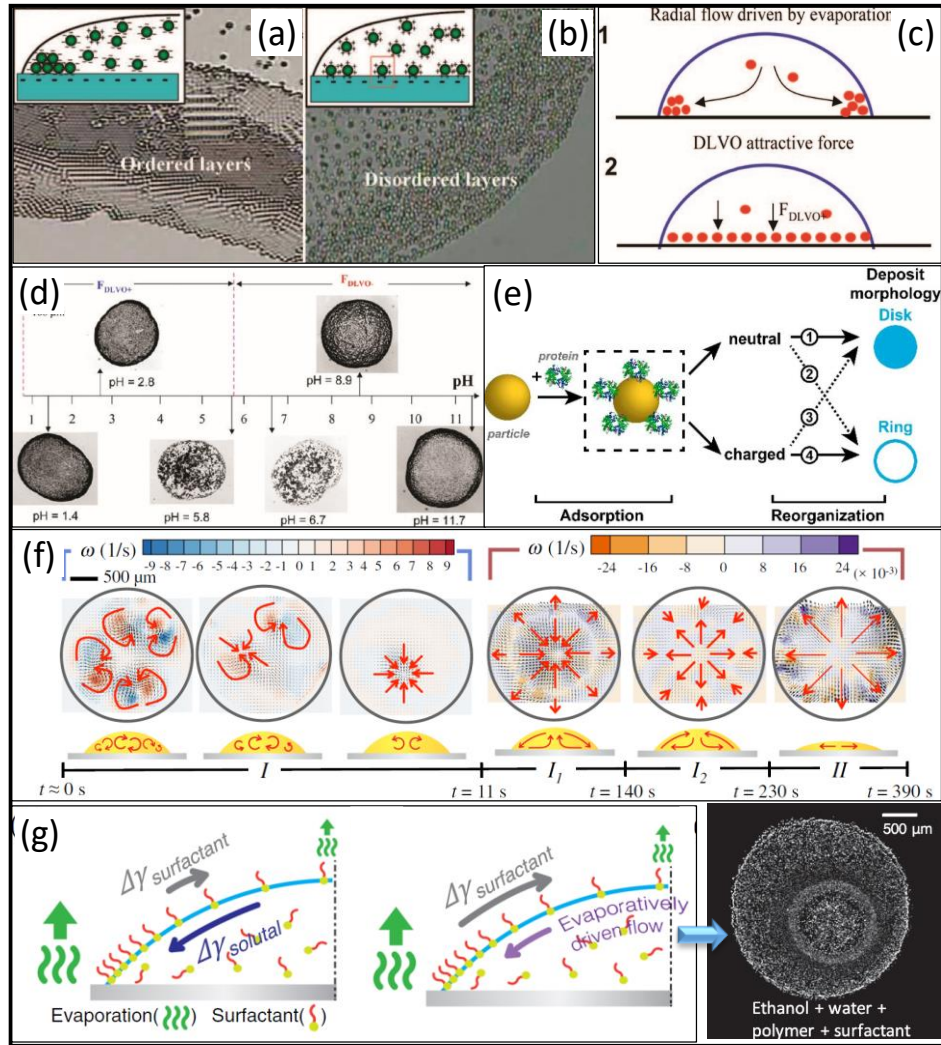


Figure 2.2: (a) Assembly of negatively charged colloidal particles and (b) positively charged colloidal particles at the edge of the sessile droplet on a negatively charged glass substrate, which demonstrated the order to disorder assembly structures at the contact line.⁷⁵ (c) Schematic illustration of the impact of DLVO force on the particle deposition, where a system lacking the DLVO interaction results in a ring formation, while having such attractive DLVO force renders more uniform particle depositions and (d) particles deposition change with respect to pH value.⁷⁶ (e) Illustration of the influence of protein adsorption on the particle deposition. Manipulating the surface charge of the colloidal particles resulted in different particle-particle and particle-substrate electrostatic and hydrophobic interactions as indicated by the four routes.⁷⁷ (f) Flow field pattern representations observed in a drying Whisky droplet, and (g) schematics of solutal and surfactant Marangoni flows. The ethanol/water and surfactant mixtures do not produce uniform particle deposition unless they are combined with a polymer to enhance the particle adhesion to the substrate.⁴³

Bhardwaj et al. examined the particle deposition obtained from drying nanoliter droplets containing titania nanoparticles on glass substrates.⁷⁶ Changing the pH of the suspension resulted in different particle depositions ranging from ring-like to uniform deposition structures. This transition in deposit patterns was explained by the Derjaguin-Landau-Verwey-Overbeek (DLVO) interactions (i.e., electrostatic and van der Waals forces) between the particles and the substrate. The zeta potential of the particles changed from positive to negative when the pH level of the suspension increased from low (acidic) to high (basic) conditions, whereas the glass substrate retained negative zeta potentials for most of the pH conditions. The deposition of titania nanoparticles at different pH values is presented in Figures 2.2c and 2.2d. At an extreme acidic environment, the particle deposition had a thin uniform film of particles with a thick ring of particles at the TCL. The particles close to the substrate were attracted toward the substrate under the attractive DLVO force as a result of the particle-substrate interaction, forming a uniform thin layer of nanoparticles. However, since the Debye length was much less than the droplet height, the rest of the suspended particles were carried by the capillary flow to the contact line, resulting in a thicker ring at the periphery. The titania nanoparticles were observed to agglomerate and randomly scatter throughout the deposits at intermediate pH values. At this point, the titania nanoparticles became nearly neutral leading to a weaker particle-substrate DLVO interaction than the van der Waals forces among the particles. Extremely basic environments, on the other hand, enhanced the repulsive particle-particle and particle-substrate DLVO interactions preventing the nanoparticles from depositing onto the substrate. As a result, most of the particles followed the outward radial flow and accumulated at the contact line.

Devineau et al. investigated how the adsorption of charged proteins on colloidal particles can alter the particle deposition on a glass substrate.⁷⁷ The amount of the adsorbed protein and the charge

on the original colloidal particles affect the electrostatic interactions between the particles and the substrate in a similar way as described above, and correspondingly alter the final deposition structures (Figure 2.2e).

Anyfantakis and coworkers studied the influence of the particles' hydrophobicity on the deposit morphology.⁷⁸ The surface wettability of silica nanoparticles were controlled by the reaction of silanol group with dichlorodimethylsilane. Based on the hydrophobicity and concentration of nanoparticles in the suspension, the particle deposition varied from ring to dome-like shape. While most hydrophilic particles always tend to deposit along the droplet periphery, the hydrophobic particles tend to lump in the center of the droplet. The variation in deposit morphology is attributed to the particle-particle interactions determined by the surface chemistry of the colloidal particles. The interparticle interactions were repulsive due to the negative charges on the non-modified nanoparticles (100% SiOH). However, decreasing the SiOH groups has weakened the particle-particle electrostatic repulsion that generated dome-like morphologies as a result of the hydrophobic particle-particle interactions. The authors also pointed out that the gel transition played an important role in their system, which contributed to the dome-like deposition of hydrophobic particles under high solid concentrations. A similar gelation strategy has been utilized in limiting the evaporation-induced flow to change the particle deposition.⁴¹

Kim et al. investigated the influence of binary solvent mixture, surface-active surfactant, and surface-adsorbed polymer on the final deposition pattern.⁴³ The motivation behind this study was to identify the mechanism of the uniform particle deposition left after drying Whisky droplets and to replicate its uniform deposition using controlled sessile droplets. The Whisky is an ethanol/water mixture with diverse dissolved molecules. Different flow behaviors were recorded as the Whisky droplet evaporated and organized as follows: i) chaotic mixing, ii) radially outward

flow along the air-liquid interface and radially inward flow along the substrate, iii) radially outward flow along the substrate and radially inward flow along the air-liquid interface, and iv) outward capillary flow at the final stages of solvent evaporation (Figure 2.2f). In order to mimic the flow patterns of a drying Whisky droplet, an ethanol/water mixture (35:65 wt%) was used as a solvent. The flow patterns of i) and ii) were obtained due to the solutal Marangoni flow, however, the absence of the last two flow patterns resulted in failure in the formation of uniform particle depositions. The notion behind the uniform particle deposition obtained from drying Whisky droplets is the natural phospholipids (natural surfactant) and natural polymers (i.e., lignin and polysaccharides). Introducing sodium dodecyl sulfate (SDS) to the ethanol/water mixture helped to replicate the same flow patterns observed in evaporating Whisky droplets. Solutal and surfactant Marangoni flows were observed during the drying process because of the higher ethanol evaporation rate followed by the SDS accumulation at the edge of the sessile droplet. Although the flow patterns of evaporating Whisky droplets were mimicked by introducing SDS surfactant to the ethanol/water binary mixture, the particle deposition was not uniformly distributed on the substrate. This issue was addressed by adding polyethylene oxide (PEO) polymer that resembled the natural polymers in Whisky droplets, which assisted the adherence of the suspended particles to the substrate (Figure 2.2g).

2.3 Particles Assembly at the Air-Liquid Interface

Self-assembled monolayer films of colloidal particles are excellent candidates for fabrication of functional coatings and devices.^{79,80} The recent advances in colloidal particle deposition from the air-liquid interface have mitigated or suppressed the CRE and demonstrated highly ordered monolayer assembly of the deposition structures. This provides an excellent opportunity in the

fabrication of functional coatings and devices through liquid processing. This self-assembly process does not involve particle-substrate interactions until the last stage of evaporation since the particles are adsorbed and assembled at the interface. Therefore, it is suitable for a wide variety of substrates, which reduces the dependence on the chemical and physical homogeneity of the substrates.

Several factors contribute to the self-assembly process of colloidal particles adsorbed at the air-liquid interface such as capillary, Van der Waals, and electrostatic forces.⁸¹ The latter two interactions are included in the DLVO forces. Perhaps the most important particle-particle interaction at the interface is the lateral capillary force initiated by interfacial deformation.⁸²⁻⁸⁵ The basic concept behind this interaction is minimizing the interfacial deformation energy that is greatly affected by the particle's size, shape, and wetting property. Flootation forces (originated by gravity and buoyancy) and immersion forces (due to the wetting properties of the particles) induce interfacial deformation around the particles. The capillary interaction between these particles can be attractive or repulsive, depending on whether the overlapping interfacial deformation around the two particles are analogous.⁸²⁻⁸⁵ Monodisperse particles with similar wetting properties result in attractive capillary interactions at the air-liquid interface. Similarly, strong and long-ranged capillary attractions have been reported for ellipsoidal particles at an oil-water interface,⁸⁶ which can be approximately two orders of magnitude stronger than their spherical counterparts.⁸⁷ In addition, surface curvature also plays a critical role in the capillary assembly.⁸⁸

When the particles adsorb at the interface, they experience the capillary attraction (in most cases) along with the DLVO forces to form self-assembled structures at the interface. In this section, I will review different routes of delivering colloidal particles to the air-liquid interface.

2.3.1 Particles Pushed to and Adsorbed at the Interface

Bigioni and coworkers formed monolayer depositions of dodecanethiol-ligated gold nanoparticles in toluene by pushing them to the air-liquid interface of the sessile droplets.⁸⁹ Direct, real-time and real-space observations of the self-assembly of colloidal particles have been observed on the air-liquid interface during the solvent evaporation process. The nucleation and growth of the monolayer islands of gold nanoparticles were controlled via evaporation kinetics and particle-interface interactions. The mechanism of such self-assembly process requires two key steps: i) rapid solvent evaporation that segregates the colloidal particles near the air-liquid interface, where the interface descending velocity must be higher than the diffusion velocity of the colloidal particles; ii) Once the colloidal particles reach the interface, the attractive particle-particle capillary interactions facilitate the network formation with exceptional long-range ordering (Figure 2.3a). The monolayer formation at the air-liquid interface was found highly dependent on the excess amount of dodecanethiol ligand in the system, where no nucleation and growth of gold islands were observed when the system was cleaned of excess dodecanethiol and vice versa. Although the details of the underlying mechanism have not been unveiled in the original paper, it is hypothesized that the hydrophobic dodecanethiol-functionalized gold particles play a critical role in pushing the particles to the interface and forming the floating islands through self-assembly. Boley and coworkers demonstrated a hybrid self-assembly of thiol-capped Ga-In particles using a cosolvent system (a mixture of ethanol/water).⁹⁰ The cosolvent in the sessile droplet segregated during the solvent evaporation, resulting in a concentrated shell of the solvent with high vapor pressure (ethanol) near the droplet interface and a water enriched core. Consequently, the suspended particles, being hydrophobic and more stable in ethanol, favored to transport toward the air-liquid

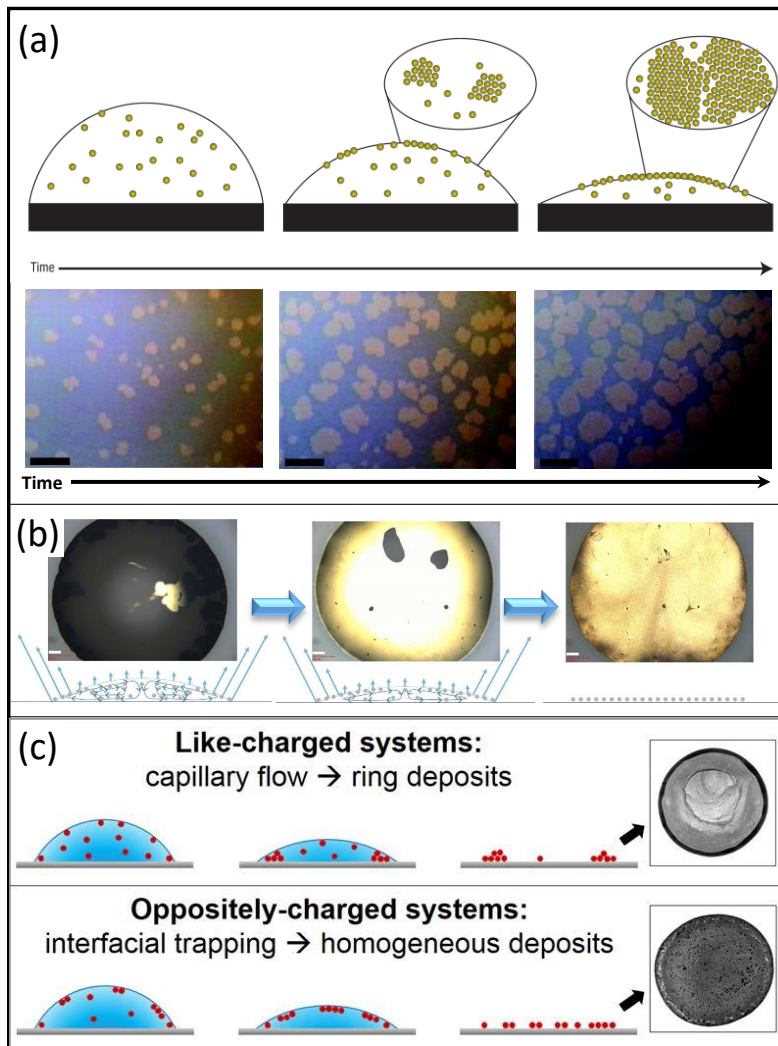


Figure 2.3: (a) Illustration of the particle self-assembly at the air-liquid interface during solvent evaporation (the top row). The second row is the optical images showing monolayer islands formation of dodecanethiol-passivated gold nanocrystals at the interface during the evaporation process. Scale bars are 50 μm .⁸⁹ (b) Optical images showing the self-assembly of thiol-capped Ga–In nanoparticles at the air-liquid interface in a cosolvent system (water/ethanol mixture), presented at different stages of solvent evaporation.⁹⁰ (c) Schematic illustration of the surfactant-mediated electrostatic and hydrophobic interactions among the particles, the air-liquid, and liquid–substrate interfaces. For a system with like-charged particle/surfactant mixtures, a ring-like particle deposition was obtained after solvent evaporation. However, uniform particle deposits were obtained when utilizing oppositely charged systems.⁹¹

interface. Once the particles were carried to the surface of the droplet, they self-assembled into orderly monolayer films due to the particle-interface interactions (Figure 2.3b).

Anyfantakis et al. studied the influence of surfactant-mediated interactions on the particle deposition morphology.⁹¹ Introducing surfactant to the system affected the particle-particle,

particle-interface, and particle-substrate electrostatic and hydrophobic interactions, which dictated the final deposit morphology. Such interactions were modulated based on surfactant type and concentration, charges on the particles, and the substrate. When the colloidal particles possessed surface charges similar to the polarity of the surfactant available in the system, a ring-like particle deposition was always the case. However, introducing surfactants with opposite charges of the colloidal particles generated different outcomes, where different particle deposit morphologies have been reported, ranging from ring-like to disk-like deposits. In this case, intermediate surfactant concentrations resulted in lower absolute zeta potential values and higher particle hydrophobicity, leading to homogeneous particle depositions. In addition, some of the colloidal particles were noticed to adsorb at the air-liquid interface, forming a skin of colloidal particles during the evaporation process (Figure 2.3c). In contrast, higher surfactant concentrations resulted in charge reversal of the colloidal particles by which the ring-like deposits were retrieved. Similar ring-like particle depositions were observed at low surfactant concentrations.

Zhang et al. examined the self-assembly of thiolated single-stranded DNA-functionalized Au nanoparticles (ssDNA-AuNPs) at the vapor-solution interface by manipulating salt concentrations.⁹² Although the interfacial assembly did not occur in an evaporating droplet, this work introduced some interesting mechanisms driving the colloidal particles to the interface. A trough containing the colloidal suspension with various salt concentrations was placed inside a sealed chamber to monitor the self-assembly process, using liquid surface X-ray scattering. While the hydrophobic nature of the nanoparticles facilitated the particle transport to the interface, the assembly and crystallization process was influenced by the critical salt concentration as a result of charge screening of the DNA. A similar observation has been reported when manipulating pH and

salt concentration of colloidal suspensions containing AuNPs functionalized with alkylthiol-terminated poly(acrylic acid) (PAA).⁹³

Anyfantakis et al. also reported the possibility of colloidal particle adsorption and network formation at the air-liquid interface. Surfactant concentrations below the critical micelle concentration (CMC) enhanced the particle adsorption and assembly, without significantly affecting their surface charge and wetting properties.⁹⁴ The particle adsorption was attributed to the preferential adsorption of the surfactant to the interface, which reduced the energy barrier between the interface and the like-charged particles. This facilitated the adsorption of particles at the interface. The author also commented on the degree of the packing and arrangement of particles at the interface influenced by particle and surfactant concentrations. However, since the assembly process is much slower compared to typical droplet evaporation, it was not applied to evaporating droplets in this work. Interested readers can refer to the article for more details.

2.3.2 Particles Captured by the Descending Air-Liquid Interface

Li and coworkers proposed a different mechanism to suppress the CRE through capturing and self-assembling the colloidal particles onto the rapidly descending air-liquid interface.⁹⁵ Evaporation of the colloidal droplet was performed in an environmental chamber with a constant temperature and humidity. Elevating the evaporation temperature reduced the number of particles deposited at the periphery of the evaporative sessile droplet, producing more uniform particle deposition (Figure 2.4a). On the contrary, if the same colloidal droplets were left to dry under normal conditions, a ring-like structure could evolve, especially when the contact lines remain pinned. This behavior was explained by the particle adsorption and assembly at the descending interface.

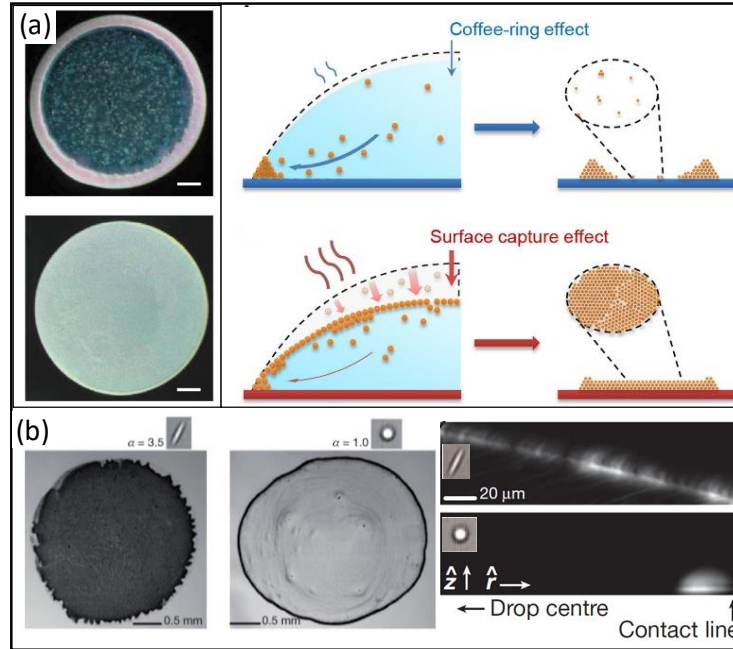


Figure 2.4: (a) Ring formation of colloidal droplets dried at room temperature versus uniform particle deposition of evaporating the same colloidal system in an environmental chamber at an elevated temperature. The colloidal particles were captured by the fast descending interface, forming uniform particle deposition. Scale bars are 0.5 mm.⁹⁵ (b) Effect of particle shape on the particle deposition.³⁷ The ellipsoidal particles tend to adsorb at the air-liquid interface during the evaporation, resulting in uniform depositions as opposed to the ring-like depositions of spherical particles. The confocal microscope images shown on the right demonstrate the adsorption of ellipsoidal particles at the air-liquid interface and accumulation of the spherical particles at the contact line.

At a sufficiently high evaporation temperature, the descending rate of the air-liquid interface is faster than the diffusion rate of the colloidal particles returning to the bulk, which facilitates capturing the neighboring particles by the interface. In this case, the particle jam at the interface increases the surface viscosity much higher than that of the bulk to resist the outward capillary flow, leading to more uniform particle deposition. The author also reported that transitional particle deposition composed of the particles accumulated at the edge of the deposit along with the particles adsorbed at the interface could be obtained at moderate evaporation temperatures.

Changing the particle shape is another approach proposed for eliminating the CRE, where elongated particles have been observed to adsorb at the air-liquid interface during solvent evaporation process. Yunker and coworkers proved experimentally that the particle anisotropy is

a crucial factor in determining the uniformity of particle depositions during the solvent evaporation process.³⁷ Polystyrene particles were stretched asymmetrically to different aspect ratios and dispersed in water. Then, the colloidal droplets were left to dry on a glass slide. While spherical or slightly deformed (aspect ratio $\alpha = 1 - 1.1$) colloidal particles were efficiently transported to the contact line by the evaporative-driven capillary flow, ellipsoidal particles with aspect ratio $\alpha > 1.1$ were deposited uniformly during solvent evaporation. In a similar fashion, as their spherical counterparts, the ellipsoidal particles were entrained to the edge of the sessile droplet by virtue of the outward capillary flow until they were caught by the descending air-liquid interface. Once the particles were captured by the interface, they experienced strong, long-range interparticle attraction forces, forming loosely-packed arrested structures at the interface (Figure 2.4b). Additionally, the adsorption of ellipsoidal particles to the interface increases the local viscosity, which resists the outward capillary flow. Spherical colloidal particles, however, were desorbed from the interface back to the bulk of the droplet due to much weaker interparticle attraction forces than that of ellipsoidal particles. The author also demonstrated that mixing ellipsoidal particles with spherical ones helped suppressing the ring formation, where the spherical particles joined the assembled structure, producing a uniform particle deposition. Kim et al. further elaborated on the interparticle capillary force and the hydrodynamic force exerted on the ellipsoidal particles using an analytical model.⁹⁶ When the capillary force is greater than the hydrodynamic force, the ellipsoids form a stable network at the interface inhibiting their migration to the TCL. On the other hand, when the hydrodynamic force is greater than the capillary force, the particles could not remain at the interface, instead they are transported to the TCL under the dominating hydrodynamic force. The experiments agreed reasonably well with the analytical analysis. No such adsorption of ellipsoidal particles at the air-liquid interface were reported when surfactant was

introduced to the system due to the decrease in the surface tension of the droplet and lowering the interface deformation energy.³⁷

Dugyala and Basavaraj investigated the charge effect of colloidal hematite ellipsoids on the interfacial adsorption and final particle deposition. pH modulation and the DLVO interactions have been adopted to tune the charge and zeta potential of the ellipsoids.³⁶ A similar general trend has been observed as in the work of Bhardwaj et al., i.e., ring formation occurred for extreme acidic and basic conditions while uniform deposition was observed for the intermediate pH levels (pH 6.5 and 8).⁷⁶ However, the Dugyala and Basavaraj attributed the uniform deposition to the adsorption of particles at the interface due to the weakened image charge effect in the low dielectric medium (air). This hypothesis was partially supported by the fact that the ellipsoidal hematite particles adsorbed to the surface of a pendant droplet in a decane medium under intermediate pH conditions, whereas no particle adsorption occurred in extreme acidic solutions. The colloidal droplet was suspended in the decane medium to avoid the solvent evaporation. This also showcases the complexity of the multibody interactions involved in the evaporation of colloidal particles on a solid substrate.

CHAPTER 3 Interfacial Self-Assembly of Colloidal Nanoparticles in Dual-Droplet Inkjet Printing

3.1 Introduction

When a particle-laden droplet evaporates on a substrate, very often the particles form a ring at the TCL when the solvent evaporates. This well-known CRE is a result of faster evaporation at the droplet TCL, driving the colloidal particles to convectively transport toward the droplet edges.^{33,34,97} For applications in printed electronics, this non-uniform deposition is particularly detrimental to the device performance. The complex multibody interactions, e.g., droplet–substrate interaction, particle–substrate interaction, and droplet–environment interaction, ultimately determine the final deposition and morphology of the printed patterns.^{17,32,41,98–100} Various approaches have been explored to modify these interactions in order to control the TCL dynamics and/or to induce Marangoni flow, driven by the surface tension gradient, at the air–droplet interface, including tuning substrate wettability,^{12,101} application of surfactant additives and cosolvent systems to the droplet,^{102,103} vapor absorption of low-surface tension solvents to the droplet,³⁵ etc. In these techniques, the colloidal particles are carried back to the center of the droplet either by the depinned TCL or by Marangoni flow to suppress the CRE. In addition, stronger interactions between colloidal particles and substrates, e.g., electrostatic and van der Waals interactions,⁷⁶ and increased adhesion through substrate treatment,⁴³ etc. also facilitate a uniform deposition. Recently, attempts have been made to push the colloidal particles onto the droplet surface to facilitate the particle self-assembly at the air–droplet interface.⁸⁹ Boley et al. have employed a cosolvent system for the colloidal particles.⁹⁰ During evaporation, the colloidal particles which were well-dispersed in the solvent with a higher vapor pressure were carried to the droplet surface due to faster evaporation of this solvent component. Li et al. have accelerated the

solvent evaporation rate to trap the particles at the droplet interface by elevating the environment temperature.⁹⁵ At a high environment temperature, the air–droplet interface shrinkage rate exceeds the particle diffusion rate such that the colloidal particles are captured by the descending surface, producing a particle jam, which prevents the particles from being transported to the droplet edge. The charges of surfactant-decorated particles have also been tuned to become nearly neutral,^{77,91} which promotes particle trapping at the air–droplet interface to render a homogeneous deposition. In this work, we employ a dual-droplet configuration to transform the Langmuir–Blodgett (LB) concept to the picoliter droplets, generated by inkjet printing. Deposition of monolayer nanoparticle films is achieved by consecutive dual-droplet printing of a supporting droplet and a wetting droplet (Figure. 3.1).

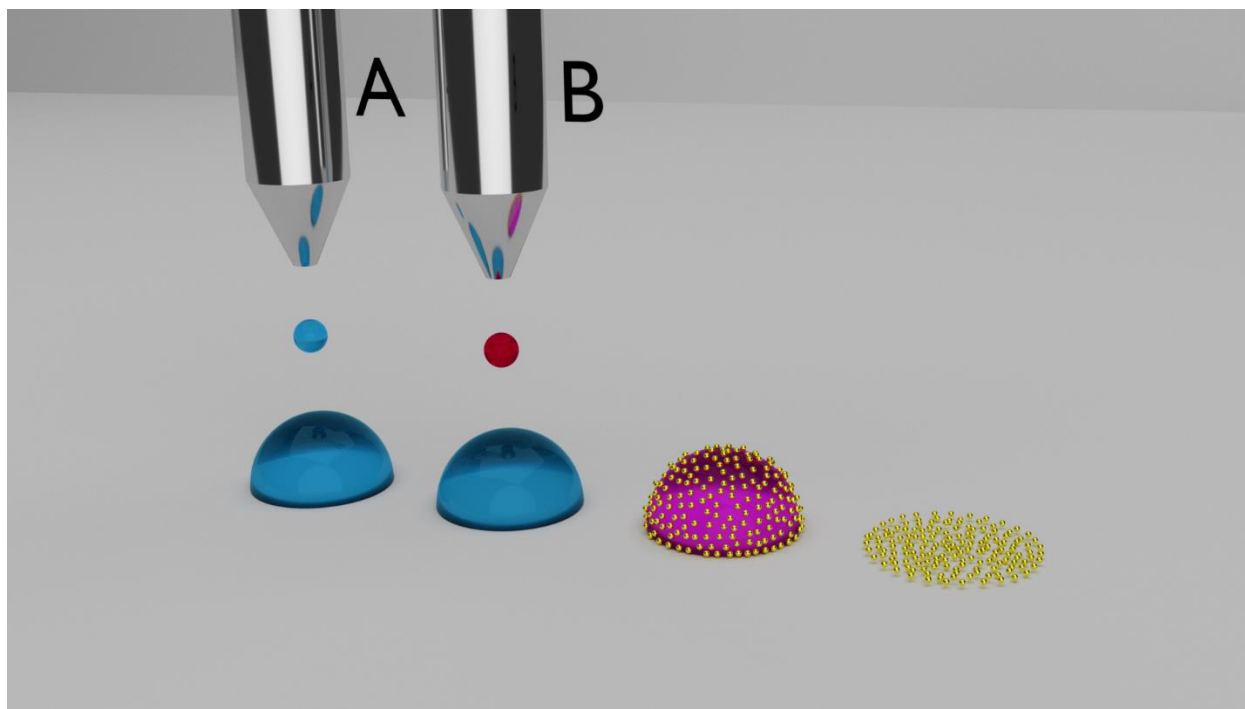


Figure 3.1: Schematic of the dual-droplet printing process. Blue represents the supporting droplet; red is the wetting droplet; and gold represents the PS nanoparticles.

The supporting droplet acts as the LB trough, and the wetting droplet contains colloidal nanoparticles. The colloidal particles spread over the supporting droplet surface and assemble at

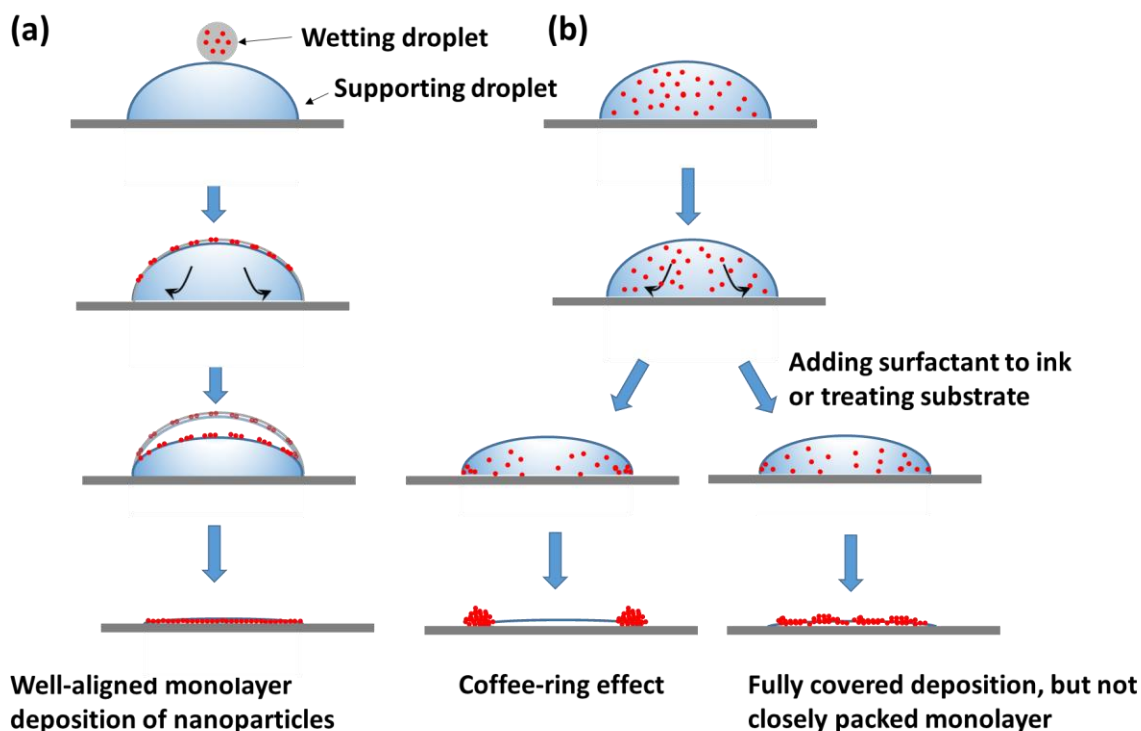


Figure 3.2: Schematics of (a) dual-droplet printing (this work); and (b) conventional inkjet printing, causing either coffee-ring formation or not well controlled deposition morphology.

the interface as the solvent dries to produce a uniform, nearly monolayer deposition of the nanoparticles. Three main steps take place toward the monolayer self-assembly: (i) spreading of the wetting droplet and colloidal nanoparticles over the supporting droplet; (ii) packing and assembly of nanoparticles at the interface between the wetting droplet and supporting droplet; and (iii) settling of nanoparticle film layer onto the substrate upon evaporation of the supporting droplet. Figure 3.2 compares the assembly mechanism during the dual-droplet printing process with those in the conventional inkjet printing processes.

In this study, the spreading of the wetting droplet is enabled by formulating a low-surface tension ink, containing colloidal particles and a high-surface tension solvent for the supporting droplet. Deionized (DI) water was used as a solvent for supporting droplets; a mixture of ethanol/water was used as a solvent for wetting droplets. Monodispersed polystyrene (PS) nanoparticles were

used as colloidal particles. Spreading of the wetting droplet and colloidal particles at the interface has been verified through high-speed imaging. The fate of the colloidal particles, however, differs during the solvent drying process, depending on solvent composition of the wetting droplets, functionalization, and the amount of PS nanoparticles deposited onto the supporting droplet. Some nanoparticles get trapped at the interface till the final deposition onto the substrate, while some may diffuse into the bulk of the supporting droplet. As a result, the final assembly exhibits morphologies ranging from a nearly closely-packed monolayer deposition to a fully covered but not closely-packed arrangement. PS nanoparticles with different sizes have been used to fabricate optical films, which exhibit different colors due to the varying optical resonance of the particles. The implication of this dual-droplet printing process in fabricating photonic crystals and devices applications is also discussed.

3.2 Experimental section

3.2.1 Materials

Microscope glass slides (25 mm × 75 mm) were obtained from VWR. PET films (MELINEX ST505) with 125 μm thickness were supplied by TEKRA, a division of EIS, Inc. Aldehyde/Sulfate latex beads (4% w/v, 0.1 μm), Sulfate latex beads (8% w/v, 0.1, 0.2, and 0.3 μm), and Carboxyl latex beads (4% w/v, 0.1 μm) were purchased from Thermo Fisher Scientific. Tris(hydroxymethyl)aminomethane (tris) (99.8% purity), 2-(3,4-Dihydroxyphenyl)ethylamine hydrochloride (dopamine), and hydrochloric acid (37% purity) were purchased from Sigma-Aldrich. DI water with a resistivity of 18.2 MΩ.cm was produced by Direct-Q water purification system (Millipore Sigma). KOPTEC ethanol (99.5% purity) was acquired from VWR. All chemicals were used as received without further purification.

3.2.2 Substrate Treatment

All glass substrates were first cleaned with solvents following the order of hot soapy water, acetone, and isopropanol, then rinsed with DI water, and dried by a clean-compressed air. The cleaned substrates were further treated with plasma for 5 min (PDC-001-HP, 115 V from Harrick Plasma) to ensure that the substrates are thoroughly cleaned. To control the substrate wettability and enhance contact line pinning, the cleaned substrates were chemically treated with dopamine accordingly. The cleaned glass slides were immersed vertically in a freshly prepared dopamine aqueous solution (5 mg mL^{-1}) with pH buffer of 8.5 (1.2 mg mL^{-1} tris) to initiate the oxidative self-polymerization reaction. After 24 h of reaction, the substrates were rinsed with ethanol and DI water to remove the unreacted dopamine particles and dried at $40 \text{ }^\circ\text{C}$ for 10 min using a vacuum oven (89508-426, 600 W from VWR). The dopamine-treated substrate was somewhat rough with some dopamine agglomerates. The static water contact angle on the dopamine-treated substrate was $\approx 50^\circ$, measured by a goniometer (OCA 15) from Dataphysics.

3.2.3 Ink Preparation

The as-received suspensions of PS particles were ultrasonicated for 10 min to re-disperse the particles. The suspensions were then diluted by a mixture of ethanol/water with weight fractions ranging from 50 wt%/50 wt% to 100% ethanol to obtain the printable inks with a particle concentration of 10 mg mL^{-1} .

3.2.4 Dual-Droplet Inkjet Printing Process

The inkjet printing platform (Jetlab 4, MicroFab) consists of four printing stations, two of which were used in this study. Supporting droplets and wetting droplets were jetted from two piezoelectric nozzles with different orifice sizes of $30 \text{ }\mu\text{m}$ (MJ-ATP-01-30-8MX, MicroFab) and $80 \text{ }\mu\text{m}$ (MJ-ATP-01-80-8MX, MicroFab), driven by a waveform generator (Jetdriver III,

MicroFab). Firstly, a supporting droplet was generated by jetting multiple bursts of DI water (2000 droplets with a total volume ≈ 110 nL) on the substrate at a frequency of 500 Hz. Then, wetting droplets containing PS nanoparticles were jetted at the center of the supporting droplet using the 80 μm nozzle at a frequency of 1 Hz. This ensured a complete impact and spreading of the wetting droplet before subsequent droplets. Careful adjustment of the jetting parameters, such as droplet speed and volume, was required for a successful dual-droplet printing in which nearly monolayer, ordered depositions were produced. In this work, a jetting speed of ≈ 1.3 m s⁻¹ and a droplet volume of ≈ 550 pL (diameter ≈ 100 μm) were used for the wetting droplet.

3.2.5 In Situ Observation of Droplet Impact and Solvent Evaporation

The wetting and spreading of wetting droplets on the interface of supporting droplets were investigated in situ by a high-speed camera (Phantom, MIRO-LAB3a10) at 5000 fps. The camera was connected to a high magnification zoom lens (Navitar 6000, 12 \times) and positioned at an angle of $\approx 50^\circ$ from the side of the nozzle to capture the droplet impact dynamics. A regular CMOS camera (THORLABS, DCC1645C) was used to capture the solvent evaporation process at 25 fps.

3.2.6 Morphology Characterization

An ultrahigh-resolution scanning electron microscope (HITACHI SU-70 FE-SEM) with 5 kV and 15 mm scanning distance was used for morphology characterization of the printed patterns. To minimize charging effect of the PS nanoparticles, the samples were coated with platinum using a platinum sputter (Denton Vacuum Desk V) for 60 s.

3.2.7 Optical Spectrum Characterization

A UV-vis spectrophotometer (Evolution 220, Thermo Fisher Scientific) was utilized to analyze the reflection spectrum of the printed films. The light spectrum range was set between 200 and 800 nm with a scanning speed of 400 nm min⁻¹.

3.2.8 Image Analysis

All the image analyses were carried out in MATLAB 2015a. The RGB values for each pixel in the optical images were obtained. The blue color contrast (BCC) intensity was defined as $\sqrt{(B - R)^2 + (B - G)^2}$. The intensity profile of the deposit patterns was averaged along the angular direction, i.e.,

$$I(r) = \frac{1}{2\pi} \int_0^{2\pi} i(r, \theta) d\theta, \quad 3.1$$

where $i(r, \theta)$ is the local BCC intensity, and r and θ are the cylindrical coordinates on the circular deposition. The intensity profile was then normalized with the maximum intensity $I(r)$, obtained from the printed patterns of Aldehyde/Sulfate-PS nanoparticles since they exhibited the highest color contrast. In addition, the radial distribution of the nanoparticles was normalized with the deposition radius.

3.2.9 COMSOL Simulation

Full-field simulations were conducted for spherical PS particles with diameters of 75 to 325 nm at a 5 nm resolution and wavelengths of 250 to 800 nm at a 10 nm resolution. One perfect unit cell, having one PS particle at the center and one quarter of a PS particle at each of the four corners, was simulated with periodic conditions to make a perfect hexagonal closely-packed surface. A port was used to excite the surface perpendicularly from the top, and a perfect layer was used beyond the substrate to limit reflection to that of the surface. The reflection intensity was calculated based on the perpendicular scattering from the port to itself.

3.3 Results and Discussion

3.3.1 Dual-Droplet Inkjet Printing

The first step for a controlled nanoparticle assembly in the dual-droplet printing is to realize the spreading of the wetting droplet onto the supporting droplet. Similar double-shot inkjet printing has been employed to print organic semiconductor films through anti-solvent crystallization,^{104,105} where the wetting (or spreading), dewetting, and sinking regimes were identified when a microdroplet was added onto a chemically different sessile droplet. Surface tension of the wetting droplet needs to be lower than that of the supporting droplet to enable initial spreading, as shown in the spreading parameter $S = \gamma_{SG} - (\gamma_{SW} + \gamma_{WG}) > 0$, where γ is the interfacial surface tension; subscripts S, W, and G represent supporting droplet, wetting droplet, and gas phase, respectively. The interfacial surface tension between the miscible solvents is negligible in this system. We use DI water (surface tension of 72.5 mN m^{-1}) to generate the supporting droplets and ethanol (surface tension of 21.8 mN m^{-1}) or a mixture of ethanol/water for the wetting droplets. The highest surface tension used for the wetting droplets is 28.51 mN m^{-1} for 50 wt%/50 wt% ethanol/water mixture at $20 \text{ }^\circ\text{C}$.¹⁰⁶ The modified Weber number,¹⁰⁵

$$We' = \frac{\rho_w v_w^2 d_w^3}{\gamma_s} \left(\frac{V_s}{f(\theta)} \right)^{\frac{2}{3}}, \quad 3.2$$

compares the inertial energy of the wetting droplet to the deformation energy of the supporting droplet surface, where ρ_w is the density of the wetting droplets, v_w is the impact velocity of the wetting droplet, d_w is the wetting droplet diameter, V_s is the supporting droplet volume, $f(\theta)$ is eq. 3.3,

$$f(\theta) = \pi \frac{2 - 3\cos\theta - \cos^3\theta}{3(1 - \cos\theta)^3}, \quad 3.3$$

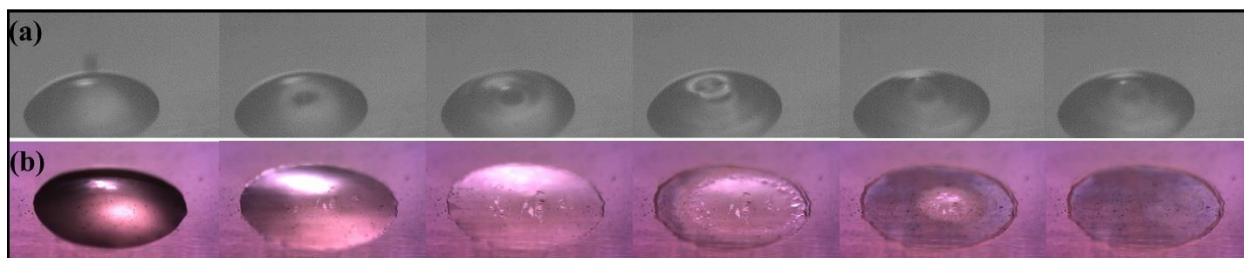


Figure 3.3: (a) Wetting droplet impact onto a supporting droplet by high-speed imaging (time interval of 0.2 ms between each image). (b) Images of PS nanoparticle film floating on the interface during the evaporation process ($t = 0, 51.5, 69.9, 78.3, 80.3,$ and 80.6 s). The suspension of sulfate-functionalized PS nanoparticles prepared with 100% ethanol was used for the wetting droplets, three of which were deposited onto the supporting droplet. The PS nanoparticle size is 100 nm in diameter.

and θ is the contact angle of the supporting droplet on the substrate. A smaller We' favors spreading of the wetting droplets, and a larger We' tends to bring the wetting droplet into the supporting droplet and enhances chaotic mixing of the wetting and supporting droplets. Therefore, smaller wetting droplets with slower impact speeds and larger supporting droplets with higher contact angles facilitate the spreading of the wetting droplet. The derivation of We' and the effect of impact speed of the wetting droplet are provided elsewhere.¹⁰⁷ In this work, the supporting droplet is generated by multiple bursts of inkjet droplets, equivalent of a ≈ 110 nL water droplet. One wetting droplet with a volume of ≈ 550 pL is deposited onto the supporting droplet by a secondary printhead. The jetting configurations described in the Experimental Section were used in all the experiments unless noted otherwise. The dimensionless We' was kept < 0.42 during all the experiments. High-speed photography was employed to capture the wetting droplet impact onto the supporting droplet, revealing the realtime impact dynamics. Upon the initial impact, as shown in Figure 3.3a, the wetting droplet creates a crater on the supporting droplet surface. In less than 20 ms, however, the latter surface is totally recovered after a few oscillation and damping cycles. Only one oscillation is shown in Figure 3.3a. Immediately after the droplet impact, the PS nanoparticles on the supporting droplet surface move along with the Marangoni flow, created by

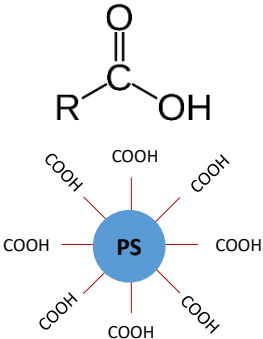
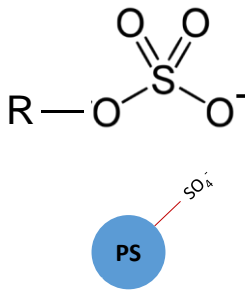
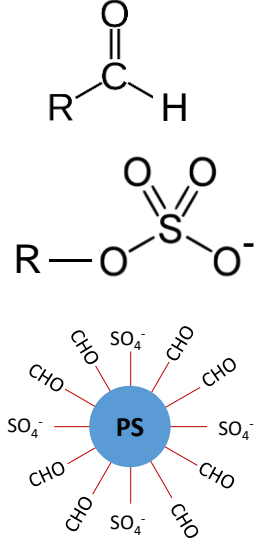
the ethanol/water surface tension gradient. A film of the colloidal PS nanoparticles can also be identified in Figure 3.3b.

Individual PS nanoparticles collide and assemble into larger islands and monolayer networks at the interface by lateral capillary force (i.e., particle–interface interactions),^{108,109} which are trapped at the air–water interface in an energetically favorable state due to the interfacial deformation, caused by the fractal shape of the agglomerates compared to individual spherical nanoparticles.⁸⁶ In addition, the quick evaporation of ethanol solvent in the wetting droplet also contributes to the network formation on the supporting droplet surface. During evaporation of the supporting droplet, the PS particle film is maintained at the air–water interface, further being compressed by the reduced surface area. When the water solvent in the supporting droplet completely evaporates, a deposition of PS nanoparticles forms as shown in the last image in Figure 3.3b. The example in Figure 3.3b shows a nearly monolayer, closely-packed assembly of PS nanoparticles (more characterization is provided in the following sections), which is enabled by a successful wetting droplet spreading and a trapped nanoparticle film on the supporting droplet surface. However, some PS nanoparticles, which are originally located at the air–water interface, may diffuse into the bulk of the supporting droplet depending on the solvent composition of the wetting droplets, the functional groups on the PS particles, and the amount of nanoparticles deposited on the supporting droplet. The morphology of PS nanoparticle assembly and their forming mechanisms under various conditions are discussed in the following sections.

3.3.2 Effect of Solvent Composition on the PS Nanoparticle Deposition

In order to study the effect of solvent composition in the wetting droplet on the PS nanoparticle deposition, we have selected the aldehyde/sulfate-functionalized PS particles. The detailed information about the functionalized particles is provided in Table 3.1.

Table 3.1: Parameters of the functionalized PS nanoparticles used in this work (from the vendor).

	Carboxyl latex, 4% w/v,	Sulfate latex, 8% w/v	Aldehyde/Sulfate Latex, 4% w/v
Density of PS particles	1.055 g/cm ³	1.055 g/cm ³	1.055 g/cm ³
PS particle size	0.1 μm	0.1 μm	0.1 μm
Surface functional group			
Surface charge density	2.9 μC/cm ²	0.2 μC/cm ²	N/a
Charge titration data	17.2-18.5 μEq/g	1.5 μEq/g	Aldehyde charge: 104.4 μEq/g Sulfate charge: 18.5 μEq/g
Number of function groups per particle	5.5-8.2 × 10 ³	4.9 × 10 ²	-

The as-received aqueous suspension of aldehyde/sulfate-functionalized PS particles was diluted in 100% ethanol, 80 wt%/20 wt% ethanol/ water, and 50 wt%/50 wt% ethanol/water to formulate the inks for wetting droplets with a PS nanoparticle concentration of 10 mg mL⁻¹. The amount of nanoparticles is controlled by the number of wetting droplets deposited onto the supporting droplet. The ink diluted with 100% ethanol gives the best nearly monolayer PS nanoparticle deposition, especially for a lower nanoparticle amount (e.g., one wetting droplet), indicated by the blue structural color as shown in Figure 3.4a.

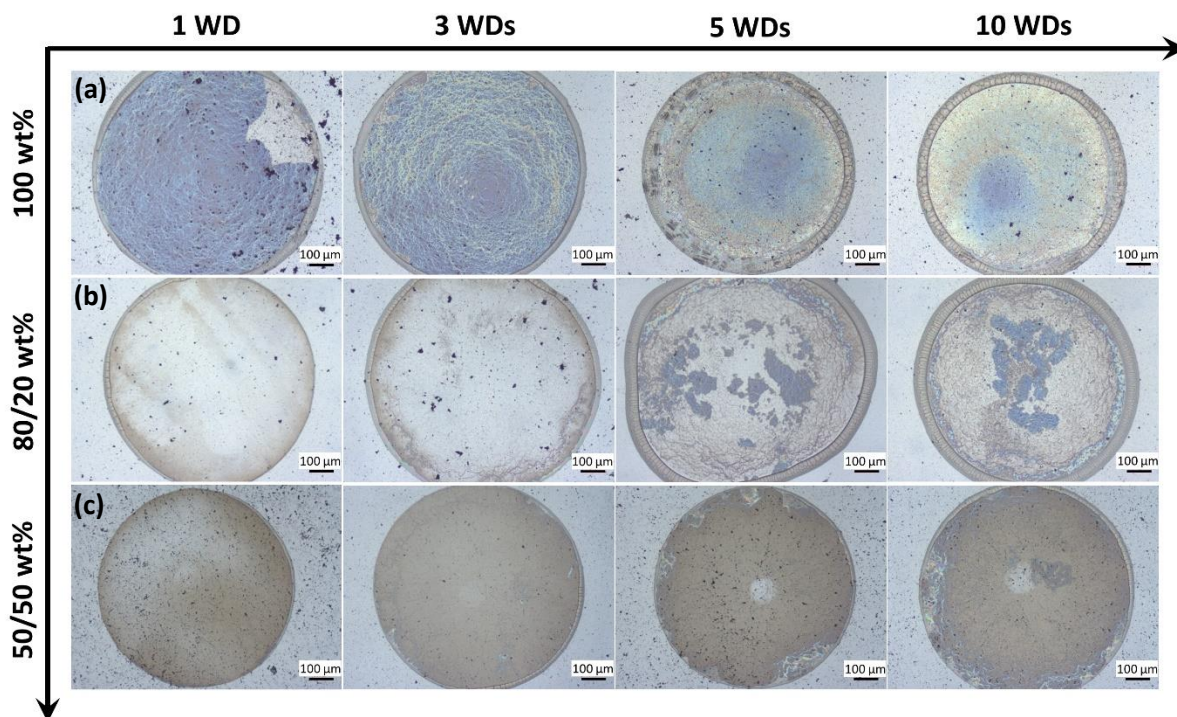


Figure 3.4: Optical images of aldehyde/sulfate-functionalized PS nanoparticle deposition at (a) 100% ethanol; (b) 80 wt%/20 wt% ethanol/water; and (c) 50 wt%/50 wt% ethanol/water-diluted inks in the wetting droplets. The four columns represent various nanoparticle amounts of one, three, five, and ten wetting droplets (WDs), respectively. The scale bar is 100 μm . A dopamine-treated substrate was used, and the PS nanoparticle size is 100 nm in diameter.

This can be attributed to the scattering of resonant modes within the spherical nanoparticle cavities (see Section 3.3.6). The nearly monolayer PS nanoparticle deposition is confirmed by scanning electron microscopy (SEM) images (Figure 3.5). The incomplete coverage of the entire droplet footprint is due to the insufficient particle density in the single wetting droplet, as well as some nanoparticle deposition at the contact line edges.

The gray “ring” at the periphery of the deposition is a result of reflective light scattering in the light microscopic image, indicating a different assembly mechanism. It is hypothesized that the surface modifier dopamine⁴³ attracts and captures the PS particles at the edges through Derjaguin–Landau–Verwey–Overbeek (DLVO) interactions.⁷⁶ This likely occurs when the wetting droplet spreads on the supporting droplet upon impact. It is worth noting that we purposely do not use the

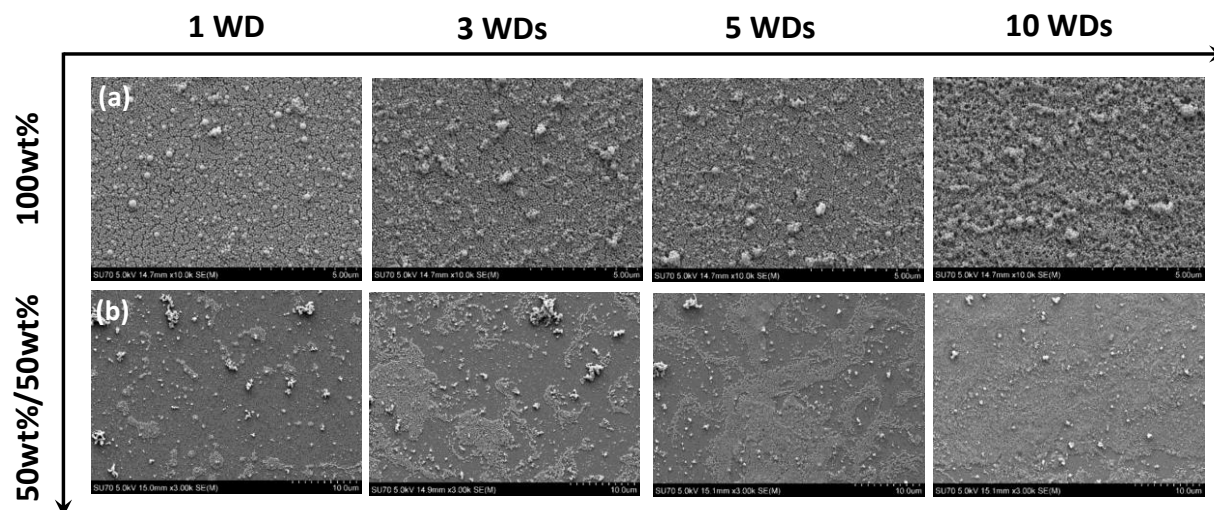


Figure 3.5: SEM images of Aldehyde/sulfate-functionalized PS nanoparticle deposition at (a) 100% ethanol; the scale bar is 5 μm ; and (b) 50wt%/50wt% ethanol/water diluted inks in the wetting droplets; the scale bar is 10 μm . The four columns represent various nanoparticle amounts of one, three, five and ten wetting droplets (WDs), respectively. A dopamine-treated substrate was used. The PS nanoparticle size is 100 nm in diameter.

term “coffee ring” because it has totally different forming mechanisms. The traditional “coffee ring” forms due to the evaporation-induced convective capillary flow carrying the colloidal particles toward the TCL, while the ring formed in this dual-drop printing process is attributed by the attractive interactions between the interface-trapped particles and the dopamine-coated substrate. Positively charged groups from protonation of amine groups of the dopamine surface¹¹⁰ could attract the negatively charged PS particles at the droplet TCL. The ring formation consumes some of the PS particles; however, it does not change the self-assembly mechanism in the majority of the deposition with a nearly closely-packed monolayer. For high PS nanoparticle amounts (e.g., 5–10 wetting droplets), the monolayer films are compressed during solvent evaporation, leading to formation of multilayers and/or buckled films. As a result, the structural color fades away (Figure 3.4a), because the order of arrangement decreases in the PS particle film which broadens

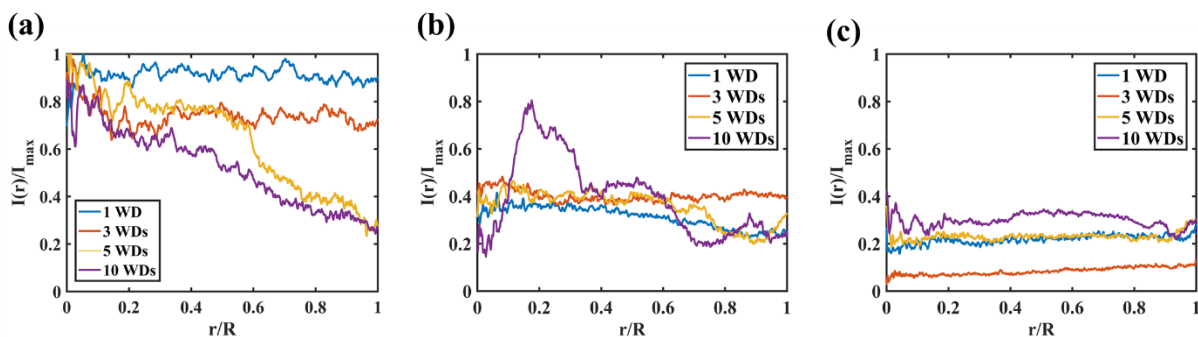


Figure 3.6: Normalized BCC from the center to the periphery of the nanoparticle depositions shown in Figure 3.4 using (a) 100% ethanol-diluted inks, (b) 80 wt%/20 wt% ethanol/water-diluted inks, and (c) 50 wt%/50 wt% ethanol/water-diluted inks for the wetting droplets. WD: wetting droplet.

and weakens the resonance. The profiles of blue color contrast (BCC) along the deposition radius are plotted in Figure 3.6 for each of the optical microscope images.

The BCC exhibits significant correspondence in monolayer deposition across the droplet footprint. The image analysis and postprocessing are described in detail in the Materials and Methods. For the optimum nanoparticle amount, the BCC is nearly constant over the entire droplet, corresponding to the one wetting droplet in Figure 3.6a. For a higher nanoparticle amount, the BCC is high in the center and gradually decreases toward the edge of the deposition. In those cases, the excess amount of nanoparticles at the air–droplet interface were pushed toward the edge of the supporting droplet and were captured by the dopamine-coated substrate at the TCL, which is shown by the wide rings at the periphery of the droplet deposition. For the same reason, less ordered multilayer deposition forms toward the TCL region, which reduces the BCC. Figure 3.5a shows SEM images of the PS nanoparticle deposition, printed with various particle amounts over the interface of the supporting droplet. The nearly monolayer depositions at lower particle amounts are compared with the multilayer agglomerates at higher particle amounts. As water was added to the wetting droplet solvent, e.g., 80 wt%/20 wt% ethanol/water, the structural color of the final deposition disappeared (Figure 3.4b), indicating the absence of the closely-packed monolayer PS

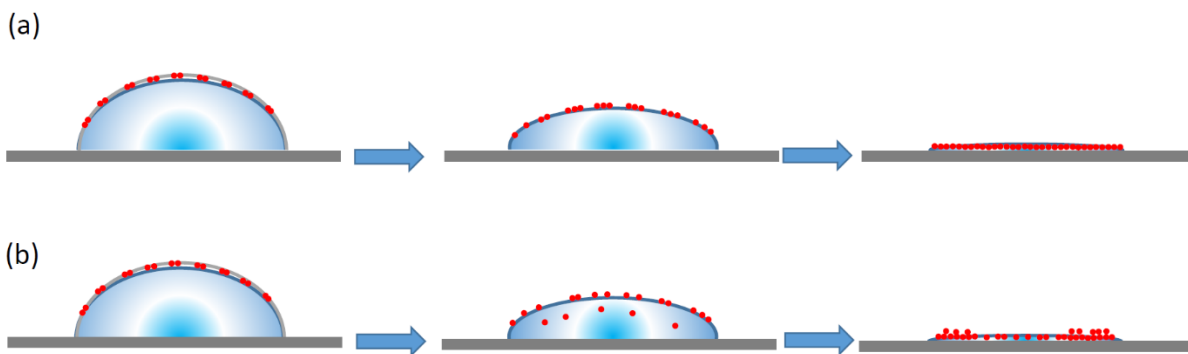


Figure 3.7: Schematics of two regimes of self-assembly through (a) particle–interface interaction; and (b) combination of particle–interface, particle–substrate, and particle–flow field interactions.

deposition. Fragments of blue color films is observed in the middle of deposits at high particle amounts. We hypothesize that during the supporting droplet evaporation, some hydrophilic aldehyde/sulfate-functionalized PS particles diffuse and mix into the supporting droplet due to the addition of water solvent. In addition, electrostatic repulsion between the particles also facilitates the nanoparticles diffusion into the supporting droplet. Different from the assembly driven by the dominant particle–interface interactions (Figure 3.2a), the particles experience an intricate combination of particle–interface, particle–substrate, and particle–flow field interactions as illustrated in Figure 3.7.

The evaporation-driven capillary flow inside the supporting droplet carries those particles toward the edges. When they touch the dopamine-coated substrate, the PS particles likely are captured and immobilized on the substrate. The final deposition morphology is attributed to the particles residing at the interface (self-assembled with blue color PS fragments) and the particles in the bulk of the supporting droplet. When more water was added into the wetting droplet solvent, e.g., 50 wt%/50 wt% ethanol/water, as shown in Figure 3.4c, none of the depositions demonstrated any blue color. Please refer to Figure 3.5b for the SEM images of the deposits. It is worth pointing out

that adding water to the wetting droplet solvent does not change the spreading of the wetting droplet.¹⁰⁵ The surface tension of the 50 wt%/50 wt% ethanol/water is still much lower than that of water. The wetting droplet spreads on the supporting droplet upon impact as verified by the high-speed imaging. However, majority of the PS nanoparticles diffuse into the supporting droplet during the evaporation. At the same time, the gray “ring” at the periphery of the deposition does not grow much as the nanoparticle amount increases, which also supports that only a small fraction of the PS nanoparticles remained at the interface. Figure 3.6b and 3.6c clearly correlates the orderliness of the assembly to the BCC intensity.

3.3.3 Effect of Functional Groups on the PS Nanoparticle Deposition

Three different kinds of functionalized PS nanoparticles, i.e., carboxyl-, sulfate-, and aldehyde/sulfate-functionalized PS nanoparticles, diluted in 100% ethanol are used to generate the wetting droplets. The detailed information about the functionalized nanoparticles is provided in Table 3.1. The nanoparticle concentration in the wetting droplets is kept the same as 10 mg mL^{-1} . Sulfate functional groups are the most hydrophilic in nature due to its acidity. However, the sulfate-PS particles have a surface charge density about $\approx 1/12^{\text{th}}$ of that on the aldehyde/sulfate- and carboxyl-PS particles. Fewer functional groups and weaker electrostatic interactions among the particles facilitate the formation of a particle “skin” on the air–droplet interface, which consists of a monolayer of nanoparticles and multilayers of agglomerates. The SEM images of the nanoparticle deposition for one and five wetting droplets are shown in Figure 3.8.

Compared to the aldehyde/sulfate-PS particles, a relative uniform blue color across the deposition, yet not as bright, is obtained for the sulfate-PS particles for various amounts of nanoparticles deposited onto the supporting droplet (Figure 3.9a). Sulfate-PS nanoparticles demonstrate more

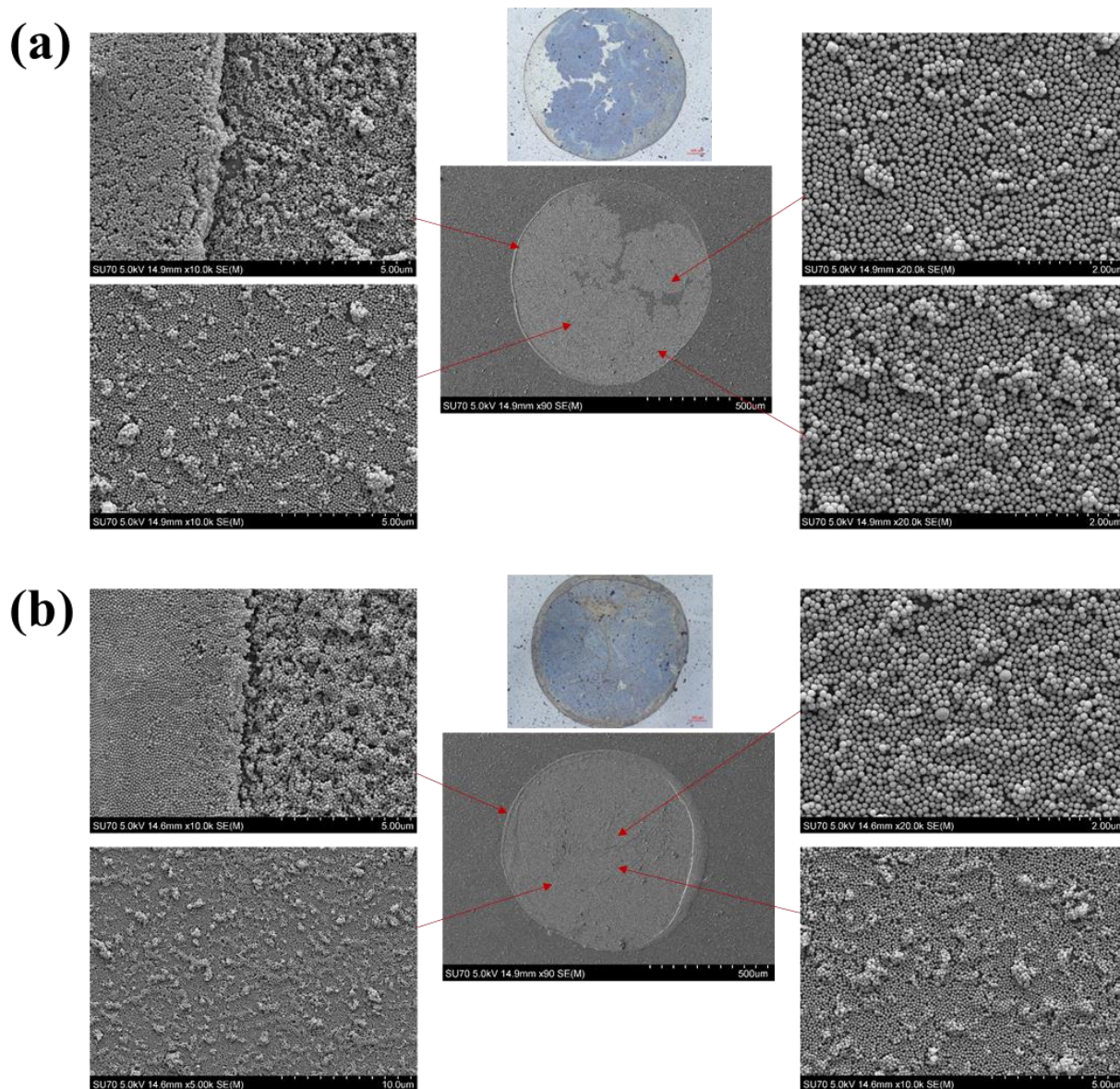


Figure 3.8: SEM images of sulfate-functionalized PS nanoparticles deposition at various locations of the circular depositions of (a) one wetting droplet and (b) five wetting droplets. The wetting droplet ink is prepared with 100% ethanol and the PS nanoparticle size is 100 nm in diameter.

robustness in achieving the closely-packed deposition against addition of water into the wetting droplet solvent.

When water was added to the wetting droplet solvent, e.g., 80 wt%/20 wt% ethanol/ water, a monolayer of sulfate-PS particles as well as their agglomerates were trapped at the interface,

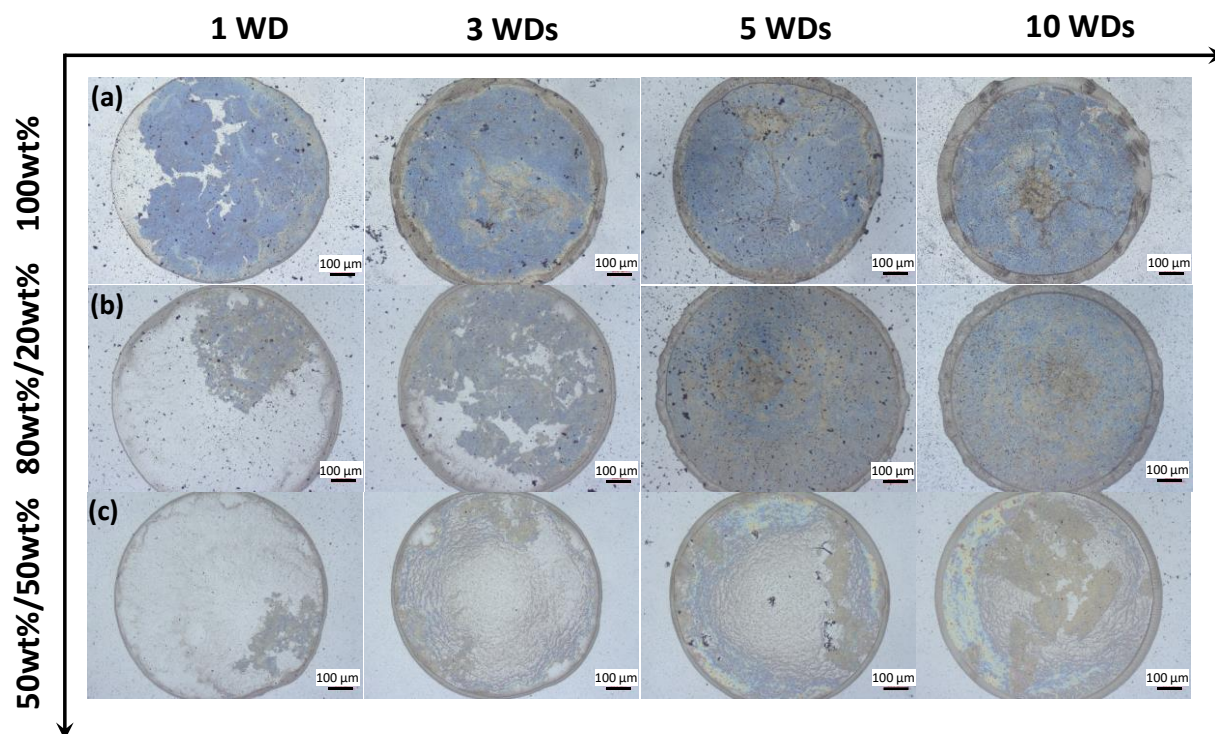


Figure 3.9: Optical images of sulfate-functionalized PS nanoparticle deposition at (a) 100% ethanol; (b) 80 wt%/20 wt% ethanol/water; and (c) 50 wt%/50 wt% ethanol/water-diluted inks of the wetting droplets. The four columns represent various nanoparticle amounts of one, three, five, and ten wetting droplets, respectively. The scale bar is 100 μm . A dopamine-treated substrate was used, and the PS nanoparticle size is 100 nm in diameter.

indicated by the bluish-brown islands on the final deposition, as shown in Figure 3.9b for the one and three wetting droplets. An incomplete coverage of the deposition with the three wetting droplets supports the hypothesis of agglomeration formation, as compared to the full coverage and higher BCC intensity with 100% ethanol. The deposition still shows a certain degree of orderly structure for higher nanoparticle amounts. Aldehyde/sulfate and carboxyl-PS particles, on the other hand, exhibit stronger hydrophilicity and repel each other due to their higher surface charge densities. Some particles diffuse into the bulk of the supporting droplet as a result of stronger hydrophilicity and electrostatic interactions. The final deposition shows a nonuniform irregular morphology contributed by particles residing at the air–droplet interface and in the bulk of the supporting droplet. Compared to the aldehyde/sulfate- and the sulfate-PS particles, carboxyl-PS

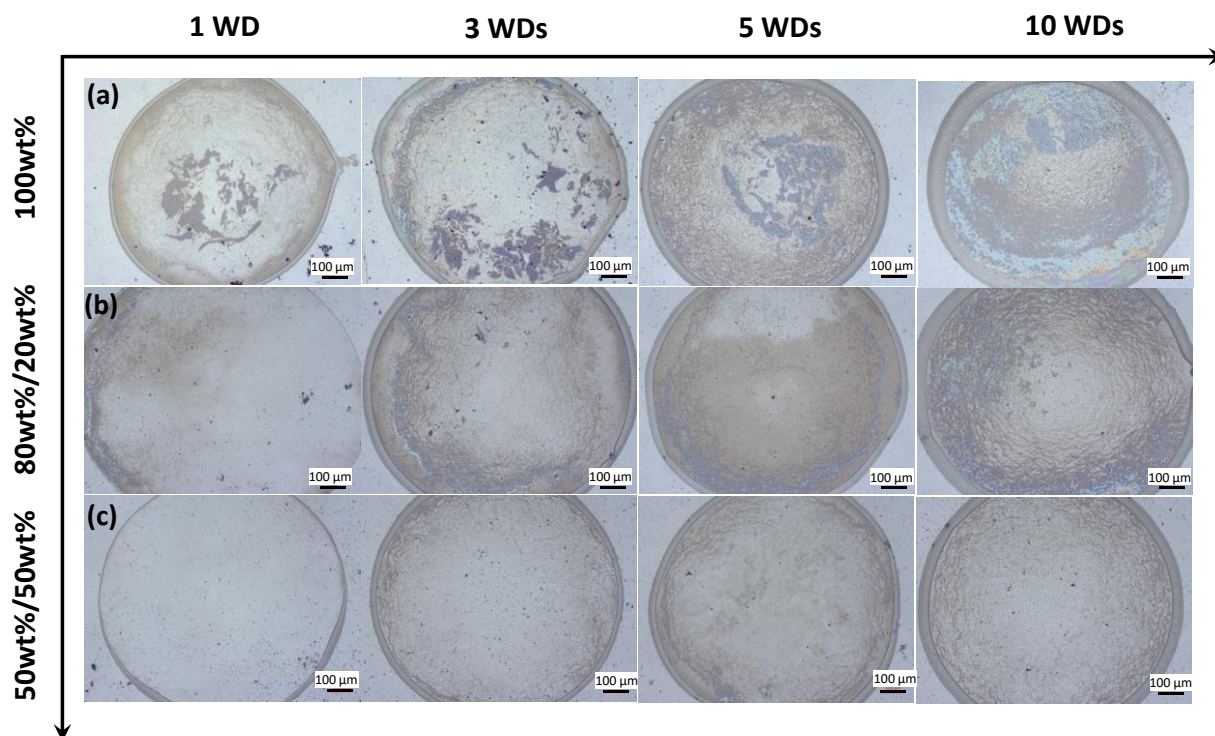


Figure 3.10: Optical images of carboxyl-functionalized PS nanoparticle deposition at (a) 100% ethanol; (b) 80wt%/20wt% ethanol/water; and (c) 50wt%/50wt% ethanol/water diluted inks of the wetting droplets. The four columns represent various nanoparticle amounts of one, three, five and ten wetting droplets (WDs), respectively. The scale bar is 100 μm . A dopamine-treated substrate was used, and the PS nanoparticle size is 100 nm in diameter.

particles did not produce decent orderly structures even with 100% ethanol. The deposition morphologies are shown in Figure 3.10. Carboxyl groups are strongly hydrophilic, which can lose a proton to form a negatively charged carboxylate ion (COO^-). Although carboxyl groups are less hydrophilic than sulfate groups in nature, the number of carboxyl groups per particle is more than 10 times larger than that of sulfate groups on a sulfate-PS particle (Table 3.1), providing more affinity toward water. For the aldehyde/sulfate-PS particles, a large number of aldehyde functional groups alternate with fewer sulfate groups on the PS particle surface, which reduces the hydrophilicity of these PS nanoparticles. Therefore, with comparable charge densities of carboxyl and sulfate groups on the PS nanoparticle surfaces, the carboxyl-PS particles experience stronger affinity to water than the aldehyde/sulfate-PS particles. As a result, the carboxyl-PS particles

readily diffuse into the supporting droplet during solvent evaporation, and the final deposition exhibits absence of orderly arrangement.

3.3.4 Effect of Substrate on the PS Nanoparticle Deposition

In this dual-droplet printing process, the colloidal particles are spread and trapped at the air-droplet interface, eliminating the particle–fluid and particle–substrate interactions. Theoretically, the closely-packed nanoparticle deposition should be transferrable to other substrates. In this study, an isopropyl alcohol cleaned polyethylene terephthalate (PET) substrate is compared to the dopamine-coated glass slide to investigate the effect of substrate on the deposition morphology. The static water contact angle on the PET substrate is about 70°. The printing parameters, e.g., 100% ethanol dilution as the wetting droplet solvent, sulfate-PS nanoparticles, and wetting droplets of one, three, five, and ten, were applied. As expected, a blue-colored nanoparticle deposition on the PET substrate indicates the well-ordered nanoparticle assembly as shown in Figure 3.11a. For the deposition with only one wetting droplet, a broken gray ring forms along circumference of the deposition, probably due to the local contact line receding. For higher nanoparticle amounts, the excess nanoparticles assist the contact line pinning, resulting in continuous gray rings. Different from dopamine-coated substrates, the rings on the periphery of the deposition on PET substrates are less severe than their counterparts, indicating weaker interaction between the interface trapped nanoparticles and the PET substrate. Since fewer nanoparticles are consumed at the contact line and the supporting droplet possesses a smaller footprint (due to larger contact angles), more wrinkling and folding occur on the deposition with five and ten wetting droplets. When a wetting droplet with 50 wt%/50 wt% ethanol/water was deposited onto the supporting droplet, obvious coffee-ring formation has been demonstrated on the PET substrate. For lower nanoparticle amounts (e.g., one and three wetting droplets), as shown

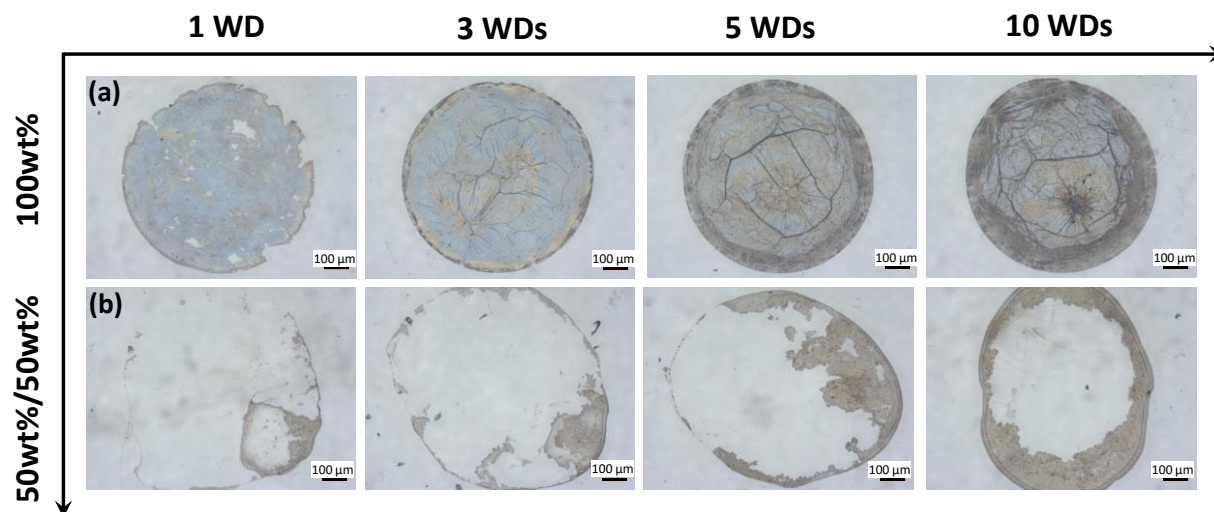


Figure 3.11: Optical images of sulfate-functionalized PS nanoparticle deposition on a PET substrate at (a) 100% ethanol and (b) 50 wt%/50 wt% ethanol/ water-diluted inks in the wetting droplets. The four columns represent the four conditions of one, three, five, and ten wetting droplets, respectively. The scale bar is 100 μm and the PS nanoparticle size is 100 nm in diameter.

in Figure 3.11b, the contact line depined during the supporting droplet evaporation, pushing the particles to a pinned spot (e.g., a local defective site) on the contact line. For higher nanoparticle amounts (e.g., five and ten wetting droplets), the contact line was pinned, assisted by the particle deposition from the interface. The majority of the nanoparticles were diffused into the supporting droplet and carried to the TCL by the evaporation-induced capillary flow. On the other hand, the not-so-obvious coffee-ring formation on the dopamine-coated substrate is probably due to DLVO interactions and possible surface roughness effect. Particles inside the supporting droplet were attracted and deposited onto the dopamine-coated substrate during their transport to the edges. Therefore, when the particles were successfully trapped and maintained at the air–droplet interface, the particle–interface interaction dominated, and a monolayer deposition of the colloidal particles was obtained. The self-assembly process is insensitive to substrates. When some particles diffuse and migrate into the bulk of the supporting droplet, however, the final particle deposition does not possess the close packing any more due to the introduced particle–flow field and particle–

substrate interactions. They may produce a coffee-ring if the substrate is relatively smooth (e.g., PET) and the particles deposit in the proximity of the contact line; or they may still produce a “uniform” deposition, but not closely-packed one, if the substrate is coated with absorbing polymers or treated with oppositely charged surfactants to capture those particles.

3.3.5 Discussion

In all the previous studies, including the ones of manipulating capillary flows inside colloidal droplets and those of pushing the particles to the air–droplet interface, the particle depositions are more uniform compared to coffee-ring deposition, but they usually do not exhibit closely-packed, ordered assembly. Different from these previous studies, this dual-droplet printing directly deposits and spreads the particles on the interface following the quick spreading and evaporation of wetting droplets. Under the right conditions of functional groups on the particles and solvent composition of the wetting droplet, these colloidal particles can self-assemble into a particle film layer on the surfaces of the supporting droplets. Eventually, a nearly monolayer, closely-packed particle assembly is obtained on the substrate. Compared to other self-assembly of nanoparticle and nanowires at the air–water interface,^{111,112} our approach combines the nanoparticle self-assembly and drop-on-demand into one printing process. During the dual-droplet printing, the wetting droplet spreading is controlled by surface tensions and volume ratio of the wetting droplet and supporting droplet, as well as the impact speed of the wetting droplet. The spreading of the wetting droplet carries the particles to spread on the supporting droplet surface, forming small or big islands of nearly closely-packed particles depending on the amount of particles deposited onto the supporting droplet. The key to a perfect monolayer deposition is to keep these particles on the supporting droplet surface during solvent evaporation. The solvent composition in the wetting

droplet and functionalization of the colloidal particles determine if those particles are kept on the surface or diffused into the bulk of the supporting droplet. This nanoparticle self-assembly mechanism is superior to the mechanisms of pushing the nanoparticles from the bulk to the droplet surface, since in the latter configurations, there are always a small amount of particles in the bulk following the capillary flow toward the droplet edges. In addition, when the particles are gradually transported to the droplet surface, overlapping and particle agglomeration could occur. As a result, absence of ordered arrangement of the nanoparticles (yet relatively uniform deposition) is usually obtained in the final deposition morphology. On the other hand, the self-assembly mechanism during the dual-droplet printing process enables not only a uniform, but also nearly monolayer closely-packed assembly structure, which can bring potential applications in printed electrical and optical functional devices.

3.3.6 Implication in Printed Optical Devices

The capability to fabricate and control the assembly and periodic arrangement of colloidal particles is significant, especially when they work as photonic crystals⁸⁰ in fast-response sensors,^{113,114} displays and color filters,^{115–117} and anticounterfeiting features.¹¹⁸ Various approaches, e.g., photolithography templating,¹¹⁹ combination of additive patterning and self-assembly,³² and inverse opal photonic crystals,¹²⁰ have been employed for patterning colloidal particles. Among those, inkjet printing provides an efficient way to pattern the colloidal particles into functional devices.¹²¹ In this study, we have fabricated optical films with the self-assembled PS nanoparticles by the dual-droplet printing process. As shown in Figure 3.12a–c, these self-assembled PS particles display structural colors that strongly depend on the assembly morphology and diameter of the PS particles. Figure 3.12d–f shows the SEM images of those assembly structures. Larger nanoparticle

sizes result in more ordered assembly, while smaller ones have exhibited some overlapping or multilayers of deposition locally. Figure 3.12g presents the measured reflection spectra with different PS nanoparticles of 100, 200, and 300 nm, which exhibit one single peak, double peaks, and triple peaks, respectively. The first-order peaks red-shift from 316 to 548 and ≈ 690 nm as the particle size increases from 100 to 300 nm, and the reflection peaks become broader in wavelength. The average offset in the reflection spectra (12%–13%) is likely attributed to the dopamine layer, whose spectrum is provided elsewhere.¹⁰⁷ To understand the origin of the film's reflection spectra, full field simulations of the PS nanoparticle assembly with particle diameters ranging from 75 to 325 nm were conducted using the finite element method (COMSOL Multiphysics). The reflection normal to the surface is calculated for a closely-packed hexagonal monolayer of PS nanoparticles on a silicon dioxide substrate, where the wavelength-dependent refractive index of PS was assumed to be of bulk PS in the material database of an ellipsometer from J. A. Woollam. The results are shown in Figure 3.12h, and the reflection peaks observed in experiment are marked as circles. In general, we achieved a good agreement in the peak locations between the simulation and the experiment, while the discrepancies at short wavelengths (e.g., <300 nm) can be attributed to variations in the refractive index of the PS nanoparticles as compared to the bulk PS. The good agreement between the simulated and the experimental reflection spectra indicates the good quality of the printed PS nanoparticle assembly for engineering applications in optics. Due to the size of the particles being on the order of the wavelength of light, the optical response is most likely attributed to Mie resonances. In this case, we also plotted the resonance peak spectral position as determined from analytical Mie theory¹²² (black dotted lines in Figure 3.12h) for spherical particles on a substrate and obtained excellent agreement between the simulation and experimental results.

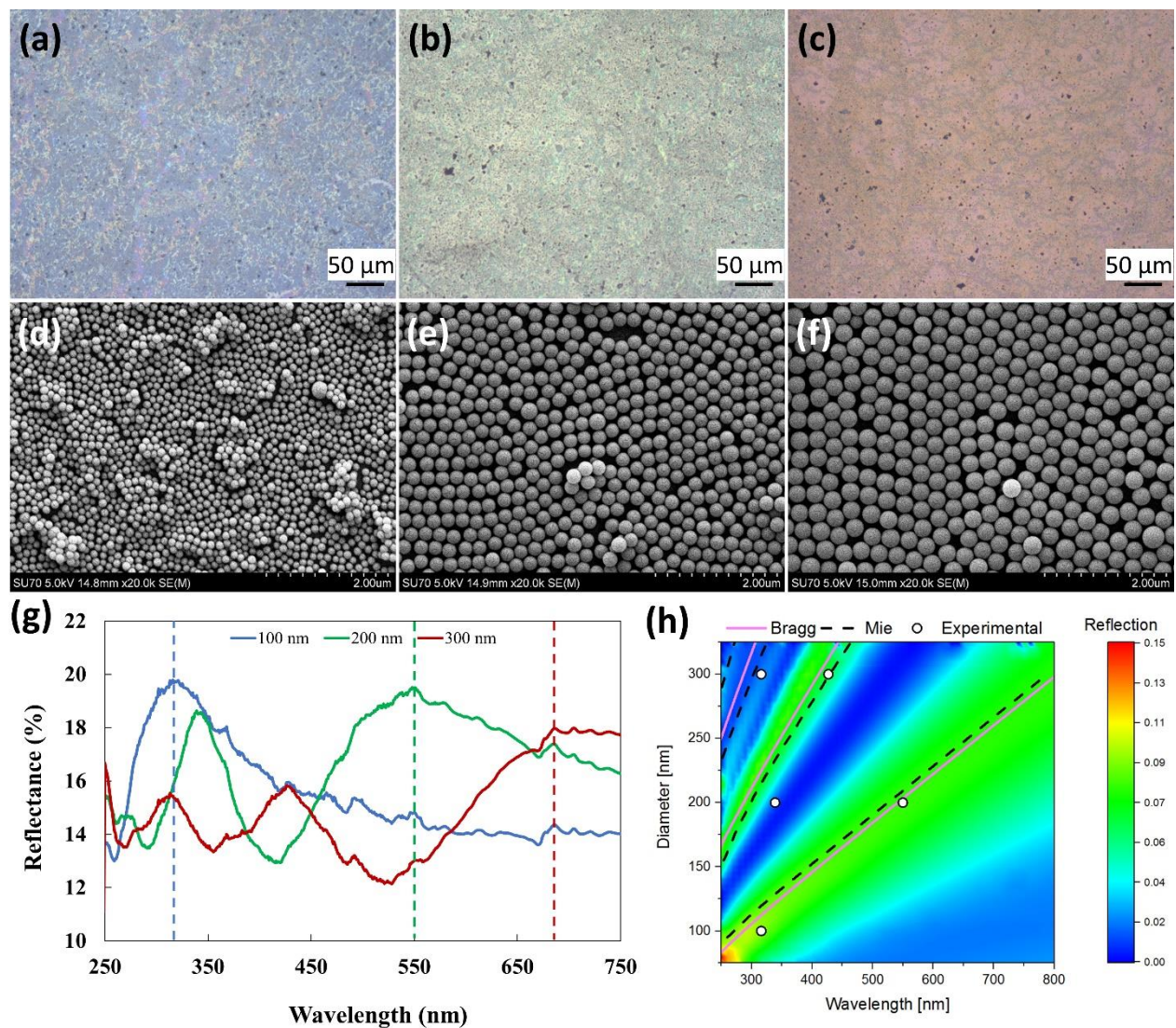


Figure 3.12: Optical images of PS nanoparticle assembly with diameters of (a) 100 nm, (b) 200 nm, and (c) 300 nm. The scale bar is 50 μm . (d–f) SEM images of these assembly of (a–c). The scale bar is 2 μm . (g) UV–vis reflection spectra; (h) comparison of the full-field simulation, the Braggs calculations (pink solid line), the Mie calculations (black dotted line), and the measured reflection peak locations (circles).

However, Mie theory can be difficult to calculate for many cases, and a simpler approach that provides guidance would be useful. In this case, the periodic assembly of the monolayer is treated as a diffractive surface, which occurs due to the far-field interference of the many sources of scattered light (e.g., nanoparticles). As a result, we can approximate the position of the reflection peaks using Bragg’s formalism eq. 3.4.¹²³

$$\lambda_{r,peak} = \frac{n_{eff}d(\sin\theta_i + \sin\theta_m)}{m} \quad 3.4$$

where $\lambda_{r,peak}$ is the peak reflection wavelength, m is the order of diffraction, n_{eff} is the refractive index adjusted by the packing fraction and the surrounding medium, d is the particle diameter, and θ_i and θ_m are the angles of incidence and observation from the normal direction, respectively. The reflection peak determined from Bragg formalism is shown in comparison to the prior methods in Figure 3.12h. Although this approach leads to some additional error in the predicted resonance position, the ease of the formula makes it a useful method to obtain an estimate for the optical response for a particular film without the need for expensive numerical software or complex analytical calculations.

3.4 Conclusion

In summary, we have demonstrated the ability to produce nearly monolayer, closely-packed depositions of PS nanoparticles through a novel dual-droplet inkjet printing process. Acting as a LB trough, a supporting droplet is deposited on the substrate followed by a wetting droplet, which contains colloidal particles. The nanoparticles spread at the supporting droplet surface as a result of the wetting droplet spreading. A particle network forms among the colloidal particles when the nanoparticles are trapped and maintained at the interface during the solvent evaporation. Well-ordered monolayer deposition is obtained, where the colloidal nanoparticle–interface interaction is the main driving force. When some particles diffuse and mix into the supporting droplet, due to addition of water into the wetting droplet, higher nanoparticle amounts, more surface charge density on the nanoparticles, etc., the well-ordered structure disappears in the particle assembly. The final deposition morphology is a result of particles trapped at the air–droplet interface and

particles diffused into the bulk of supporting droplet, which follows the capillary flow inside the supporting droplet. The nearly monolayer, closely-packed structure brings unique structural colors to the printed features. We fabricated optical films exhibiting different colors depending on the nanoparticle sizes. This study suggests a new printing strategy to control the colloidal particle deposition with well-ordered monolayer structures. This printing process is not limited to PS nanoparticles and also insensitive to substrates, which holds enormous potentials to assemble functional colloidal particulates for applications in printed optical and electrical devices.

CHAPTER 4 pH-Modulated Self-Assembly of Colloidal Nanoparticles in a Dual-Droplet Inkjet Printing Process

4.1 Introduction

Deposits acquired by evaporation of particle-laden droplets and films with controlled assembly are of considerable importance in fundamental science and engineering that influence a variety of technologies ranging from thin film coatings to printing functional devices.^{60,111,124} Recently, the evaporation-induced self-assembly process has received much attention as a technique that enables control over deposits to produce high-quality planar colloidal crystal films.^{125,126} However, the formation of ring-shaped deposits during solvent evaporation process, especially when the TCLs of the particle-laden sessile droplets are pinned, makes this phenomenon rather complicated.⁵⁶ The evaporation of sessile droplets is a non-equilibrium process. The complex fluid dynamics of a droplet stems from the non-uniform evaporation flux of the solvent over its liquid-vapor interface.^{9,33} As a result, the suspended particles are driven to the droplet's edge by the action of evaporation-induced flow forming this ubiquitous ring-like pattern, known as the coffee-ring effect (CRE).^{34,58} Significant research efforts have been devoted to mitigate or suppress the coffee-ring formation by means of, controlling the drying conditions of solvents (e.g., substrate temperature,¹¹ relative humidity,¹⁵ and volatile solvents³⁵), modifying particle shapes,^{36,37} adjusting substrate wettability,^{12,38} and intentionally inducing Marangoni flow due to surface tension gradient that is generated by temperature difference across the interface, surfactant, or cosolvent,³⁹⁻⁴³ etc. It is worth noting that the CRE is considered as a detrimental defect in printing and coating technologies; nonetheless, this stain phenomenon has been harnessed in a number of technological applications.¹²⁷⁻¹²⁹ Among the research endeavors in tuning deposits of colloidal sessile droplets,

Bharadwaj et al. experimentally investigated the role of Derjanguin-Landau-Verwey-Overbeek (DLVO) interactions on deposits left by evaporating sessile droplets containing titania nanoparticles on a glass substrate.⁷⁶ As the pH of the solution changes, the morphology of nanoparticle deposits varies accordingly from rings to uniform disks. Devineau et al. analyzed the deposit morphology of drying droplets containing protein functionalized polystyrene (PS) particles with different surface properties.⁷⁷ Protein adsorption on the surface of the suspended particles alters the surface charge of the PS particles. The authors assert that the CRE can be suppressed when the particles are neutralized by the protein adsorption. Even though an immense experimental and theoretical work have been diligently undertaken to improve the understanding of drying mechanism and pattern formation upon evaporation of particle-laden sessile droplets,¹³⁰ not much attention has been given to creating uniform depositions with nearly a monolayer of self-assembled colloidal particles. Very recently, we have demonstrated the ability to produce a well-ordered assembly of a nearly monolayer of PS nanoparticles by employing a dual-droplet inkjet printing process.¹⁰⁷ By tuning the surface tension, droplet size, and droplet speed, a wetting droplet that contains PS nanoparticles successfully spreads on the surface of a supporting droplet.

In this study, we investigate the effect of pH modulation of the supporting droplet on the nanoparticle depositions as a result of particle-particle interactions, particle-interface interactions, and particle-substrate interactions. Negatively charged PS particles with different surface functionalization groups were utilized and the electrostatic interactions were tuned via the pH value of the supporting droplet. This study uncovers a facile technique to control the colloidal assembly upon solvent evaporation in enormous industrial and research applications, especially for inkjet printing, coating processes, and fabricating functional devices involving liquid processing of colloidal inks.

4.2 Materials and Methods

4.2.1 Materials

Microscope glass slides (25 mm × 75 mm), sodium hydroxide solution (10.0 N), and KOPTEC ethanol (99.5% purity) were obtained from VWR. Sulfate latex beads (8% w/v, 0.1 mm) and carboxyl latex beads (4% w/v, 0.1 mm) were purchased from Thermo Fisher Scientific. Tris(hydroxymethyl)aminomethane (Tris) 99.8% purity, 2-(3,4-Dihydroxyphenyl)ethylamine hydrochloride (dopamine), and hydrochloric acid (37% purity) were acquired from Sigma-Aldrich. Deionized (DI) water with a resistivity of 18.2 MΩ.cm was produced by Direct-Q water purification system (Millipore Sigma). All chemicals were used as received without further purification.

4.2.2 Substrate Treatment

All glass substrates were first cleaned with solvents following the order of hot soapy water, acetone, and Isopropanol, then rinsed with DI water and dried by clean compressed air. The cleaned substrates were further treated with plasma for 5 min (PDC-001- HP-115 V from Harrick Plasma) to ensure that the substrates are thoroughly cleaned. The cleaned substrates were chemically treated with dopamine to enhance the TCL pinning of the jetted droplets by the following procedure: the cleaned glass slides were vertically immersed in a freshly prepared dopamine aqueous solution (5 mg/mL) with pH buffer of 8.5 (1.2 mg/mL tris) to initiate the oxidative self-polymerization reaction; after 24 h reaction, the substrates were rinsed with ethanol and DI water successively to remove the physically unattached dopamine particles and dried at 40 °C for 10 min using a vacuum oven (89508-426, 600W from VWR).

4.2.3 Ink Preparation

The as-received suspensions of polystyrene particles were ultra-sonicated for 5 min to ensure a homogeneous suspension of the nanoparticles. Then, the suspensions were diluted by ethanol to obtain the inks for wetting droplets with a particle concentration of 10 mg/mL. The suspension was ultra-sonicated for another 5 min before printing. The solvent for supporting droplets is DI water, where its pH value was adjusted either by adding HCL or NaOH with known concentrations.

4.2.4 Dual-Droplet Inkjet Printing Process

The inkjet printing platform (Jetlab 4, MicroFab) consists of four printing stations, two of which were used in this study. Supporting droplets and wetting droplets were jetted from two piezoelectric nozzles with different orifice sizes of 30 mm (MJ-ATP-01-30-8MX, MicroFab) and 80 mm (MJ-ATP-01-80-8MX, MicroFab), driven by a waveform generator (Jetdriver III, MicroFab). In brief, a supporting droplet was generated by jetting multiple bursts of DI water with a total volume of ~110 nL on the substrate at a jetting frequency of 500 Hz. Then, wetting droplets containing PS nanoparticles were jetted to the center of the supporting droplet using the 80 mm nozzle at a frequency of 1 Hz. This ensures a complete impact and spreading of the wetting droplet before subsequent droplets. In this work, we have used a jetting speed of ~1.3 m/s and a droplet volume of ~ 550 pL (diameter ~100 mm) for the wetting droplets.

4.2.5 Morphology Characterization

An ultra-high-resolution scanning electron microscope (HITACHI SU-70 FE-SEM) with 5 kV and 15 mm scanning distance was used for morphology characterization of the printed patterns. To minimize charging effect of the PS nanoparticles, the samples were coated with platinum using a platinum sputter (Denton Vacuum Desk V) for 60 s.

4.2.6 Surface Profilometry

Height profiles of the nanoparticle deposits were characterized using a stylus profilometer (Dektak 150, Veeco) with a stylus diameter of 12.5 μm . The measurements were recorded using a stylus force of 2 mg, scanning resolution of 0.1 μm , and scanning length of 2 mm.

4.2.7 Zeta Potential Characterization of Colloidal Nanoparticles and Dopamine-Coated

Substrates

The PS particles were dispersed in water with different pH values, which were adjusted either by adding HCL or NaOH with known concentrations. Zeta potential measurements were conducted using Malvern zetasizer (ZS). The pH value of the suspensions was measured by a benchtop pH meter (sensION + MM374, HACH, USA) with accuracy of ± 0.1 pH. The zeta potential of the dopamine-coated glass slide was determined by an electrokinetic analyzer (SurPASS 3, Anton Paar, USA). Streaming current measurements were performed in asymmetric mode using a clamping cell. 1 mM KCL solution was used as the measuring electrolyte where 0.05 M of HCL and 0.05 M of NaOH were utilized to adjust the pH range accordingly. Three repetitions of zeta potential measurements were performed at each pH value for each tested sample.

4.3 Results and Discussion

4.3.1 Self-Assembly of Nanoparticles at Different pH Values

Very recently, we have successfully demonstrated a nearly monolayer, closely-packed deposition of colloidal nanoparticles through a dual-droplet inkjet printing process. Nanoparticle-laden wetting droplets were jetted over a supporting droplet, which was firstly deposited. Regulating surface tensions, droplet speeds, and droplet volumes resulted in effective particle spreading over the interface of the supporting droplet. The dynamics of wetting droplet impacting the supporting

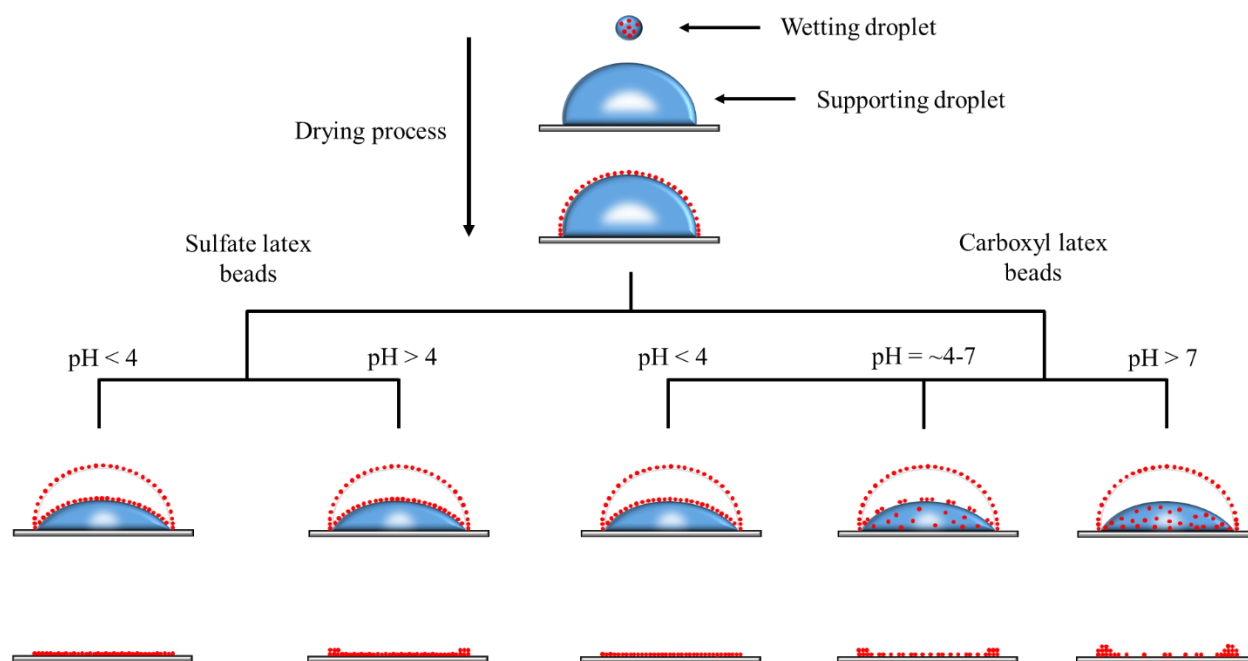


Figure 4.1: Schematic of the dual-droplet inkjet printing, where different interparticle and particle-substrate interactions are initiated at the interface and in the bulk of the supporting droplet. As the solvent evaporates, different deposition patterns are obtained depending on the type of the nanoparticles utilized and the pH value of the supporting droplet.

droplet, spreading of nanoparticles, and drying of solvents were discussed in detail in our earlier report.¹⁰⁷ In this study, we conducted a systematic investigation of particle-particle, particle-interface, and particle-substrate interactions initiated by the pH change of the supporting droplet in the dual-droplet inkjet printing. The supporting droplet was generated by multiple bursts of inkjet droplets that is equivalent to ~110 nL of water. One and three wetting droplets with a single droplet volume of ~550 pL were deposited onto the supporting droplet by a secondary printhead. In all the experiments, the modified Weber number (We') is controlled below 0.42 to ensure the spreading of the wetting droplet on the surface of the supporting droplet.^{105,107} Figure 4.1 illustrates the complex multibody interactions, presented by the negatively charged PS particles accompanied with pH variation in the supporting droplet. Upon the wetting droplet impact on the supporting droplet, the PS particles spread on the interface of the supporting droplet. Consequently, the

particles experience various types of interactions such as particle-interface and particle-particle interactions, where the capillary forces compete with the particle electrostatic interactions and the particles' water affinity at the interface to facilitate the skin formation of PS particles. The self-assembly process is strongly influenced by the protonation and deprotonation of the supporting droplet, which, in turn, controls the surface charge magnitude of the particles at the interface.

In this study, carboxyl- and sulfate-functionalized PS nanoparticles were selected because the former is sensitive to the pH change due to protonation and deprotonation of the carboxyl group while the latter is not. The protonation and deprotonation of the carboxyl group follows the reversible reaction equation, $R - COOH_{aqueous} \rightleftharpoons R - COO^-_{aqueous} + H^+_{aqueous}$. For pH 7, the reaction to the right and the reverse reaction to the left reach an equilibrium with a certain concentration of $R - COO^-$ in the system. When the solution is more acidic (pH < 7), more H^+ protons present in the system, pushing the reverse reaction to the left, leading to a suppressed $R - COO^-$ formation. Both the prominence of H^+ protons and suppression of $R - COO^-$ formation contribute to the significant decrease in the zeta potential (absolute value) in acidic environments. For pH > 7, the opposite trend, i.e., less protons and promotion of $R - COO^-$ formation, is obtained, leading to an increase in the zeta potentials (absolute value) of the carboxyl-PS particles. On the other hand, the sulfate group ($R - SO_4^-$) is not affected by the concentration of H^+ in the system. At various pH conditions, the zeta potential of the sulfate-PS particles changes as a result of changing proton concentrations. Zeta potential measurements of suspensions with carboxyl- and sulfate-functionalized PS nanoparticles also support this analysis. As shown in Figure 4.2, the zeta potential of carboxyl- and sulfate-PS nanoparticles show similar trends, where the net negative charges of the particles decrease with the decrease in pH value, and vice versa. However, carboxyl-PS nanoparticles experience drastic changes compared to the sulfate-PS particles, due to the

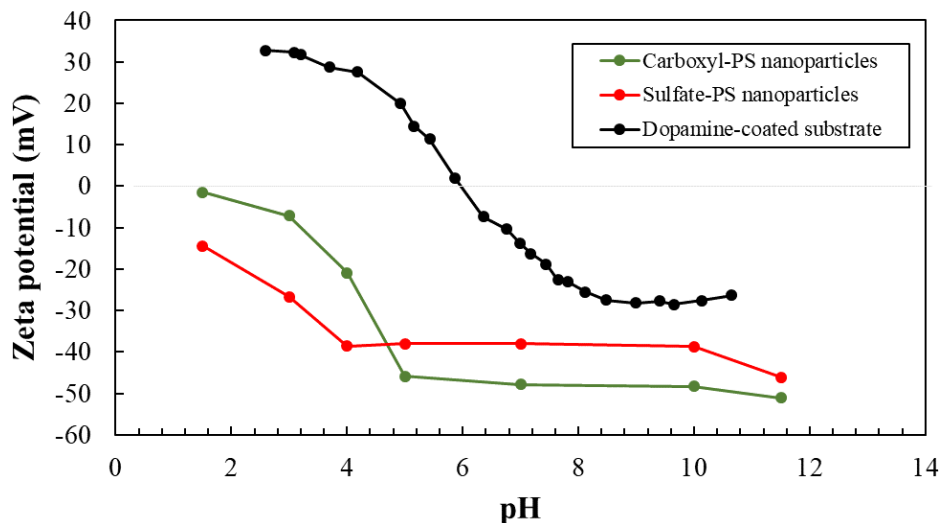


Figure 4.2: The measured zeta potentials of carboxyl- and sulfate-PS particles in water and surface zeta potential of the dopamine-coated glass slide with respect to different pH values. The standard deviations for the colloidal particles and the dopamine-coated substrates are ~1 mV and ~3 mV, respectively.

abovementioned protonation and deprotonation processes. None of the colloidal suspensions reaches the isoelectric point (IEP) even when the pH value is dropped to 1.5. This observation is consistent with the results reported elsewhere.¹³¹

In this study, the printing conditions were tuned so that the wetting droplets would not impinge into and mix with the supporting droplets. The wetting droplets carrying the colloidal nanoparticles successfully spread over the interface of supporting droplets, as a result of an instantaneous Marangoni flow due to the surface tension gradient, emanated from the initial mixing of solvents upon the impact. Both carboxyl and sulfate functional groups have strong affinity to water, and the functionalized PS nanoparticles would diffuse and mix into the supporting droplet if no other forces prevent them from this process. Upon the wetting droplet spreading, capillary forces arise to compete against the interparticle electrostatic repulsion forces at the interface to push these nanoparticles to bridge and eventually agglomerate together forming various sizes of monolayer networks. Compared to individual spherical nanoparticles, these monolayer “islands” are trapped

at the interface in an energetically favorable state due to the interfacial deformation caused by the fractal shape of the agglomerates.⁸⁴ Therefore, the nanoparticles at the interface may experience two different and competing movements: (i) particle diffusion and mixing into the supporting droplet, and (ii) particle assembly to “islands” of monolayer networks at the interface, which are determined by the capillary interactions of particle-particle and particle-interface, particle-particle electrostatic interactions, and particles’ affinity to water.⁸⁹ When the pH value of the supporting droplet changes, the particle-particle electrostatic force varies (Figure 4.2), which correspondingly affects the assembly process at the interface and final deposition on the substrate. Depending on the type of PS particles and the pH value utilized, various assembly structures of nanoparticle deposits were obtained from a nearly monolayer with well-ordered structures to relatively uniform but less-ordered deposits, and to depositions with ring-like morphologies. More details are presented in the following sections. It is worth pointing out that for sulfate-PS nanoparticles at pH 7, besides the monolayer deposition in most of the deposits, a ring of nanoparticles was observed at the edge of the deposits, which is attributed to the nanoparticles at the interface interacting with the dopamine-coated substrate. When the pH changes from an acidic to a basic environment, as shown in Figure 4.2, the zeta potential of the dopamine-coated substrate also varies from positive to negative, with an isoelectric point at pH 6.2. As a result of the particle-substrate interaction, the pH value of the supporting droplet strongly affects the morphology of the final deposits.

4.3.2 Effect of pH on Deposit Morphology of Carboxyl-PS Nanoparticles

To elucidate the mutual effect of the multibody interactions experienced by carboxyl-PS particles during the assembly, pH values of the supporting droplets were systematically controlled. As

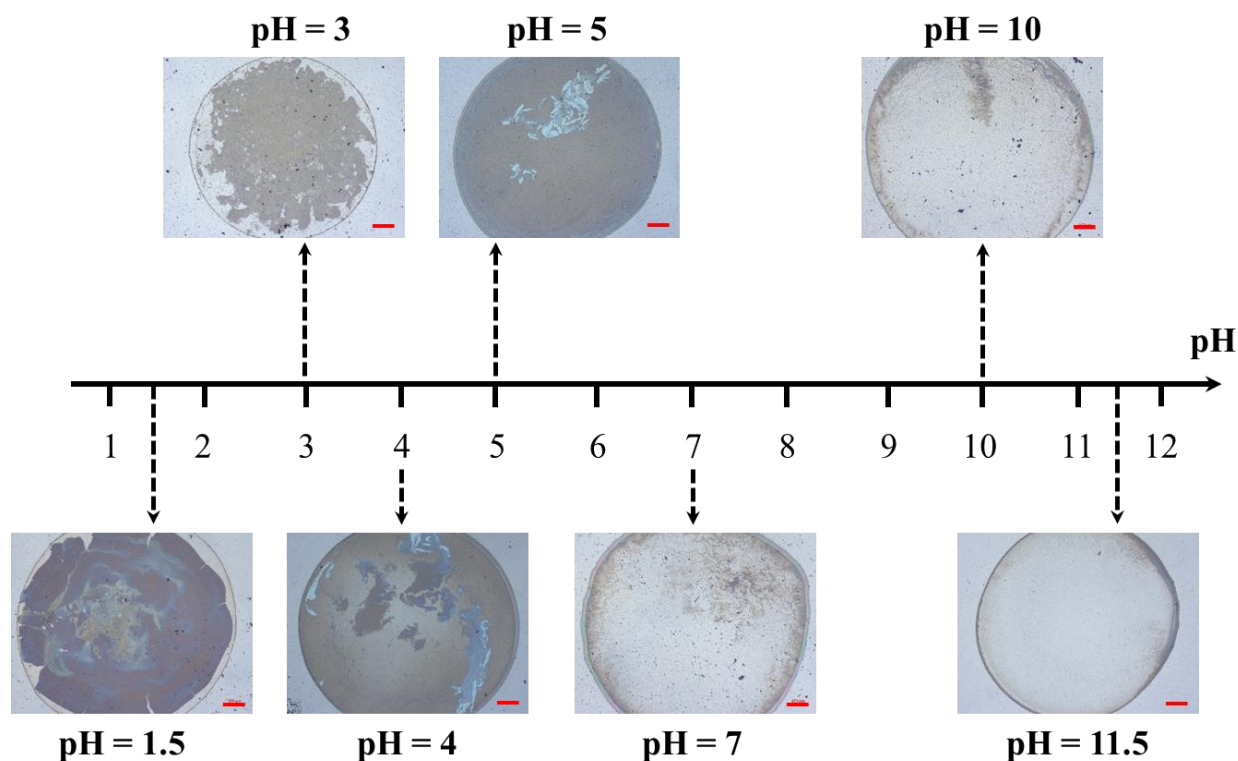


Figure 4.3: Deposit patterns obtained from jetting one wetting droplet with carboxyl-PS particles on supporting droplets with different pH values. The scale bar is 100 μm .

illustrated in Figure 4.1, the carboxyl-PS particles assemble differently according to the pH value utilized. For pH conditions of < 4 , $\sim 4-7$, and > 7 , nearly monolayer depositions without ring formation, non-uniform deposition with ring formation, and exclusive ring formation are obtained, respectively. The morphology of depositions composed of carboxyl-PS particles at various pH values are presented in Figure 4.3 for one wetting droplet. The self-assembly mechanism and multibody interactions are illustrated in Figure 4.4a and elaborated in detail as follows. The assembly of the carboxyl-PS particles was first examined with a supporting droplet of pH 7. It is worth noting that when the self-assembled “islands” at the interface deposit onto the substrate, structural colors are generated due to the well-ordered periodic structures among the nearly monolayer nanoparticle assembly. On the other hand, lack of the structural colors indicates no ordered assembly present in the deposits. As shown in Figure 4.3, at pH 7, the nanoparticle

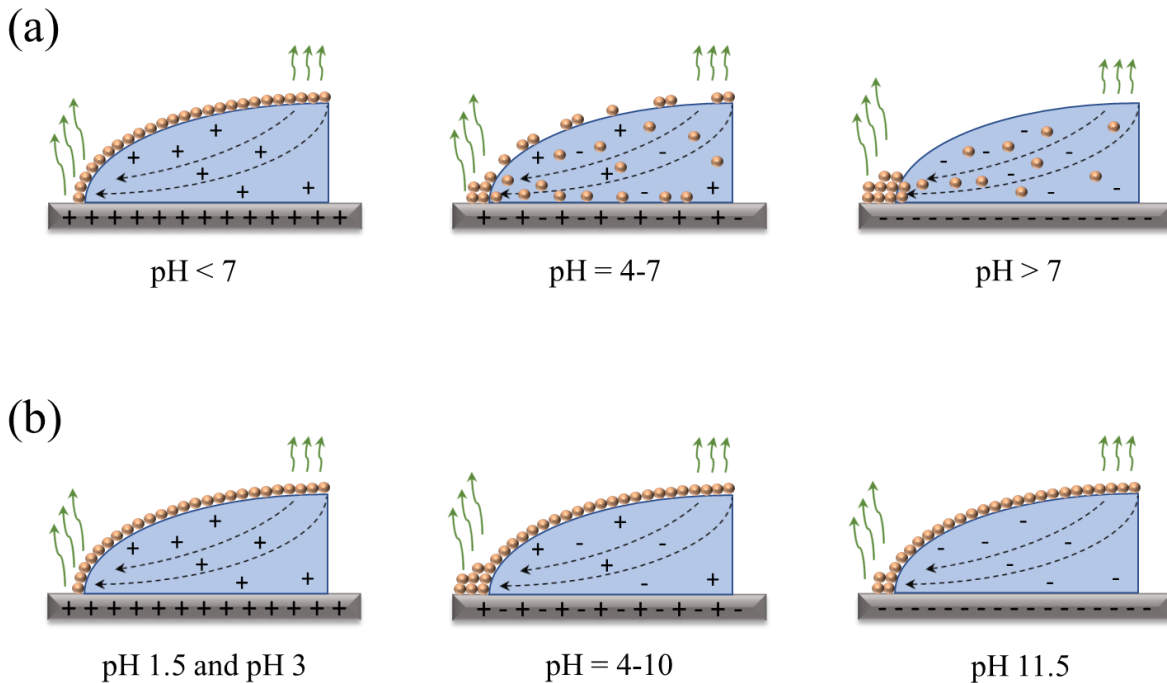


Figure 4.4: Illustration of the multibody interactions at different pH values for (a) carboxyl-PS particles, and (b) sulfate-PS particles. The positive and negative signs represent ions available in the supporting droplet at various pH values.

deposition exhibits no structural color. We deduce that most of the spreading nanoparticles diffused into the bulk of the supporting droplet due to their strong hydrophilicity and strong particle-particle electrostatic repulsion forces (with a zeta potential of - 47.8 mV), which inhibited the network formation at the interface. Some of the particles inside the supporting droplet were carried by the evaporation-induced flow to the edge of the sessile droplet while the rest were deposited inside the footprint due to particle-substrate interactions. Even though the dopamine-coated substrate shows the isoelectric point near pH of 6–7, it is hypothesized that the adsorbed zwitterionic dopamine has the ability to catch nanoparticles in the bulk of the supporting droplet by DLVO interactions.¹¹⁰ The final deposition (Figure 4.3 and Figure 4.5) exhibits a non-uniform irregular morphology, contributed mostly by the particles diffused into the bulk of the supporting droplet.

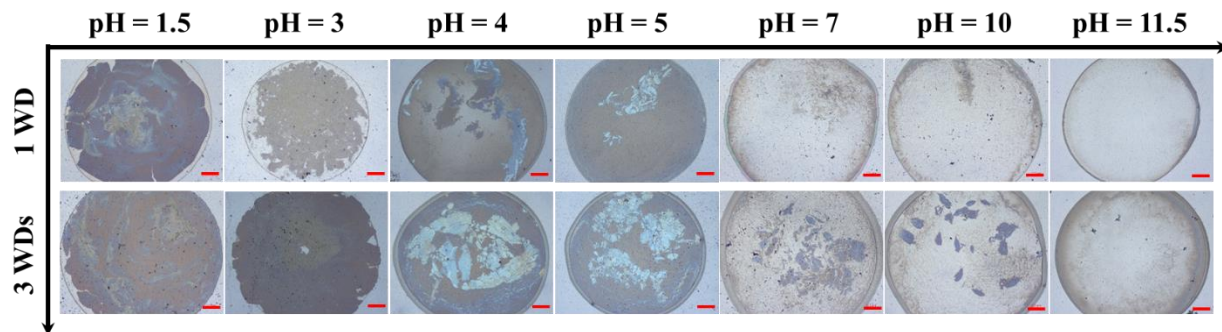


Figure 4.5: Deposit pattern evolution obtained from jetting one wetting droplet (WD) and 3WDs with carboxyl-PS particles on the supporting droplets with different pH values. More particles tend to diffuse into the supporting droplet as the pH value increases. The scale bar is 100 μm .

When the supporting droplet gets more acidic (e.g. pH 5), the surface charge on the carboxyl-PS slightly decreases with a zeta potential of -45.9 mV. Upon the wetting droplet spreading on the supporting droplet, a small fraction of the nanoparticles survived and remained at the interface during the evaporation due to the slightly decreased interparticle electrostatic repulsion force. As shown in Figure 4.3, agglomerate islands (bluish color) are observed on top of the final deposits, which are attributed to the self-assembled floating “islands” of nanoparticles at the interface. A darker brown color of the deposition indicates that the nanoparticles inside the supporting droplet were captured by the dopamine-coated substrate, due to the particle–substrate attractive force, noticing that the dopamine-coated substrate has a positive zeta potential at pH 5 (14.4 mV).

When the pH value of the supporting droplets further decreases, e.g. pH 4, the protonation reaction of the carboxyl group is further suppressed, resulting in a large decrease in zeta potential (-20.9 mV). Such a condition facilitates more nanoparticles to be self-assembled and trapped at the interface. Nonetheless, a large number of nanoparticles diffused and mixed into the bulk of the supporting droplet. As shown in Figure 4.4a, these nanoparticles experience strong particle–substrate electrostatic interactions (attractive force) that assists in trapping some of the particles in the middle of the deposit while the rest of the particles are carried to the TCL by the evaporation-

induced capillary flow. As a result, the final deposition obtained at pH 4 is composed of self-assembled particles at the interface of the supporting droplet, which is indicated by the bluish color, and the particles diffused in the bulk during solvent evaporation that presents the brown color as shown in Figure 4.3. This behavior is more pronounced at a higher particle loading such as jetting three wetting droplets (Figure 4.5). A drastic change in the nanoparticle assembly is observed when the pH value decreases to 3 with a zeta potential of -7.2 mV. Due to the significantly decreased electrostatic repulsion among the nanoparticles, they tend to form agglomerates at the interface. On one hand, the agglomerates prevent the nanoparticles from diffusing and mixing into the supporting droplet as described earlier, where the majority of the particles were trapped at the interface during the evaporation. On the other hand, the agglomerates were formed in a 3D configuration instead of a monolayer network. No structural colors are exhibited in the deposition due to the lack of regular and periodic arrangement among the nanoparticle assembly. When the pH of the supporting droplet is further reduced to 1.5, the carboxyl-PS particles exhibit the lowest surface charge (-1.43 mV) that results in minimal particle-particle electrostatic repulsions. In this case, the interparticle capillary forces (and possibly van der Waals forces) were strong enough to dominate the self-assembly process of nanoparticles at the interface. Interestingly, in this strong acidic environment, the nanoparticles may experience “melting and bridging” to form a nearly monolayer film of joined nanoparticle branches, as shown in Figure 4.6. No such melting behavior is perceived at pH values equal to or higher than 3. Although the supporting droplets and the substrate are strongly positively charged at this low pH value, their influences are not significant since all the particles prefer to stay at the interface (Figure 4.4a) because of the weak interparticle repulsion interactions.

Compared to the condition of pH 7, zeta potential of the carboxyl-PS particles slightly increases when the supporting droplet becomes basic with pH values higher than 7. Interactions among the charged particles at the interface, both negatively charged particles and dopamine-coated substrate result in similar yet still distinct deposit morphologies as shown in Figure 4.3. For conditions of pH 7 and pH 10, due to the minimal difference in zeta potentials of the nanoparticles (~ 0.5 mV), we hypothesize that the particles behave in a similar fashion at the interface, i.e., most of the particles diffuse and mix into the supporting droplet and only a very small population of particles could be present at the interface. Nonetheless, the particles diffusion into the bulk of the supporting droplet exhibited a different behavior. Notice the zeta potential of the substrate increases to (-27.5 mV) in the basic environment. In this case, in addition to the evaporation-induced flow, which carried those particles to the TCL of the supporting droplet, they also experienced stronger particle-substrate repulsion forces that eased the particle migration to the TCL. Figure 4.4a illustrates the multibody electrostatic interactions at $\text{pH} > 7$. Although all the mechanisms pushed the particles to migrate to the edge of the supporting droplet, some of them could be observed in the middle of the deposits after the drying process. This could be attributed to: (i) zwitterionic dopamine polymer, adsorbed on the substrate surface, attracts to some negatively charged PS particles, and (ii) we hypothesize that some PS particle might be trapped by the substrate surface roughness during their migration path to the edge of the supporting droplet. Surprisingly, no particles were deposited in the middle of the footprint when pH 11.5 was utilized (Figure 4.6). In this case, the substrate, the supporting droplet, and the PS particles were all highly negatively charged. This exemplifies a scenario that upon the particles spreading on the interface, they fail to assemble into agglomerates or networks at the interface due to strong interparticle repulsion interactions; instead, they diffuse and mix into the supporting droplets due to their strong hydrophilicity. Furthermore,

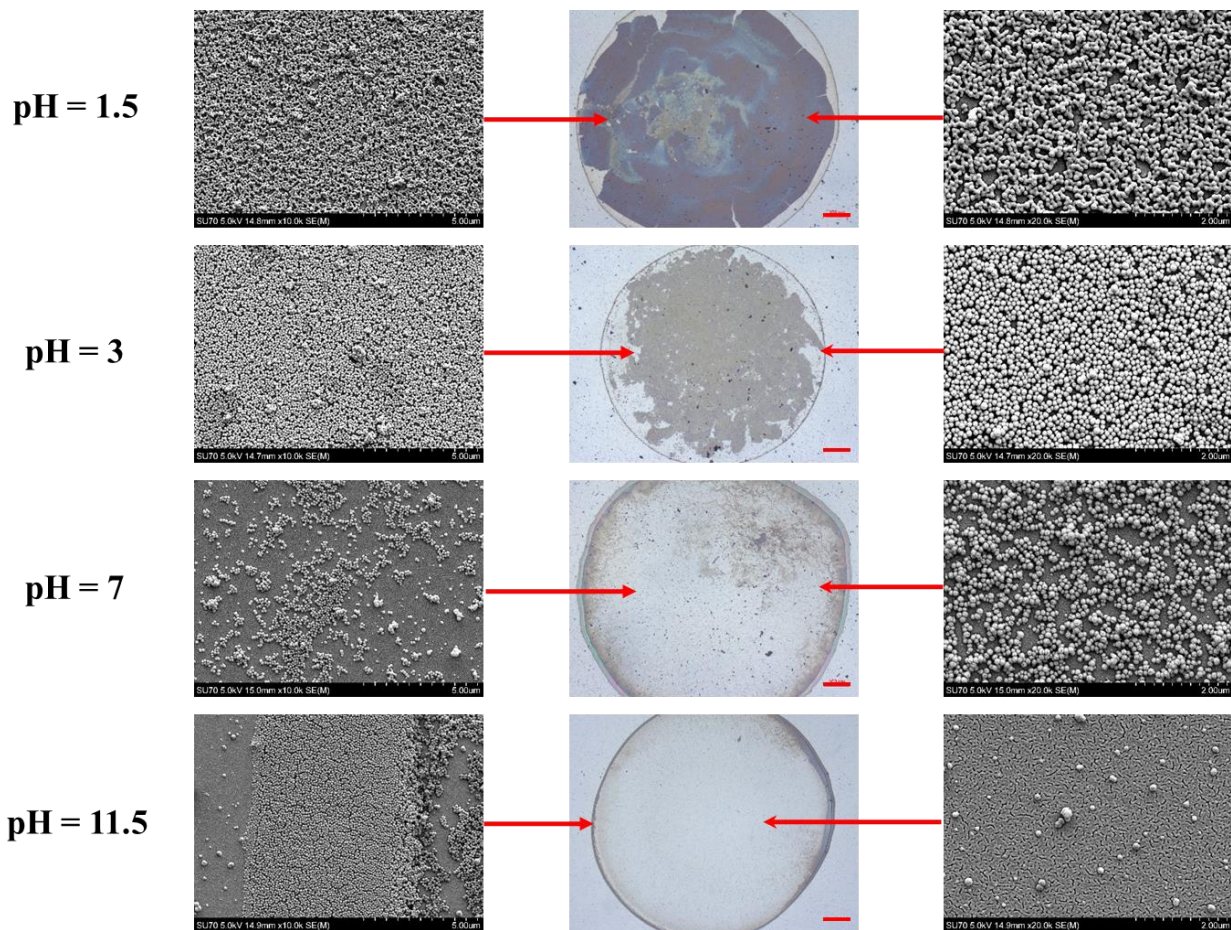


Figure 4.6: SEM images of deposits with carboxyl-PS particles at various pH values. The scale bar in the optical images is 100 μm .

all these particles transport to the edge of the supporting droplet by the action of the evaporative-induced capillary flow. Due to the strong particle-substrate repulsion interactions, all these particles could not deposit onto the substrate until they reached the TCL of the supporting droplet, producing the conventional “coffee-ring” effect.

4.3.3 Effect of pH on Deposit Morphology of Sulfate-PS Nanoparticles

To assess the effect of pH on the sulfate-PS particle assembly, the pH of the supporting droplet was systematically adjusted from 1.5 to 11.5. Figure 4.1 and Figure 4.4b illustrate the effect of pH on deposits produced by sulfate-PS particles and multibody interactions involved in this assembly process. Sulfate functional groups are the most hydrophilic in nature due to their acidity. However,

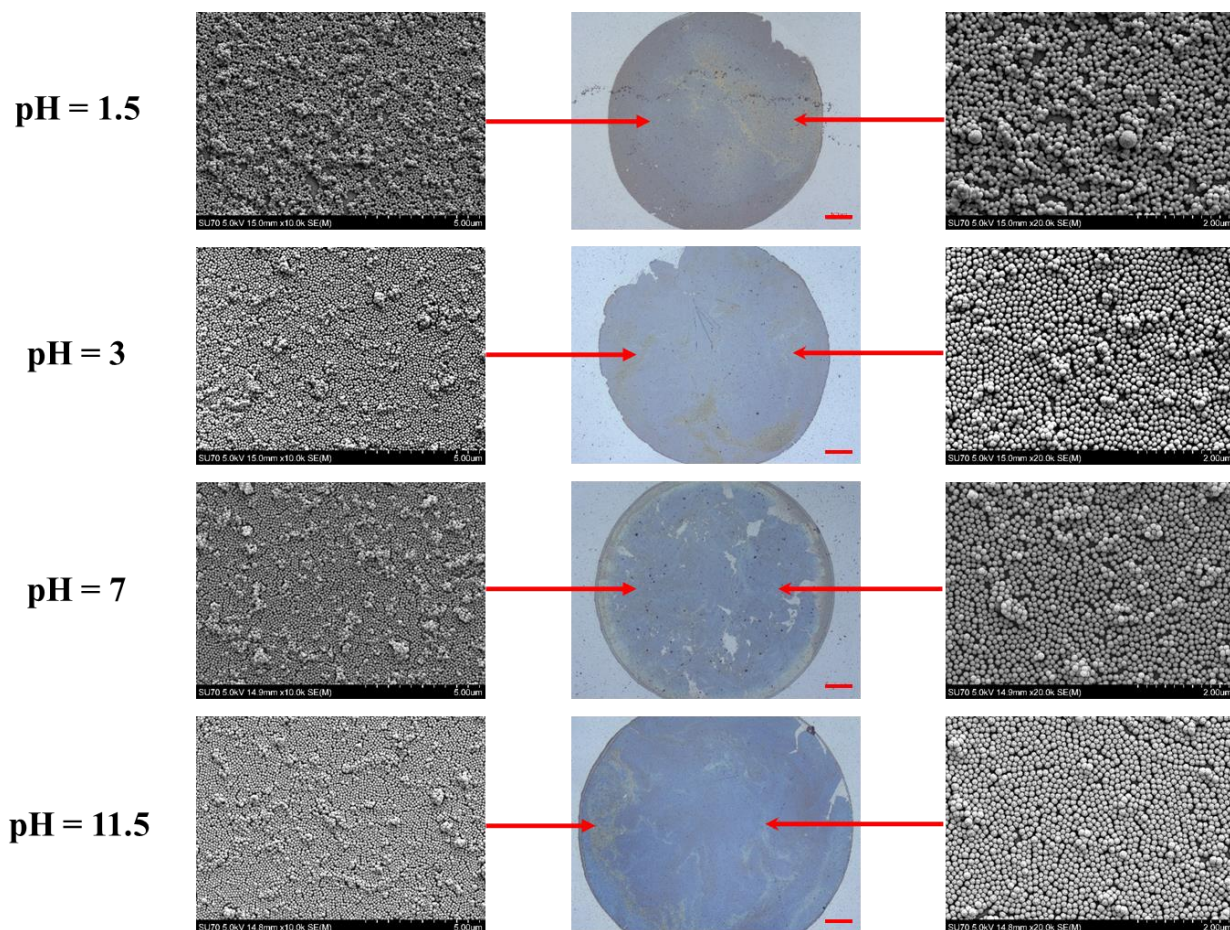


Figure 4.7: SEM images of deposits with sulfate-PS particles at various pH values. The scale bar in the optical images is 100 μm .

the sulfate-PS particles in this study have only about $\sim 1/12^{\text{th}}$ functional groups per particle of those on the carboxyl-PS particles (Table 3.1). Fewer functional groups and lower zeta potentials lead to weaker interparticle repulsion interactions and less affinity to water, which facilitate the skin formation at the interface and correspondingly reduce the number of nanoparticles diffusing into the supporting droplet. Yet, fewer functional groups on the particle and less surface charge density are also responsible for more particle agglomerations as compared to the carboxyl-PS particles (Figure 4.7). The sulfate-PS particles gave strikingly different outcomes from the carboxyl counterparts when utilizing various pH values in the supporting droplet. Such

nanoparticles are less prone to the pH change, where the fully covered, nearly monolayer deposition is always the case (Figure 4.8).

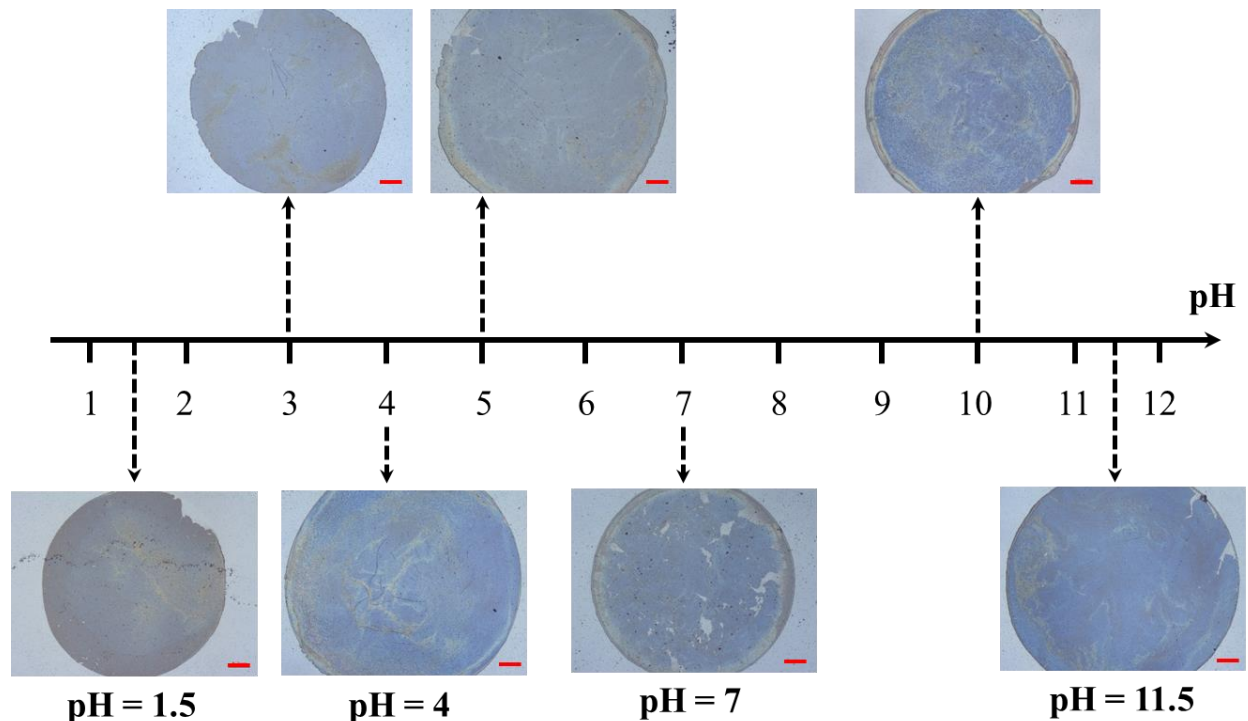


Figure 4.8: Deposit patterns obtained from jetting one wetting droplet with sulfate-PS particles on the supporting droplets with different pH values. The scale bar is 100 μm .

At pH 11.5, the sulfate-PS particles have a zeta potential of -46.1 mV, which is comparable to that of carboxyl-PS particles at the pH 4. However, the sulfate-PS particle's affinity to water is much weaker than its counterpart due to the fewer sulfate functional groups on the PS particles. As a result, even at this most basic condition and with the strongest interparticle repulsive interactions, the sulfate-PS particles successfully self-assemble into nearly monolayer networks at the interface and deposit the well-ordered assembly onto the substrate upon solvent evaporation. The bluish structural color exhibited in Figure 4.8 indicates the high quality and orderliness of the particle assembly, which stems from the periodic optical cavities in depositions produced at different acidic and basic environments. The optical images in Figure 4.8 and the SEM images in Figure 4.7

support the hypothesis that in all the pH conditions, the sulfate- PS particles self-assemble into monolayer networks at the interface, maintaining the well-ordered assembly structure until final deposition, despite the change in zeta potentials.

Differences, however, do exist in the deposition morphology of the sulfate-PS particles at various pH conditions. At pH 1.5, akin to the carboxyl-PS particles, the sulfate-PS particles “melt” and join each other at the interface, forming a solid skin of nanoparticles, during the drying process. This behavior is observed at pH 1.5 even though the sulfate functional groups are not pH sensitive. Further increase in pH value (e.g., pH 4 and 5 with zeta potentials -38 mV) has led to higher interparticle repulsion interactions by which the close packing of the nanoparticles is slightly affected as shown in Figure 4.7. However, the capillary force at the interface of the supporting droplet dominated the other forces. The dopamine-coated substrate at such pH levels is highly, positively charged that attracts the excess amount of the floating particles at the interface contributing to the ring formation (Figure 4.4b).

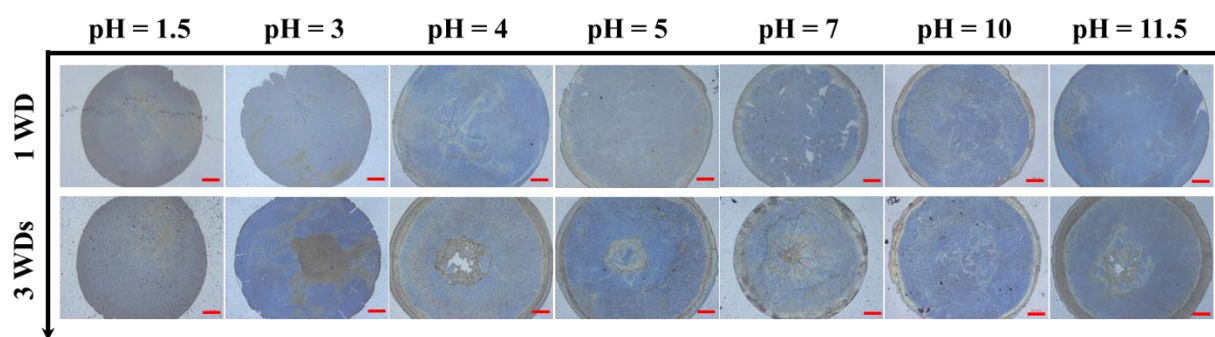


Figure 4.9: Deposit pattern evolution obtained from jetting one WD and 3WDs with sulfate-PS particles on the supporting droplets with different pH values. Sulfate-PS particles are more robust toward pH change, where the nearly monolayer of PS particles is always present. The scale bar is 100 μm .

The ring-like pattern can be clearly seen at a larger particle loading, e.g. three wetting droplets, as shown in Figure 4.9. It should be noted that the ring formed of sulfate-PS particles originates from particles trapped at the interface of the supporting droplet. While the ring composed of carboxyl-

PS particles, especially at $\text{pH} > 3$, is a combination of particles diffusing in the bulk and particles at the interface of the supporting droplet.

When the pH of the supporting droplet increases to 6 or 7, the zeta potential of the nanoparticles does not change much (-38 mV), while the dopamine-coated substrate exhibits an isoelectric point at $\text{pH} 6.2$. As described in the previous section, the positively charge amine groups could capture the negatively charged PS particles even though the overall charge on the dopamine-coated substrate is neutral. This provides an explanation to the ring formed at this particular pH value. A repulsion force arises between the particles and the substrate at $\text{pH} > 7$, where the substrate, the supporting droplet, and the nanoparticles are all negatively charged.

This repulsion force reduces the amount of the nanoparticles deposited at the ring by forcing them back to the surface of the supporting droplet (more details are provided in Section 4.3.4). Further increasing the pH to 11.5 has boosted the particle-substrate repulsive interactions (Figure 4.4b), where the surface charges become highly negative. The basic solution not only significantly reduced the amount of the particles deposited at the ring, but also enhanced the formation of highly-ordered, closely-packed monolayers of nanoparticle assembly by squeezing the nanoparticles back to the interface. Consequently, the blue color contrast is the brightest at $\text{pH} 11.5$. The SEM images of the deposits are presented in Figure 4.7.

Finally, because the sulfate-PS particles are more robust against the pH change, where most of the particles remain trapped at the interface of the supporting droplet, buckling and folding of the formed skins have been observed at higher particle loadings (e.g. three wetting droplets). A similar observation of the film buckling phenomenon at high particle loadings have been reported by Boley et al.⁹⁰

4.3.4 Discussion

In this dual-droplet printing process, the final structure of the particle assembly depends on the particle's affinity to water (type of functional groups and density), the charge level of the PS particles (zeta potential), and the pH of the supporting droplet. For sulfate-PS particles, much fewer functional groups per particle make the particles less hydrophilic. Even when the zeta potential increases to -46.1 mV and the sulfate-PS particles experience strong electrostatic repulsion, they still self-assemble into monolayer networks at the interface. On the other hand, carboxyl-PS particles are much more hydrophilic due to the large number of functional groups on the particle surface. Self-assembly of carboxyl-PS particles is only obtained for zeta potential of -7.2 mV or lower, corresponding to pH of 3 or less. As the zeta potential increases (along with the increase in pH), less carboxyl-PS particles can self-assemble and maintain at the interface. When the zeta potential increases to -51.1 mV (at pH 11.5), no particles survive at the interface during the evaporation; and instead, all the particles diffuse and mix into the supporting droplet.

When the sulfate-PS particles are trapped at the interface during the evaporation, they maintain the well-ordered assembly structure and deposit onto the substrate upon drying. However, very small amount of particles still get captured by the dopamine surface at the contact lines of the supporting droplet, especially for conditions of pH 4–10. Dopamine surface has a positive zeta potential for $\text{pH} < 6$. This means that the negatively charged PS particles at the interface can be attracted to the TCL and deposited at the edge due to electrostatic interactions. Furthermore, dopamine is a zwitterionic polymer, which is capable of attracting some negatively charged PS particles at the interface, even when its zeta potential is negative (for pH of 7–10). As a result of this deposition, a ring forms at the edges of the supporting droplet (Figures 4.9 and 4.10). In addition, the particles diffusion and mixing into the supporting droplet also contribute to the ring formation, particularly

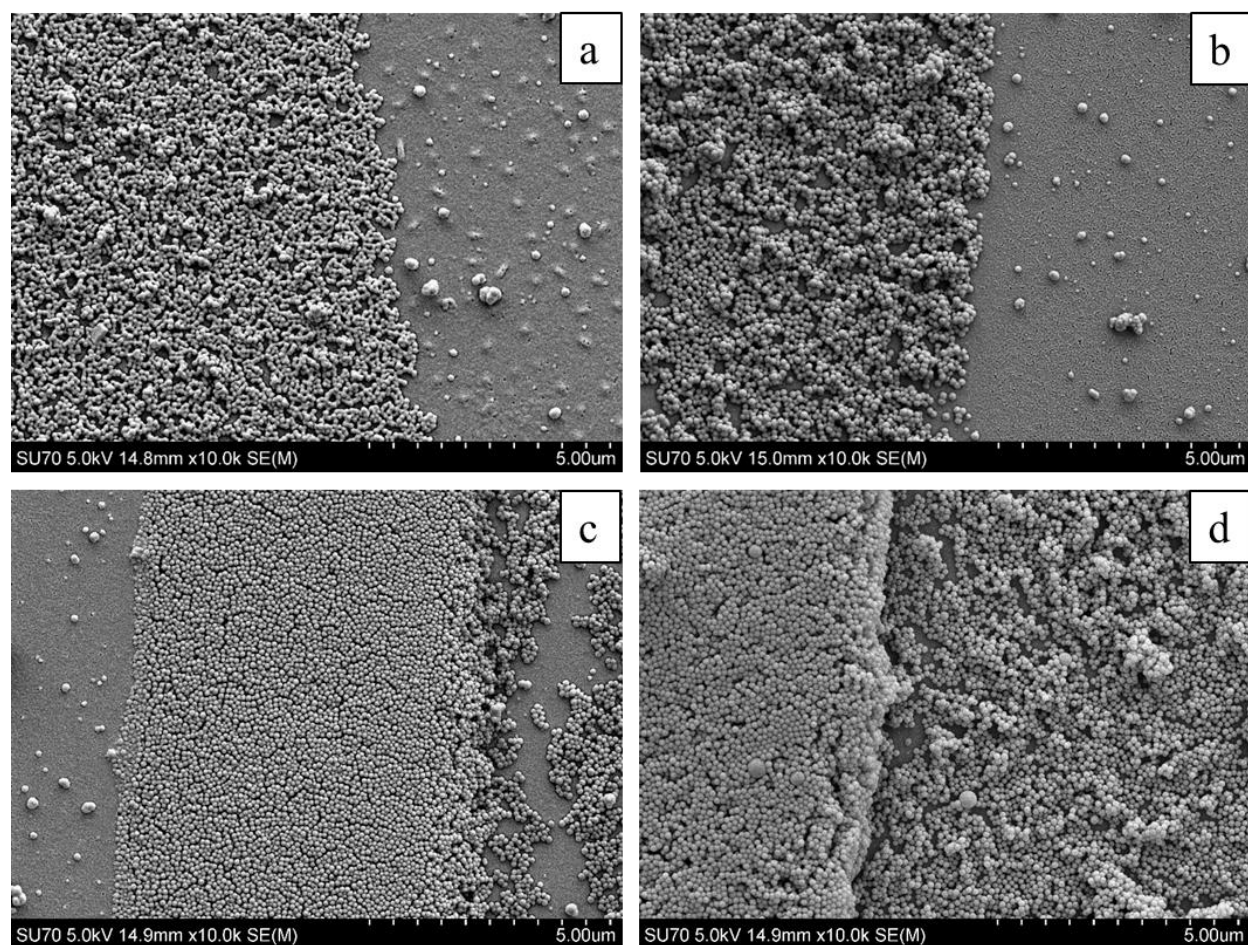


Figure 4.10: SEM images showing the deposit edges at different pH values; (a) deposition of one WD of carboxyl-PS particles at pH 1.5, (b) deposition of one WD of sulfate-PS particles at pH 1.5, (c) deposition of one WD of carboxyl-PS particles at pH 11.5, and (d) deposition of one WD of sulfate-PS particles at pH 7.

for carboxyl-PS particles (Figures 4.5 and 4.10). Those particles follow the evaporation-induced capillary flow inside the supporting droplet and move towards the TCL. During their journey, some particles may get captured and randomly deposit on the dopamine-coated substrate due to the aforementioned electrostatic interactions, zwitterionic nature of the dopamine surface, and/or roughness of the dopamine surface. The rest of the particles deposit near the edges of the supporting droplet. When the zeta potential of the dopamine surface increases to -28.5 mV for $\text{pH} > 10$, the negatively charged particles could not deposit onto the dopamine surface due to strong electrostatic repulsion. Therefore, for the extreme case of carboxyl-PS particles at pH 11.5, all the

particles diffused into the supporting droplet are repelled by the substrate and accumulated near the edges of the supporting droplet, producing the conventional coffee ring.

Figure 4.11a illustrates the height profile of the carboxyl-PS particle deposits measured by the profilometer. At low pH values (e.g. pH 1.5 and pH 3), the floating particles at the interface of the supporting droplet have low charges that eased the network formation by the action of capillary forces. The particles were held firmly in their network, where a negligible amount of particles deposited onto the dopamine surface at the TCL regardless the favorable attractive electrostatic force between the particles and the dopamine-coated substrate. Therefore, the rings at the low pH values have negligible thicknesses. The ring is measured to be $\sim 1 \mu\text{m}$ in height at pH 4. When the pH further increases, the rings become thicker and wider, reaching $\sim 2 \mu\text{m}$ in height for pH 10. This growth is contributed by the particles from both the interface and the bulk of the supporting droplet. However, for pH 11.5, the ring turned into a narrow and tall peak (3.3 mm in height) since all the particles exclusively deposited near the edges and no particles in the middle of the deposit due to the strong repulsion from the dopamine coated substrate.

On the other hand, the sulfate-PS particles are less susceptible to pH change, where the interface of the supporting droplet is always covered with the self-assembled nanoparticles. Figure 4.11b presents the height profile of deposits with sulfate-PS nanoparticles. Since the sulfate-PS particles successfully self-assemble at the interface with negligible particles mixing into the supporting droplet, the formed ring with the sulfate-PS particles is mostly from the particles at the interface. Similar to the carboxyl nanoparticles, low pH values (e.g. pH 1.5 and pH 3) give monolayers of sulfate-PS particles and no accumulation of particles at the contact lines. An increase in particle loading (i.e. three wetting droplets) did not produce a ring (Figure 4.9). Instead, we have observed

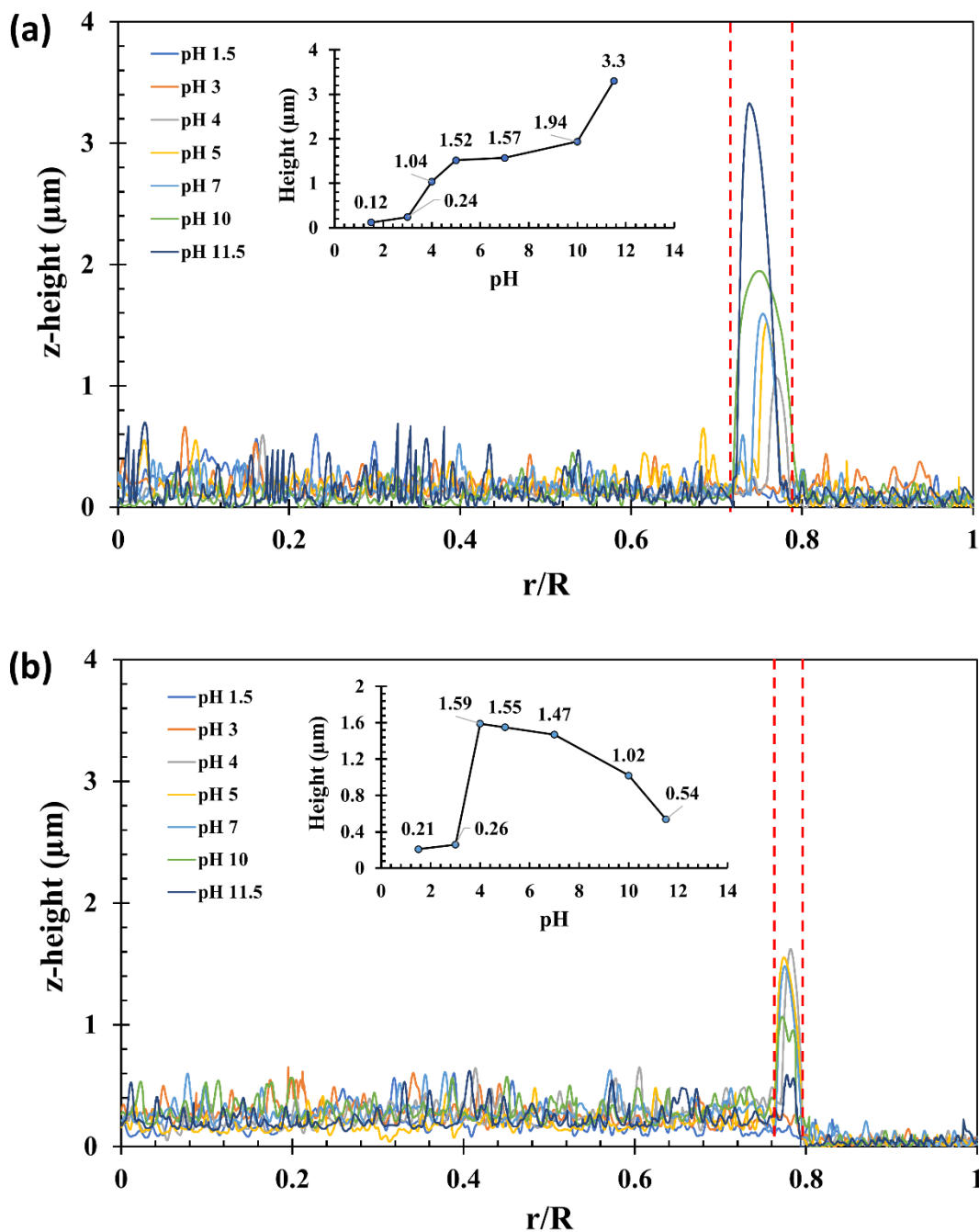


Figure 4.11: Height profiles near the deposit edges obtained from dual-droplet printing of (a) carboxyl-PS particles, and (b) sulfate-PS particles at different pH values. The red dash lines represent the ring region while the inset shows the z-height of each individual peak with its corresponding pH value. (For interpretation of the references to color in this figure legend, the reader is referred to the web version of this article.)

that jetting more wetting droplets creates a hole in the self-assembled film and induces vortices close to the interface of the supporting droplet. Analogous observation of such eddies has been

reported by Parsa et al. in an effort to study the effect of substrate temperature on pattern formation.¹¹ However, the ring started to develop at pH 4 due to the increase in the attractive electrostatic interactions between the particles at the interface and the dopamine-coated substrate at the TCL. The rings are very similar among the deposits in pH values between 4 and 7 with the highest peak of $\sim 1.6 \mu\text{m}$. The situation significantly changed at pH 11.5. The substrate became highly negatively charged that pushed the nanoparticles near the TCL back to the interface of the supporting droplet, resulting in a monolayer assembly with a higher degree of closely-packed deposition. Consequently, the amount of nanoparticles present at the ring of the deposit significantly reduced, which is contrary to rings obtained at the same pH level with carboxyl-PS particles. Both Figure 4.11a and 4.11b show some peaks ($\sim 0.5 \mu\text{m}$) in the middle of the deposits that correspond to PS particles (particularly the sulfate-PS particles) and dopamine agglomerates.

4.4 Conclusion

In this work, we have demonstrated controlling deposition morphology in the dual-droplet inkjet printing by pH-modulation along with the associated electrostatic interactions of nanoparticles. It is worth emphasizing that majority of the prior research efforts on colloidal particle depositions from droplets are based on homogeneous particle-laden sessile droplets, ranging from tens of microns to millimeter size in diameter. Various approaches have been employed to alter the evaporation-induced flow field, particle-particle, and particle-substrate interactions, resulting in different deposition morphology of the colloidal particles, e.g. dome-shape depositions,¹⁰¹ line patterns,¹³² spider web and radial spoke structures,¹³³ relatively uniform depositions with suppressed coffee-ring formation,^{11,12,15,35-38} etc. However, depositions with nearly a monolayer of self-assembled colloidal particles have rarely been obtained. Recent efforts have been made to

push the colloidal particles to the droplet interface during the solvent evaporation, leading to some well-ordered depositions.^{90,91,95}

Different from these depositions from particle-laden sessile droplets, interfacial self-assembly is the driving mechanism in the deposition formation during the dual-droplet printing. The colloidal particles are spread on the air-water interface of the supporting droplet when the wetting droplet impacts onto the supporting droplet. The self-assembly of the particles occurs at the interface, and in favorable conditions the particle entities remain at the interface during solvent evaporation, till finally deposit onto the substrate. pH modulation of the supporting droplet affects the interfacial self-assembly through the multibody interactions among the nanoparticles, and the particle-interface and particle-substrate interactions. The final structure of the particle assembly is determined by the particle affinity to water (type of functional groups and density), charge level of the PS particles (zeta potential), and the pH of the supporting droplet.

The carboxyl-PS particles have higher affinity to water and is more prone to pH change. At pH values as low as 3, the particles tend to self-assemble at the interface of the supporting droplet, where the interparticle interactions are minimal due to the low surface charge. However, they diffuse and mix into the supporting droplet as the pH increases. For extreme pH values (i.e. pH 10 and pH 11.5), most of the particles at the interface diffuse into the supporting droplet, where they get entrained by the evaporation-induced capillary flow to the TCL, producing the conventional CRE. The sulfate-PS particles, on the other hand, is marginally affected by the pH change. Its low surface charge density facilitates the self-assembly of the nanoparticles at the interface of the supporting droplet regardless of the pH value utilized. Contrary to the carboxyl-PS particles, the sulfate-PS particles, even at extreme basic and acidic environments, successfully self-assemble

into nearly monolayer networks at the interface and deposit the well-ordered assembly onto the substrate upon solvent evaporation.

Finally, reducing the pH value of the supporting droplet to 3 or less produces self-assembled networks regardless the type of nanoparticles employed, where no ring formation is observed. Future works include investigating the interfacial self-assembly of anisotropic colloidal nanoparticles in the dual-droplet inkjet printing process; and employing functional materials (e.g. noble metals) to fabricate low-cost, high-performance functional devices, e.g. surface enhanced Raman scattering (SERS) substrates. Incorporating the scalable dual-droplet inkjet printing technique with the ability to control the assembly structures of the deposits can become a promising approach to printing functional optical and electronic devices.

CHAPTER 5 Probing the Colloidal Particle Dynamics in Drying Sessile Droplets

5.1 Introduction

Accumulation and assembly of colloidal particles at edges of evaporative particle-laden droplets have been intensively studied in the past few decades.^{9,56} During the solvent evaporation course, the colloidal particles are forced to transport to the TCL region by virtue of the evaporation-induced flow, especially when no natural convection or Marangoni flow is present.^{40,58} Depending on many factors, presented in detail in the previous chapters, the transported colloidal particles might deposit near the edge of the sessile droplet, producing the ubiquitous CRE.³³

In an effort to investigate the behavior of binary particles near the periphery of sessile droplets, Monteux and Lequeux examined the building of colloidal deposition generated at the edge of evaporative sessile droplet with respect to time.⁶⁵ When bidisperse mixtures of colloidal particles were utilized, particle separation phenomenon in vicinity of the TCL region have been identified, where smaller particles always tended to penetrate further into the leading edge of the droplet as opposed to bigger particles. Recently, Marín et al. studied the segregation of charged particles with different densities during solvent evaporation. Changing substrate wettability and particle charge-mass ratios in low ionic strength solutions influenced the segregation of binary colloidal suspensions.⁶⁴ The highly negatively charged particles were observed to transport and deposit in vicinity of the TCL at a faster pace than those with less particle charge density. Additionally, the author identified the strong dependence of particle depositions on receding contact angle of the substrate, which is directly correlated to the so-called “wedge effect”. Such particle arrangement phenomenon near the TCL has been demonstrated as a feasible solution for sorting out biological entities in sessile droplets (e.g., proteins, micro-organisms, and mammalian cells).⁶³

In this study, we have investigated the particle pinning in vicinity of the TCL, formed in conventional sessile droplets, and demonstrated an alternative mechanism of particle pinning, initiated by the air-liquid interface, through implementing the dual-droplet inkjet printing. Confocal microscopy was utilized to directly image the particle transport and pinning. Furthermore, the differences between the two pinning mechanisms were investigated by introducing colloidal particles into both the wetting droplet and the supporting droplet during the dual-droplet printing. Depending on particle size and concentration, different particle depositions have been obtained in vicinity of the TCL, such as a ring of particles mainly from the air-liquid interface, blended ring, and stratified ring of particles dispersed in the bulk and particles floating at the interface of the supporting droplet.

Three characteristic times, t_{evp} , t_{ps} , and t_{pw} , which represent the total time for solvent evaporation, time required for colloidal particles in vicinity of the TCL in the bulk of the supporting droplet to reach and form the first layers at the TCL, and time needed for particles at the interface to reach the TCL, respectively, were calculated and compared to determine the final particle deposition. The characteristic time ratio (t_{ps}/t_{evp}) resembles whether the particles in the bulk of the supporting droplet have an adequate amount of time to reach the TCL before solvent evaporation completes. On the other hand, the characteristic time ratio (t_{ps}/t_{pw}) determines the competition between particles pinning in the bulk of the supporting droplet and particles at the interface during solvent evaporation. The ability of controlling such particle deposition and assembly could have a direct implication in developing facile, cost-effective technologies essential for patterning heterogeneous structured devices and coatings.

5.2 Materials and Methods

5.2.1 Materials. Polyethylene terephthalate (PET) films (MELINEX ST505) with 125 μm thickness were supplied by TEKRA, a division of EIS, Inc. Sulfate latex beads (8% w/v, 300 nm), carboxyl latex beads (4% w/v, 20 nm, 100 nm, 500 nm, and 1 μm), sulfate latex beads (2% solid, 200 nm) with yellow-green fluorescent dye, carboxyl latex beads (2% solid, 20 nm) with a Nile red fluorescent dye, and fluorescein F1300 dye were purchased from Thermo Fisher Scientific. KOPTEC ethanol (99.5% purity) was acquired from VWR. Deionized (DI) water with a resistivity of 18.2 $\text{M}\Omega\cdot\text{cm}$ was produced by Direct-Q water purification system (Millipore Sigma). All chemicals were used as-received without further purification.

5.2.2 Confocal Microscopy Characterization. In order to monitor the particle pinning and deposition at the TCL, confocal laser scanning microscopy (Zeiss, LSM 710) was implemented in this study. A 60 \times oil lens with a numerical aperture of 1.4 was employed with a working distance of 0.19 mm and a scanning area of 140 $\mu\text{m} \times 140 \mu\text{m}$. The LSM has a lateral resolution of approximately 174 nm (or 184 nm) and a vertical resolution of 498 nm (or 524 nm) based on the 488 nm (or 514 nm) argon laser utilized to excite the fluorescent dyes. Glass slides were used as transparent substrates required for the confocal microscopy. Briefly, a coverslip glass slide with 170 μm thickness was rinsed with DI water and dried by nitrogen before use. The measured apparent water contact angle on the cover slip is $\sim 60^\circ \pm 2^\circ$.

In case of scanning the supporting droplet without colloidal particles, a 110 μL droplet of DI water with 0.1 mg/mL concentration of fluorescein F-1300 was dispensed on the cover slip and scanned using the 488 nm argon laser to capture the interface of the supporting droplet. In order to capture the nanoparticles at the air-liquid interface, 5 μL suspension containing 200 nm sulfate-PS particles (10 mg/mL particle concentration in ethanol) with yellow-green fluorescent dye was carefully

dispensed onto the supporting droplet (contains DI water only) using a micro-dispenser. The 514 nm laser was utilized to image the nanoparticles at the interface. The interval between the scanned slices was 200 nm in case of imaging the supporting droplet and the nanoparticle assembly at the air-liquid interface. To avoid the crosstalk between the fluorescent dyes of nanoparticles in the bulk and at the interface of the supporting droplet, a 110 μ L droplet of DI water with 0.5 mg/mL concentration of 20 nm carboxyl-PS particles labelled with Nile red was tested separately. The latter was scanned with the 514 nm laser and a 20 nm step size to capture the particle migration from the bulk of the supporting droplet to the TCL.

5.2.3 Ink Preparation. The as-received suspensions of polystyrene particles were ultra-sonicated for 5 min to ensure a homogeneous suspension of the nanoparticles. Then, two kinds of inks were prepared to perform the dual-droplet inkjet printing. The as-received carboxyl-PS particles (4% w/v, 20 nm, 100 nm, 500 nm, and 1 μ m) were diluted with DI water to obtain colloidal suspensions with particle concentrations of 0.2 mg/mL and 0.5 mg/mL that were utilized as inks for the supporting droplet. The printing ink for the wetting droplet was prepared by diluting the sulfate-PS particles (8% w/v, 300 nm) with ethanol to obtain colloidal suspension with a particle concentration of 10 mg/mL that was jetted over the supporting droplet. Each suspension was ultra-sonicated for another 5 min before printing.

5.2.4 Dual-Droplet Inkjet Printing Process. The inkjet printing platform (Jetlab 4, MicroFab) consists of four printing stations, two of which were used in this study. Supporting droplets and wetting droplets were jetted from two piezoelectric nozzles with orifice diameters of 80 μ m (MJ-ATP-01-80-8MX, MicroFab), driven by a waveform generator (Jetdriver III, MicroFab). Briefly, a supporting droplet was generated by jetting multiple bursts of colloidal suspensions of DI water with different sizes of carboxyl-PS particles (a total volume \sim 110 nL) on the substrate at a jetting

frequency of 500 Hz. Then, wetting droplets containing sulfate-PS nanoparticles were jetted to the center of the supporting droplet using the second 80 μm nozzle at a frequency of 1 Hz. In this work, we have used a jetting speed of ~ 1.3 m/s and a droplet volume of ~ 550 pL (diameter ~ 102 μm) for the wetting droplets. This is to ensure spreading of the wetting droplet over the interface of the supporting droplet upon impact. PET films (MELINEX ST505) were used as substrates for the dual-droplet inkjet printing. The apparent water contact angle on a clean PET substrate is $\sim 70^\circ \pm 2^\circ$ and the receding angle is $\sim 44^\circ \pm 2^\circ$.

5.2.5 Morphology Characterization. An ultra-high-resolution scanning electron microscope (HITACHI SU-70 FE-SEM) with 5 kV and 15 mm scanning distance was used for morphology characterization of the printed patterns. To minimize charging effect of the PS nanoparticles, the samples were coated with platinum using a platinum sputter (Denton Vacuum Desk V) for 120 s.

5.2.6 Analytical Analysis. In this study, an analytical analysis based on the Hu-Larson model is considered to comprehend the driving mechanism behind the particle deposition and assembly and to predict the characteristic times for particle pinning at the TCL region in the dual-droplet printing process. The characteristic time for two adjacent particles in vicinity of TCL to meet each other has been proposed and experimentally verified to describe the coffee ring formation.¹⁶ The comparison of the characteristic time for particle pinning to the total evaporation time determines the coffee ring formation.^{16,100,134} We have implemented this approach in the dual-droplet printing configuration, to evaluate and compare the particle pinning from the interface of the supporting droplet, the particle pinning from the supporting droplet, and the total evaporation time.

In the present model, the following assumptions are made: (i) in the bulk of the supporting droplet, the particles are homogeneously dispersed; (ii) the interface of the supporting droplet is uniformly covered with nanoparticles as a result of spreading the wetting droplets over the former one; (iii)

the air-liquid interface of the supporting droplet is assumed to be a spherical cap and the gravitational effect is neglected since the Bond number is $Bo = \frac{\rho g d_0^2}{\sigma} < 0.002$, where ρ is the density of water (note, the ethanol over the interface of the supporting droplet is not considered since its volume fraction is less than 5% of the entire volume of the supporting droplet even when nine wetting droplets are jetted), g is the gravitational acceleration, d_0 is the inflight diameter of the jetted droplets, and σ is the surface tension; (iv) solvent evaporation across the interface of the supporting droplet is assumed to be diffusion-limited and the air-liquid interface is considered to be in phase equilibrium; (v) particle motion in the bulk and at the interface of the supporting droplet are governed by the diffusion and evaporation induced-flow approximated at the initial particle concentration.

The time required for the solvent of the supporting droplet to totally evaporate, with a TCL close to 90° (in this study, $\theta = 70^\circ$), can be approximated by the following equation,¹³⁵

$$t_{evp} = f(\theta) \frac{\rho R_{depo}^2}{D(1 - RH)c_v} \quad (5.1)$$

where $f(\theta) = \frac{2 - 3 \cos(\theta) + \cos^3(\theta)}{6 \sin^3(\theta)}$, R_{depo} is the radius of supporting droplet deposition, D is the diffusivity of solvent vapor in air, RH is the relative humidity, and c_v is the saturated vapor concentration.

With the assumption that the colloidal nanoparticles in the bulk of the supporting droplet are homogeneously dispersed, the mean distance L_m between two colloidal particles are estimated by eq. 5.2,¹⁶

$$L_{m,B} = (V_0/N_s)^{1/3} \quad (5.2)$$

where V_0 is the initial volume of the supporting droplet, N_s is the total number of particles in the bulk of the supporting droplet, and the subscript B refers to the bulk of the supporting droplet. On the other hand, the mean distance between two colloidal nanoparticles at the interface of the supporting droplet is estimated by eq. 5.3,

$$L_{m,I} = (S_{cap}/N_w)^{1/2} \quad (5.3)$$

where S_{cap} stands for the spherical cap surface area of the supporting droplet, N_w is the number of particles in the wetting droplet (therefore at the interface), and the subscript I refers to the interface of the supporting droplet. Bearing this in mind, the diffusion time scale of particles in the bulk and at the interface of the supporting droplet could be evaluated by the Einstein diffusion equation $t_{diff} = L_m^2/2D_p$.¹³⁶ D_p is the diffusion constant of spherical particles in a liquid flow with low Reynolds numbers, $D_p = k_B T/6\pi\eta R_p$, where k_B is the Boltzmann constant, T is the absolute temperature, η is the dynamic viscosity of the fluid, and R_p is the radius of the colloidal particle. Accordingly, the mean diffusion velocity of colloidal particles in the bulk and at the interface of the supporting droplet can be calculated by eq. 5.4,¹³⁴

$$u_{diff} = k_B T / 3\pi\eta L_m R_p \quad (5.4)$$

Solvent evaporation across the interface of the supporting droplet is a non-uniform process.^{33,34} This, in turn, induces a lateral evaporative flow that entrains the colloidal particles to the TCL region. The initial radial velocity of the induced capillary flow present in the evaporating supporting droplet can be expressed by eq. 5.5 derived in the Hu-Larson model.¹³⁷

$$u_r = \frac{R_{depo}}{t_{evp}} \left\{ \frac{3}{8} \frac{1}{\check{r}} [(1 - \check{r}^2) - (1 - \check{r}^2)^{-\lambda(\theta)}] \left(\frac{z^2}{h^2} - 2 \frac{z}{h} \right) + \frac{\check{r} h_0 h}{R_{depo}^2} [J\lambda(\theta)(1 - \check{r}^2)^{-\lambda(\theta)-1} + 1] \left(\frac{z}{h} - \frac{3z^2}{2h^2} \right) \right\} \quad (5.5)$$

where \check{r} is a dimensional radius, $z(r)$ and $h(r)$ are the local height in the bulk and the local maximum height at the interface of the supporting droplet, respectively, $\lambda(\theta)$ is a parameter indicates the uniformity of evaporation across the surface of sessile droplets, which could be evaluated by $\lambda(\theta) = 1/2 - \theta/\pi$, and J is the evaporation flux at $\check{r}=0$,¹³⁷

$$J = \left(t_{evp} / \rho h_0 \right) \left(D_{c_v} (1 - RH) / R_{depo} \right) (0.27\theta^2 + 1.3) [0.6381 - 0.2239(\theta - \pi/4)^2]. \quad (5.6)$$

Particle depositions obtained in the dual-droplet inkjet printing is composed of particles in the bulk and particles at the interface of the supporting droplet, where both the particle motion and solvent evaporation come into play. Particle size and concentration utilized in the system have a significant impact on the particle velocity u_p , which consists of the diffusion velocity and advection velocity, driven by the evaporation-induced flow. In this study, radial velocity is considered as the advection velocity since the particle pinning involves radial movement of the particles toward the TCL. The particle velocity is expressed as, $u_p = u_{diff} + u_r$, assuming the particles follow the evaporation-induced flow perfectly.

The radial velocity in eq. 5.5 is evaluated at distance \check{r} near the TCL of the supporting droplet where $\check{r} = 1 - (L_{m,B} + L_{p,B}) / R_{depo}$ and at vertical height of $\sim 10\%$ of particle diameter lifted from the substrate surface.¹⁶ Herein, $L_{p,B}$ is defined as a finite distance between the initial pinning position of the TCL and the first layer of the outer ring deposition,¹⁶

$$L_{p,B} = R_p / \tan(\theta/2) \quad (5.7)$$

In this model, the characteristic time for the particle in the bulk of the supporting droplet to reach and form the first layers of particles at the TCL region can be evaluated by $t_{ps} = L_{m,B}/u_{p,B}$.

Likewise, the radial velocity for the particles at the interface is evaluated at

$\dot{r} = 1 - (L_{m,I} + L_{p,I}) \cos \theta / R_{depo}$, where $L_{p,I} = R_p / \sin \theta$. The schematics of particles in the TCL

region in the bulk of the supporting droplet and at the interface of the supporting droplet are shown in Figure 5.1. For simplicity, the advection velocity along the interface is taken as the radial

velocity multiplied by $1/\cos \theta$. The characteristic time for the particles at the interface to travel

toward the substrate and form the first layers of particles at the TCL can be expressed by $t_{pw} =$

$L_{m,I}/u_{p,I}$, where the mean distance between two particles in this case is approximated by eq. 5.3.

The competition among the characteristic times (i.e., t_{evp} , t_{ps} , and t_{pw}) determine the morphology of particle deposition in vicinity of the TCL, produced at the completion of solvent evaporation.

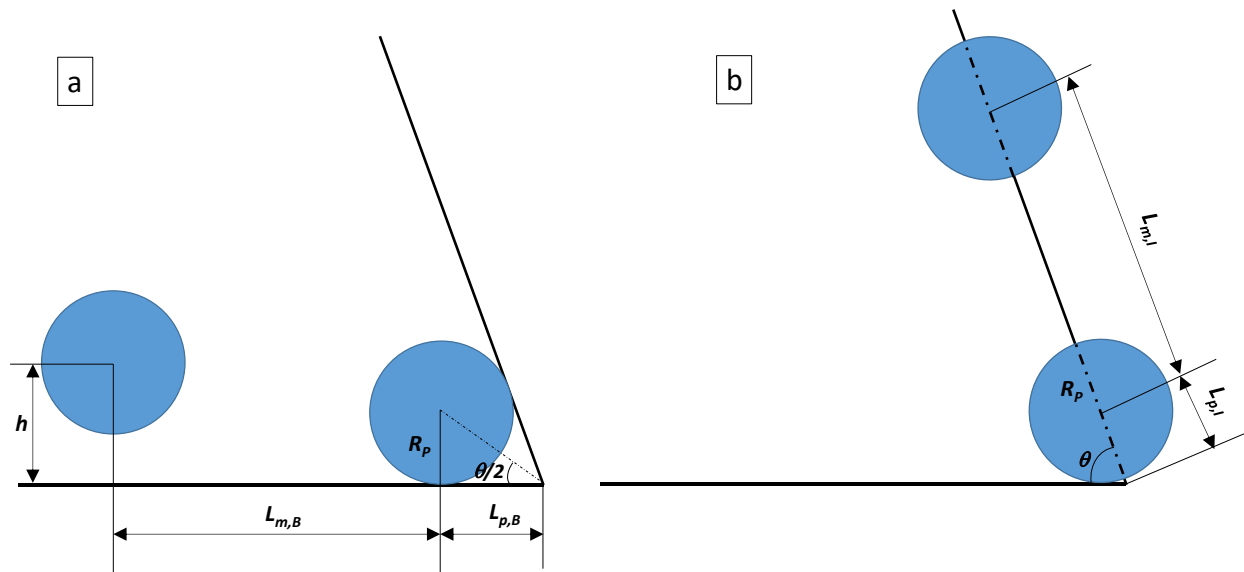


Figure 5.1: Schematics of the particles at the contact line (a) in the bulk of the supporting droplet; (b) at the interface of the supporting droplet.

5.3 Results and Discussion

5.3.1 Particle Pinning and Assembly in Conventional and Dual-Droplet Inkjet Printing

Solvent contact line pinning of evaporative sessile droplets is an intricate process, which is usually determined by the substrate wetting property through introducing surface roughness^{13,14} or chemical heterogeneities.^{63,79,138} Nevertheless, the initial pinning on substrates could be enhanced by introducing suspended particles to anchor the TCL.³³ Particle pinning at the TCL is a critical prerequisite condition for the well-known coffee-ring formation, where the colloidal particles migrate to the TCL region during solvent evaporation. In order to compare the mechanism of particle pinning at the TCL from particles spread on the interface to that of conventional direct-printing of particle-laden droplets, we first printed colloidal suspensions of carboxyl-PS particles dispersed in DI water on a PET substrate to determine at which condition the particle pinning is achieved. It is worth noting that the water receding angle on the PET substrate is $\sim 44^\circ \pm 2^\circ$, which is different from the typical requirement of pinned contact lines for the “coffee-ring” formation. This high receding angle also implies that the “wedge effect”, i.e., formation of particle depletion zones near the TCL, is insignificant for various sizes of PS particles.⁶⁴

Carboxyl-PS particle-laden droplets of ~ 110 nL were jetted on the PET substrates. Figure 5.2 shows the particle assembly with respect to different carboxyl-PS particle sizes and concentrations in sessile droplets directly printed on PET substrates. Smaller particles such as 20 nm and 100 nm tend to consistently migrate with the evaporation-induced flow, where they deposit and form the outmost layers of particle deposition at TCL. However, the contact lines obtained from printing colloidal suspensions of 20 nm PS particles with 0.2 mg/mL and 3 mg/mL particle concentrations

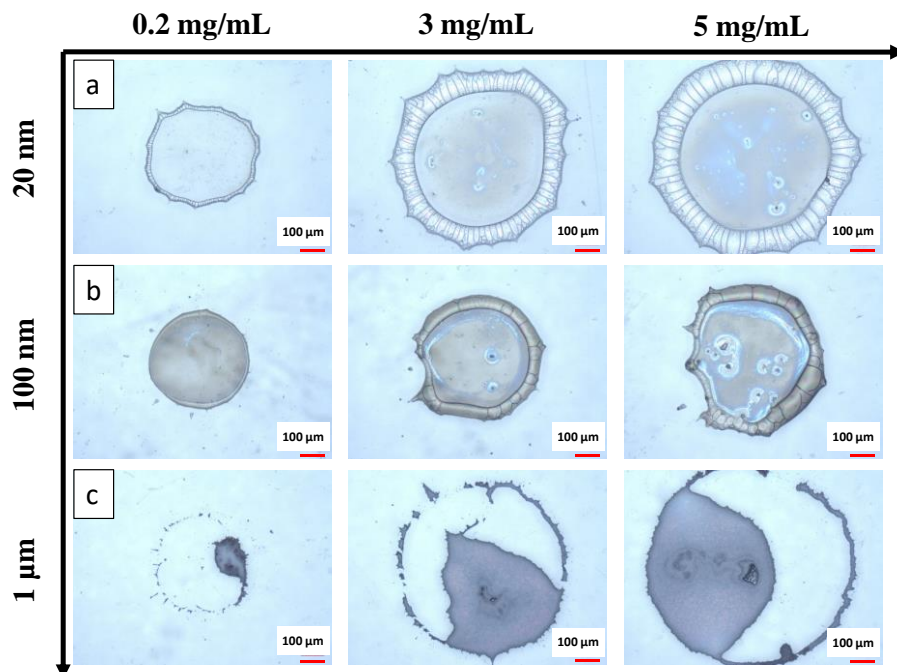


Figure 5.2: Conventional inkjet printing of particle-laden droplets on the PET substrates with different particle concentrations. (a) 20 nm carboxyl-PS particles, (b) 100 nm carboxyl-PS particles, and (c) 1 μm carboxyl-PS particles. The scale bar is 100 μm .

depin, followed by a secondary TCL pinning at a later stage of solvent drying. In conventional inkjet printing of sessile droplets, the particle pinning/depinning behaviors at the TCL are governed by forces exerted on colloidal particles in the evaporating sessile droplet such as drag force,³⁴ van der Waals force,^{36,139} electrostatic force,⁷⁵ and capillary force.⁹⁶ In early stages of solvent evaporation when the contact lines are initially pinned, the drag force initiated by the outward motion of the evaporation-induced flow is dominant. In this case, the particles are forced to migrate to the rim of the sessile droplet. However, at later stages of solvent drying, capillary forces become dominant, prompting the particles to depin along with the receding contact lines.¹⁴⁰ Capillary forces tend to sweep the particles back toward the center of the supporting droplet while van der Waals and electrostatic attraction between the particles and the substrate tend to lock the particles at the TCL region.¹⁴¹ If the particle concentration is low, as shown in Figure 5.2a and 5.2b,

the capillary force dominates the particle-substrate interactions, leading to particle depinning phenomenon of the initial TCL. However, a secondary pinning line forms, where the particles successfully pin along with the new TCL, leading to a coffee-ring formation. This occurs whenever the swept particles along with particles migrating from the bulk of the sessile droplet toward the TCL have sufficient particle-substrate interactions to cause the secondary contact line pinning. It should be mentioned that the PET substrate has some surface defects by which the motion of the receded contact lines is somewhat affected.

In contrast, the particles pin at the original TCL when printing colloidal suspension with a higher particle concentration (e.g., 5 mg/mL) using the same particle size. Under this condition, contact line receding is excluded, and the contact lines remain pinned till the solvent is completely evaporated. Increasing particle loading means more particles are carried to the TCL. This, in turn, increases the particle-substrate van der Waals and electrostatic interactions at the TCL region resulting in contact line pinning.¹⁴⁰ In addition, the evaporation-induced convective flow transports almost all the nanoparticles to the edge of the sessile droplet, producing a thick ring with several cracks. Crack development is attributed to the strong capillary stresses generated at later stages of solvent evaporation process.¹⁴² This observation of crack formation is consistent with the results reported elsewhere.⁷⁸

Similarly, jetting sessile droplets with 100 nm carboxyl-PS particles gave similar results as the 20 nm particles with regards to the particle pinning at the secondary TCL. Yet, the contact lines of the printed deposits depin even though the particle concentration is increased to 5 mg/mL. The increase in particle size decreases the crack density obtained in the formed rings. Nevertheless, all the 100 nm and 20 nm PS particles experience the coffee-ring formation in their deposits, through either initial particle pinning (20 nm with 5 mg/mL particle concentration) or secondary particle

pinning (all other cases). Further increase in particle size (e.g., 1 μm PS particles) generated different outcomes. The biggest difference is the failure of the secondary pinning at the later stages of solvent evaporation. Low particle concentration (i.e., 0.2 mg/mL) yields irregular patterns due to the low number of particles, which, in turn, results in weak particle-substrate interactions. At 3 mg/mL particle concentration, the depinning/pinning behaviors are observed, while at higher particle concentration (i.e., 5 mg/mL) the particles pinning at the initial TCL is sustained. For both cases, however, as the evaporation process proceeds, the solvent depins from the initially formed or the secondary contact lines, sweeping most of the colloidal particles toward the center of the deposit. Unlike smaller particles (i.e., 20 nm and 100 nm carboxyl-PS particles), most of the 1 μm PS particles do not get sufficient time to transport to the edge of the droplet before the TCL recedes. Instead, they are swept by the depinned receding TCL and lumped in the middle of the deposit. In other words, for very dilute colloidal suspensions of the 1 μm particles, the number of particles is insufficient to pin the solvent contact line. As a result, no coffee-ring formation occurs for the 1 μm PS particles. Figure 5.3a and 5.3b illustrate the particle assembly in conventional particle-laden droplets with a moderate receding contact angle. Very recently, we have successfully demonstrated a nearly monolayer, closely-packed deposition of colloidal nanoparticles through a dual-droplet inkjet printing process. Nanoparticle-laden wetting droplets were jetted over a supporting droplet, which was firstly deposited. Regulating surface tensions, droplet speeds, and droplet volumes resulted in effective particle spreading over the interface of the supporting droplet. The dynamics of wetting droplet impacting the supporting droplet, spreading of nanoparticles, and solvent evaporation were discussed in detail in our earlier report.¹⁰⁷ Different from the conventional direct inkjet printing process, the dual-droplet inkjet printing offers an alternative concept for particle pinning at the TCL. Figure 5.3 demonstrates the difference in contact line

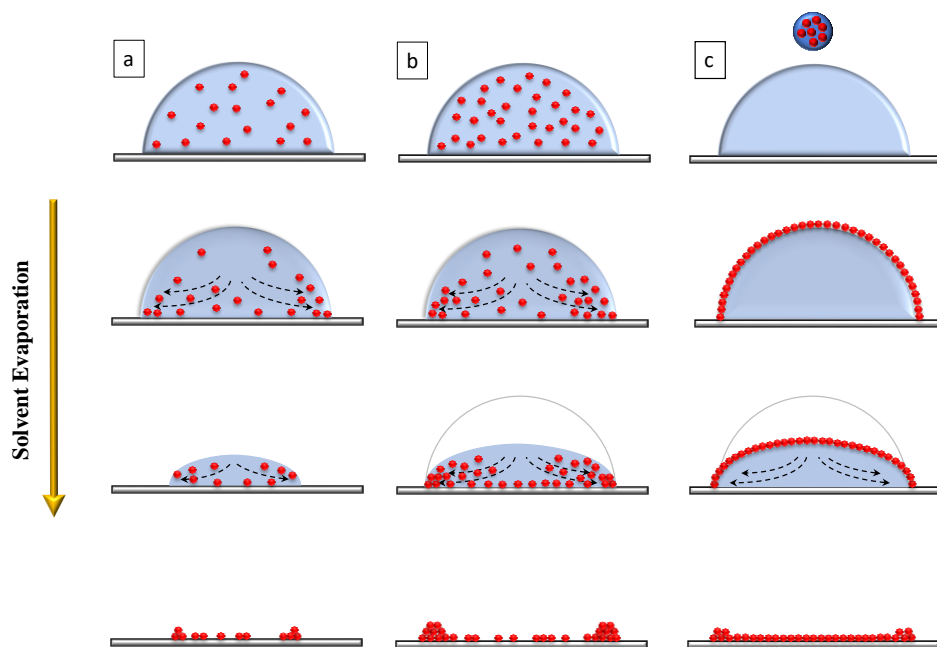


Figure 5.3: Schematics of conventional inkjet printing and dual-droplet inkjet printing of particle-laden droplets. (a) Conventional inkjet printing of sessile droplet with low particle loading that depicts the depinning/pinning behaviors of the contact line. (b) Conventional inkjet printing of particle laden-droplets with high particle loading. The particles migrate and concentrate at the contact line by virtue of the evaporation-induced flow, causing the contact line pinning. (c) Dual-droplet printing process, where the contact lines remain pinned during solvent evaporation. The middle of the deposit is composed of nearly closely-packed monolayer of nanoparticles.

pinning mechanism between the dual-droplet inkjet printing and conventional inkjet printing processes. Upon the initial impact of the wetting droplet on the interface of the supporting droplet, the sulfate-PS nanoparticles spread at the air-liquid interface under the influence of Marangoni flow, established by ethanol/water surface tension gradient. Consequently, the colloidal PS nanoparticles agglomerate and self-assemble at the interface, driven by capillary forces (i.e., particle-particle interactions), to likely form monolayer networks of nanoparticles.^{107,143} These particle networks remain arrested at the air-liquid interface of the supporting droplet in an energetically favorable state due to the interfacial deformation, caused by the fractal shape of the floating particle networks.⁸⁶ As the floating particles along the air-liquid interface reach the substrate, van der Waals and electrostatic interactions between the particles and the substrate become the driving forces for pinning the particles at the TCL region. Thus, the particle coverage

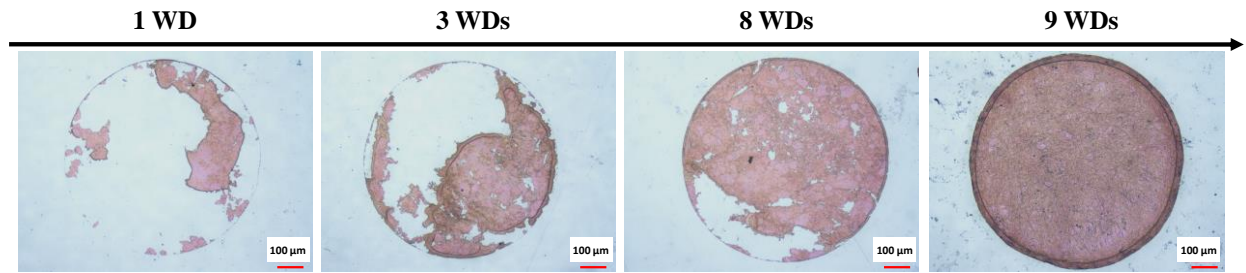


Figure 5.4: Optical images of particle depositions of the dual-droplet printing various numbers of wetting droplets (WDs): (a) one WD, (b) three WDs, (c) eight WDs, and (d) nine WDs. 300 nm sulfate-PS particles were used in the wetting droplet(s), and no particles were in the bulk of the supporting droplet. The scale bar is 100 μm .

at the air-liquid interface affects the particle pinning at the TCL, which influences the deposition structure through the interfacial self-assembly. Figure 5.4 shows the particle deposits, produced by jetting wetting droplets with the 300 nm sulfate-PS particles on supporting droplets of water. Partial pinning occurs when insufficient particles present at the interface, where the self-assembled “islands” deposit preferably to a region with perfect solvent pinning at the TCL. Nearly full coverage at the interface may cause either holey deposition of the particles and good particle pinning at the TCL, or locally depinned deposition at the TCL and closely-packed structure within the deposition. A full coverage with a slight surplus of the floating particles at the interface facilitates the particle pinning at the TCL.

As illustrated in Figure 5.3c, the particles transport toward the substrate along the air-liquid interface of the supporting droplet, causing the particle pinning at the TCL as a result of particle-substrate interactions. This particle pinning mechanism from air-liquid interface is insensitive to the receding contact angle unlike the conventional contact line pinning of sessile droplets. Such pinning process is highly dependent on particle concentration and particle size based on the premise that the particles successfully self-assemble into floating networks at the interface.

At high enough particle concentration (e.g., seven wetting droplets, with individual droplet size of ~ 550 pL, which corresponds to a particle concentration of 2.98×10^6 particle/mm²), the particle pinning at the TCL was achieved. However, this particle number density is not sufficient to cover the entire interface of the supporting droplet. For this reason, higher particle number density (i.e., nine wetting droplets that corresponds to particle concentration of 3.83×10^6 particle/mm²) is needed to pin the particles at the TCL and give a complete coverage of nanoparticles at the interface. In this case, once the sulfate-PS particles reach the TCL, the capillary force initiated by solvent evaporation and the impeding receding TCL could not fold the nearly monolayer of the particles assembled at the air-liquid interface. Thus, the TCL remains pinned during the evaporation process. On the other hand, depinning of the TCL is observed when less than seven wetting droplets were used (Figure 5.4). This could be attributed to the insufficient amount of nanoparticles reached the TCL, which, in turn, results in weak particle-substrate interactions. Based on this observation, nine wetting droplets is used in the following binary particle deposition, which corresponds to 3.83×10^6 particle/mm². It is worth pointing out that the ring formed at the TCL is a result of the evaporation-induced flow at the interface and particle-substrate interactions in the contact line region (e.g., electrostatic and van der Waal interactions). Especially during last stages of solvent evaporation, the particles at the interface may experience “rush hour” effect.¹⁴⁴ This ring formation can be mitigated or suppressed by adjusting the pH of the supporting droplet and the particle-substrate interactions.¹⁴³ In other words, the particle pinning at the contact line still occurs even without the ring structure in this dual-droplet configuration.

5.3.2 Confocal Imaging of Particle Pinning at the Contact Line

Direct imaging of particle pinning at the TCL from the particles at the interface of the supporting droplet and those in the bulk of the supporting droplet were obtained, using three-dimensional (3D)

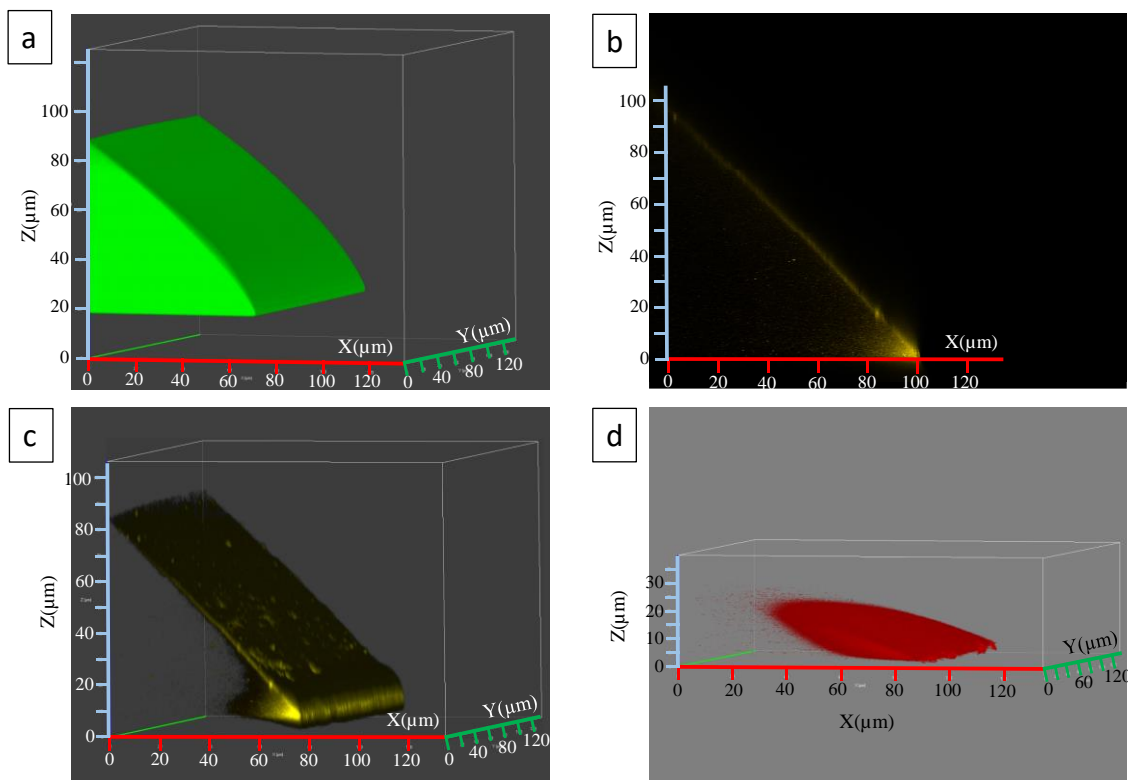


Figure 5.5: Confocal microscope images of (a) a supporting droplet of DI water on a coverslip glass slide with no particles in the bulk and at the air-liquid interface, (b) and (c) 200 nm sulfate-PS particles self-assembled at the interface of the supporting droplet and particle pinning at the contact line, (d) 20 nm carboxyl-PS particle transporting to the contact line of the supporting droplet.

confocal microscopy. Figure 5.5a presents a confocal image of a 110 μL water droplet with 0.1 mg/mL concentration of fluorescein F-1300 on a coverslip glass slide. This is meant to represent the supporting droplet and the air-liquid interface with no particles in the bulk or floating at the interface of the supporting droplet. Careful dispensing of sulfate-PS particles (5 μL) on the interface of the supporting droplet (water only) resulted in spreading of nanoparticles at the air-liquid interface. Figure 5.5b and Figure 5.5c are side view and three-dimensionally stacked images of the same supporting droplet that clearly confirm the film formation of nanoparticles at the interface of the supporting droplet. Figure 5.5d, on the other hand, shows the 20 nm carboxyl-PS nanoparticles circulating in the bulk of the supporting droplet, where the particles transport and concentrate at the TCL region empowered by the evaporation-induced flow. To avoid the crosstalk

between the fluorescent dyes of nanoparticles, imaging the 20 nm carboxyl-PS particles in the bulk and the 200 nm sulfate-PS particles on the interface of the supporting droplet were carried out separately. It should be mentioned that the images shown in Figure 5.5b and Figure 5.5c were taken right after dispensing the colloidal particles on the surface of the supporting droplet. The particles at the interface get pinned at the contact lines of the supporting droplet quickly after the wetting droplet spreading. However, for the colloidal particles in the supporting droplet only (Figure 5.5d), the 3D image was taken at ~ 30 min after dispensing the droplet, which is selected in order to demonstrate a clear particle pinning and coffee-ring formation at the TCL of the supporting droplet. The 3D image represents the average particle motion captured within ~ 15 min scanning interval elapsed between the first and last scanned slice (30 μm z-height distance). However, this is not a concern for particles assembled at the interface of supporting droplet since the particle networks are very robust at the interface till the final stages of solvent evaporation.

5.3.3 Binary Particle Deposition in Dual-Droplet Printing

In this study, we investigate the particle pinning and accumulation near the contact lines by introducing nanoparticles into both the wetting droplet and the supporting droplet through dual-droplet printing. The supporting droplet was generated by multiple bursts of inkjet droplets that was equivalent to ~110 nL of DI water with carboxyl-PS particles. Nine wetting droplets with sulfate-PS particles (single droplet volume of ~550 pL) were deposited on the supporting droplet by a secondary printhead. The modified Weber number (We') was controlled below 0.42 to ensure the spreading of the wetting droplet over the surface of the supporting one.^{105,107} Our main objective is to examine the particle arrangement in the TCL region, initiated by the self-assembled particles from the air-liquid interface and its competition against particles transported from the bulk of the supporting droplet to the TCL.

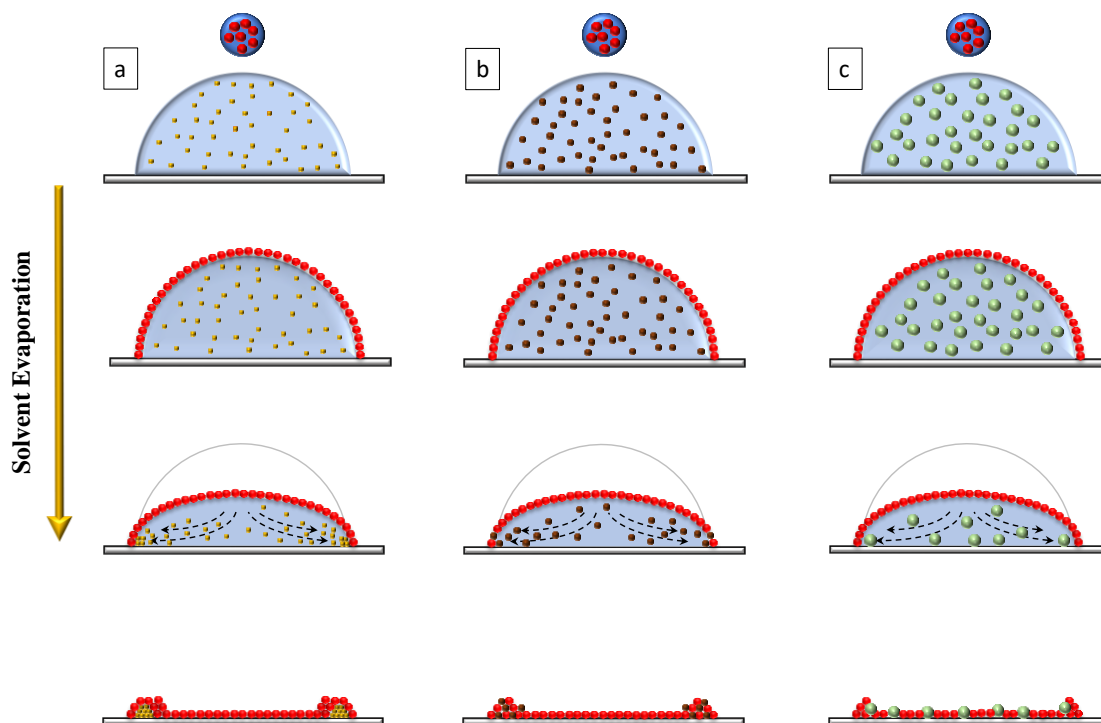


Figure 5.6: Schematic of dual-droplet inkjet printing that demonstrates the monolayer formation of nanoparticles at the interface (300 nm sulfate-PS) and different particle assembly obtained near the three-phase contact line depending on the particle size in the supporting droplet, (a) 20 nm carboxyl-PS particles forming stratified ring structure, (b) 100 nm carboxyl-PS particles resulting in blended ring structure, and (c) 1 μm carboxyl-PS particles leading to scattered particle deposition among the particle assembly from the interface.

Figure 5.6 illustrates the different particle deposition obtained in dual-droplet inkjet printing with respect to different particle sizes in the supporting droplet. Smaller particles (i.e., the 20 nm carboxyl-PS particles) in the bulk of the supporting droplet tend to exclusively transport and deposit to construct the outermost ring of the supporting droplet, while particles coming from the interface (i.e., the 300 nm sulfate-PS particles) of the supporting droplet tend to concentrate in the inner region surrounded by the 20 nm particles, forming a stratified ring deposition (Figure 5.6a).

Utilizing bigger particle size in the supporting droplet (i.e., 100 nm carboxyl-PS particles) results in a similar behavior, where the particles transport to the TCL region. However, the 100 nm carboxyl-PS particles mix with the 300 nm sulfate-PS particles at the contact line region forming a blended ring structure (Figure 5.6b). Contrary to the 20 nm and 100 nm PS particles, not all the

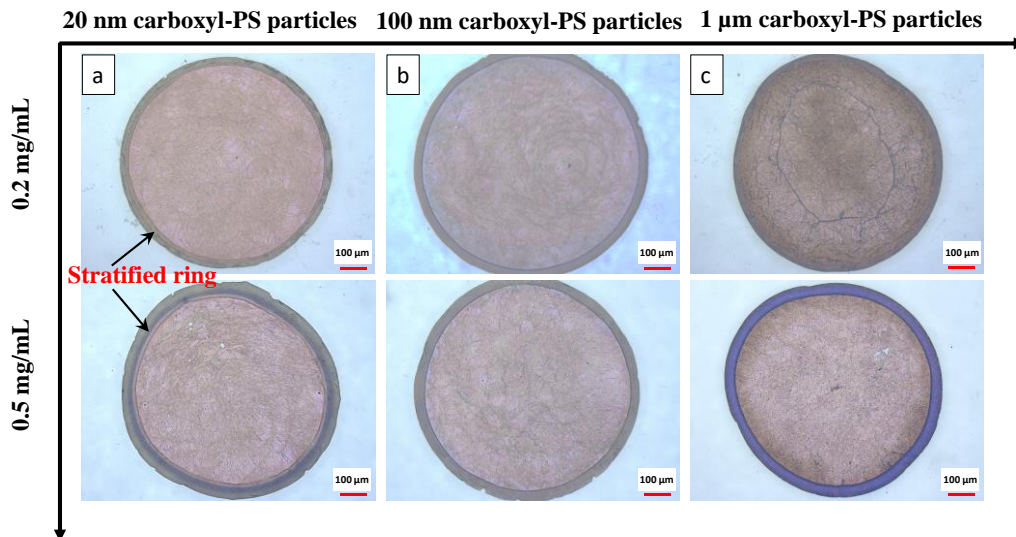


Figure 5.7: Optical images of the particle depositions generated by dual-droplet printing of nine wetting droplets with 300 nm sulfate-PS particles and different sizes and concentrations of carboxyl-PS particles in the supporting droplet. (a) 20 nm carboxyl-PS particles, (b) 100 nm carboxyl-PS particles, and (c) 1 μm carboxyl-PS particles. The scale bar is 100 μm .

bigger particles in the bulk of the supporting droplet (i.e., 1 μm carboxyl-PS particles) transport to the TCL region by the evaporation-induced flow. Instead, the 1 μm carboxyl-PS particles are scattered throughout the deposition footprint (Figure 5.6c). In this case, the ring in such deposits is mainly composed of particles coming from the interface decorated with a few 1 μm carboxyl-PS particles coming from the bulk (more information is provided in the following section).

Figure 5.7 presents optical images of particle depositions generated via dual-droplet inkjet printing process with different carboxyl-PS particle sizes and concentrations in the bulk of the supporting droplet. The red color shown in the middle of each particle deposition indicates the monolayer formation of nanoparticles obtained by jetting nine wetting droplets over the supporting droplet. Figure 5.8 and Figure 5.9 demonstrate the particle assembly obtained at the TCL region using different carboxyl-PS particle sizes and concentrations in the bulk of the supporting droplet.

The ring width is influenced by the higher concentration of carboxyl-PS particles in the supporting droplet (Figure 5.7 and Figure 5.9). Specifically, the ring becomes wider for the 20 nm particles,

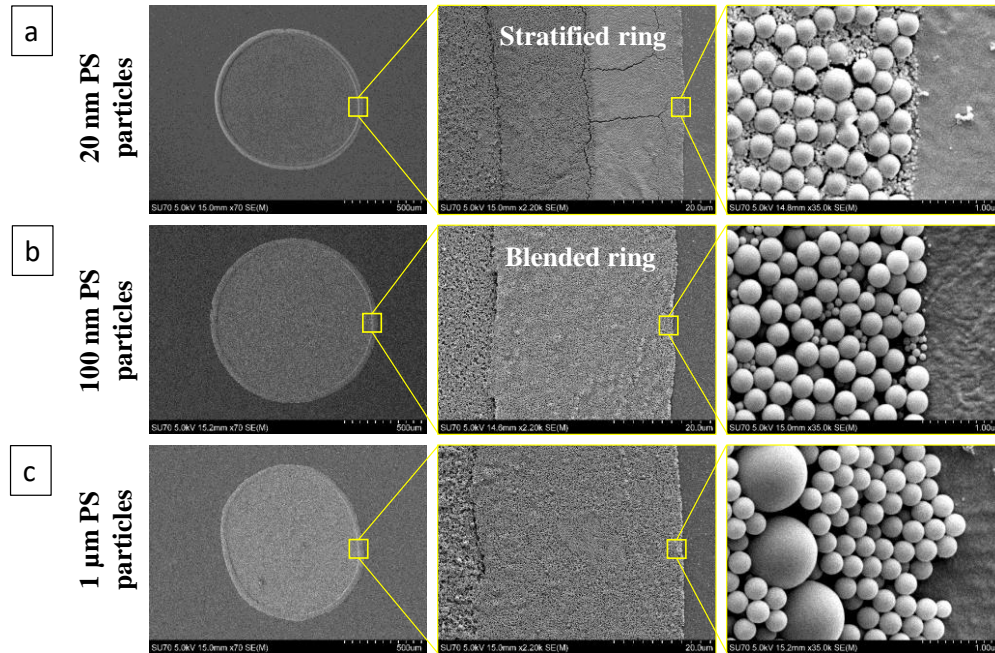


Figure 5.8: SEM images of the particle deposits shown in Figure 5.7, demonstrating the versatile particle assembly obtained in vicinity of the contact line region. (a) Stratified ring (20 nm carboxyl-PS particles), (b) blended ring (100 nm carboxyl-PS particles), and (c) ring of 300 nm sulfate-PS particles decorated with a few 1 μm carboxyl-PS particles. Carboxyl-PS nanoparticles of 0.2 mg/mL were used in the supporting droplet.

which is attributed to the increased number of particles in the TCL region. The 1 μm particles are covered by monolayer assembly of particles from the interface during solvent evaporation, which likely “fall off” those 1 μm particles due to capillary forces, generated by their neighboring particles. This pushes more 300 nm sulfate-PS particles to the TCL region, especially for high concentration of carboxyl-PS particles.

5.3.4 Discussion

In order to get a better understanding of binary particles arrangement in the TCL region produced by dual-droplet inkjet printing, the Hu-Larson model was implemented in this study. Particle velocity, a combination of advection and diffusion velocities, is calculated near the TCL of the supporting droplet at the specified \check{r} and vertical locations. Figure 5.10 shows the advection and diffusion velocities, calculated by eq. 5.4 and eq. 5.5 respectively, for the particles in the bulk and

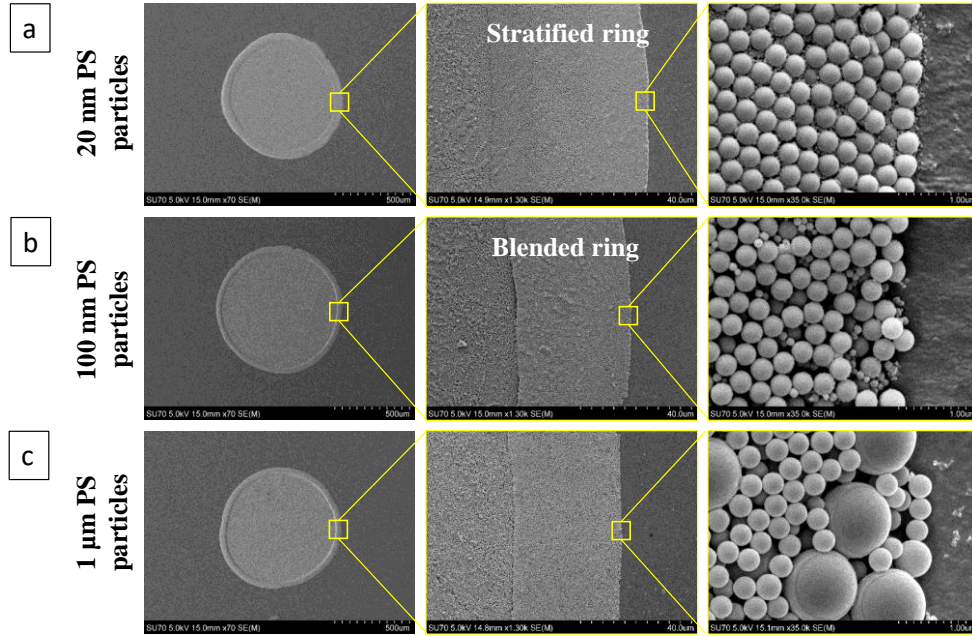


Figure 5.9: SEM images of the binary particle depositions shown in Figure 5.7, demonstrating the versatile particle configuration obtained in vicinity of the contact line region. (a) Stratified ring (20 nm carboxyl-PS particles/300 nm sulfate-PS particles), (b) blended ring (100 nm carboxyl-PS particles/300 nm sulfate-PS particles), and (c) ring of 300 nm sulfate-PS particles decorated with a few 1 μm carboxyl-PS particles. Particle concentration in the supporting droplet was 0.5 mg/mL.

at the interface of the supporting droplet approximated at the initial contact angle. The advection velocities calculated at various vertical locations are provided elsewhere.¹⁴⁵ On the other hand, the advection velocity of particles spread on the interface of the supporting droplet (i.e., sulfate-PS particles) was evaluated at the air-liquid interface only.

The experimental findings suggest that smaller particles transport at a faster pace to the TCL. This observation is verified by the calculated advection and diffusion particle velocities as shown in Figure 5.10. For smaller particles (i.e., 20 nm and 100 nm particles), diffusion velocity dominates over the advection velocity. As the particle concentration further increases, both the diffusion and the advection velocities increase. According to eq. 5.4, the increase in diffusion velocity is attributed to the incremental decrease in the mean distance between two colloidal particles with respect to higher particle concentration. The advection velocity is comparable for the various

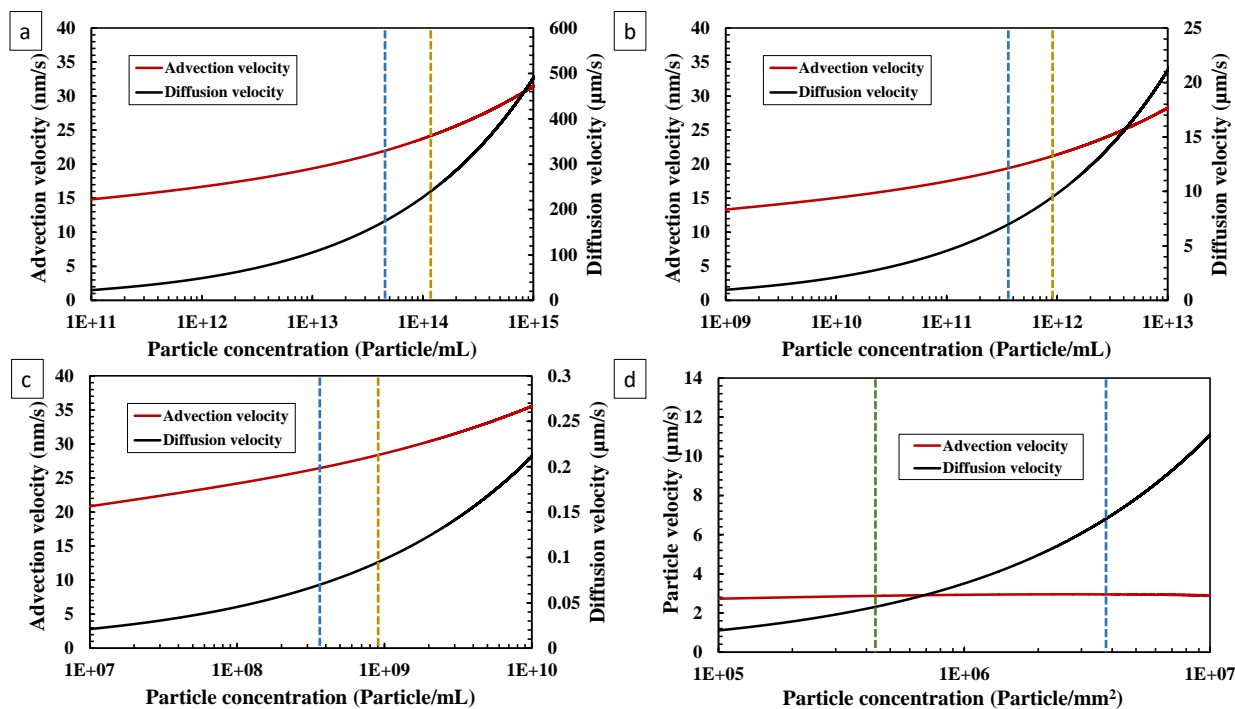


Figure 5.10: (a)-(c) Calculated advection and diffusion velocities of the 20 nm, 100 nm, and 1 μm carboxyl-PS particles in the bulk of the supporting droplet, respectively. The dashed lines represent 0.2 mg/mL and 0.5 mg/mL particle concentrations used in the experimental study. (d) Calculated advection and diffusion velocities of the 300 nm sulfate-PS particles at the interface of the supporting droplet. The dashed lines represent the range of particle concentrations obtained from jetting one to nine wetting droplets.

particle sizes used in this work. The calculated advection velocity is the velocity of the evaporation-induced flow. For different particle sizes, the evaporation-induced flow is the same, but the advection velocities are calculated at different locations. On the other hands, the diffusion velocity decreases up to three orders of magnitude for larger particles, e.g., from a few hundred micron per second for 20 nm particles to a fraction of a micron per second for 1 μm particles. By comparing the advection and diffusion velocities of colloidal particles, it is evident that the 20 nm carboxyl-PS particles have the highest particle velocity among their counterparts, which renders the particle pinning outside the 300 nm particle assembly.

In order to generalize the findings and construct the phase diagram of particle deposition especially in the TCL region, we further calculated the characteristic time for particle pinning from the bulk

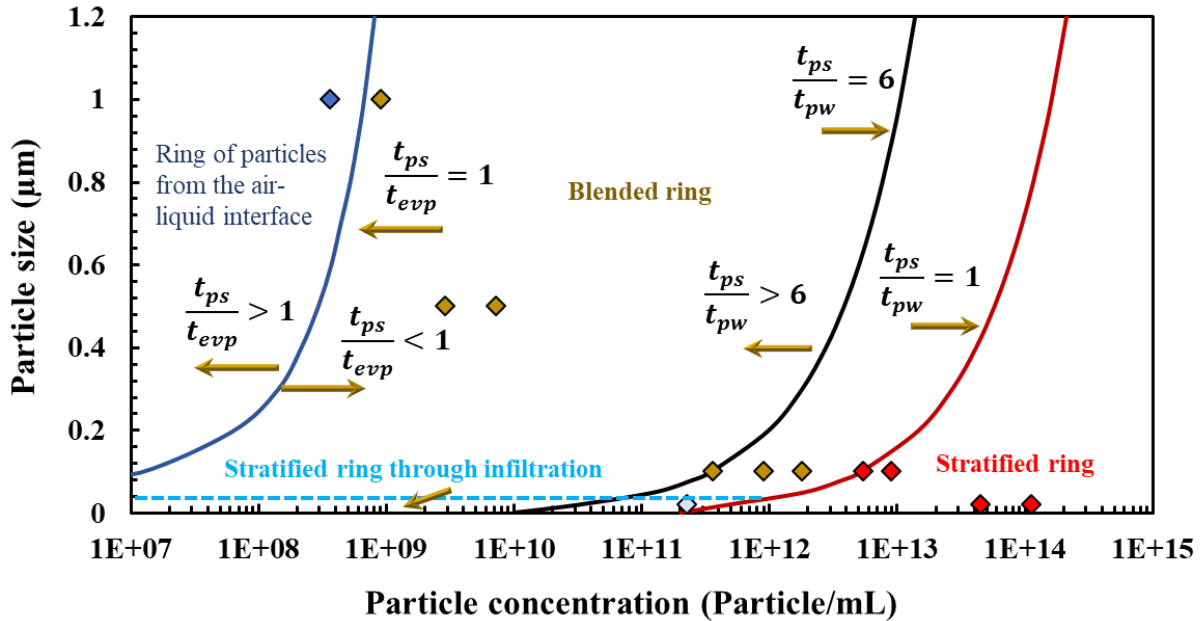


Figure 5.11: Phase diagram of the deposition morphology showing its dependence on the particle size and concentration in the supporting droplet. Diamond dots indicate the experimental data. Different dot colors correspond to different ring structures.

of the supporting droplet (t_{ps}), characteristic time for the particles at the interface to reach the contact line (t_{pw}), and total time for solvent evaporation (t_{evp}) for various particle sizes and particle concentrations. Figure 5.11 manifests the competition among the solvent evaporation, particle pinning from the bulk, and particle pinning from the interface of the supporting droplet. Specifically, characteristic time ratio t_{ps}/t_{evp} , determines if the particles from the bulk of the supporting droplet can reach the TCL before solvent evaporation completes. However, the characteristic time ratio t_{ps}/t_{pw} evaluates the competition between particle pinning from the bulk and at the interface of the supporting droplet. When the characteristic time ratio $t_{ps}/t_{evp} > 1$, this implies that solvent evaporation is relatively faster than the time required for the particles to reach the TCL, resulting in suppression of the ring formation of colloidal particles at the edge of the supporting droplet. Yet, $t_{ps}/t_{evp} \ll 1$ indicates that the colloidal particles reach the TCL before the completion of the solvent evaporation, facilitating the ring formation of particles from the bulk

of the supporting droplet. In addition, for $t_{ps}/t_{pw} < 1$, the colloidal particles in the supporting droplet reach and deposit near the TCL faster than those at the interface of the supporting droplet, forming stratified ring structure. On the other hand, $t_{ps}/t_{pw} \gg 1$ describes the fast arrival and pinning of the interface floating particles to the TCL than those dispersed in the bulk of the supporting droplet, producing either the mixed ring structure or a ring that is mainly composed of particles from the interface with scattered particles from the bulk of the supporting droplet. It is worth pointing out that t_{pw}/t_{evp} is much smaller than one (3.32×10^{-4}) in the current dual-droplet configuration, indicating that the particles at the interface reach and pin at the TCL much faster than the solvent evaporation.

In case of using the 20 nm carboxyl-PS particles in the bulk and 300 nm sulfate-PS particles at the air-liquid interface, the characteristic time ratios $t_{ps}/t_{evp} \ll 1$ and $t_{ps}/t_{pw} \ll 1$ are obtained for the 0.2 mg/mL and 0.5 mg/mL particle concentration. This indicates that the 20 nm PS particles reach and deposit near the contact lines faster than the 300 nm PS particles, producing particle deposition with stratified ring structure. All the 20 nm PS particles have been observed to migrate to the TCL region, leaving a monolayer of the 300 nm PS particles in the middle of the deposit (Figure 5.8a and 5.9a). This is different from the shrunk ring structure shown in Figure 5.2a under the same particle concentration. One possible explanation is that some 300 nm PS particles pin at the contact lines, effectively anchor the solvent contact line and prevent sweeping the 20 nm particles back to the center, which facilitated the pinning of the 20 nm particles (Figure 5.12). During the last stage of solvent evaporation, some 300 nm PS particles get accumulated at the contact lines and delaminated from the first ring of the 20 nm PS particles, forming the stratified ring structures. It is worth pointing out that when the 300 nm particles pin at the TCL, the 20 nm

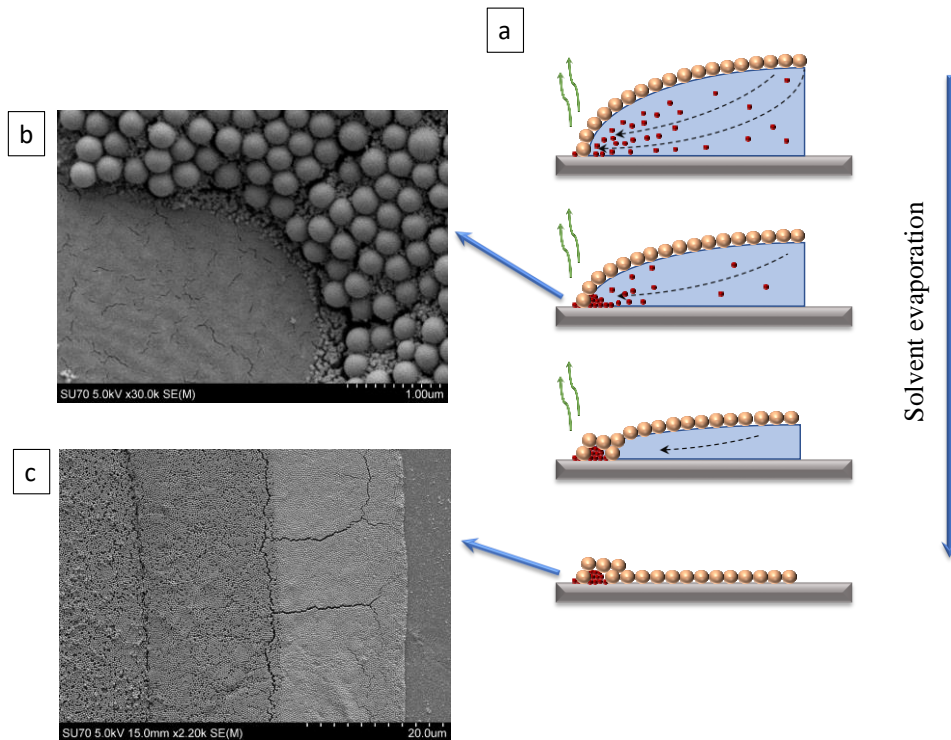


Figure 5.12: (a) Further illustration of the formation of stratified ring structure; (b) SEM image showing that the 20 nm PS particles can pass the 300 nm PS particles and deposit closer to the leading edge of the supporting droplet. The local concave shape of the particle pinning line has kept the 20 nm particles from completely going under the 300 nm PS particles. (c) SEM image of the stratified ring structure.

particles might still infiltrate through the 300 nm particles through the interstices, forming a stratified ring structure. Figure 5.13 shows the stratified ring structure obtained when 20 nm particles with solid concentration of 0.001 mg/mL are used in the supporting droplet. Therefore, a dashed line is added to the diagram as an infiltration threshold (46.4 nm), which corresponds to the maximum particle size fitting into the interstices of closely-packed 300 nm particles. Underneath the dashed line, particle infiltration may occur leading to stratified ring structures. When $t_{ps}/t_{pw} \ll 1$, for small particles, the stratified ring formation could be attributed to both the fast particle pinning and the particle infiltration.

Changing the particle size in the bulk of the supporting droplet to 100 nm along with the 300 nm sulfate-PS particles at the interface have led to a different scenario. In this case, for particle

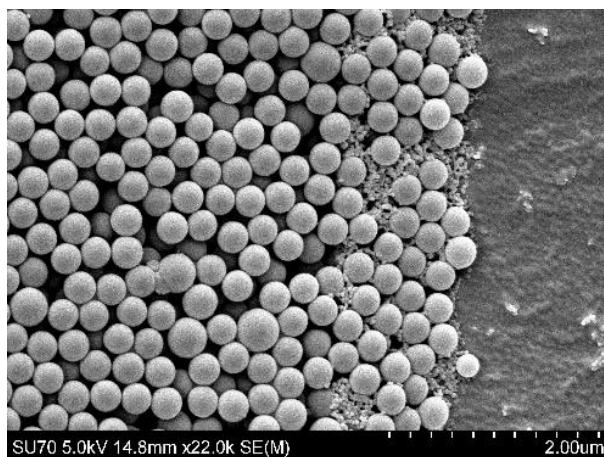


Figure 5.13: Stratified ring structure formed by 20 nm carboxyl-PS particles (0.001 mg/mL) in the supporting droplet and 300 nm sulfate-PS particles in the wetting droplets. The 20 nm particles could migrate to the contact line via infiltration through the interstices of the 300 nm particles.

concentration of 0.2 mg/mL and 0.5 mg/mL, the characteristic time ratios become $t_{ps}/t_{evp} \ll 1$ and $t_{ps}/t_{pw} \sim 3-6$, which corresponds to the blended ring structure. Figure 5.8b and Figure 5.9b show the particle deposition of 100 nm carboxyl-PS particles in the bulk and 300 nm sulfate-PS particles at the interface of the supporting droplet, respectively. In a similar fashion, the majority of the 100 nm PS particles are transported to the TCL region; however, the ring produced is a blend of particles from the bulk and particles at the air-liquid interface. In order to validate the analytical model, higher concentrations of 100 nm particles, i.e., 1, 3 and 5 mg/mL were tested as shown in Figure 5.11. The stratified ring structure in the cases of 3 mg/mL and 5 mg/mL become more obvious, while the deposition of 1 mg/mL shows the transition from blended ring structure to stratified ring structure. The results are presented elsewhere.¹⁴⁵

The characteristic time ratios become $t_{ps}/t_{evp} \approx 1$ and $t_{ps}/t_{pw} \gg 1$ when the 1 μm PS particles (0.2 mg/mL) were utilized in the bulk of the supporting droplet. Accordingly, the particles could not reach and pin at the TCL of the supporting droplet as the solvent being evaporated. Instead, the 1 μm PS particles are scattered throughout the deposit and no particle accumulation form at the

TCL, which is consistent with the experimental results (Figure 5.8c). The contact line pinning in this case occurs only by the contribution of particles from the air-liquid interface. In addition, 500 nm carboxyl-PS particles with solid concentrations of 0.2 mg/mL and 0.5 mg/mL were used to generate the blended ring structures, which agrees with the model prediction.¹⁴⁵

It is worth noting that the boundaries between the stratified ring, blended ring, and the ring of particles formed from the air-liquid interface are not absolutely sharp. We have noticed that the majority of the 100 nm PS particles deposit in the TCL region forming the blended rings with the 300 nm PS particles, however, there is a trace amount of particles deposited onto the middle of the self-assembled 300 nm PS film.¹⁴⁵ Nevertheless, this phase diagram provides valuable information in understanding the effect of particle pinning on the assembly structures of binary particles in evaporative droplets.

5.4 Conclusion

In this study, two mechanisms of particle pinning at the contact lines, i.e., pinning from the bulk of a sessile droplet and pinning from the interface of a sessile droplet, have been investigated through the dual-droplet inkjet printing. The competition of these two mechanisms has been systematically studied by introducing PS particles to the wetting droplet and the supporting droplet. Depending on the particle size and concentration of the particles dispersed in the bulk of the supporting droplet, versatile particle arrangement near the TCL such as stratified rings, blended rings, and rings with particles mainly from the air-liquid interface, have been obtained. An analytical analysis was conducted using the Hu-Larson model to understand the binary particle arrangement near the TCL of the supporting droplet. It qualitatively agrees well with the experimental results. For small nanoparticles such as 20 nm carboxyl-PS particles in the bulk and

300 nm sulfate-PS particles at the air-liquid interface, the calculated characteristic time ratios are $t_{ps}/t_{evp} \ll 1$ and $t_{ps}/t_{pw} \ll 1$, which suggest the stratified ring formation due to the fast movement of the carboxyl-PS particles toward the TCL as compared to the particles at the air-liquid interface, while particle infiltration through the interstitial space of the 300 nm particles may also contribute to the stratified ring formation. Changing the particle size in the bulk of the supporting droplet to 100 nm with moderate concentrations results in blended rings due to the comparable particle size and particle velocities in the system. On the other hand, the characteristic time ratios become $t_{ps}/t_{evp} \approx 1$ and $t_{ps}/t_{pw} \gg 1$ when the 1 μm PS particles are utilized in the bulk of the supporting droplet. For such big colloidal particles, the evaporation-induced flow and particle diffusion are insufficient to drive the particles to the rim of the supporting droplet. As a result, the 1 μm PS particles are scattered throughout the deposit, and the contact lines are pinned by the particles mainly from the air-liquid interface. Understanding the transport mechanism of colloidal particles and controlling the deposition assembly from the bulk and at the interface of sessile droplets could potentially lead to a new strategy for producing functional coatings and devices.

CHAPTER 6 Inkjet Printing of Magnetic Particles Toward Anisotropic Magnetic Properties

6.1 Introduction

One-dimensional (1D) chain structures have attracted tremendous attention during the past decades owing to their unique shape anisotropies and magnetic characteristics.¹⁴⁶ The major benefit of 1D particle assemblies is the ability to tailor magnetic, mechanical, electrical, and optical properties.¹⁴⁷ Such particle assemblies are of tremendous interest in many technological applications such as high density data storage systems,¹⁴⁸ magnetic sensors,¹⁴⁹ and magnetic refrigerators,¹⁵⁰ to name a few.

The chaining effect of nanoparticles, or the so-called magnetosomes, is a result of intrinsic magnetic anisotropy, where the particles orient and assemble with their easy magnetization axes (magnetization vectors) parallel to the magnetic field vector to minimize the magnetostatic energy of individual nanoparticles.¹⁵¹ This chaining phenomenon combines the magnetic moments present in every magnetic particle in a particular direction, which is considered a promising venue for fabricating functional devices.^{152,153}

One candidate that has a great potential in designing and fabricating magnetic devices is inkjet printing. Unlike thin-film deposition and photolithography techniques, inkjet printing is a versatile, cost-effective tool by which the alignment and chaining of magnetic particles could be well-controlled.¹⁵⁴ However, the well-known coffee-ring effect (CRE) is considered a detriment in inkjet printing applications, and it should be addressed before broad adoption of this approach.^{1,68,100} The CRE phenomenon has been the subject of intensive investigation and scrutiny to unveil the underlying mechanisms.^{54,56} Under certain conditions, when a particle-laden droplet

is left to dry on a nonporous substrate, the colloidal particles transport to the three-phase contact line (TCL) resulting in a ring-like particle deposition.^{9,77} To date, most of the research dedicated to mitigate or suppress the CRE was focused on conventional means, such as controlling the solvent drying conditions,^{11,15,35} modifying particle shapes,^{36,37} tuning solvent properties,⁶⁰ adjusting substrate wettability,^{12,38} and reversing the lateral-convective flow through introducing Marangoni flow.⁴⁰⁻⁴³ However, the effects of porous substrates and external magnetic field on the CRE when particles are magnetic require further investigations.

The main objective of this study is to elucidate the effect of external magnetic field on the magnetic particle assembly during inkjet printing to obtain anisotropic magnetic patterns through particle chaining with suppressed CRE formation. Ferromagnetic Gd_5Si_4 magnetic particles were formulated in terpineol oil and printed onto a porous substrate to form patterned films. A porous substrate (photopaper) is used in this study to quickly remove the solvent through imbibition, which suppresses the CRE to a certain degree. When no magnetic field is applied, patterns ranging from uniform deposits to clear coffee-rings have been produced depending on the droplet size and particle loading. With the magnetic field, however, the CRE can be suppressed or significantly reduced through assembling the magnetic particles into chains, producing anisotropic magnetic patterns. Three characteristic time scales, namely the critical time for solvent imbibition into the substrate (t_{im}), the time for particles to chain in the direction of the magnetic field (t_{ch}), and the time for the particles to reach the substrate in the vertical direction (t_{pz}) under the magnetophoretic force, are considered in this work. These characteristic times demonstrate the competition between particle chaining and deposition versus solvent imbibition in the presence of magnetic field, which are directly related to the morphology of the particle deposition. Such ability in controlling the

magnetic particle deposition and assembly through inkjet printing provides a great potential for many engineering and technological applications.

6.2 Methods

6.2.1 Inkjet Printing of Magnetic Particles

In this study, a photopaper (Kodak, 8.5×11" Gloss) was cut into 20 mm × 20 mm and used as a porous substrate for the inkjet printing process. Gd₅Si₄ magnetic particles were prepared by ball milling at the Ames laboratory.^{155,156} The particles were dispersed in terpineol oil (Alpha-Terpineol, 96% purity, Alfa Aesar) to obtain particle concentrations of 10 mg/mL and 25 mg/mL. In order to enhance the adhesion of the Gd₅Si₄ particles with the substrate, 0.15 wt% ethyl cellulose (18-22 mPa·s, 5% in Toluene + Ethanol (80:20) at 25°C, TCI America) was added to the dispersion to form the magnetic ink formulation. Then, the magnetic ink was ultrasonicated for 10 min before printing.

The magnetic suspension with different particle concentrations were jetted on the photopaper substrate via an inkjet printer (Jetlab 4, MicroFab). A piezoelectric nozzle with an orifice size of 80 μm (MJ-ATP-01-80-8MX, MicroFab) was employed in this study, driven by a waveform generator (Jetdriver III, MicroFab). The nozzle was heated to 50 °C to facilitate the jetting process of terpineol oil. The size of the jetted droplets on the photopaper was controlled by the number of bursts, where the volume of individual jetted droplet was ~500 pL generated at 200 Hz jetting frequency. The alignment of the magnetic particles was achieved by placing a neodymium permanent magnet (BC14-N52, K&J Magnetics) underneath the substrate to force the nanoparticles to align along the direction of the externally applied magnetic field. Samples with random particle orientations were printed without the permanent magnet.

6.2.2 Morphology Characterization

An ultra-high-resolution scanning electron microscope (HITACHI SU-70 FE-SEM) with 5 kV and 15 mm scanning distance was used for morphology characterization of the printed patterns. To minimize charging effect of the printed magnetic particles, the samples were coated with platinum using a platinum sputter (Denton Vacuum Desk V) for 120 s.

6.2.3 Magnetic Characterization

The magnetic properties of the printed patterns were characterized via Physical Property Measurement System (PPMS) from Quantum Design. The size of the printed films was adjusted to 4 mm × 4 mm, printed with the ink of 25 mg/mL particle concentration. To obtain the magnetic moment versus magnetic field curves, the magnetization cycle of the PPMS was set from −30,000 Oe to +30,000 Oe with a step rate of 10 Oe/s. Each sample was measured in both the parallel and the normal direction of the magnetic field at 300 K.

6.2.4 Numerical Simulation of Magnetic Field and Particle Motion

Two simulation domains were constructed in COMSOL Multiphysics to estimate the characteristic times (t_{ch}) and (t_{pz}). The first simulation domain couples the magnetic field and particle tracking with the fluid flow together to simulate the characteristic time (t_{pz}) needed for the particles to migrate toward and reach the substrate from a distance L_m away the substrate surface. With the assumption that the colloidal magnetic particles are homogeneously dispersed in the bulk of the sessile droplet, the distance L_m is taken as the mean distance between two colloidal magnetic particles, as estimated by eq. 6.1,¹⁶

$$L_m = (V_0/N)^{1/3} \quad (6.1)$$

where V_0 is the initial volume of the sessile droplet and N is the total number of particles in the bulk of the droplet. In COMSOL, the magnetic field strength H is calculated by solving the Gauss' law equation for magnetism,

$$-\nabla(\mu_0 \nabla V_m - \mu_0 M) = 0 \quad (6.2)$$

where $H = -\nabla V_m$; M is magnetization; μ_0 is the vacuum permeability; and V_m is scalar magnetic potential. The particle motion is governed by Lagrangian equation (eq. 6.3) that involves various forces such as drag force F_D , magnetophoretic force F_{MG} , Brownian force F_b , gravitational force F_g , and buoyancy force F_{bo} ,

$$m \frac{d^2 s}{dt^2} = F_{MG} + F_D + F_b + F_g + F_{bo} \quad (6.3)$$

where m , s , and t are the mass of the particle, the spatial coordinate of the particle, and time, respectively. The magnetophoretic force (F_{MG}) is defined as:

$$F_{MG} = 2\pi r_p^3 \mu_0 \mu_{r,f} K \nabla H^2 \quad (6.4)$$

where r_p is the radius of the particle; and K is defined as:

$$K = \frac{\mu_{r,p} - \mu_{r,f}}{\mu_{r,p} + 2\mu_{r,f}} \quad (6.5)$$

where $\mu_{r,p}$ is the relative permeability of the ferromagnetic particles and $\mu_{r,f}$ is the relative permeability of the fluid. In COMSOL the drag force (F_D) is expressed by eq. 6.6,

$$F_D = \left(\frac{1}{\tau_p} \right) m_p (u - v) \quad (6.6)$$

where τ_p is the particle response time; m_p is the particle mass; u is the fluid velocity; and v is the velocity of the particle. The particle velocity response time for spherical particles in stokes flow is given by eq. 6.7,

$$\tau_p = \frac{\rho_p d_p^2}{18\mu} \quad (6.7)$$

where ρ_p is the density of the particle, d_p is the particle diameter, and μ is the fluid viscosity. In this model, we assume the average particle size is 5 μm , and 30 nL droplet size as the simulation domain in which the particles are released. A particle size larger than 1 μm usually does not show large Brownian motion, particularly in a highly viscous fluid such as terpineol oil. Furthermore, the gravitational and buoyancy forces have been included in our initial simulations, and we verified that they do not make noticeable contributions to the results. Therefore, only the magnetophoretic force and the drag force are considered in this study.

On the other hand, estimating the characteristic time for the magnetic particles to chain (t_{ch}) required only the particle tracking in the droplet. The terpineol oil is considered as the fluid in the domain. Two particles were released in the domain and treated as magnetic dipoles in a uniform magnetic field. The two particles can be treated as two magnetic dipoles, whose magnetic moments orient in the same direction as the external magnetic field. The induced magnetic dipoles in the applied magnetic field was calculated according to the specifications of the magnet used in our experiments. Figure 6.1 is the two-dimensional (2D) spatial representation of a magnetic dipole pair. The magnetic forces between the two dipoles are derived in both x- and y- directions as expressed in eq. 6.8 and eq. 6.9,¹⁵⁷

$$F_x = \frac{3\mu_0 m_1 m_2 [1 - 5\cos^2(\alpha)] \sin(\alpha)}{4\pi r^4} \quad (6.8)$$

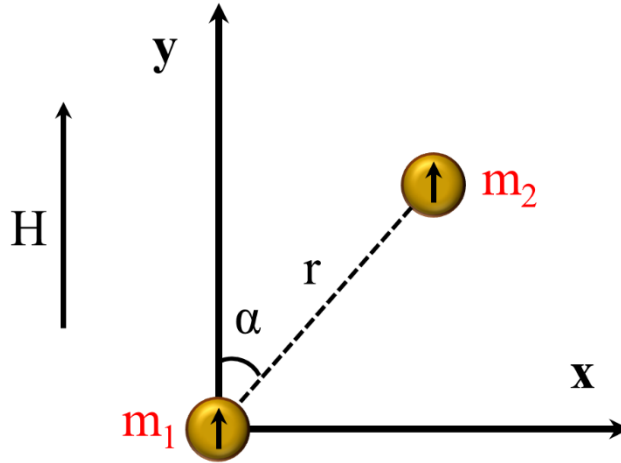


Figure 6.1: Spatial representation of two magnetic dipoles in a uniform magnetic field.

$$F_y = \frac{3\mu_0 m_1 m_2 [3 - 5\cos^2(\alpha)] \cos(\alpha)}{4\pi r^4} \quad (6.9)$$

where m_1 and m_2 are the two magnetic dipole moments, $m_1 = m_2 = 4\pi K r_p^3 H$; α is the orientation angle of the dipoles with respect to the magnetic field; r is the dipole-dipole distance. The estimated characteristic times (t_{ch}) and (t_{pz}) were compared with the experimentally determined critical time for solvent imbibition (t_{im}) to identify the conditions for chain formation and CRE suppression.

6.3 Results and Discussion

Particle-laden droplets were jetted on a photopaper substrate, where the solvent removal through infiltration and evaporation occur simultaneously. However, for terpineol oil, the infiltration occurs at a much faster rate than the solvent evaporation. In this study, the size of the printed droplets was controlled by jetting multiple bursts of colloidal droplets, where the solvent contact lines of terpineol oil remain pinned during the solvent imbibition as shown in Figure 6.2. It should

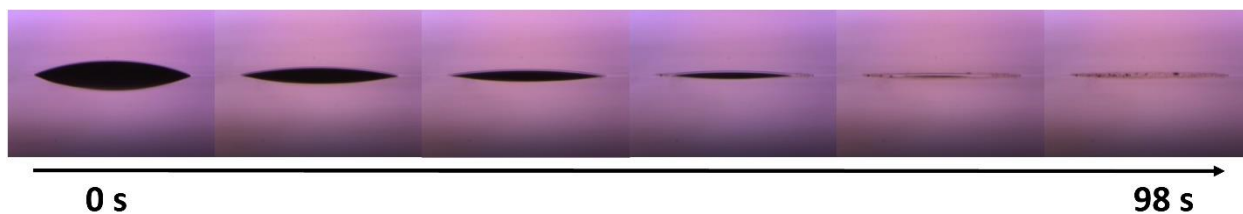


Figure 6.2: Illustration of the solvent imbibition process and the contact line pinning. The droplet size is 30 nL. Particle concentration is 25 mg/mL.

be mentioned that solvent contact line pinning on solid substrates is usually determined by the substrate wetting property, which is mainly dependent on surface roughness^{13,14} and chemical homogeneity.^{63,79,138} The initial pinning of solvents on substrates could be further enhanced by introducing suspended particles to anchor the contact line.^{33,145} The contact line pinning of terpineol oil with ferromagnetic particles on the porous substrate could be attributed to fast solvent imbibition, surface roughness of the photopaper, and low surface tension and high viscosity of terpineol oil. Generally, the non-uniform evaporation flux across the curved interface of sessile droplets initiates a radial evaporation-induced flow that drives the particles to the TCL. This is usually combined with particle diffusion in the bulk of the deposited droplets. Yet, the low vapor pressure and high viscosity of terpineol oil results in extremely low particle radial and diffusion velocities (Figure 6.3). Therefore, it is reasonable to neglect the evaporation of terpineol oil and the associated radial particle transport and particle diffusion in the following discussion.

Without applied magnetic field, different particle deposition patterns were observed depending on particle concentration and droplet volume. Different from the conventional CRE, where colloidal particles transport to the edge of sessile droplets by virtue of the evaporation-induced capillary flow, in this study, solvent imbibition is the main driving mechanism that dictates the particle deposition pattern, particularly, when no magnetic field is applied. Small droplets (e.g., < 30 nL) can be fully imbibed into the porous substrate, where the colloidal nanoparticles are immobilized

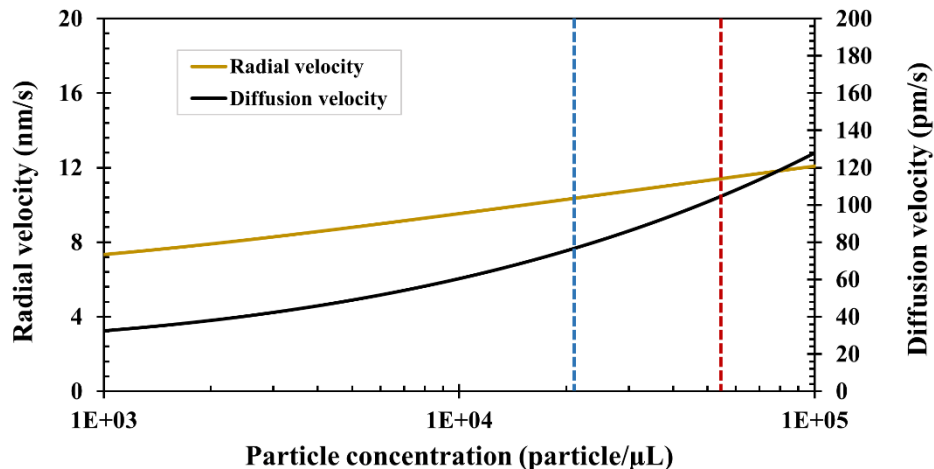


Figure 6.3: Evaporation-induced radial and diffusion velocities of the magnetic particles in terpineol oil. The mean particle size is 5 μm . The blue and red dash lines represent the particle concentrations of 10 mg/mL and 25 mg/mL, respectively. Please refer to chapter five for the calculation of radial and diffusion velocities in an evaporating sessile droplet.

and deposited onto the substrate due to the fast solvent removal. However, the solvent is partially imbibed into the porous substrate for bigger droplets, followed by a much slower lateral imbibition (secondary stage) into the surrounding regions near the droplet deposition. In this case, the colloidal particles are most likely driven to the TCL during the secondary imbibition process, producing deposits affected by the CRE. The images in the top row of Figure 6.4 present the

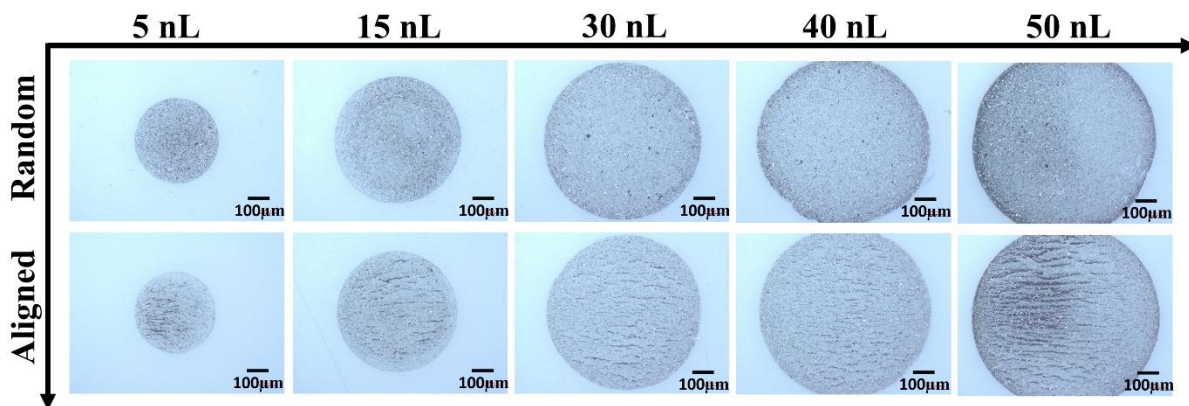


Figure 6.4: Optical images of particle depositions of different droplet volumes, printed with 25 mg/mL ink concentration. “Random” refers to samples printed without applying external magnetic field and “Aligned” refers to samples with one-dimensional chains of particles when the magnetic field is applied during the printing process.

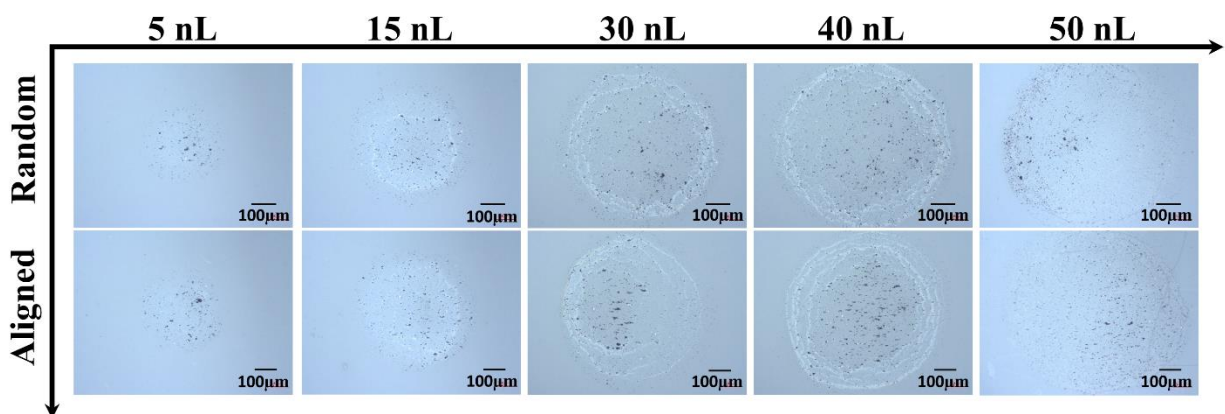


Figure 6.5: Optical microscope images of particle depositions of different droplet volumes, printed with 10 mg/mL particle concentration. “Random” refers to samples printed without applying external magnetic field and “Aligned” refers to samples with one-dimensional chains of particles when the magnetic field is applied during the printing process.

particle deposition patterns for various sizes of printed colloidal droplets when no magnetic field is applied. For small droplet volumes (e.g., < 30 nL), uniform particle deposition with no particle accumulation at the TCL is observed owing to the fast solvent imbibition that prevents the particle transport to the periphery of the jetted droplet. However, the particle accumulation at the edge of the sessile droplet becomes noticeable at droplet volumes larger than 30 nL. This is attributed to the higher number of particles transported to the TCL during the removal process of the remaining solvent. Printing colloidal inks with a lower particle concentration follows a similar trend in the pattern formation whereas the CRE becomes visible at droplet volumes higher than 40 nL (Figure 6.5).

Duo and Derby reported a different observation of particle accumulation at edges of sessile droplets on various porous substrates such as photopapers and ceramic powder beds.^{158,159} In their work, Marangoni flow has been induced to suppress the CRE due to the change in solvent composition during evaporation when depositing the droplets on a solid non-porous substrate. In case of the photopapers and ceramic powder beds, Marangoni flow was reduced inside the sessile

droplet since the solvent composition does not change during the imbibition process, leading to ring formation. However, the authors did not explore the influence of droplet volume on the type of particle deposition. The effects of different droplet and particle sizes as well as pore diameters on the CR formation were investigated by Pack and coworkers.¹³⁴ In their study, the substrate possessed only vertical pores that dictated a vertical solvent imbibition (no lateral imbibition). Therefore, when the solvent is partially imbibed into the substrate, the CR formation was determined by the evaporation of the remaining solvent. For substrates with large pore sizes, CRE was suppressed as a result of the fast solvent removal and vice versa.

The mechanism of solvent removal in this study is completely different, where the terpineol oil is being infiltrated into the porous substrate rather than being evaporated. A 30 nL sessile droplet takes about 98 s to be completely drained, whereas a 50 nL droplet drains within approximately 143 s. The former can be considered as the critical characteristic imbibition time for ring formation, since the particle accumulation at the contact line is observed for droplet volumes larger than 30 nL. Figure 6.6 illustrates the process of solvent drainage into the photopaper.

The location on which the sessile droplet is deposited has a limited capacity of solvent absorption. Once the jetted droplet touches the photopaper, it loses approximately 11% of its entire volume within 500 ms by imbibition. Then, the solvent further seeps in at a slower rate into the porous substrate isotropically in all directions. If the deposition area underneath the droplet becomes saturated with terpineol oil, the solvent can only infiltrate laterally beyond the original footprint of the droplet. We note that the TCL of the droplet is pinned on the substrate and solvent seepage refers to the solvent infiltrated into the substrate. This, in turn, generates a radial flow that drives some of the particles to the TCL. However, this is not a concern for small sessile droplets (i.e., droplet volumes < 30 nL), where the solvent is completely absorbed by the photopaper before

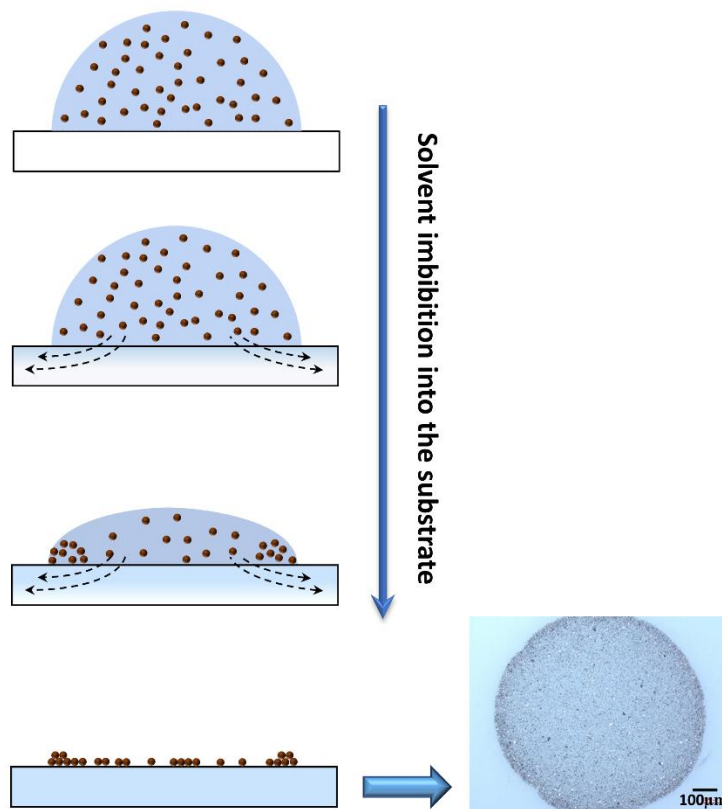


Figure 6.6: Illustration of solvent infiltration mechanism into the photopaper for droplets bigger than 30 nL. Dashed arrows indicate the solvent infiltration. When no magnetic field is applied, the particles follow the direction of the flow as the solvent seeps into the porous substrate beyond the three-phase contact line, resulting in a ring-like particle deposition.

particle transport to the TCL, resulting in a uniform particle deposition through immobilizing the colloidal particles (Figure 6.4 and Figure 6.5). For larger droplets, the solvent eventually generates a larger footprint as it continues to seep through the photopaper, resulting in a deposition of magnetic particles on the photopaper, surrounded by a ring of terpineol oil. Nilghaz et al. reported a similar observation in an effort to study the dye stain formation on paper substrates, that is the solvent wicking front propagates further into the porous substrate than the dye where the dye molecules were separated from and left behind the water solvent.¹⁶⁰ They attributed this behavior to the capillary penetration process into the paper, where the dye molecules were preferentially retained by the paper fibers. In our study, the colloidal particles are much bigger than the pore size

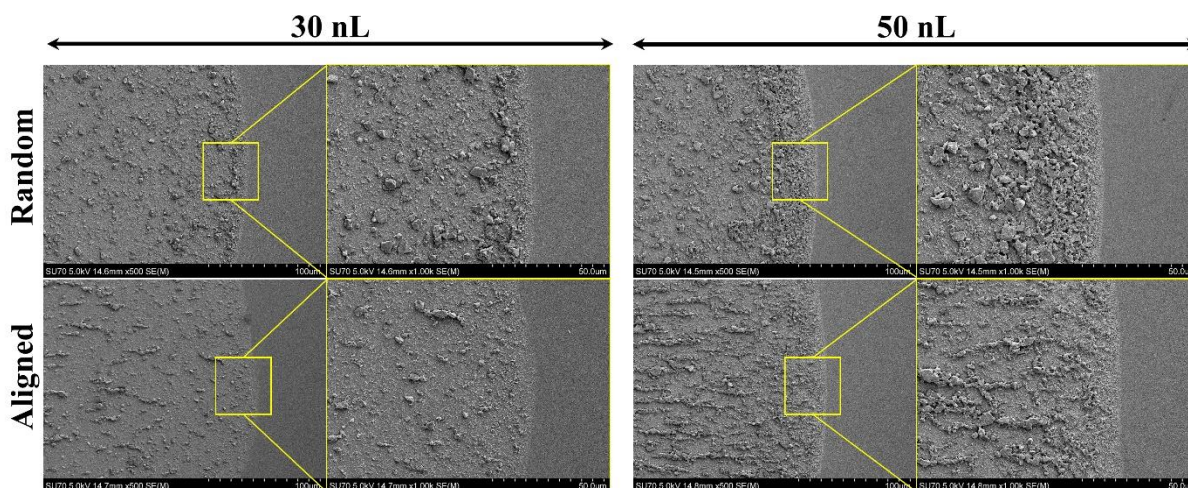


Figure 6.7: SEM images demonstrating the difference in particle accumulation at the TCL region with and without applying magnetic field for droplet volumes of 30 nL and 50 nL. The images present a clear evidence of the reduced number of particles deposited at the TCL when the magnetic field was applied. Ink concentration is 25 mg/mL.

of the photopaper, therefore, the particle penetration is excluded. Instead, the particles deposit on the surface of the photopaper, forming different particle deposition patterns depending on droplet volume and particle concentration.

The application of an external magnetic field significantly impacts the colloidal ferromagnetic particle deposition in sessile droplets.¹⁶¹ In this study, the magnetic anisotropy of the Gd_5Si_4 magnetic particles results in strong dipole interactions among the particles. These particles are forced to chain and assemble along the direction of the magnetic field that is known as the “easy axis” of magnetization. The horizontal component of the magnetic field drives the magnetic particles to form long chains, especially for the larger droplets. In addition, applying magnetic field significantly suppresses the CR formation. The mechanism of suppressing the CRE by exerting magnetic field can be described by two aspects: (i) magnetic particles transport toward the substrate under the magnetophoretic force, represented by the magnetic field gradient in a direction perpendicular to the substrate, which inhibits the radial particle transport and deposition at the TCL due to solvent imbibition, especially for larger droplets; (ii) chain formation of magnetic

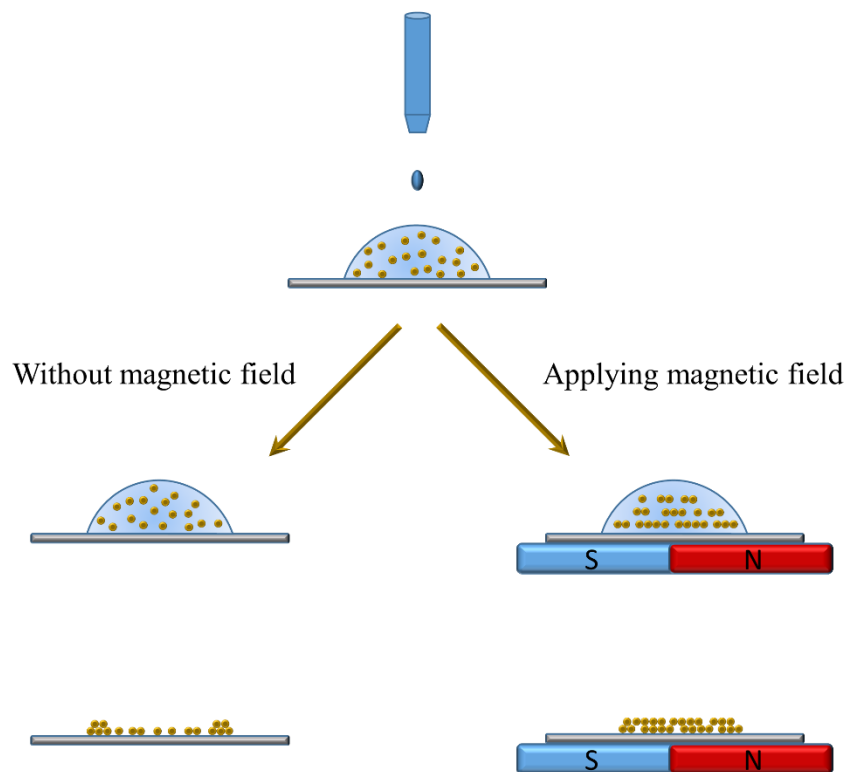


Figure 6.8: Schematic illustration of the magnetic field effect on ferromagnetic particle deposition. Ring-like depositions are produced when no magnetic field is applied, whereas, aligned chain-like patterns with much suppressed CRE are formed when a magnetic field is applied.

particles, which possibly decreases the particle mobility and transport driven by the solvent imbibition process. Figure 6.7 displays the chain formation and the CRE suppression when printing droplets with colloidal magnetic particles under the influence of magnetic field. The ring formation has been significantly suppressed, especially for the 50 nL droplets. Figure 6.8 illustrates the difference between particle deposition patterns with and without the presence of magnetic field.

In order to better understand the influence of applying external magnetic field on ferromagnetic particle deposition, COMSOL Multiphysics was employed to simulate the particle chaining and deposition processes. To simulate the particle chaining, only two magnetic dipoles were introduced to the simulation domain, where the interaction force between the two dipoles was significantly

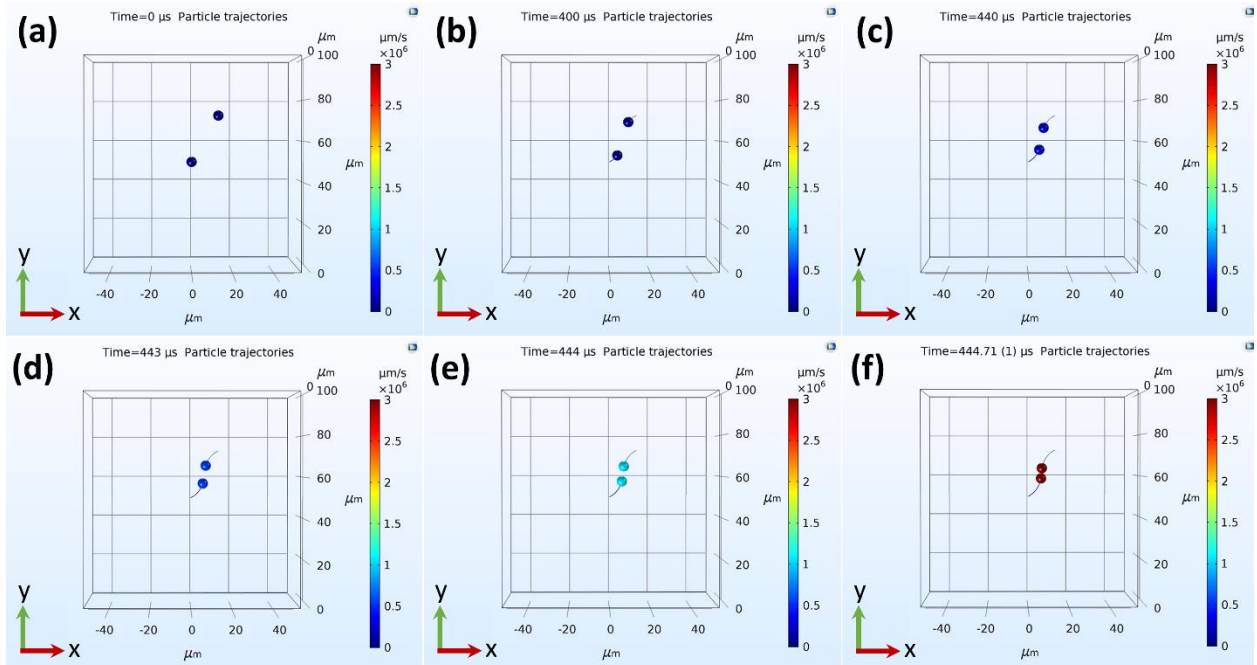


Figure 6.9: (a-f) Demonstration of chaining process of two magnetic dipoles in the presence of magnetic field at the angle $\alpha = 30^\circ$. The magnetic field is in the positive y-axis. The elapsed time for the two dipoles to collide is 446 μs . In this case, the dipoles travel in elliptical path until they align and collide.

affected by their orientation angle (α) with respect to the external magnetic field (Figure 6.1).

Figure 6.9 and Video S6.1 demonstrate the chaining process of two dipoles, one of which is placed at the center of the domain, whereas the second dipole is positioned at 30° to the first one with respect to the y-axis (i.e., the direction of the magnetic field). The distance between the two dipoles is selected as the mean particle distance (L_m), calculated at 25 mg/mL particle concentration. Details about the modeling are provided in the Methods section. Videos S6.1-6.5 display the chaining process of dipoles positioned at different angles such as zero, 30° , 45° , 60° , and 90° , and Figure 6.10 presents the time elapsed for the dipoles to collide and chain (t_{ch}). Figure 6.11 shows the interaction forces exerted on each particle at different initial orientation angles, which determines if they approach or move away from each other. When both dipoles are placed on the x-axis ($\alpha = 90^\circ$), the force is repulsive and the dipoles move apart. On the contrary, the dipoles attract each other the most when $\alpha = 0^\circ$ as shown in video S6.2. In this case, the particle velocity

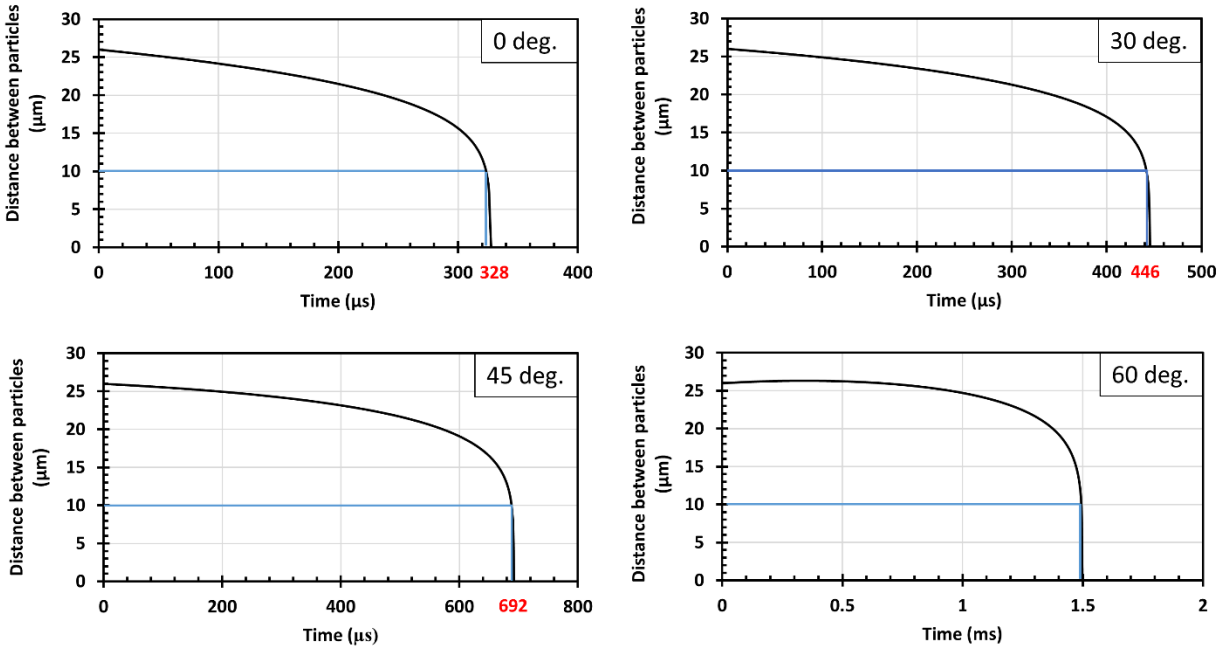


Figure 6.10: Distance between the two dipoles during the chaining process. The characteristic time for the two dipoles to collide is obtained when this distance reaches 10 μm , which is two times of the particle radius. The characteristic times for chaining t_{ch} are 328 μs , 446 μs , 692 μs , and 1.5 ms, for the orientation angles of zero, 30°, 45°, and 60°, respectively.

continuously increases until the dipoles collide. For any other orientation ($0^\circ < \alpha < 90^\circ$), the dipoles follow an elliptical trajectory until they collide and align themselves with the y-axis, i.e., with the direction of the magnetic field. The chaining characteristic time (t_{ch}) varies in these cases,

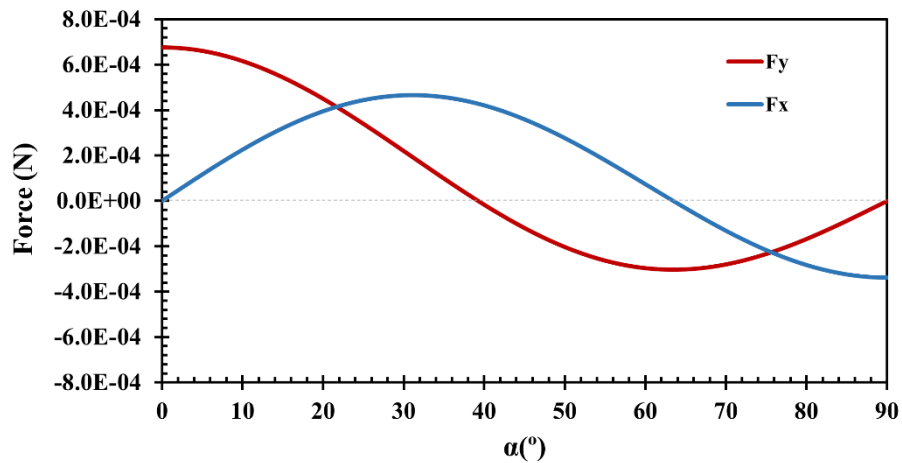


Figure 6.11: Interaction forces acting between the two dipoles in the simulation domain. Positive forces represent attractive forces between the two particle dipoles; and the negative forces are repulsive forces.

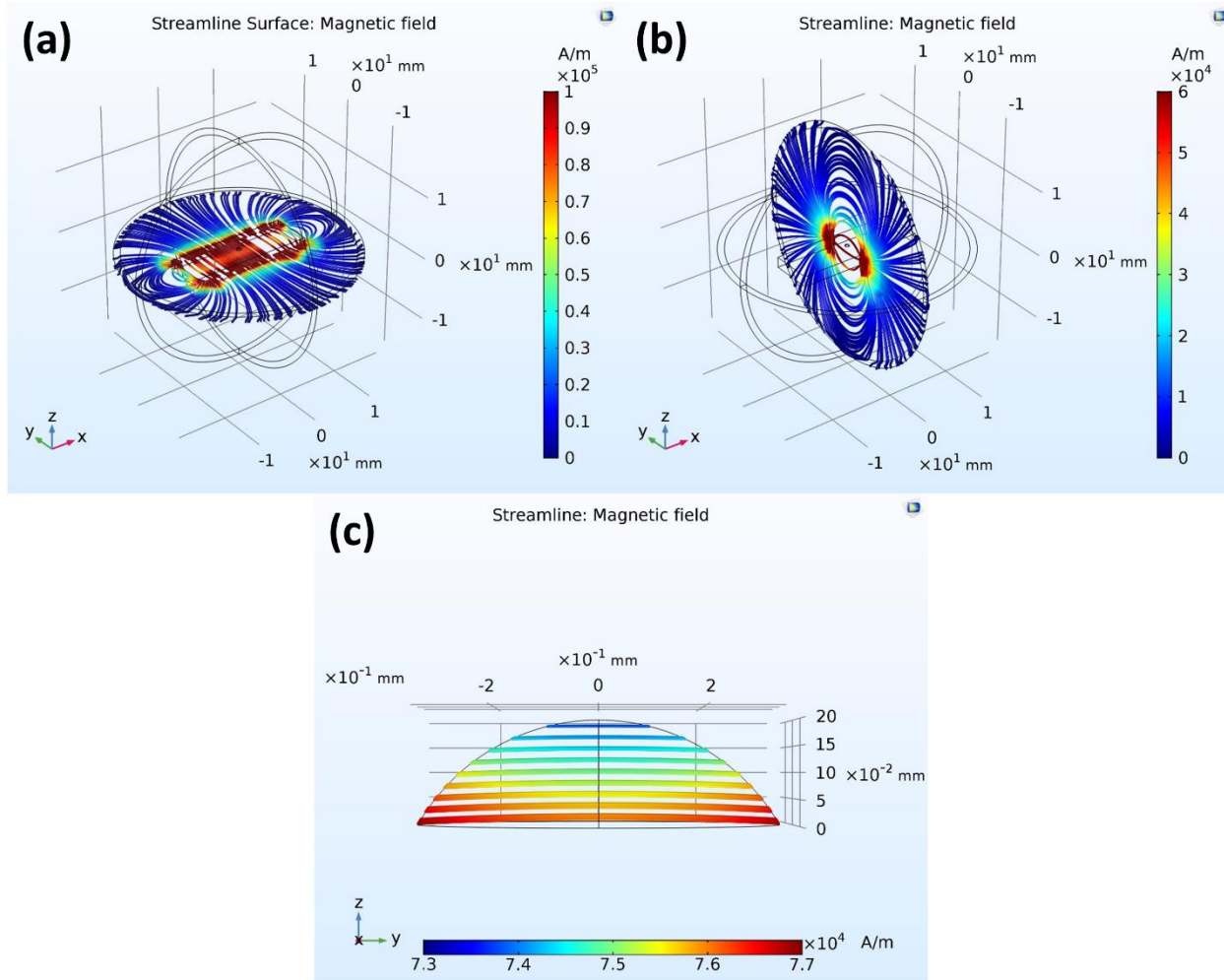


Figure 6.12: (a) and (b) Magnetic field simulation, which illustrate the magnetic field in XY and YZ planes. One droplet is placed on the top center of the permanent magnet. (c) Illustration of the magnetic field gradient inside the sessile droplet.

where longer particle chaining time is observed when the orientation angle (α) approaches 90° . This could be attributed to development of the successive, mutual repulsion or attraction forces obtained at different dipole orientations (Figure 6.11).

The magnetophoretic force suppresses the CRE through attracting the magnetic particles toward the substrate. This force is generated by the magnetic gradient in the z-direction perpendicular to the substrate as a result of positioning the permanent magnets underneath the substrate. The full magnetic field of the simulation domain is shown in Figure 6.12a and 6.12b. Figure 6.12c shows

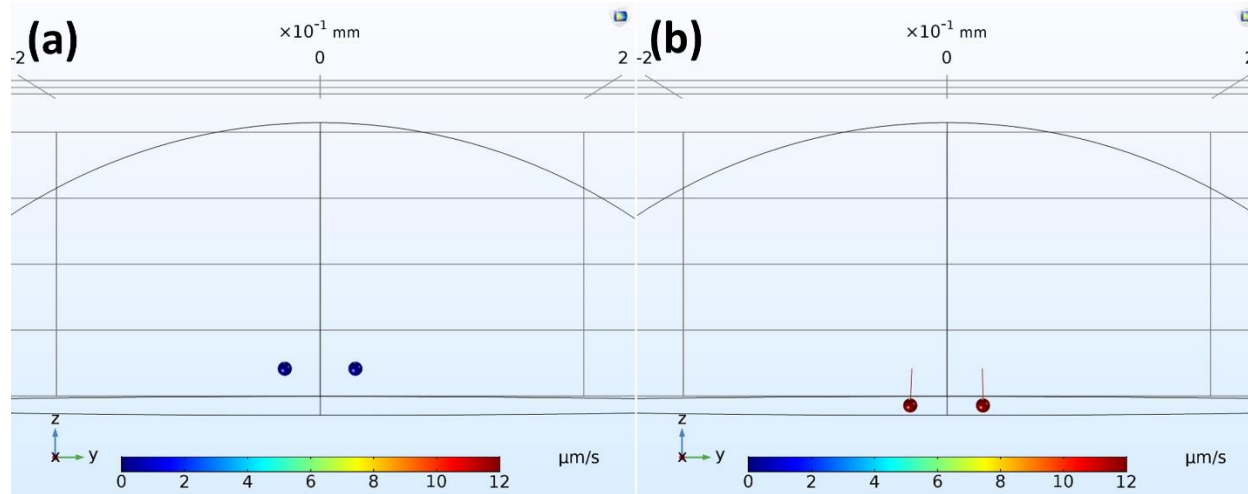


Figure 6.13: (a) Two particles released in the simulation domain with an initial velocity of zero; (b) particle migration in the z-direction toward the substrate under the influence of the magnetophoretic force and drag force. The particles are positioned at a vertical distance (L_m) away from the substrate, to calculate the characteristic time (t_{pz}) for the magnetic particles to reach the substrate.

the magnetic field gradient in the z-direction developed inside the droplet. In this domain, the particles are released at a distance (L_m) away from the substrate in order to estimate the characteristic time (t_{pz}) needed for magnetic particles to reach the substrate under the magnetophoretic force (Figure 6.13). At the early stages of particle motion, the particle velocity starts to gradually increase, reaching the maximum of $108 \mu\text{m/s}$ in 238 ms, and remains constant until the particles reach the substrate (Video S6.6).

The influence of exerting magnetic field on particle assembly and deposition can be determined by comparing the characteristic time needed for the particles to chain (t_{ch}) and the time elapsed for particles transported vertically toward the substrate (t_{pz}) with the critical time for solvent imbibition (t_{im}). The characteristic time ratios (t_{pz}/t_{im}) and (t_{pz}/t_{ch}) determine the final particle deposition and assembly in the presence of magnetic field. The characteristic time ratio (t_{pz}/t_{im}) determines whether the colloidal particles have sufficient time to reach the substrate before the solvent is completely drained. $t_{pz}/t_{im} > 1$ indicates the CR formation, where the particles transport

toward the substrate under the magnetophoretic force much slower than the imbibition process, resembling no magnetic field condition. In this case, the particles follow the infiltration flow, resulting in the CR formation. However, $t_{pz}/t_{im} < 1$ implies suppressing the CRE, where the particles deposit on the substrate under the magnetophoretic force before the solvent is completely drained. On the other hand, the characteristic time ratio (t_{pz}/t_{ch}) exemplifies the competition between the particle chaining and particle deposition when the magnetic field is applied. For $t_{pz}/t_{ch} < 1$, the magnetic particles deposit onto the substrate forming uniform but random depositions without obvious chain formation. In contrast, $t_{pz}/t_{ch} > 1$, describes the chain formation in the liquid phase before the particles are deposited on the substrate. In other words, the particles form chains before they reach the substrate, which probably constrains the particle motions inside the sessile droplet, therefore, also suppressing the CRE.

The experimental outcomes are corroborated by the analysis of characteristic time ratios when considering the critical solvent imbibition time for a 30 nL droplet. The corresponding characteristic time ratio $t_{pz}/t_{im} = 2.5 \times 10^{-3}$, which is orders of magnitude smaller than 1. This indicates suppression of the CRE, where the particles rapidly transport toward and deposit on the substrate before the solvent is completely infiltrated. In addition, the characteristic time ratios t_{pz}/t_{ch} for the orientation angles of zero, 30°, 45°, and 60° are, respectively, 762.2, 560.5, 361.3, and 72.1. Hence, for all simulated cases except $\alpha = 90^\circ$, the particles chain in the liquid phase before depositing on the substrate. This explains the effect of magnetic field on the chain formation, as well as suppression of CRE, which is in a good agreement with our experimental observations.

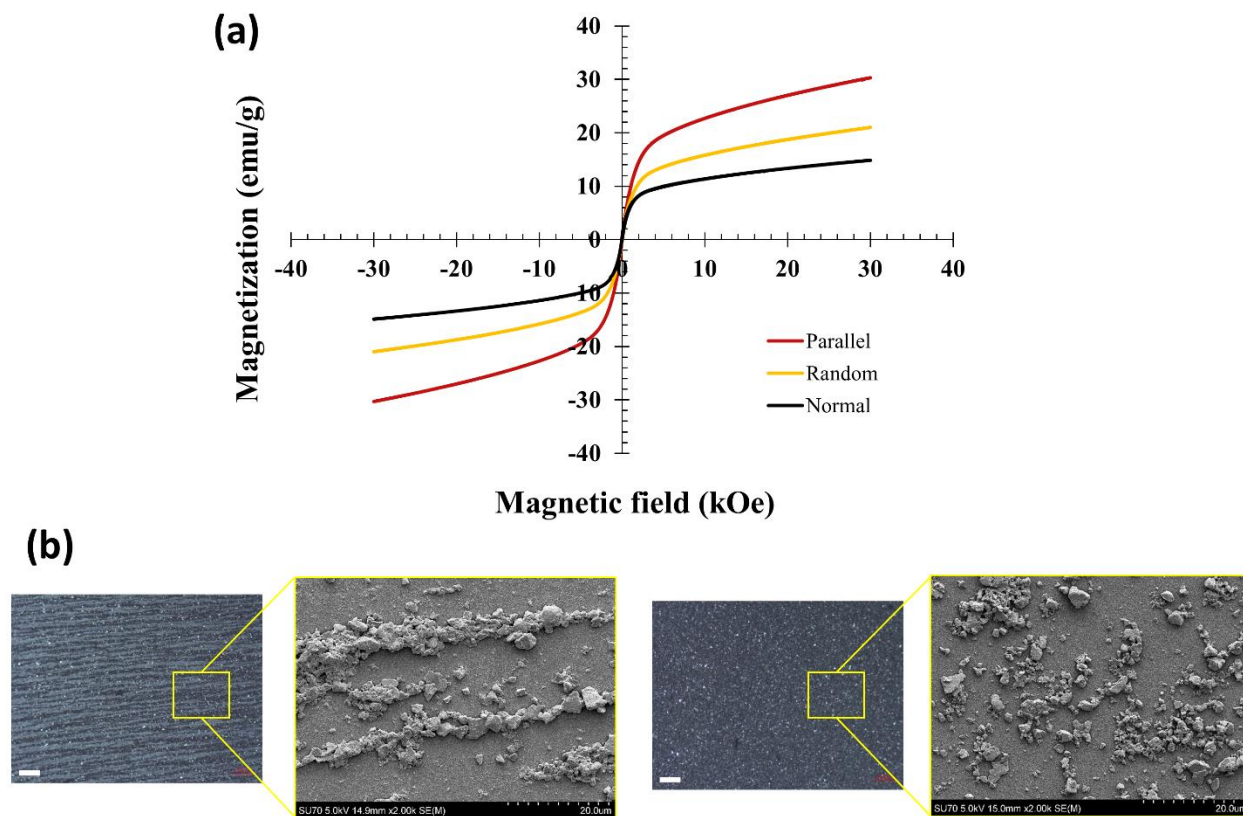


Figure 6.14: (a) Magnetization curves of the films with chains of particles and the films with random particle deposition. “Random” refers to the magnetization curve of the films fabricated without external magnetic field (i.e., random particle deposition). “Parallel” and “Normal” refers to the magnetization curves of films with magnetic particle chains, when the testing magnetic field is parallel to the chain direction and perpendicular to the chain direction, respectively. (b) Optical and SEM images of the printed films with magnetic field (left) and without magnetic field (right). Clear chain formation is observed on the films fabricated with external magnetic field. The scale bar is 100 μm.

6.3.1 Implication in Printed Anisotropic Magnetic Films

In order to evaluate the anisotropic magnetic properties of the magnetic particles, continuous films were printed by this inkjet printing process with and without external magnetic field. The printed films were characterized with Physical Property Measurement System (PPMS) and electron scanning microscopy (SEM). Figure 6.14a presents hysteresis curves of the printed films at room temperature. Magnetic moments parallel and normal to the direction of the magnetic field were measured for each sample. Higher magnetization values were obtained when measuring films with 1D chains parallel to the direction of the applied magnetic field as compared to the magnetization

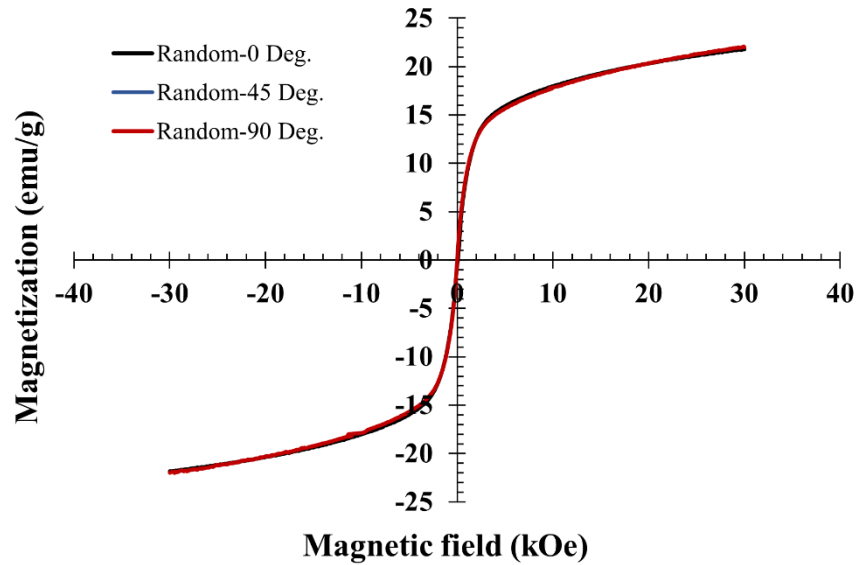


Figure 6.15: Magnetization curves of the printed “Random” films at different orientation angles with respect to the testing magnetic field. “Random” refers to films printed without applying magnetic field with random particle deposition.

values of films with random particle orientation. This is attributed to the total magnetic moment that equals the sum of the magnetic moment induced in every magnetic particle in the chains whose easy axis is aligned along the direction of the externally applied magnetic field. Conversely, lower magnetization values were observed when the 1D chains were placed normal to the direction of the magnetic field as compared to samples with random particle orientation. The difference in the induced magnetic moments indicates the effect of both magnetocrystalline and shape anisotropy of the assembled Gd_5Si_4 magnetic particles. The particle assembly and chain structures under the influence of the magnetic field are shown in Figure 6.14b. Samples with random particle orientation (i.e., without applying magnetic field) were tested at different orientations with respect to direction of the testing magnetic field as shown in Figure 6.15. It should be mentioned that the photopaper exhibited a slight response to the applied testing magnetic field as presented in Figure 6.16. This background magnetization effect of the substrate was subtracted from the magnetization

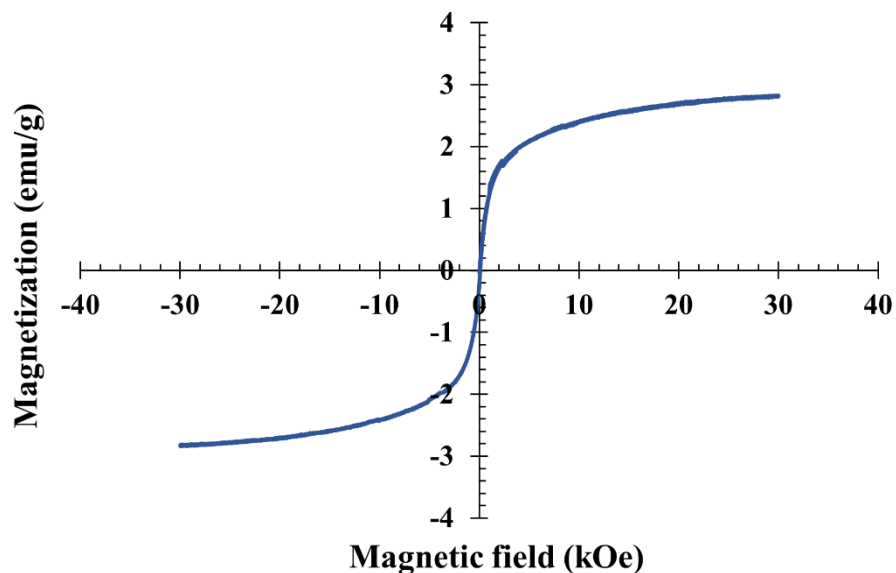


Figure 6.16: Magnetization curve of the photopaper.

data of the printed films in order to evaluate the pure response of the magnetic particle assemblies to the testing magnetic field.

6.4 Conclusion

In summary, 1D chain structures of magnetic particles with suppressed CR formation have been obtained on porous substrates through the magnetic-field assisted inkjet printing process. Gd_5Si_4 magnetic particles were formulated in terpineol oil and printed on photopapers. Unlike the conventional evaporative particle-laden droplets, the particle deposition morphology in this study is determined by solvent imbibition, particle chaining, and particle transport under magnetophoretic effect. When no magnetic field was applied, different particle depositions were observed depending on the particle concentration and the volume of the jetted droplet. For small droplets (i.e., < 30 nL), no CR formation was observed because the solvent can imbibe into the substrate in a short period of time (i.e., less than the critical imbibition time). However, the solvent

imbibition time for large colloidal droplets (i.e., > 30 nL) exceeds the critical imbibition time mostly due to the second stage of solvent seepage. This, in turn, generates a radial flow that may drag some of the colloidal particles to the periphery of the particle deposition. Applying magnetic field enables the formation of the 1D chain structure through assembling the magnetic particles along their easy axes. It also significantly suppresses the CRE through the particle transport under magnetophoretic effect, especially for larger droplets. Our numerical solution predicted that the colloidal magnetic particles assemble in the liquid phase before they vertically transport and deposit on the substrate, which agrees very well with our experimental findings. Finally, the printed films have exhibited an anisotropic magnetic response to the applied magnetic field due to the 1D assembly structure, which holds a great potential in many engineering applications.

CHAPTER 7 Direct Embedment of Silver Nanowires by Inkjet Printing for Stretchable Conductors

7.1 Introduction

Stretchable electronics have drawn tremendous interest in the past few years,^{162–168} as they exceed the scope of conventional electronics, manufactured on rigid circuit boards for many applications such as light-emitting diodes,^{169–171} thin film transistors,^{172,173} energy-harvesting and energy-storage devices,^{174–176} and deformable conductors for human-machine interfaces.^{177–180} Stretchable conductors are vital and indispensable components of soft electronics owing to their significant role in interconnectors and sensing devices.^{181,182}

Several strategies have been adapted so far to integrate conductive materials into stretchable conductors, one of which is depositing conductive materials on top of elastomer substrates or embedding conductive materials into the surface of elastomer substrates by transfer processing.^{183,184} However, the mechanical instability, represented by buckling and fracturing of the deposited/transferred conductive materials after cyclic loading, leads to an irreversible increase in electrical resistance of the fabricated stretchable electrodes. The alternative approach is to make stretchable conductors directly by using composite inks of liquid elastomers with conductive fillers. Nevertheless, high concentration of conductive fillers (e.g., silver flakes), as high as 60-80 wt%, is needed to render the required electrical conductivity, which significantly sabotages the achievement of high stretchability, as well as the fabrication cost.¹⁸⁵ Direct embedment of conductive materials into a liquid elastomer, on the other hand, provides an effective and facile technique to fabricate stretchable conductors, which can potentially overcome the abovementioned problems.^{186,187}

Conductive nanomaterials, including metal nanomaterials (e.g., metal nanoparticles¹⁸⁷⁻¹⁹⁰ and metal nanowires^{191,192}), carbon nanotubes,¹⁹³ and graphene¹⁷³ have been actively explored for stretchable conductors. Among these conductive materials, silver nanomaterials are considered very promising candidates because of their high conductivity and excellent mechanical compliance.^{194,195} Different low-cost, scalable manufacturing printing techniques, such as inkjet printing,^{190,196-198} screen/stencil printing,^{166,189,199} spray printing,²⁰⁰ and extrusion printing,^{186,201} have been extensively used to pattern and fabricate functional devices with both high electrical and mechanical performance.²⁰² Recently, inkjet printing, as a non-contact additive manufacturing process, has been proven to be an effective and precise method to deposit silver nanowires (AgNWs).^{183,203,204}

In this study, we have fabricated stretchable conductors by employing the inkjet printing technique, where colloidal droplets of AgNWs were directly printed and embedded into Polydimethylsiloxane (PDMS) layer. The single step printing and embedment of the AgNWs were achieved by controlling the thickness of the liquid PDMS layer, the substrate underneath the PDMS layer, and the post-printing treatment of the printed lines. The viscous PDMS liquid shapes the printed AgNW lines into tens of micrometer in diameter, which significantly enhanced the printing resolution as compared to that of the traditional inkjet printing process. Moreover, the printed AgNW lines exhibited alignment along the printing direction, which enhanced the electrical performance of the fabricated stretchable conductors during multiple bending and stretching/releasing cycles. The initial conductivity of a single AgNW printed line is approximately 852 S/cm, which demonstrates the potential of our stretchable conductors for wide range of engineering and manufacturing applications.

7.2 Experimental Section

7.2.1 Materials. Polyethylene terephthalate (PET) films (MELINEX ST505) with 125 μm thickness were supplied by TEKRA, a division of EIS. Polyvinylpyrrolidone (PVP-K30) and silver nitrate (99%, ACS reagent) were purchased from Sigma-Aldrich. Poly(dimethyl)siloxane (PDMS) precursor and curing agent (Sylgard 184) were obtained from Dow Corning. KOPTEC ethanol (99.5% purity), acetone (99.5% purity), Isopropanol (99.5% purity), and ethylene glycol (100% purity) were acquired from VWR. Deionized (DI) water with a resistivity of 18.2 $\text{M}\Omega\cdot\text{cm}$ was produced by Direct-Q water purification system (Millipore Sigma). All materials were used as received without further purification.

7.2.2 Preparation of the Liquid PDMS Layer. PDMS base was mixed with a curing agent in the proportion of 10:1 by weight to prepare the PDMS precursor. The precursor was put into a vacuum chamber for degassing. PET films were used as supporting substrates to deposit the liquid PDMS precursor. The films were rinsed by isopropyl alcohol and deionized water, respectively, then dried with a clean air. After cleaning, the PET substrates were coated with liquid PDMS using drop casting method to produce elastomer layers with 1.5 mm thickness. Thinner PDMS layers were obtained by spin coating at 600, 1000, and 3000 rpm for 20 sec. to produce layers with thicknesses of 250 μm , 100 μm , and 40 μm , respectively.

7.2.3 Preparation of the AgNW Ink. AgNWs with average diameter of ~ 100 nm and average length of ~ 14.5 μm were chemically synthesized using the modified polyol reduction method.^{205,206} Briefly, 0.5 g of polyvinylpyrrolidone (PVP) was added to 50 mL ethylene glycol in a round-bottomed flask under stirring speed of 400 rpm. The solution was kept at 170 $^{\circ}\text{C}$ in an oil-bath for 1 h to form a homogeneous solution. Then, 150 μL of 0.1 mmol/L NaCl/ethylene glycol solution was added into the homogeneous solution. After 10 min, 0.5 g of silver nitrate (AgNO_3), dissolved

in 50 mL ethylene glycol, was dripped into the flask with a volumetric flow rate of 2.5 mL/min. The reaction was continued for another 20 min at 170 °C. Finally, the flask was cooled down to the room temperature, and the AgNWs were precipitated by acetone and centrifuged at 3000 rpm for 20 min. The AgNWs were washed three times with ethanol through centrifugation to remove the excess PVP, then re-dispersed in ethanol to obtain a solid concentration of 10 mg/mL for the inkjet printing process.

7.2.4 Fabrication of Embedded AgNW Lines. The printing of the AgNW ink was performed by an inkjet printing platform (Jetlab 4, MicroFab). The printing station was driven by a waveform generator (Jetdriver III, MicroFab) with an 80 µm nozzle (MJ-ATP-01-80-8MX, MicroFab). The printing frequency was set to 500 Hz to generate a stable jet with an inflight droplet size of ~ 400 pL with droplet speed of 1.2 m/s. Different printing passes with 50 µm in-line droplet spacing and 25 µm shift among the printed passes were utilized to fabricate the embedded AgNW lines.

In order to investigate the effect of drying conditions on the morphology of the printed lines, the printed lines were subjected to three different drying conditions (i.e., Post-printing treatment) such as immediate thermal curing the PDMS after printing for 10 min at 90 °C, resting the samples for 30 min at room temperature then curing for 10 min at 90 °C, and curing at the room temperature for 24 h. After ethanol evaporation and curing the PDMS layer, stretchable conductors composed of embedded AgNW lines were fabricated. Finally, the stretchable conductors were peeled off the PET substrate to test their electrical performance.

7.2.5 Characterization. The microstructures and alignment of the printed AgNWs assembly were characterized by field-emission scanning electron microscopy (FE-SEM, HITACHI SU-70), operated at 5 kV. After printing and resting the sample for 30 min, the uncrosslinked PDMS layer was dissolved by cyclohexane, leaving AgNWs on the substrate for SEM characterization. The

cross-sectional images of the embedded AgNW lines were obtained by focused ion beam scanning electron microscope (FIB-SEM, Zeiss Auriga), and the static contact angle measurements were performed using a goniometer (OCA 15) from Dataphysics at room temperature.

7.2.6 Electrical Characterization of the Embedded AgNW Lines. Before examining the electrical performance of the fabricated samples, the samples were thermally treated at 150 °C for two hours. Then, a PDMS layer with a 500 μm thickness was added via spin coating on top of the printed samples to facilitate samples handling. The samples were then peeled off the PET substrate and placed on a PDMS substrate with a thickness of 1 mm for bending and stretching/releasing tests. The samples were kept for four hours to give sufficient time for the two PDMS layers to bond with each other. The edges of the samples were sputtered with gold and smeared with silver paste to make the contact pads for electrical measurements.

7.2.7 Viscosity Characterization

The viscosity of the freshly prepared PDMS was measured by the Rheometer (Physica MCR-301, Anton Paar) using plate/plate geometry (diameter 50 mm) with a gap of 1 mm. Fixed measuring point durations was selected with a linear shear rate ramp of 0.01 to 100 1/s. After measuring the viscosity of the fresh PDMS, the measurements were repeated after 30 min to mimic the experimental conditions.

7.3 Results and Discussion

7.3.1 Direct Inkjet Printing and Embedding of AgNWs into an Elastomer Substrate. Figure 7.1 illustrates the fabrication process of stretchable conductors. Previously, we have demonstrated that the ultrasonication-shortened AgNWs, dispersed in pure ethanol with a solid concentration of

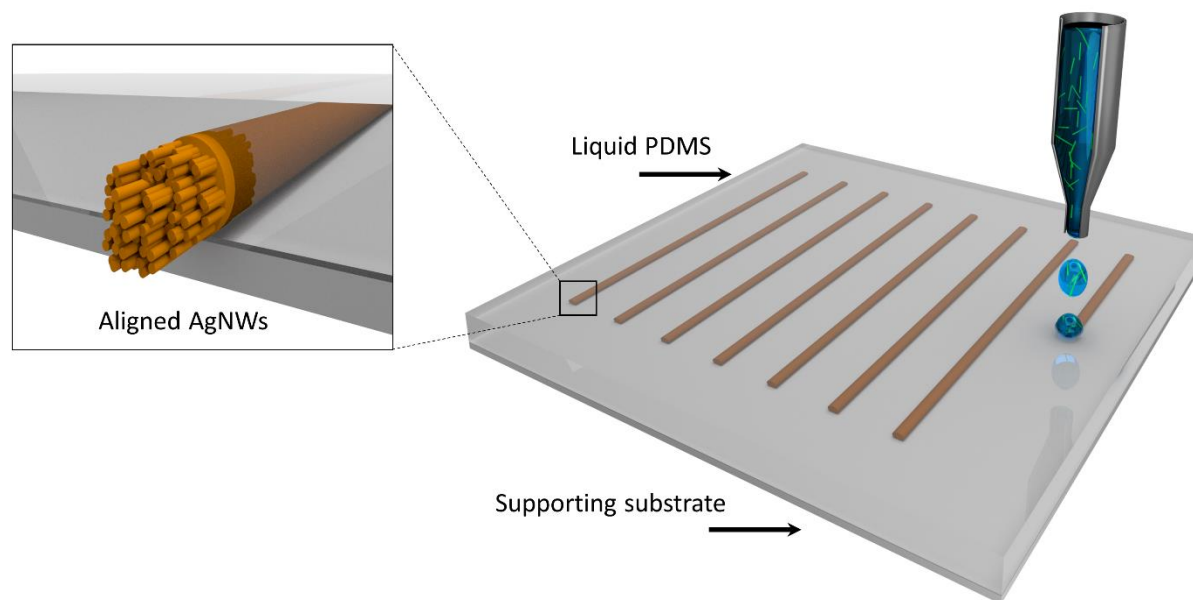
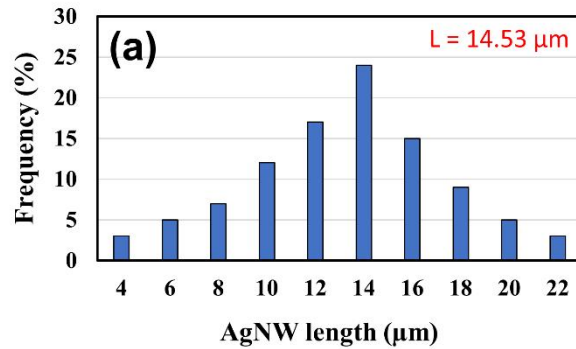


Figure 7.1: Illustration of the direct embedment of AgNWs into an elastomer layer by inkjet printing.

10 mg/mL, is suitable for inkjet printing process.¹⁸³ In this study, by optimizing the printing parameters, the as-synthesized AgNWs with average length of $\sim 14.5 \mu\text{m}$ and 10 mg/mL solid concentration were utilized (without ultrasonication) to fabricate the stretchable conductors (Figure 7.2). As illustrated in Figure 7.1, the colloidal suspension of AgNWs was jetted into a liquid PDMS layer, which was firstly spin coated on a PET substrate. Once the jetted colloidal droplets penetrate the liquid PDMS layer, they coalesce to form a connected line. Herein, the PET film is utilized as a supporting substrate for the liquid PDMS layer to facilitate the fabrication process of stretchable conductors as elaborated in detail in the following discussion.

To understand the mechanism of fabricating embedded AgNW lines, we first examined the effect of liquid PDMS layer thickness and the number of printing passes on the morphology and the penetration depth of the printed AgNW lines in the liquid PDMS layer. Four different PDMS layer thicknesses were tested such as 1.5 mm, 250 μm , 100 μm , and 40 μm . For each film thickness,



As-synthesized AgNWs

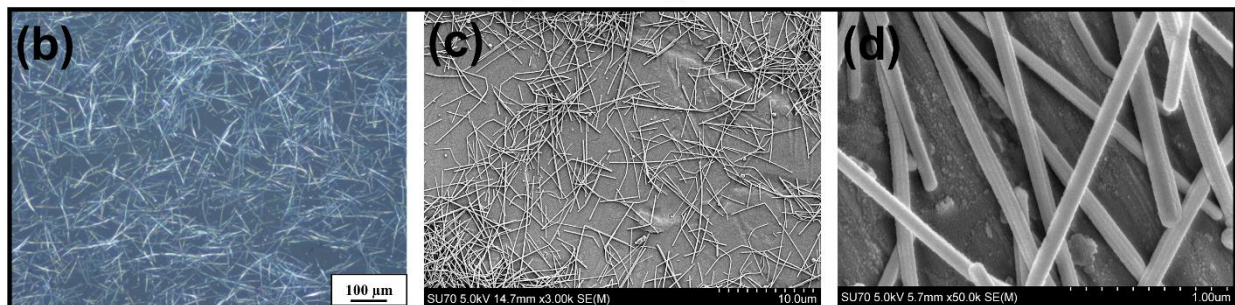


Figure 7.2: (a) Histograms of AgNWs length distribution. (b) Optical image of the as-synthesized AgNWs. (c) and (d) SEM images of the as-synthesized AgNWs, where the AgNW diameter is $\sim 100 \text{ nm} \pm 20 \text{ nm}$.

one to nine printing passes were examined as shown in Figure 7.3. The coalescence of the jetted colloidal droplets inside the liquid PDMS layer and the thickness of the PDMS layer dictate the morphology and integrity of the printed lines. In this study, we have adjusted the individual inflight droplet size to approximately 400 pL with droplet speed of 1.2 m/s. This renders the colloidal droplet the required momentum to penetrate into the liquid PDMS. The jetted droplets locally deform the surface of the liquid PDMS as they impinge into the PDMS layer. This initiates a drag force as the colloidal droplets traverse the liquid PDMS, which slows down and eventually stops the droplets at a certain penetration depth. The following droplets need to penetrate the same depth into the PDMS layer in order to coalesce with former printed droplets, forming a continuous line. Any local variation in the PDMS layer thickness, or jetting conditions may affect the penetration depth.

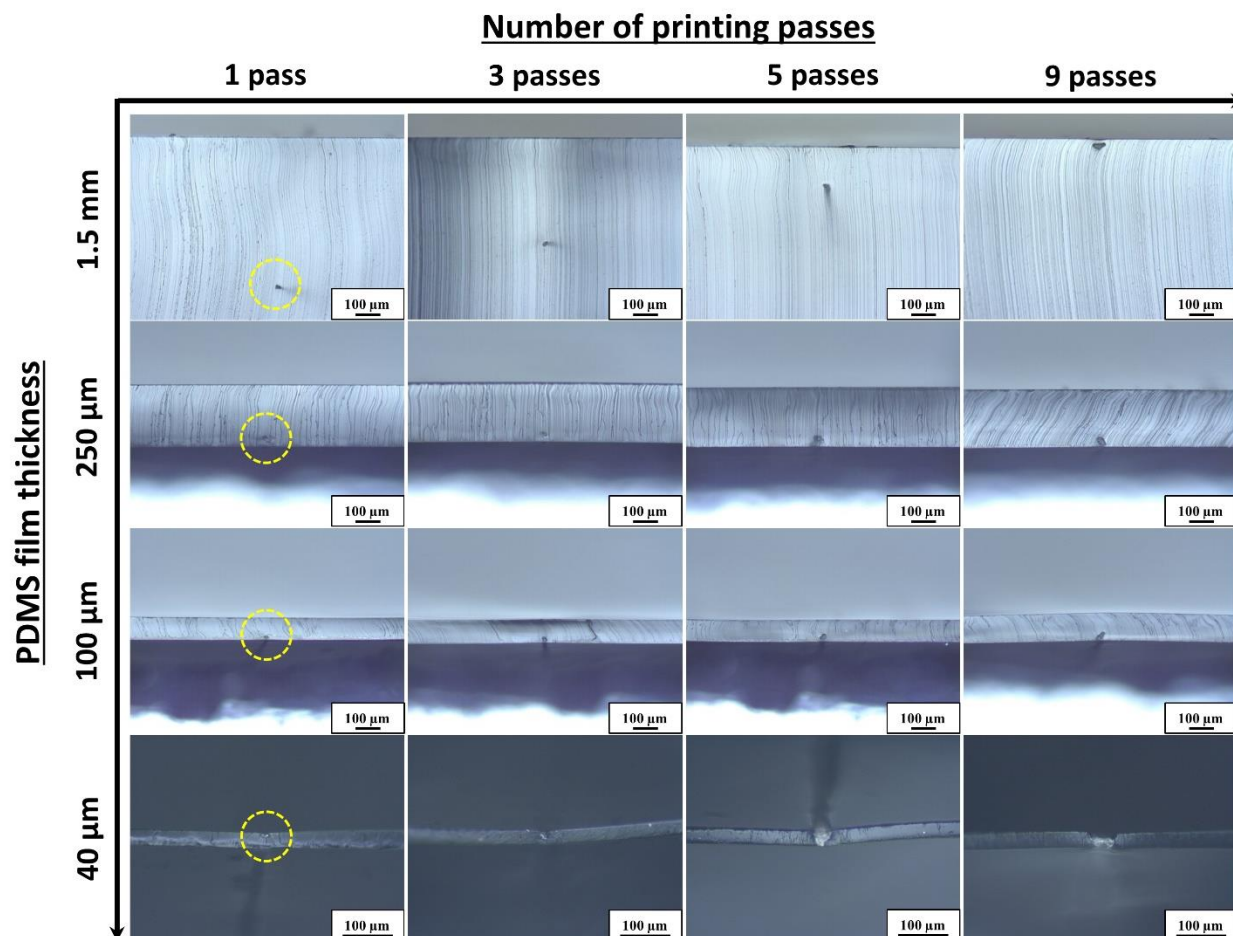


Figure 7.3: Demonstration of the penetration depth of AgNW lines with respect to the number of printing passes and PDMS layer thickness. Different penetration depths of AgNW lines were obtained for various printing passes when utilizing a thick PDMS layer (i.e., 1.5 mm). However, the AgNW lines were found to deposit in the vicinity of the supporting PET substrate when using PDMS layer thickness less than 250 μm. The yellow circles highlight the location of printed AgNW lines.

When the liquid film thickness of the elastomer is 1.5 mm, the AgNW lines were observed to form at different penetration depths depending on the number of printed passes (Figure 7.3). This behavior could be attributed to the evaporation of ethanol present inside the PDMS layer. Figure 7.4 illustrates different scenarios taking place when printing multiple passes for each film thickness. In our system, once the jetted colloidal droplet of AgNWs and ethanol is encapsulated by the liquid PDMS, the ethanol has nowhere to go but to escape the PDMS layer through evaporation. For this particular PDMS layer thickness (i.e., 1.5 mm), the AgNW line formation

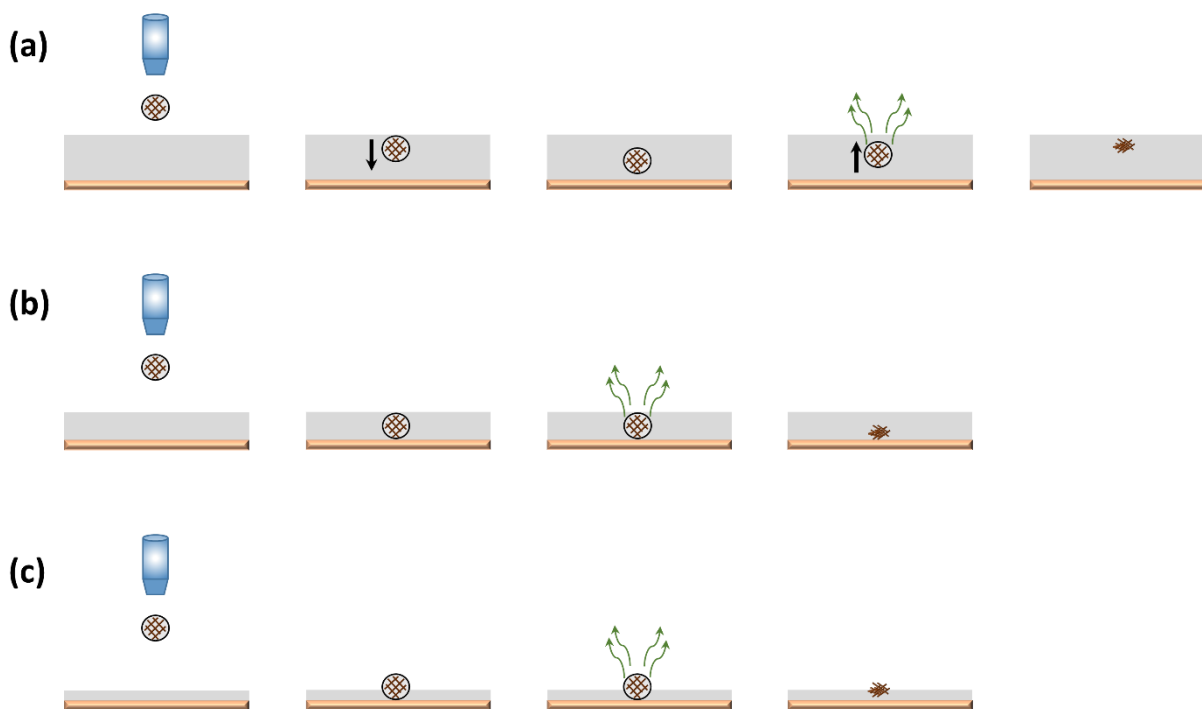


Figure 7.4: Illustration of the fabrication process of embedded AgNW lines. (a) Represents printing on a liquid PDMS layer with 1.5 mm thickness. (b) Represents printing on a liquid PDMS layer with a 100 μm thickness. (c) Represents the case of printing on a liquid PDMS layer with a 40 μm thickness.

could be described by two stages: the primary stage in which the jetted droplet penetrates the liquid PDMS layer to a certain depth, followed by coalescence with the upcoming colloidal droplet. The secondary stage is ethanol evaporation and AgNWs migration toward the surface of the liquid PDMS. During this process, the ethanol may drag the AgNWs to the surface of the PDMS layer, as shown in Figure 7.3 and illustrated in Figure 7.4. Increasing the number of printing passes means more ethanol trapped inside the liquid PDMS layer, and consequently, the AgNW line becomes closer to the surface of the PDMS (Figure 7.3). It should be mentioned that AgNW lines might break to small segments as they do not survive this multistage process.

Decreasing the liquid PDMS layer thickness (e.g., 250 μm and 100 μm), however, produced different outcomes, where the printed AgNW lines remained at the bottom of the liquid PDMS layer regardless the number of printed passes. In this case, the jetted droplets were able to reach

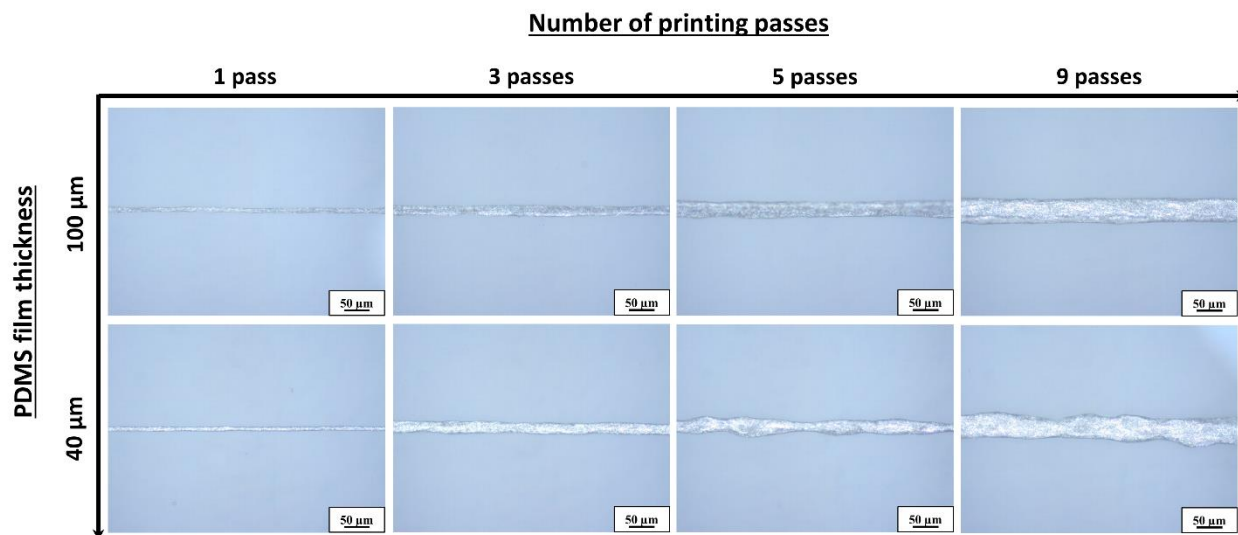


Figure 7.5: Optical images of the printed AgNW lines with respect to the number of printed passes and PDMS layer thickness. The top row represents lines produced when printing into a 100 μm layer thickness, while the bottom row represents lines printed into a 40 μm layer thickness. Bulging and waviness were observed when printing more than three passes for PDMS layer thicknesses that are less than 100 μm .

and coalesce in vicinity of the supporting PET substrate, where the droplet-substrate interactions assisted to anchor the colloidal droplet in place. In other words, the ethanol was not able to drag the AgNWs to the surface of the PDMS during the evaporation process as a result of the droplet-substrate interactions. This droplet-substrate interaction is explained in the following section.

With further decreasing the PDMS layer thickness to 40 μm , the printed AgNW lines became exposed to the top surface of the PDMS film (Figure 7.3). In this study, the jetted droplets were on the order of ~ 100 μm inflight diameter. Therefore, once colloidal droplet break through the thin PDMS layer and deposit on the surface of the supporting PET substrate, part of the droplet's cap become above the PDMS layer, exposed in the air. In this case, the coalescence is likely to occur at the exposed portion of the PDMS layer, which drags the rest of the droplets to the PDMS surface (Figure 7.4). As a result, the printed lines are located at top of the PDMS layer, producing nonuniform, wavy morphology compared with those anchored at the supporting PET substrate (Figure 7.5). Thus, the thickness of the liquid PDMS layer is a critical parameter for the formation

of embedded AgNW lines. Thinner PDMS films with thickness of $\sim 100\ \mu\text{m}$, which is comparable to the diameter of the jetted droplet ($\sim 100\ \mu\text{m}$), produces the best results. During the inkjet printing process, the jetted droplets impinge on the PET supporting substrate, where the droplets coalesce to uniform AgNW lines that remain at the bottom of the PDMS film (i.e., fully embedded) after solvent evaporation and PDMS curing. Furthermore, this comparable film thickness and droplet's diameter facilitates the ethanol evaporation process. Figure 7.5 presents the morphology of the AgNW lines with respect to the number of printed passes. Occasionally, single pass produces broken lines due to possible missing jets (since in this study, only one nozzle is employed for printing). Three and five printing passes give better results, and nine printing passes introduce too much ethanol, generating bulged and wavy lines. Therefore, in this study, five printing passes have been used to generate AgNW lines embedded into PDMS layers.

We have also examined the effect of the supporting substrate on the penetration depth of the printed AgNW lines. Compared to the PET supporting substrates, a cured PDMS film was used as the supporting substrate. In the latter case, the embedded AgNWs migrated slightly upward, approximately located in the middle of the elastomer layer as the printed samples were thermally cured. Figure 7.6a/b and Figure 7.6d/e present the top view and cross-section of the embedded AgNWs under these two conditions. Figure 7.6c shows a contact angle of $\sim 20^\circ$ of AgNW ink on the PET substrate, when immersed in the liquid PDMS to mimic the experimental conditions. The lower contact angle, the stronger adhesion of AgNW ink with the PET substrate. On the other hand, using a cured PDMS film as a supporting substrate gave different results. The AgNW ink exhibited a contact angle of $\sim 145^\circ$ on the supporting PDMS substrate, indicating its weak adhesion (Figure 7.6f). In other words, PDMS substrates resulted in poor droplet-substrate interactions due

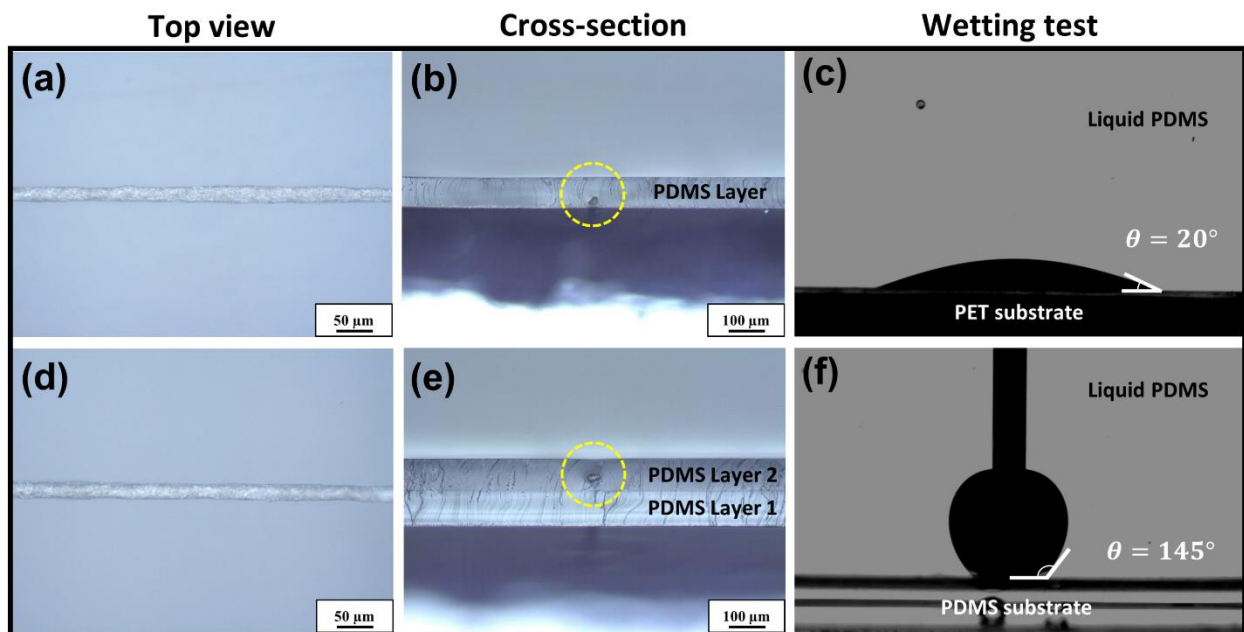


Figure 7.6: (a) and (b) show the top and the cross-sectional views of AgNW lines, printed with five passes on a PDMS layer with 100 μm thickness on a PET substrate. The printed line was deposited in vicinity of the supporting substrate. (d) and (e) are the top and cross-sectional views of AgNW lines, printed with five passes on a PDMS layer with 100 μm thickness that was spin-coated on a cured PDMS supporting substrate. (c) and (f) present the contact angles of the AgNW ink on PET and PDMS substrates when submerged into liquid PDMS, indicating the strong droplet-substrate interactions on the PET substrate.

to their low surface energy. Consequently, the coalescent droplets would not stick to the cured PDMS substrate but migrate slightly upward during the solvent evaporation. It should be noted that all the samples presented in Figures 7.3, 7.5, and 7.6 were kept at room temperature for 30 min, then thermally cured at 90 $^{\circ}\text{C}$ for 10 min to give a sufficient time for the ethanol to evaporate. Post-printing treatment, which affects the evaporation of ethanol and the location of the AgNW lines, is another crucial factor for fabricating embedded AgNW lines. Three different post-printing treatment conditions were studied: immediate thermal curing of PDMS after printing for 10 min at 90 $^{\circ}\text{C}$, resting the samples for 30 min at room temperature then curing for 10 min at 90 $^{\circ}\text{C}$, and room temperature curing for 24 h. It has been reported that the liquid PDMS shows no curing

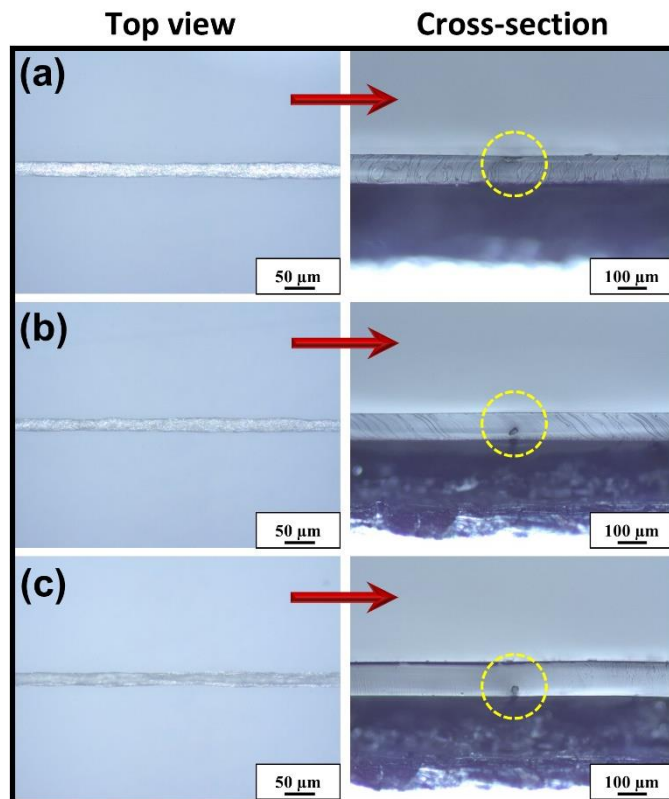


Figure 7.7: Penetration depth of AgNW line with respect to curing temperature. (a) Shows the lifted AgNW line to the surface of the PDMS when the sample was directly cured after printing. (b) and (c) present embedded AgNW lines when the samples were left to rest for 30 min then cured at 90 °C for 10 min, and samples cured at the room temperature for 24 h., respectively. Five printing passes were used and the PDMS thickness is ~100 μm.

ability in the presence of ethanol.²⁰⁷ However, as the ethanol gradually evaporates, the PDMS layer can be fully cured by one of abovementioned processes.

It can be clearly seen from Figure 7.7a that printing followed by immediate thermal curing at 90 °C for 10 min pushed the AgNWs to the surface of the PDMS as the ethanol is forced to quickly evaporate through the PDMS layer. In this case, the lift force, generated by ethanol evaporation, overcomes the adhesion force between the droplet and the PET substrate in addition to the viscous drag exerted by the surrounding liquid PDMS. However, for the latter two drying conditions (Figure 7.7b and 7.7c), the initial slow evaporation of ethanol couldn't push the AgNWs to the surface of the elastomer. This occurred due to the increase in viscosity of the PDMS layer after 30

min at room temperature that is sufficient to withstand the lift force created by the fast evaporation of the residual ethanol during thermal curing. The viscosity of the freshly prepared PDMS was increased from 3.11 mPa.s to 3.54 mPa.s with the span of 30 min. Therefore, the printed wires remained at the bottom of the PDMS layer and became fully embedded into the cured PDMS film.

7.3.2 Alignment Process of the Embedded AgNWs. In addition to the advantage of direct printing and embedding AgNWs in the elastomer layer, this printing process aligns the AgNWs along the printing direction, which may lead to desirable electrical performance for stretchable electronics. In this study, the printed samples were soaked in cyclohexane to remove the liquid PDMS in order to examine the effect of the surrounding liquid PDMS on the alignment of AgNWs. As shown in Figure 7.8, the AgNWs are well-aligned along the printing direction. Figure 7.8a shows a schematic illustration of the formation mechanism of aligned AgNWs combined with a FIB-SEM cross-sectional image of a single pass printed AgNW line. Figure 7.8b and 7.8c are SEM images that clearly demonstrate the alignment of AgNWs along the printing direction for one and five printing passes, respectively. The coalescence of the jetted droplets was controlled by utilizing 50 μm in-line spacing and 25 μm shift among the printed passes. During the printing process, the jetted droplets coalesce with an overlap of $\sim 50\%$ to form connected lines, since the inflight diameter of the colloidal droplet is $\sim 100 \mu\text{m}$. As the ethanol solvent evaporates, the AgNWs are squeezed by the surrounding liquid PDMS. Such squeezing force can align the AgNWs to be lengthwise parallel to the printing direction. Single printing pass gives a line width of $\sim 10 \mu\text{m}$, where the alignment of the AgNWs can be seen in both at the center and the edge (Figure 7.8b). To the best of our knowledge, this is one of the smallest AgNW line width, obtained by printing methods as compared to work reported elsewhere.^{183,192,203,208,209} Three and five printing passes produced line widths of $\sim 40 \mu\text{m}$ and $60 \mu\text{m}$, respectively. However, the alignment of the printed

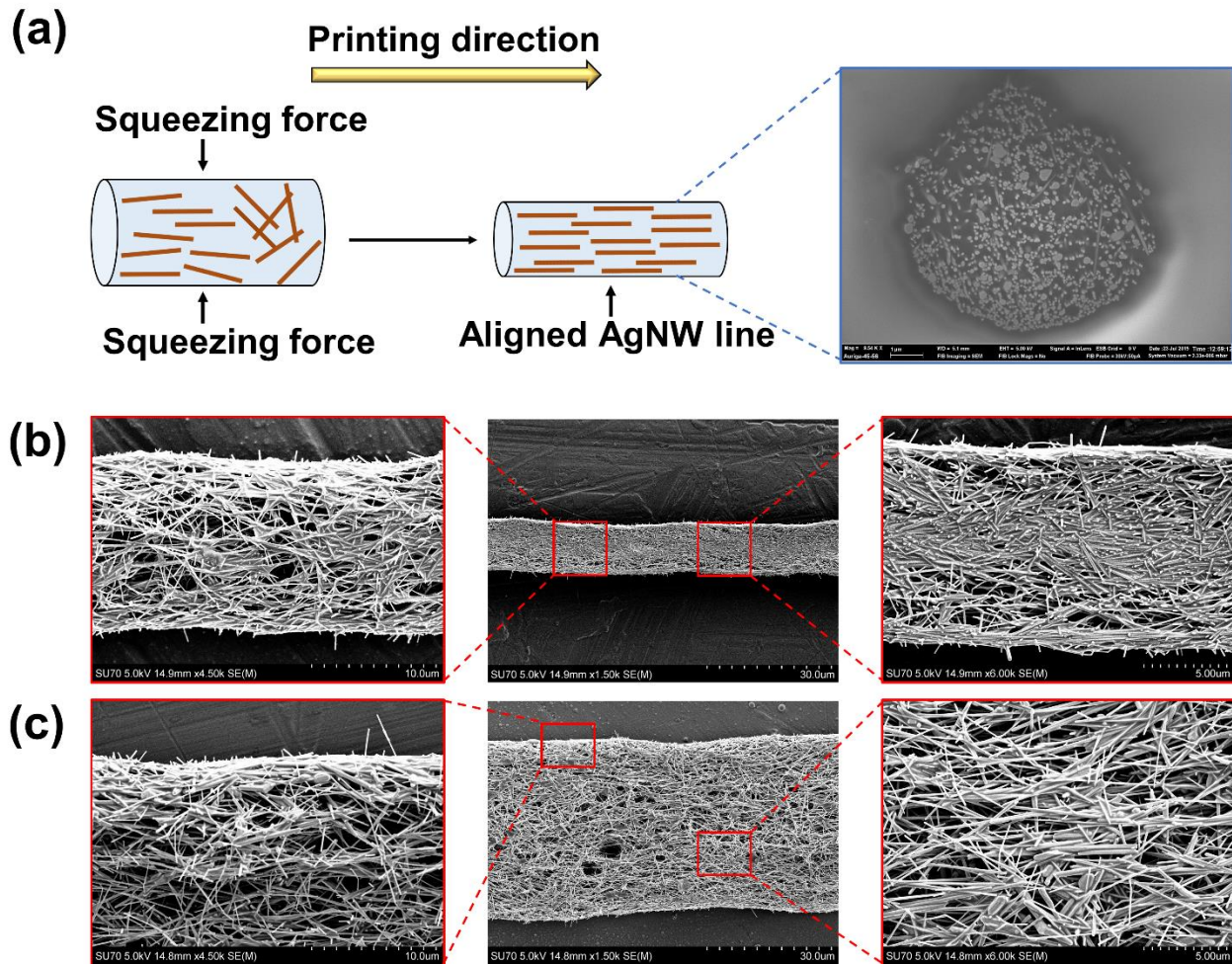


Figure 7.8: (a) Schematic illustration of the formation mechanism of aligned AgNWs and FIB-SEM cross-sectional image of an AgNW line printed with a single pass. (b) and (c) are SEM images of AgNW lines printed with one and five passes, respectively.

AgNWs decreases with multiple printing passes. The alignment effect can be explained as follows: for a single printing pass, relatively fewer AgNWs are printed. Thus, it is much easier to be squeezed by surrounded liquid PDMS. For three and five printing passes, much more AgNWs are deposited, therefore, it is more challenging to squeeze the AgNWs by the surrounding PDMS. Similarly, smaller printing nozzles may produce AgNW lines with even better alignment. Nevertheless, the alignment can still be clearly seen in the AgNWs with five passes as shown in Figure 7.8c. This alignment of AgNWs along the printing direction may enhance the electrical

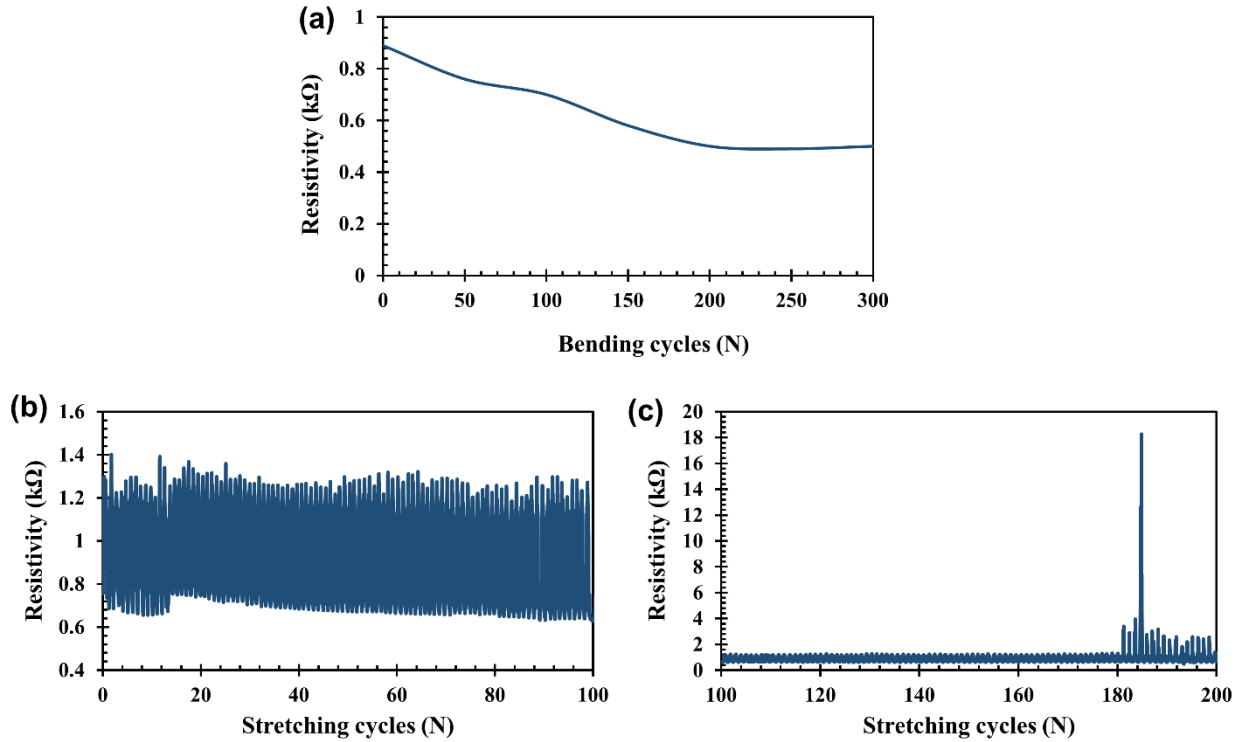


Figure 7.9: (a) Bending test of a sample with two AgNW lines printed with 5 printing passes. The line length is ~25 mm with initial resistance (R_0) of 0.88 kΩ. The bending radius is ~6 mm. (b) Resistance change of embedded AgNW lines during the first 100 stretching/releasing cycles, tested at 10% strain, and (c) is resistance change between 100 to 200 stretching/releasing cycles. The samples were composed of two AgNW lines printed with five passes.

performance during stretching-releasing cycles through increasing the wire-to-wire contact area.^{210,211}

7.3.3 Electrical Characterization of the Embedded AgNWs. In order to evaluate the electrical performance of the embedded AgNW lines, bending and stretching/releasing tests were carried out by a homemade stretcher in a direction parallel to the longitudinal axis of the printed samples. Samples with two printed AgNW lines, made of five printing passes, were used for these tests. After transferring the sample to the elastomer substrate, the sample edges were sputtered with gold and smeared with silver paste prior to the electrical resistance measurements. The initial resistance (R_0) of the fabricated sample is 0.88 kΩ with 25 mm line length. Figure 7.9a shows the change in resistance with respect to bending cycles. The bending radius used in this test is ~6 mm, which

makes a bending angle of $\sim 180^\circ$. Surprisingly, the resistance started to decrease after the first few bending cycles. After 50 bending cycles, the resistance dropped from $0.88 \text{ k}\Omega$ to $0.76 \text{ k}\Omega$, which represents a 13.6 % decrease of the initial resistance. This behavior could be attributed to the conditioning process of the AgNWs embedded into the elastomer, where the AgNWs may gradually align themselves to make better wire-to-wire contact due to the cyclic loading, especially for wires with no close packing assembly (Figure 7.8a). As a result, the resistance continued to decrease till reaching a plateau ($\sim 43.2\%$ of the initial resistance) at around 200 bending cycles. Beyond 300 cycles, the resistance measurements were not stable as the contact pads started to degrade. Nevertheless, the fabricated AgNW lines retained their integrity without any noticeable damage when examined under the light microscope. The fact that the embedded AgNW lines can survive hundreds of bending cycles indicates the significance of elastomer encapsulation despite their extremely small cross-sectional areas.

The same homemade stretcher was implemented to test the electrical performance of the printed samples during multiple stretching/releasing cycles. The samples were strained up to 10% then released to their initial position for 200 cycles at stretching rate of 0.2 mm/s as shown in Figure 7.9b and Figure 7.9c. It should be mentioned that initial resistance could vary slightly from one sample to another due to possible necking in the cross-sectional area of the printed wires. This behavior could be attributed to the possible missing jets as a result of implementing only one printing station to fabricate the stretchable conductors. For the stretching/releasing test, the resistance (R_0) of the fabricated sample increased during the 10% strain to $1.30 \text{ k}\Omega$ then returned to the initial value (i.e., $0.76 \text{ k}\Omega$) as demonstrated in Figure 7.9b. However, after the second stretching cycles, the resistance decreased from $0.76 \text{ k}\Omega$ to $0.68 \text{ k}\Omega$, which corresponds to 10.5% decrease of the initial resistance (R_0). After 90 stretching/releasing cycles, the resistance became

stable, reaching a value of 0.63 k Ω , which represents a 17.1 % decrease in resistance. The sample retained this stable resistance value till 180 stretching/releasing cycles, after which some high peaks were observed as a result of degrading the contact pads (Figure 7.9c). This stable resistance of our fabricated stretchable conductors could be attributed to the well-aligned AgNWs along the printing direction (i.e., the direction of the stretching/releasing test) in addition to the benefit of the PDMS encapsulation that significantly enhanced the AgNW recovery upon releasing the strain. This makes this approach a promising venue for fabricating stretchable electronic applications such as stretchable sensors.

7.3.4 Discussion. Direct inkjet printing and embedding of AgNWs into elastomer provides a facile approach to fabricate flexible and stretchable conductors. Different from printing of conductive inks on solid substrates, where the resolution of printed features is affected by substrate wettability and surface tension of the ink, in this study, the shaping effect by the surrounding PDMS improves the printing resolution through generating lines with circular cross-sections. As a result, it can produce conductors with tens of microns in diameter (or even smaller depending on the size of the printing nozzle). Compared with the conventional pattern-and-transfer methods, this approach eliminates the transferring step by direct patterning the conductive materials inside the stretchable elastomer, which significantly reduces the fabrication cost, especially in manufacturing settings. Another advantage is the enhanced adhesion between the conductive materials and the elastomer layer. The fabricated devices from our previous work and many others have suffered the poor mechanical robustness of AgNWs transferred or deposited onto elastomer substrates, where the AgNWs buckled up after cyclic stretching/releasing.^{183,190} Wrinkles and cracks developed at the surface of the elastomers and the AgNWs/elastomer composites drastically affected the resistance of the printed patterns. By embedding the AgNWs directly into the elastomer, the

mechanical robustness and integrity of the printed patterns have been significantly enhanced. Unlike the previously reported work of direct embedment of silver nanoparticles in elastomers to produce conductive microconductors,¹⁸⁷ this work employed AgNWs, which enables desirable stretchability of the printed conductors. The AgNWs align along the printing direction by virtue of the isotropically continuous compression, exerted by the surrounding liquid PDMS on the AgNW assembly as the solvent gradually evaporates. In addition, tuning the elastomer layer thickness and targeting the right supporting substrates facilitate droplet coalescence and line formation through anchoring the printed patterns in vicinity of the supporting substrate during solvent evaporation.

On the other hand, there are areas to be improved in this direct printing and embedding process. The conductivity in the embedded AgNW lines is relatively lower than those obtained by the pattern-and-transfer methods, because in the latter, sintering or local melting have often been implemented before transferring onto the elastomer substrates to reduce the contact resistance between the conductive wires. Future efforts will be made to improve the conductivity of the printed AgNW conductors, e.g., sintering of the embedded AgNWs by surface plasma resonance. In addition, the printed lines with multiple passes also reduce the conductivity, likely due to insufficient “squeezing” or shaping to assemble and align a large amount of AgNWs into a line. From this aspect, reducing the nozzle size has a potential to enhance the AgNW alignment and conductivity, in addition to a better printing resolution.

7.4 Conclusion

In summary, we have demonstrated the ability to fabricate stretchable conductors by inkjet printing of AgNWs into elastomer substrate in a single step. Colloidal suspension of AgNWs dispersed in

ethanol was directly printed into a liquid PDMS layer, supported by a PET substrate. The morphology of the embedded AgNW lines were dictated by the thickness of the liquid PDMS layer, the substrate underneath the PDMS layer, and the post-printing treatment of the printed lines. Well-connected uniform lines were obtained for PDMS thickness close to 100 μm , where the AgNWs were anchored and assembled in vicinity of the supporting substrate due to the droplet-substrate interactions. For thick PDMS layers, the jetted droplets didn't reach the bottom of the PDMS layer and the penetration depth of the printed lines varied depending on the amount of ink materials present inside the liquid PDMS. In this particular case, the assembly process of the AgNW lines undergone two stages, which are defined by the assembly stage (droplet coalescence and line formation) and the upward migration of AgNWs due to solvent evaporation. This, in turn, easily resulted in broken lines as a result of this multistep process. For PDMS film thickness much less than 100 μm , the jetted droplets coalesced at the surface of the PDMS layer since the jetted colloidal droplet formed a spherical cap above the surface of the PDMS. When the jetted droplets coalesce and form lines with the assistance of the supporting substrate, the shaping effect of the surrounding PDMS layer generates fully-embedded lines with aligned AgNWs, which not only enhanced the mechanical robustness and integrity of the printed AgNW conductors but also improved their electrical performance during various bending and stretching/releasing cycles. This makes the direct embedment of AgNWs in elastomers by inkjet printing a promising venue for engineering flexible and stretchable conductors.

CHAPTER 8 Concluding Remarks

8.1 Review of the Results and Conclusions

The main objective of this study is to comprehend the material interactions and self-assembly in inkjet printing applications. The direct effect of liquid processing on fabrication and performance of the functional devices was profoundly investigated at different length scales. The findings of this study suggest that adjusting the multibody interactions (i.e., particle-particle, particle-substrate, particle-interface interactions) is critical to control the deposition morphology and printing resolution. In conventional inkjet printing process, where sessile droplets are directly printed on substrates, particle depositions are usually associated with the well-known, undesirable CRE due to the high solvent evaporation rate at the edges of the printed droplets. Such particle accumulation phenomenon in vicinity of the TCL of sessile droplets significantly sabotages the printing resolution and device functionality. In order to investigate the effect of the multibody interactions on particle deposition morphology after solvent evaporation, the dual-droplet inkjet printing of colloidal particles was implemented to specifically examine the self-assembly of colloidal nanoparticles at the air-liquid interface and the particle accumulation at the TCL. This was achieved by jetting wetting droplets, containing colloidal nanoparticles dispersed in solvents with high vapor pressure, over supporting droplets composed of water only. By tuning the surface tensions and controlling the jetting parameters of the jetted droplets, monolayers with closely-packed deposition of colloidal nanoparticles were demonstrated. The multibody interactions (i.e., particle-particle, particle-interface, and particle substrate interactions) were tuned by pH modulation of the supporting droplets to control particle deposition morphology. The final structure of the particle assembly was determined by the particles' affinity to water (type of functional groups and density), charge level of the PS particles (zeta potential), and the pH of the

supporting droplet. High quality of closely-packed, nearly monolayer of nanoparticles with minimal particle accumulation at the TCL were generated by setting a mutual repulsion between the particles at the interface and the substrate. These monolayer optical films exhibited different structural colors depending on the nanoparticle sizes, which is of huge interest in fabricating optical and electronic devices.

In addition, another preventative solution to the CRE is proposed in this study such applying magnetic field to direct the self-assembly of colloidal particles. The magnetic-field assisted inkjet printing process was implanted to form 1D chain structures of magnetic particles with suppressed CRE on porous substrates. Unlike the conventional evaporative particle-laden droplets, the particle deposition morphology in this study is determined by solvent imbibition, particle chaining, and particle transport under the magnetophoretic effect. The printed films exhibited anisotropic magnetic response to the applied magnetic field due to the 1D assembly structure, which holds a great potential in many engineering applications.

Finally, fabrication of functional devices such as stretchable conductors has been also demonstrated by inkjet printing of AgNWs into elastomer substrate, where the viscous liquid elastomer layer shaped the printed silver wire lines into tens of micrometers in diameter, and aligned the silver nanowires along the printing direction, resulting in wires with good mechanical stability and electrical performance. The printing techniques and the outcomes presented in this study can be harnessed in engineering and manufacturing a wide range of technological applications ranging from high-performance optical and electronic devices to stretchable conductors and sensors.

8.2 Key Differences Between Conventional and Dual-Droplet Inkjet Printing

Solvent contact line pinning of evaporative sessile droplets is an intricate process, which is usually determined by the substrate wetting property through introducing surface roughness or chemical heterogeneities. The solvent contact line pinning is crucial in inkjet printing applications. The initial solvent pinning on substrates could be enhanced by introducing suspended particles to anchor the contact line, which significantly influence the printing morphology, resolution, and functionality. In conventional inkjet printing, where sessile particle-laden droplets are directly deposited on substrates, the colloidal particles are driven to the TCL by virtue of the capillary flow, resulting in a ring-like particle deposition. Even though there are scarce number of studies that reported the feasibility of exploiting the CRE in some applications such as particle separation and disease detection, such phenomenon is deemed detrimental and must be avoided in many technological applications such as producing coatings and patterns with mono or multilayers of closely-packed particles, fabricating functional microarrays, and detecting biomolecules by various spectroscopy techniques. Although considerable efforts have been devoted to counteract the colloidal particles' migration to the contact lines by means of, controlling the drying conditions of solvents (e.g., substrate temperature, relative humidity, and volatile solvents), modifying particle shapes, changing solvent density and viscosity, adjusting substrate wettability, initiating acoustic field, and exerting electrowetting, these proposed preventative solutions have failed in producing closely-packed, monolayer of particles.

Different from the conventional inkjet printing, the dual-droplet inkjet printing offers an alternative concept for self-assembly and particle pinning at the TCL. Deposition of monolayer nanoparticle films is achieved by consecutive dual-droplet printing of supporting droplets and wetting droplets. The colloidal particles spread over the supporting droplet surface and assemble at the interface as

the solvent dries to produce a uniform, nearly monolayer deposition of the nanoparticles. Three main steps take place toward the monolayer self-assembly: (i) spreading of the wetting droplet and colloidal nanoparticles over the supporting droplet; (ii) nanoparticle packing and assembly at the interface between the wetting droplet and supporting droplet; and (iii) settling of nanoparticle film layer onto the substrate upon evaporation of the supporting droplet. Once the colloidal particles arrive at the air-liquid interface and reach the substrate, the particle-substrate interactions cause the contact line to pin. This particle pinning mechanism from air-liquid interface is insensitive to the receding contact angle unlike the conventional contact line pinning of sessile droplets. Such pinning process is highly dependent on particle concentration and particle size based on the premise that the particles successfully self-assemble into floating networks at the interface. Therefore, the capillary forces, initiated by solvent evaporation of the supporting droplet, is not sufficient to buckle or rupture the monolayer particle network formed at the air-liquid interface. In addition, the contact line pinning in case of the dual-droplet inkjet printing is achieved at much lower particle concentration compared to that of drying of colloidal sessile droplets, which highlights the significance of this novel printing technique.

8.3 Future Works

The self-assembly of colloidal particles has been widely recognized as a viable approach to generate a variety of nanostructures. It also holds a great potential to be implemented in many engineering disciplines at different length scales. In spite of the considerable advances, particle interfacial assembly in evaporating sessile droplets is still in its early stages. Future works of experimental, theoretical, and computational investigations should be conducted to promote a thorough understanding of the mechanisms behind the resultant particle assembly and deposition,

e.g., particle transport to the interface, assembly at the interface, two-way interactions between evaporation and assembled structures, packing order of the final assembled structures, etc. Specifically, future directions in this field will likely include: (i) particle transport to the interface, especially when droplet size reduces and so does evaporation time; (ii) comprehensive understanding of the kinetics of cluster nucleation at the interface, cluster growth and compression of the assembled clusters/films on the interface during solvent evaporation, and the effect of interfacial hydrodynamic flow on the assembled structure; (iii) interfacial assembly of anisotropic particles (shape anisotropy, e.g., nanowires and nanosheets; composition anisotropy, e.g., Janus particles) and binary particles in an evaporating droplet; (iv) factors and mechanisms affecting the packing order and density of the final assembled structure; and (v) further exploration of potential applications. The well-ordered monolayer deposition enabled by particle interfacial assembly in evaporating droplets is a promising venue that holds great potential in fabrication of functional coatings, optical and electronics devices.

References

- (1) Derby, B. Inkjet Printing of Functional and Structural Materials: Fluid Property Requirements, Feature Stability, and Resolution. *Annu. Rev. Mater. Res.* **2010**, *40*, 395–414.
- (2) Singh, M.; Haverinen, H. M.; Dhagat, P.; Jabbour, G. E. Inkjet Printing-Process and Its Applications. *Adv. Mater.* **2010**, *22*, 673-685.
- (3) Wood, V.; Panzer, M. J.; Chen, J.; Bradley, M. S.; Halpert, J. E.; Bawendi, M. C.; Bulovi, V. Inkjet-Printed Quantum Dot-Polymer Composites for Full-Color AC-Driven Displays. *Adv. Mater.* **2009**, *21*, 2151-2155.
- (4) Jang, J.; Ha, J.; Cho, J. Fabrication of Water-Dispersible Polyaniline-Poly(4-Styrenesulfonate) Nanoparticles for Inkjet-Printed Chemical-Sensor Applications. *Adv. Mater.* **2007**, *19*, 1772-1775.
- (5) Krebs, F. C. Fabrication and Processing of Polymer Solar Cells: A Review of Printing and Coating Techniques. *Solar Energy Materials and Solar Cells.* **2009**, *93*, 394-412.
- (6) Sekitani, T.; Noguchi, Y.; Zschieschang, U.; Klauk, H.; Someya, T. Organic Transistors Manufactured Using Inkjet Technology with Subfemtoliter Accuracy. *Proc. Natl. Acad. Sci.* **2008**, *105*, 4976-4980.
- (7) Kang, B.; Lee, W. H.; Cho, K. Recent Advances in Organic Transistor Printing Processes. *ACS Appl. Mater. Interfaces* **2013**, *5*, 2302-2315.
- (8) Zhan, Z.; An, J.; Wei, Y.; Tran, V. T.; Du, H. Inkjet-Printed Optoelectronics. *Nanoscale* **2017**, *9*, 965-993.

- (9) Sun, J.; Bao, B.; He, M.; Zhou, H.; Song, Y. Recent Advances in Controlling the Depositing Morphologies of Inkjet Droplets. *ACS Appl. Mater. Interfaces* **2015**, *7*, 28086–28099.
- (10) De Gans, B. J.; Duineveld, P. C.; Schubert, U. S. Inkjet Printing of Polymers: State of the Art and Future Developments. *Adv. Mater.* **2004**, *16*, 203-213.
- (11) Parsa, M.; Harmand, S.; Sefiane, K.; Biggerelle, M.; Deltombe, R. Effect of Substrate Temperature on Pattern Formation of Nanoparticles from Volatile Drops. *Langmuir* **2015**, *31*, 3354–3367.
- (12) Li, Y. F.; Sheng, Y. J.; Tsao, H. K. Evaporation Stains: Suppressing the Coffee-Ring Effect by Contact Angle Hysteresis. *Langmuir* **2013**, *29*, 7802–7811.
- (13) Christy, J. R. E.; Hamamoto, Y.; Sefiane, K. Flow Transition within an Evaporating Binary Mixture Sessile Drop. *Phys. Rev. Lett.* **2011**, *106*, 205701.
- (14) Bourgès-Monnier, C.; Shanahan, M. E. R. Influence of Evaporation on Contact Angle. *Langmuir* **1995**, *11*, 2820-2829.
- (15) Chhasatia, V. H.; Joshi, A. S.; Sun, Y. Effect of Relative Humidity on Contact Angle and Particle Deposition Morphology of an Evaporating Colloidal Drop. *Appl. Phys. Lett.* **2010**, *97*, 231909.
- (16) Shen, X.; Ho, C. M.; Wong, T. S. Minimal Size of Coffee Ring Structure. *J. Phys. Chem. B* **2010**, *114*, 5269–5274.
- (17) Lin, S. Y.; Yang, K. C.; Chen, L. J. Effect of Surface Hydrophobicity on Critical Pinning Concentration of Nanoparticles to Trigger the Coffee Ring Formation during the

- Evaporation Process of Sessile Drops of Nanofluids. *J. Phys. Chem. C*. **2015**, *119* (6), 3050–3059.
- (18) Calvert, P. Inkjet Printing for Materials and Devices. *Chem. Mater.* **2001**, *13*, 3299-3305.
- (19) Derby, B.; Reis, N. Inkjet Printing of Highly Loaded Particulate Suspensions. *MRS Bulletin* **2003**, *28*, 815-818.
- (20) Batchelor, G. K. An Introduction to Fluid Dynamics. Book. *Cambridge university press* **2000**.
- (21) Torrisi, F.; Hasan, T.; Wu, W.; Sun, Z.; Lombardo, A.; Kulmala, T. S.; Hsieh, G. W.; Jung, S.; Bonaccorso, F.; Paul, P. J.; et al. Inkjet-Printed Graphene Electronics. *ACS Nano*. **2012**, *6*, 2992-3006.
- (22) Martin, G. D.; Hoath, S. D.; Hutchings, I. M. Inkjet Printing - The Physics of Manipulating Liquid Jets and Drops. *J. Phys. Conf. Ser.* **2008**, *105*, 012001.
- (23) Shin, P.; Sung, J.; Lee, M. H. Control of Droplet Formation for Low Viscosity Fluid by Double Waveforms Applied to a Piezoelectric Inkjet Nozzle. *Microelectron. Reliab.* **2011**, *51*, 797-804.
- (24) Jung, S.; Hutchings, I. M. The Impact and Spreading of a Small Liquid Drop on a Non-Porous Substrate over an Extended Time Scale. *Soft Matter*. **2012**, *8*, 2686-2696.
- (25) Van Osch, T. H. J.; Perelaer, J.; De Laat, A. W. M.; Schubert, U. S. Inkjet Printing of Narrow Conductive Tracks on Untreated Polymeric Substrates. *Adv. Mater.* **2008**, *20*, 343-345.
- (26) He, P.; Derby, B. Inkjet Printing Ultra-Large Graphene Oxide Flakes. *2D Mater.* **2017**, *4*,

021021.

- (27) Nicolas, M. Spreading of a Drop of Neutrally Buoyant Suspension. *J. Fluid Mech.* **2005**, *545*, 271-280.
- (28) Law, K. Y.; Zhao, H. *Surface Wetting: Characterization, Contact Angle, and Fundamentals*. Book. Springer **2016**.
- (29) Singh, S. K.; Dandapat, B. S. Spreading of a Non-Newtonian Liquid Drop over a Homogeneous Rough Surface. *Colloids Surfaces A Physicochem. Eng. Asp.* **2013**, *419*, 228-232.
- (30) Duineveld, P. C. The Stability of Ink-Jet Printed Lines of Liquid with Zero Receding Contact Angle on a Homogeneous Substrate. *J. Fluid Mech.* **2003**, *477*, 175-200.
- (31) Soltman, D.; Subramanian, V. Inkjet-Printed Line Morphologies and Temperature Control of the Coffee Ring Effect. *Langmuir* **2008**, *24*, 2224–2231.
- (32) Liu, M.; Wang, J.; He, M.; Wang, L.; Li, F.; Jiang, L.; Song, Y. Inkjet Printing Controllable Footprint Lines by Regulating the Dynamic Wettability of Coalescing Ink Droplets. *ACS Appl. Mater. Interfaces* **2014**, *6*, 13344–13348.
- (33) Deegan, R. D. Pattern Formation in Drying Drops. *Phys. Rev. E* **2000**, *61*, 475–485.
- (34) Deegan, R. D.; Bakajin, O.; Dupont, T. F.; Huber, G.; Nagel, S. R.; Witten, T. A. Capillary Flow as the Cause of Ring Stains from Dried Liquid Drops. *Nature* **1997**, *389*, 827–829.
- (35) Majumder, M.; Rendall, C. S.; Eukel, J. A.; Wang, J. Y. L.; Behabtu, N.; Pint, C. L.; Liu, T. Y.; Orbaek, A. W.; Mirri, F.; Nam, J.; et al. Overcoming the “Coffee-Stain” Effect by

- Compositional Marangoni-Flow-Assisted Drop-Drying. *J. Phys. Chem. B* **2012**, *116*, 6536–6542.
- (36) Dugyala, V. R.; Basavaraj, M. G. Control over Coffee-Ring Formation in Evaporating Liquid Drops Containing Ellipsoids. *Langmuir* **2014**, *30*, 8680–8686.
- (37) Yunker, P. J.; Still, T.; Lohr, M. A.; Yodh, A. G. Suppression of the Coffee-Ring Effect by Shape-Dependent Capillary Interactions. *Nature* **2011**, *476*, 308–311.
- (38) Das, S.; Dey, A.; Reddy, G.; Sarma, D. D. Suppression of Coffee-Ring Effect: Evaporation Driven Disorder to Order Transition in Colloidal Droplets. *J. Phys. Chem. Lett.* **2017**, *8*, 4704–4709.
- (39) Zhou, C.; Han, J.; Guo, R. A Facile Strategy to Colloidal Crystals by Drying Condensed Suspension Droplets. *J. Colloid Interface Sci.* **2013**, *397*, 80–87.
- (40) Sempels, W.; De Dier, R.; Mizuno, H.; Hofkens, J.; Vermant, J. Auto-Production of Biosurfactants Reverses the Coffee Ring Effect in a Bacterial System. *Nat. Commun.* **2013**, *4*, 1757.
- (41) Talbot, E. L.; Yow, H. N.; Yang, L.; Berson, A.; Biggs, S. R.; Bain, C. D. Printing Small Dots from Large Drops. *ACS Appl. Mater. Interfaces* **2015**, *7*, 3782–3790.
- (42) Marin, A.; Liepelt, R.; Rossi, M.; Kaehler, C. Surfactant-Driven Flow Transitions in Evaporating Droplets. *Soft Matter* **2016**, *12*, 1593–1600.
- (43) Kim, H.; Boulogne, F.; Um, E.; Jacobi, I.; Button, E.; Stone, H. A. Controlled Uniform Coating from the Interplay of Marangoni Flows and Surface-Adsorbed Macromolecules. *Phys. Rev. Lett.* **2016**, *116*, 124501.

- (44) Li, J.; Ye, F.; Vaziri, S.; Muhammed, M.; Lemme, M. C.; Östling, M. Efficient Inkjet Printing of Graphene. *Adv. Mater.* **2013**, *25*, 3985-3992.
- (45) Kim, T. Y.; Amani, M.; Ahn, G. H.; Song, Y.; Javey, A.; Chung, S.; Lee, T. Electrical Properties of Synthesized Large-Area MoS₂ Field-Effect Transistors Fabricated with Inkjet-Printed Contacts. *ACS Nano* **2016**, *10*, 2819–2826.
- (46) Nguyen, P. Q. M.; Yeo, L. P.; Lok, B. K.; Lam, Y. C. Patterned Surface with Controllable Wettability for Inkjet Printing of Flexible Printed Electronics. *ACS Appl. Mater. Interfaces* **2014**, *6*, 4011–4016.
- (47) Liu, L.; Ma, S.; Pei, Y.; Xiong, X.; Sivakumar, P.; Singler, T. J. Regulation of the Deposition Morphology of Inkjet-Printed Crystalline Materials via Polydopamine Functional Coatings for Highly Uniform and Electrically Conductive Patterns. *ACS Appl. Mater. Interfaces* **2016**, *8*, 21750–21761.
- (48) Finn, D. J.; Lotya, M.; Coleman, J. N. Inkjet Printing of Silver Nanowire Networks. *ACS Appl. Mater. Interfaces* **2015**, *7*, 9254-9261.
- (49) Wu, L.; Dong, Z.; Li, F.; Zhou, H.; Song, Y. Emerging Progress of Inkjet Technology in Printing Optical Materials. *Adv. Opt. Mater.* **2016**, *4*, 1915–1932.
- (50) Gençer, A.; Schütz, C.; Thielemans, W. Influence of the Particle Concentration and Marangoni Flow on the Formation of Cellulose Nanocrystal Films. *Langmuir* **2017**, *33*, 228–234.
- (51) Chen, R.; Zhang, L.; Zang, D.; Shen, W. Blood Drop Patterns: Formation and Applications. *Adv. Colloid Interface Sci.* **2016**, *231*, 1-14.

- (52) Yakhno, T. Salt-Induced Protein Phase Transitions in Drying Drops. *J. Colloid Interface Sci.* **2008**, *318*, 225-230.
- (53) Brutin, D.; Sobac, B.; Loquet, B.; Sampol, J. Pattern Formation in Drying Drops of Blood. *J. Fluid Mech.* **2011**, *667*, 85-95.
- (54) Mampallil, D.; Eral, H. B. A Review on Suppression and Utilization of the Coffee-Ring Effect. *Adv. Colloid Interface Sci.* **2018**, *252*, 38–54.
- (55) Parsa, M.; Harmand, S.; Sefiane, K. Mechanisms of Pattern Formation from Dried Sessile Drops. *Adv. Colloid Interface Sci.* **2018**, *254*, 22–47.
- (56) Anyfantakis, M.; Baigl, D. Manipulating the Coffee-Ring Effect: Interactions at Work. *ChemPhysChem* **2015**, *16*, 2726–2734.
- (57) Deegan, R. D.; Bakajin, O.; Dupont, T. F.; Huber, G.; Nagel, S. R.; Witten, T. A. Contact Line Deposits in an Evaporating Drop. *Phys. Rev. E* **2000**, *62*, 756.
- (58) Han, W.; Lin, Z. Learning from “Coffee Rings”: Ordered Structures Enabled by Controlled Evaporative Self-Assembly. *Angew. Chem. Int. Ed.* **2012**, *51*, 1534-1546.
- (59) Dugyala, V. R.; Basavaraj, M. G. Evaporation of Sessile Drops Containing Colloidal Rods: Coffee-Ring and Order-Disorder Transition. *J. Phys. Chem. B* **2015**, *119*, 3860–3867.
- (60) Davidson, Z. S.; Huang, Y.; Gross, A.; Martinez, A.; Still, T.; Zhou, C.; Collings, P. J.; Kamien, R. D.; Yodh, A. G. Deposition and Drying Dynamics of Liquid Crystal Droplets. *Nat. Commun.* **2017**, *8*, 15642.
- (61) Mampallil, D.; Reboud, J.; Wilson, R.; Wylie, D.; Klug, D. R.; Cooper, J. M. Acoustic

- Suppression of the Coffee-Ring Effect. *Soft Matter* **2015**, *11*, 7207-7213.
- (62) Eral, H. B.; Augustine, D. M.; Duits, M. H. G.; Mugele, F. Suppressing the Coffee Stain Effect: How to Control Colloidal Self-Assembly in Evaporating Drops Using Electrowetting. *Soft Matter* **2011**, *7*, 4954-4958.
- (63) Wong, T. S.; Chen, T. H.; Shen, X.; Ho, C. M. Nanochromatography Driven by the Coffee Ring Effect. *Anal. Chem.* **2011**, *83*, 1871–1873.
- (64) Noguera-Marín, D.; Moraila-Martínez, C. L.; Cabrerizo-Vílchez, M. A.; Rodríguez-Valverde, M. A. Particle Segregation at Contact Lines of Evaporating Colloidal Drops: Influence of the Substrate Wettability and Particle Charge-Mass Ratio. *Langmuir* **2015**, *31*, 6632-6638.
- (65) Monteux, C.; Lequeux, F. Packing and Sorting Colloids at the Contact Line of a Drying Drop. *Langmuir* **2011**, *27*, 2917-2922.
- (66) Wen, J. T.; Ho, C. M.; Lillehoj, P. B. Coffee Ring Aptasensor for Rapid Protein Detection. *Langmuir* **2013**, *29*, 8440-8446.
- (67) Gulka, C. P.; Swartz, J. D.; Trantum, J. R.; Davis, K. M.; Peak, C. M.; Denton, A. J.; Haselton, F. R.; Wright, D. W. Coffee Rings as Low-Resource Diagnostics: Detection of the Malaria Biomarker Plasmodium Falciparum Histidine-Rich Protein-II Using a Surface-Coupled Ring of Ni(II)NTA Gold-Plated Polystyrene Particles. *ACS Appl. Mater. Interfaces* **2014**, *6*, 6257–6263.
- (68) Tekin, E.; Smith, P. J.; Schubert, U. S. Inkjet Printing as a Deposition and Patterning Tool for Polymers and Inorganic Particles. *Soft Matter* **2008**, *4*, 703-713.

- (69) Ooi, Y.; Hanasaki, I.; Mizumura, D.; Matsuda, Y. Suppressing the Coffee-Ring Effect of Colloidal Droplets by Dispersed Cellulose Nanofibers. *Sci. Technol. Adv. Mater.* **2017**, *18*, 316–324.
- (70) Ding, Y.; Ling, J.; Qiao, Y.; Li, Z.; Sun, Z.; Cai, J.; Guo, Y.; Wang, H. A High-Throughput Fluorimetric Microarray with Enhanced Fluorescence and Suppressed “Coffee-Ring” Effects for the Detection of Calcium Ions in Blood. *Sci. Rep.* **2016**, *6*, 38602.
- (71) Yen, T. M.; Fu, X.; Wei, T.; Nayak, R. U.; Shi, Y.; Lo, Y.-H. Reversing Coffee-Ring Effect by Laser-Induced Differential Evaporation. *Sci. Rep.* **2018**, *8*, 3157.
- (72) Li, S.; Dong, M.; Li, R.; Zhang, L.; Qiao, Y.; Jiang, Y.; Qi, W.; Wang, H. A Fluorometric Microarray with ZnO Substrate-Enhanced Fluorescence and Suppressed “Coffee-Ring” Effects for Fluorescence Immunoassays. *Nanoscale* **2015**, *7*, 18453-18458.
- (73) Baker, M. J.; Hussain, S. R.; Lovergne, L.; Untereiner, V.; Hughes, C.; Lukaszewski, R. A.; Thiéfin, G.; Sockalingum, G. D. Developing and Understanding Biofluid Vibrational Spectroscopy: A Critical Review. *Chem. Soc. Rev.* **2016**, *45*, 1803-1818.
- (74) Lai, Y. H.; Cai, Y. H.; Lee, H.; Ou, Y. M.; Hsiao, C. H.; Tsao, C. W.; Chang, H. T.; Wang, Y. S. Reducing Spatial Heterogeneity of MALDI Samples with Marangoni Flows During Sample Preparation. *J. Am. Soc. Mass Spectrom.* **2016**, *27*, 1314-1321.
- (75) Yan, Q.; Gao, L.; Sharma, V.; Chiang, Y. M.; Wong, C. C. Particle and Substrate Charge Effects on Colloidal Self-Assembly in a Sessile Drop. *Langmuir* **2008**, *24*, 11518–11522.
- (76) Bhardwaj, R.; Fang, X.; Somasundaran, P.; Attinger, D. Self-Assembly of Colloidal

- Particles from Evaporating Droplets: Role of DLVO Interactions and Proposition of a Phase Diagram. *Langmuir* **2010**, *26*, 7833–7842.
- (77) Devineau, S.; Anyfantakis, M.; Marichal, L.; Kiger, L.; Morel, M.; Rudiuk, S.; Baigl, D. Protein Adsorption and Reorganization on Nanoparticles Probed by the Coffee-Ring Effect: Application to Single Point Mutation Detection. *J. Am. Chem. Soc.* **2016**, *138*, 11623–11632.
- (78) Anyfantakis, M.; Baigl, D.; Binks, B. P. Evaporation of Drops Containing Silica Nanoparticles of Varying Hydrophobicities: Exploiting Particle-Particle Interactions for Additive-Free Tunable Deposit Morphology. *Langmuir* **2017**, *33*, 5025–5036.
- (79) Ma, H.; Hao, J. Ordered Patterns and Structures via Interfacial Self-Assembly: Superlattices, Honeycomb Structures and Coffee Rings. *Chem. Soc. Rev.* **2011**, *40*, 5457-5471.
- (80) Hou, J.; Li, M.; Song, Y. Patterned Colloidal Photonic Crystals. *Angew. Chemie Int. Ed.* **2017**, *57*, 2544–2553.
- (81) Lotito, V.; Zambelli, T. Approaches to Self-Assembly of Colloidal Monolayers: A Guide for Nanotechnologists. *Adv. Colloid Interface Sci.* **2017**, *246*, 217–274.
- (82) Kralchevsky, P. A.; Nagayama, K. Capillary Interactions between Particles Bound to Interfaces, Liquid Films and Biomembranes. *Adv. Colloid Interface Sci.* **2000**, *85*, 145-192.
- (83) Kralchevsky, P. A.; Denkov, N. D. Capillary Forces and Structuring in Layers of Colloid Particles. *Curr. Opin. Colloid Interface Sci.* **2001**, *6*, 383-401.

- (84) Loudet, J. C.; Alsayed, A. M.; Zhang, J.; Yodh, A. G. Capillary Interactions between Anisotropic Colloidal Particles. *Phys. Rev. Lett.* **2005**, *94*, 018301.
- (85) McGorty, R.; Fung, J.; Kaz, D.; Manoharan, V. N. Colloidal Self-Assembly at an Interface. *Mater. Today* **2010**, *13*, 34–42.
- (86) Loudet, J. C.; Yodh, A. G.; Pouligny, B. Wetting and Contact Lines of Micrometer-Sized Ellipsoids. *Phys. Rev. Lett.* **2006**, *97*, 018304.
- (87) Park, B. J.; Furst, E. M. Attractive Interactions between Colloids at the Oil-Water Interface. *Soft Matter* **2011**, *7*, 7676-7682.
- (88) Zeng, C.; Brau, F.; Davidovitch, B.; Dinsmore, A. D. Capillary Interactions among Spherical Particles at Curved Liquid Interfaces. *Soft Matter* **2012**, *8*, 8582-8594.
- (89) Bigioni, T. P.; Lin, X.-M.; Nguyen, T. T.; Corwin, E. I.; Witten, T. A.; Jaeger, H. M. Kinetically Driven Self Assembly of Highly Ordered Nanoparticle Monolayers. *Nat. Mater.* **2006**, *5*, 265–270.
- (90) Boley, J. W.; Hyun, S. H.; White, E. L.; Thompson, D. H.; Kramer, R. K. Hybrid Self-Assembly during Evaporation Enables Drop-on-Demand Thin Film Devices. *ACS Appl. Mater. Interfaces* **2016**, *8*, 34171–34178.
- (91) Anyfantakis, M.; Geng, Z.; Morel, M.; Rudiuk, S.; Baigl, D. Modulation of the Coffee-Ring Effect in Particle/Surfactant Mixtures: The Importance of Particle-Interface Interactions. *Langmuir* **2015**, *31*, 4113–4120.
- (92) Zhang, H.; Wang, W.; Hagen, N.; Kuzmenko, I.; Akinc, M.; Travesset, A.; Mallapragada, S.; Vaknin, D. Self-Assembly of DNA Functionalized Gold Nanoparticles at the Liquid-

- Vapor Interface. *Adv. Mater. Interfaces* **2016**, *3*, 1600180.
- (93) Zhang, H.; Nayak, S.; Wang, W.; Mallapragada, S.; Vaknin, D. Interfacial Self-Assembly of Polyelectrolyte-Capped Gold Nanoparticles. *Langmuir* **2017**, *33*, 12227–12234.
- (94) Anyfantakis, M.; Vialetto, J.; Best, A.; Auernhammer, G. K.; Butt, H.-J.; Binks, B. P.; Baigl, D. Adsorption and Crystallization of Particles at the Air–Water Interface Induced by Minute Amounts of Surfactant. *Langmuir* **2018**, *34*, 15526–15536.
- (95) Li, Y.; Yang, Q.; Li, M.; Song, Y. Rate-Dependent Interface Capture beyond the Coffee-Ring Effect. *Sci. Rep.* **2016**, *6*, 24628.
- (96) Kim, D. O.; Pack, M.; Hu, H.; Kim, H.; Sun, Y. Deposition of Colloidal Drops Containing Ellipsoidal Particles: Competition between Capillary and Hydrodynamic Forces. *Langmuir* **2016**, *32*, 11899–11906.
- (97) Fischer, B. J. Particle Convection in an Evaporating Colloidal Droplet. *Langmuir* **2002**, *18*, 60-67.
- (98) Larson, R. G. Transport and Deposition Patterns in Drying Sessile Droplets. *AIChE J.* **2014**, *60*, 1538-1571.
- (99) Patil, N. D.; Bange, P. G.; Bhardwaj, R.; Sharma, A. Effects of Substrate Heating and Wettability on Evaporation Dynamics and Deposition Patterns for a Sessile Water Droplet Containing Colloidal Particles. *Langmuir* **2016**, *32*, 11958-11972.
- (100) He, P.; Derby, B. Controlling Coffee Ring Formation during Drying of Inkjet Printed 2D Inks. *Adv. Mater. Interfaces* **2017**, *4*, 1700944.
- (101) Kuang, M.; Wang, J.; Bao, B.; Li, F.; Wang, L.; Jiang, L.; Song, Y. Inkjet Printing

- Patterned Photonic Crystal Domes for Wide Viewing-Angle Displays by Controlling the Sliding Three Phase Contact Line. *Adv. Opt. Mater.* **2014**, *2*, 34-38.
- (102) Park, J.; Moon, J. Control of Colloidal Particle Deposit Patterns within Picoliter Droplets Ejected by Ink-Jet Printing. *Langmuir* **2006**, *22*, 3506-3513.
- (103) Still, T.; Yunker, P. J.; Yodh, A. G. Surfactant-Induced Marangoni Eddies Alter the Coffee-Rings of Evaporating Colloidal Drops. *Langmuir* **2012**, *28*, 4984-4988.
- (104) Minemawari, H.; Yamada, T.; Matsui, H.; Tsutsumi, J. Y.; Haas, S.; Chiba, R.; Kumai, R.; Hasegawa, T. Inkjet Printing of Single-Crystal Films. *Nature* **2011**, *475*, 364.
- (105) Noda, Y.; Minemawari, H.; Matsui, H.; Yamada, T.; Arai, S.; Kajiya, T.; Doi, M.; Hasegawa, T. Underlying Mechanism of Inkjet Printing of Uniform Organic Semiconductor Films Through Antisolvent Crystallization. *Adv. Funct. Mater.* **2015**, *25*, 4022-4031.
- (106) Vazquez, G.; Alvarez, E.; Navaza, J. M. Surface Tension of Alcohol + Water from 20 to 50 °C. *J. Chem. Eng. Data* **1995**, *40*, 611-614.
- (107) Al-Milaji, K. N.; Ray, Secondo, R.; Nga, N. T.; Nathaniel, K.; Hong, Z. Interfacial Self-Assembly of Colloidal Nanoparticles in Dual-Droplet Inkjet Printing. *Adv. Mater. Interfaces* **2018**, *5*, 1701561.
- (108) Lin, Y.; Skaff, H.; Emrick, T.; Dinsmore, A. D.; Russell, T. P. Nanoparticle Assembly and Transport at Liquid-Liquid Interfaces. *Science* **2003**, *299*, 226-229.
- (109) Fang, X.; Li, B.; Wu, J.; Maldarelli, C.; Sokolov, J. C.; Rafailovich, M. H.; Somasundaran, P. Imaging and Estimating the Surface Heterogeneity on a Droplet

- Containing Cosolvents. *J. Phys. Chem. B* **2009**, *113*, 9636-9639.
- (110) Su, L.; Yu, Y.; Zhao, Y.; Liang, F.; Zhang, X. Strong Antibacterial Polydopamine Coatings Prepared by a Shaking-Assisted Method. *Sci. Rep.* **2016**, *6*, 24420.
- (111) Liu, D.; Li, C.; Zhou, F.; Zhang, T.; Liu, G.; Cai, W.; Li, Y. Capillary Gradient-Induced Self-Assembly of Periodic Au Spherical Nanoparticle Arrays on an Ultralarge Scale via a Bisolvent System at Air/Water Interface. *Adv. Mater. Interfaces* **2017**, *4*, 1600976.
- (112) Kim, Y.-J.; Jung, H.-T.; Ahn, C. W.; Jeon, H.-J. Simultaneously Induced Self-Assembly of Poly(3-Hexylthiophene) (P3HT) Nanowires and Thin-Film Fabrication via Solution-Floating Method on a Water Substrate. *Adv. Mater. Interfaces* **2017**, *4*, 1700342.
- (113) Wang, L.; Wang, J.; Huang, Y.; Liu, M.; Kuang, M.; Li, Y.; Jiang, L.; Song, Y. Inkjet Printed Colloidal Photonic Crystal Microdot with Fast Response Induced by Hydrophobic Transition of Poly(N-Isopropyl Acrylamide). *J. Mater. Chem.* **2012**, *22*, 21405-21411.
- (114) Bai, L.; Xie, Z.; Wang, W.; Yuan, C.; Zhao, Y.; Mu, Z.; Zhong, Q.; Gu, Z. Bio-Inspired Vapor-Responsive Colloidal Photonic Crystal Patterns by Inkjet Printing. *ACS Nano* **2014**, *8*, 11094-11100.
- (115) Arsenault, A. C.; Puzzo, D. P.; Manners, I.; Ozin, G. A. Photonic-Crystal Full-Colour Displays. *Nat. Photonics* **2007**, *1*, 468.
- (116) Lee, S. Y.; Kim, S. H.; Hwang, H.; Sim, J. Y.; Yang, S. M. Controlled Pixelation of Inverse Opaline Structures towards Reflection-Mode Displays. *Adv. Mater.* **2014**, *26*(15), 2391-2397.
- (117) Kim, S.-J.; Kim, B.-H.; Kim, S.-W.; Shin, S.-J.; Salleo, A.; Ready, S.; Street, R. Study of

- Ink Jet Printing Parameters to Fabricate LCD Color Filter. *J. Imaging Sci. Technol.* **2010**, *54*, 50307-1.
- (118) Nam, H.; Song, K.; Ha, D.; Kim, T. Inkjet Printing Based Mono-Layered Photonic Crystal Patterning for Anti-Counterfeiting Structural Colors. *Sci. Rep.* **2016**, *6*, 30885.
- (119) Masuda, Y.; Itoh, T.; Koumoto, K. Self-Assembly Patterning of Silica Colloidal Crystals. *Langmuir* **2005**, *21*, 4478-4481.
- (120) Burgess, I. B.; Mishchenko, L.; Hatton, B. D.; Kolle, M.; Lončar, M.; Aizenberg, J. Encoding Complex Wettability Patterns in Chemically Functionalized 3D Photonic Crystals. *J. Am. Chem. Soc.* **2011**, *133*, 12430-12432.
- (121) Kuang, M.; Song, Y. Inkjet Printing of Photonic Crystals. *Nanomaterials for 2D and 3D Printing*. February 2017.
- (122) Mätzler, C. MATLAB Functions for Mie Scattering and Absorption Version 2. *IAP Res Rep.* **2002**, *8*, 9.
- (123) Umh, H. N.; Yu, S.; Kim, Y. H.; Lee, S. Y.; Yi, J. Tuning the Structural Color of a 2D Photonic Crystal Using a Bowl-like Nanostructure. *ACS Appl. Mater. Interfaces* **2016**, *8*, 15802-15808.
- (124) Nguyen, T. A. H.; Hampton, M. A.; Nguyen, A. V. Evaporation of Nanoparticle Droplets on Smooth Hydrophobic Surfaces: The Inner Coffee Ring Deposits. *J. Phys. Chem. C* **2013**, *117*, 4707-4716.
- (125) Jiang, P.; Bertone, J. F.; Hwang, K. S.; Colvin, V. L. Single-Crystal Colloidal Multilayers of Controlled Thickness. *Chem. Mater.* **1999**, *11*, 2132-2140.

- (126) Wong, S.; Kitaev, V.; Ozin, G. A. Colloidal Crystal Films: Advances in Universality and Perfection. *J. Am. Chem. Soc.* **2003**, *125*, 15589–15598.
- (127) Eom, D. S.; Chang, J.; Song, Y. W.; Lim, J. A.; Han, J. T.; Kim, H.; Cho, K. Coffee-Ring Structure from Dried Graphene Derivative Solutions: A Facile One-Step Fabrication Route for All Graphene-Based Transistors. *J. Phys. Chem. C* **2014**, *118*, 27081–27090.
- (128) Li, Y.; Zhang, W.; Hu, J.; Wang, Y.; Feng, X.; Du, W.; Guo, M.; Liu, B. F. Rapid Assembly of Large Scale Transparent Circuit Arrays Using PDMS Nanofilm Shaped Coffee Ring. *Adv. Funct. Mater.* **2017**, *27*, 1606045.
- (129) Layani, M.; Gruchko, M.; Milo, O.; Balberg, I.; Azulay, D.; Magdassi, S. Transparent Conductive Coatings by Printing Coffee Ring Arrays Obtained at Room Temperature. *ACS Nano* **2009**, *3*, 3537–3542.
- (130) Zigelman, A.; Manor, O. The Deposition of Colloidal Particles from a Sessile Drop of a Volatile Suspension Subject to Particle Adsorption and Coagulation. *J. Colloid Interface Sci.* **2018**, *509*, 195-208.
- (131) Wang, H.; Singh, V.; Behrens, S. H. Image Charge Effects on the Formation of Pickering Emulsions. *J. Phys. Chem. Lett.* **2012**, *3*, 2986–2990.
- (132) Ray, M. A.; Kim, H.; Jia, L. Dynamic Self-Assembly of Polymer Colloids to Form Linear Patterns. *Langmuir* **2005**, *21*, 4786-4789.
- (133) Yang, X.; Li, C. Y.; Sun, Y. From Multi-Ring to Spider Web and Radial Spoke: Competition between the Receding Contact Line and Particle Deposition in a Drying Colloidal Drop. *Soft Matter* **2014**, *10*, 4458-4463.

- (134) Pack, M.; Hu, H.; Kim, D. O.; Yang, X.; Sun, Y. Colloidal Drop Deposition on Porous Substrates: Competition among Particle Motion, Evaporation, and Infiltration. *Langmuir* **2015**, *31*, 7953–7961.
- (135) Hu, H.; Larson, R. G. Evaporation of a Sessile Droplet on a Substrate. *J. Phys. Chem. B* **2002**, *106*, 1334-1344.
- (136) Broadbent, T. A. A.; Einstein, A.; Hertz, H.; Dryden, H. L.; Murnaghan, F. P.; Bateman, H. Investigations on the Theory of the Brownian Movement. Book. *Courier Corporation* **1957**.
- (137) Hu, H.; Larson, R. G. Analysis of the Microfluid Flow in an Evaporating Sessile Droplet. *Langmuir* **2005**, *21*, 3963–3971.
- (138) Weon, B. M.; Je, J. H. Self-Pinning by Colloids Confined at a Contact Line. *Phys. Rev. Lett.* **2013**, *110*, 028303.
- (139) Morales, V. L.; Parlange, J. Y.; Wu, M.; Pérez-Reche, F. J.; Zhang, W.; Sang, W.; Steenhuis, T. S. Surfactant-Mediated Control of Colloid Pattern Assembly and Attachment Strength in Evaporating Droplets. *Langmuir* **2013**, *29*, 1831-1840.
- (140) Jung, J. Y.; Kim, Y. W.; Yoo, J. Y.; Koo, J.; Kang, Y. T. Forces Acting on a Single Particle in an Evaporating Sessile Droplet on a Hydrophilic Surface. *Anal. Chem.* **2010**, *82*, 784-788.
- (141) Chhasatia, V. H.; Sun, Y. Interaction of Bi-Dispersed Particles with Contact Line in an Evaporating Colloidal Drop. *Soft Matter* **2011**, *7*, 10135–10143.
- (142) Routh, A. F. Drying of Thin Colloidal Films. *Reports Prog. Phys.* **2013**, *76*, 046603.

- (143) Al-Milaji, K. N.; Radhakrishnan, V.; Kamerkar, P.; Zhao, H. PH-Modulated Self-Assembly of Colloidal Nanoparticles in a Dual-Droplet Inkjet Printing Process. *J. Colloid Interface Sci.* **2018**, *529*, 234–242.
- (144) Zhao, M.; Yong, X. Nanoparticle Motion on the Surface of Drying Droplets. *Phys. Rev. Fluids* **2018**, *3*, 034201.
- (145) Al-Milaji, K. N.; Zhao, H. Probing the Colloidal Particle Dynamics in Drying Sessile Droplets. *Langmuir* **2019**, *35*, 2209-2220.
- (146) Zhang, W.; Wong, P. K. J.; Zhang, D.; Yue, J.; Kou, Z.; van der Laan, G.; Scholl, A.; Zheng, J. G.; Lu, Z.; Zhai, Y. XMCD and XMCD-PEEM Studies on Magnetic-Field-Assisted Self-Assembled 1D Nanochains of Spherical Ferrite Particles. *Adv. Funct. Mater.* **2017**, *27*, 1701265.
- (147) Tokarev, A.; Yatvin, J.; Trotsenko, O.; Locklin, J.; Minko, S. Nanostructured Soft Matter with Magnetic Nanoparticles. *Adv. Funct. Mater.* **2016**.
- (148) Speliotis, D. E. Magnetic Recording beyond the First 100 Years. *J. Magn. Magn. Mater.* **1999**, *193*, 29-35.
- (149) Xia, S.; Metwalli, E.; Opel, M.; Staniec, P. A.; Herzig, E. M.; Müller-Buschbaum, P. Printed Thin Magnetic Films Based on Diblock Copolymer and Magnetic Nanoparticles. *ACS Appl. Mater. Interfaces* **2018**, *10*, 2982-2991.
- (150) Franco, V.; Blázquez, J. S.; Ingale, B.; Conde, A. The Magnetocaloric Effect and Magnetic Refrigeration Near Room Temperature: Materials and Models. *Annu. Rev. Mater. Res.* **2012**, *42*, 305-342.

- (151) Yuan, J.; Xu, Y.; Müller, A. H. E. One-Dimensional Magnetic Inorganic-Organic Hybrid Nanomaterials. *Chem. Soc. Rev.* **2011**, *40*, 640-655.
- (152) Qin, S.; Yin, H.; Yang, C.; Dou, Y.; Liu, Z.; Zhang, P.; Yu, H.; Huang, Y.; Feng, J.; Hao, J.; et al. A Magnetic Protein Biocompass. *Nat. Mater.* **2016**, *15*, 217.
- (153) Gao, M.; Kuang, M.; Li, L.; Liu, M.; Wang, L.; Song, Y. Printing 1D Assembly Array of Single Particle Resolution for Magnetosensing. *Small* **2018**, *14*, 1800117.
- (154) Song, H.; Spencer, J.; Jander, A.; Nielsen, J.; Stasiak, J.; Kasperchik, V.; Dhagat, P. Inkjet Printing of Magnetic Materials with Aligned Anisotropy. *J. Appl. Phys.* **2014**, *115*, 17E308.
- (155) El-Gendy, A. A.; Harstad, S. M.; Vijayaragavan, V.; Gupta, S.; Pecharsky, V. K.; Zweit, J.; Hadimani, R. L. Ferromagnetic Gd₅Si₄ Nanoparticles as T₂ Contrast Agents for Magnetic Resonance Imaging. *IEEE Magn. Lett.* **2017**, *8*, 1–4.
- (156) Hadimani, R. L.; Gupta, S.; Harstad, S. M.; Pecharsky, V. K.; Jiles, D. C. Investigation of Room Temperature Ferromagnetic Nanoparticles of Gd₅Si₄. *IEEE Trans. Magn.* **2015**, *51*, 1-4.
- (157) Yung, K. W.; Landecker, P. B.; Villani, D. D. An Analytic Solution for the Force Between Two Magnetic Dipoles. *Magn. Electr. Sep.* **1998**, *9*, 39–52.
- (158) Dou, R.; Wang, T.; Guo, Y.; Derby, B. Ink-Jet Printing of Zirconia: Coffee Staining and Line Stability. *J. Am. Ceram. Soc.* **2011**, *94*, 3787-3792.
- (159) Dou, R.; Derby, B. Formation of Coffee Stains on Porous Surfaces. *Langmuir* **2012**, *28*, 5331-5338.

- (160) Nilghaz, A.; Zhang, L.; Shen, W. Coffee Stains on Paper. *Chem. Eng. Sci.* **2015**, *129*, 34-41.
- (161) Jadav, M.; Patel, R. J.; Mehta, R. V. Influence of Magnetic Field on Evaporation of a Ferrofluid Droplet. *J. Appl. Phys.* **2017**, *122*, 145302.
- (162) Fan, J. A.; Yeo, W. H.; Su, Y.; Hattori, Y.; Lee, W.; Jung, S. Y.; Zhang, Y.; Liu, Z.; Cheng, H.; Falgout, L.; et al. Fractal Design Concepts for Stretchable Electronics. *Nat. Commun.* **2014**, *5*, 3266.
- (163) Trung, T. Q.; Lee, N. E. Recent Progress on Stretchable Electronic Devices with Intrinsically Stretchable Components. *Adv. Mater.* **2017**, *29*, 1603167.
- (164) Dickey, M. D. Stretchable and Soft Electronics Using Liquid Metals. *Adv. Mater.* **2017**, *29*, 1606425.
- (165) Wang, Y.; Zhu, C.; Pfattner, R.; Yan, H.; Jin, L.; Chen, S.; Molina-Lopez, F.; Lissel, F.; Liu, J.; Rabiah, N. I.; et al. A Highly Stretchable, Transparent, and Conductive Polymer. *Sci. Adv.* **2017**, *3*, e1602076.
- (166) Matsuhisa, N.; Inoue, D.; Zalar, P.; Jin, H.; Matsuba, Y.; Itoh, A.; Yokota, T.; Hashizume, D.; Someya, T. Printable Elastic Conductors by in Situ Formation of Silver Nanoparticles from Silver Flakes. *Nat. Mater.* **2017**, *16*, 834.
- (167) Kim, D. H.; Rogers, J. A. Stretchable Electronics: Materials Strategies and Devices. *Adv. Mater.* **2008**, *20*, 4887-4892.
- (168) Qi, D.; Liu, Z.; Leow, W. R.; Chen, X. Elastic Substrates for Stretchable Devices. *MRS Bull.* **2017**, *42*, 103-107.

- (169) Sekitani, T.; Nakajima, H.; Maeda, H.; Fukushima, T.; Aida, T.; Hata, K.; Someya, T. Stretchable Active-Matrix Organic Light-Emitting Diode Display Using Printable Elastic Conductors. *Nat. Mater.* **2009**, *8*, 494.
- (170) Liang, J.; Li, L.; Tong, K.; Ren, Z.; Hu, W.; Niu, X.; Chen, Y.; Pei, Q. Silver Nanowire Percolation Network Soldered with Graphene Oxide at Room Temperature and Its Application for Fully Stretchable Polymer Light-Emitting Diodes. *ACS Nano* **2014**, *8*, 1590-1600.
- (171) Zhao, J.; Chi, Z.; Yang, Z.; Chen, X.; Arnold, M. S.; Zhang, Y.; Xu, J.; Chi, Z.; Aldred, M. P. Recent Developments of Truly Stretchable Thin Film Electronic and Optoelectronic Devices. *Nanoscale* **2018**, *10*, 5764-5792.
- (172) Xu, F.; Wu, M. Y.; Safron, N. S.; Roy, S. S.; Jacobberger, R. M.; Bindl, D. J.; Seo, J. H.; Chang, T. H.; Ma, Z.; Arnold, M. S. Highly Stretchable Carbon Nanotube Transistors with Ion Gel Gate Dielectrics. *Nano Lett.* **2014**, *14*, 682-686.
- (173) Yan, C.; Cho, J. H.; Ahn, J. H. Graphene-Based Flexible and Stretchable Thin Film Transistors. *Nanoscale* **2012**, *4*, 4870-4882.
- (174) Chen, D.; Lou, Z.; Jiang, K.; Shen, G. Device Configurations and Future Prospects of Flexible/Stretchable Lithium-Ion Batteries. *Adv. Funct. Mater.* **2018**, *28*, 1805596.
- (175) Liu, W.; Song, M. S.; Kong, B.; Cui, Y. Flexible and Stretchable Energy Storage: Recent Advances and Future Perspectives. *Adva. Mater.* **2017**, *29*, 1603436.
- (176) Jeong, C. K.; Lee, J.; Han, S.; Ryu, J.; Hwang, G. T.; Park, D. Y.; Park, J. H.; Lee, S. S.; Byun, M.; Ko, S. H.; et al. A Hyper-Stretchable Elastic-Composite Energy Harvester. *Adv.*

- Mater.* **2015**, *27*, 2866-2875.
- (177) Wang, J.; Lin, M. F.; Park, S.; Lee, P. S. Deformable Conductors for Human–Machine Interface. *Mater. Today* **2018**, *21*, 508-526.
- (178) Trung, T. Q.; Lee, N. E. Flexible and Stretchable Physical Sensor Integrated Platforms for Wearable Human-Activity Monitoring and Personal Healthcare. *Adv. Mater.* **2016**, *28*, 4338-4372.
- (179) Roh, E.; Hwang, B. U.; Kim, D.; Kim, B. Y.; Lee, N. E. Stretchable, Transparent, Ultrasensitive, and Patchable Strain Sensor for Human-Machine Interfaces Comprising a Nanohybrid of Carbon Nanotubes and Conductive Elastomers. *ACS Nano* **2015**, *9*, 6252-6261.
- (180) Yamada, T.; Hayamizu, Y.; Yamamoto, Y.; Yomogida, Y.; Izadi-Najafabadi, A.; Futaba, D. N.; Hata, K. A Stretchable Carbon Nanotube Strain Sensor for Human-Motion Detection. *Nat. Nanotechnol.* **2011**, *6*, 296.
- (181) Wang, J.; Cai, G.; Li, S.; Gao, D.; Xiong, J.; Lee, P. S. Printable Superelastic Conductors with Extreme Stretchability and Robust Cycling Endurance Enabled by Liquid-Metal Particles. *Adv. Mater.* **2018**, *30*, 1706157.
- (182) Han, F.; Su, X.; Huang, M.; Li, J.; Zhang, Y.; Zhao, S.; Liu, F.; Zhang, B.; Wang, Y.; Zhang, G.; et al. Fabrication of a Flexible and Stretchable Three-Dimensional Conductor Based on Au-Ni@graphene Coated Polyurethane Sponge by Electroless Plating. *J. Mater. Chem. C* **2018**, *6*, 8135-8143.
- (183) Huang, Q.; Al-Milaji, K. N.; Zhao, H. Inkjet Printing of Silver Nanowires for Stretchable

- Heaters. *ACS Appl. Nano Mater.* **2018**, *1*, 4528-4536.
- (184) Xu, F.; Zhu, Y. Highly Conductive and Stretchable Silver Nanowire Conductors. *Adv. Mater.* **2012**, *24*, 5117-5122.
- (185) Matsuhisa, N.; Kaltenbrunner, M.; Yokota, T.; Jinno, H.; Kuribara, K.; Sekitani, T.; Someya, T. Printable Elastic Conductors with a High Conductivity for Electronic Textile Applications. *Nat. Commun.* **2015**, *6*, 7461.
- (186) Muth, J. T.; Vogt, D. M.; Truby, R. L.; Mengüç, Y.; Kolesky, D. B.; Wood, R. J.; Lewis, J. A. Embedded 3D Printing of Strain Sensors within Highly Stretchable Elastomers. *Adv. Mater.* **2014**, *26*, 6307-6312.
- (187) Jiang, J.; Bao, B.; Li, M.; Sun, J.; Zhang, C.; Li, Y.; Li, F.; Yao, X.; Song, Y. Fabrication of Transparent Multilayer Circuits by Inkjet Printing. *Adv. Mater.* **2016**, *28*, 1420-1426.
- (188) Kim, Y.; Zhu, J.; Yeom, B.; Di Prima, M.; Su, X.; Kim, J. G.; Yoo, S. J.; Uher, C.; Kotov, N. A. Stretchable Nanoparticle Conductors with Self-Organized Conductive Pathways. *Nature* **2013**, *500*, 59.
- (189) Park, M.; Im, J.; Shin, M.; Min, Y.; Park, J.; Cho, H.; Park, S.; Shim, M. B.; Jeon, S.; Chung, D. Y.; et al. Highly Stretchable Electric Circuits from a Composite Material of Silver Nanoparticles and Elastomeric Fibres. *Nat. Nanotechnol.* **2012**, *7*, 803.
- (190) Chung, S.; Lee, J.; Song, H.; Kim, S.; Jeong, J.; Hong, Y. Inkjet-Printed Stretchable Silver Electrode on Wave Structured Elastomeric Substrate. *Appl. Phys. Lett.* **2011**, *98*, 153110.
- (191) Tybrandt, K.; Vörös, J. Fast and Efficient Fabrication of Intrinsically Stretchable Multilayer Circuit Boards by Wax Pattern Assisted Filtration. *Small* **2016**, *12*, 180-184.

- (192) Liang, J.; Tong, K.; Pei, Q. A Water-Based Silver-Nanowire Screen-Print Ink for the Fabrication of Stretchable Conductors and Wearable Thin-Film Transistors. *Adv. Mater.* **2016**, *28*, 5986-5996.
- (193) Chen, K.; Gao, W.; Emaminejad, S.; Kiriya, D.; Ota, H.; Nyein, H. Y. Y.; Takei, K.; Javey, A. Printed Carbon Nanotube Electronics and Sensor Systems. *Adva. Mater.* **2016**, *28*, 4397-4414.
- (194) Yang, T.; Xie, D.; Li, Z.; Zhu, H. Recent Advances in Wearable Tactile Sensors: Materials, Sensing Mechanisms, and Device Performance. *Mater. Sci. Eng. R Reports* **2017**, *115*, 1–37.
- (195) Huang, Q.; Zhu, Y. Printing Conductive Nanomaterials for Flexible and Stretchable Electronics: A Review of Materials, Processes, and Applications. *Adv. Mater. Technol.* **2019**, *4*, 1800546.
- (196) Kim, D.; Jeong, S.; Park, B. K.; Moon, J. Direct Writing of Silver Conductive Patterns: Improvement of Film Morphology and Conductance by Controlling Solvent Compositions. *Appl. Phys. Lett.* **2006**, *89*, 264101.
- (197) Shahariar, H.; Kim, I.; Soewardiman, H.; Jur, J. S. Inkjet Printing of Reactive Silver Ink on Textiles. *ACS Appl. Mater. Interfaces* **2019**, *11*, 6208-6216.
- (198) Kim, D.; Jeong, S.; Lee, S.; Park, B. K.; Moon, J. Organic Thin Film Transistor Using Silver Electrodes by the Ink-Jet Printing Technology. *Thin Solid Films* **2007**, *515*, 7692-7696.
- (199) Suikkola, J.; Björninen, T.; Mosallaei, M.; Kankkunen, T.; Iso-Ketola, P.; Ukkonen, L.;

- Vanhala, J.; Mäntysalo, M. Screen-Printing Fabrication and Characterization of Stretchable Electronics. *Sci. Rep.* **2016**, *6*, 25784.
- (200) Mohammed, M. G.; Kramer, R. All-Printed Flexible and Stretchable Electronics. *Adv. Mater.* **2017**, *29*, 1604965.
- (201) Guo, S. Z.; Qiu, K.; Meng, F.; Park, S. H.; McAlpine, M. C. 3D Printed Stretchable Tactile Sensors. *Adv. Mater.* **2017**, *29*, 1701218.
- (202) Dang, W.; Vinciguerra, V.; Lorenzelli, L.; Dahiya, R. Printable Stretchable Interconnects. *Flexible and Printed Electronics* **2017**, *2*, 013003.
- (203) Finn, D. J.; Lotya, M.; Coleman, J. N. Inkjet Printing of Silver Nanowire Networks. *ACS Appl. Mater. Interfaces* **2015**, *7*, 9254-9261.
- (204) Lu, H.; Lin, J.; Wu, N.; Nie, S.; Luo, Q.; Ma, C. Q.; Cui, Z. Inkjet Printed Silver Nanowire Network as Top Electrode for Semi-Transparent Organic Photovoltaic Devices. *Appl. Phys. Lett.* **2015**, *106*, 27_1.
- (205) Shen, W.; Zhang, X.; Huang, Q.; Xu, Q.; Song, W. Preparation of Solid Silver Nanoparticles for Inkjet Printed Flexible Electronics with High Conductivity. *Nanoscale* **2014**, *6*, 1622-1628.
- (206) Coskun, S.; Aksoy, B.; Unalan, H. E. Polyol Synthesis of Silver Nanowires: An Extensive Parametric Study. *Cryst. Growth Des.* **2011**, *11*, 4963-4969.
- (207) Miriyev, A.; Stack, K.; Lipson, H. Soft Material for Soft Actuators. *Nat. Commun.* **2017**, *8*, 596.
- (208) Huang, Q.; Zhu, Y. Gravure Printing of Water-Based Silver Nanowire Ink on Plastic

- Substrate for Flexible Electronics. *Sci. Rep.* **2018**, *8*, 15167.
- (209) Cui, Z.; Han, Y.; Huang, Q.; Dong, J.; Zhu, Y. Electrohydrodynamic Printing of Silver Nanowires for Flexible and Stretchable Electronics. *Nanoscale* **2018**, *10*, 6806-6811.
- (210) Trotsenko, O.; Tokarev, A.; Gruzd, A.; Enright, T.; Minko, S. Magnetic Field Assisted Assembly of Highly Ordered Percolated Nanostructures and Their Application for Transparent Conductive Thin Films. *Nanoscale* **2015**, *7*, 7155-7161.
- (211) Cho, S.; Kang, S.; Pandya, A.; Shanker, R.; Khan, Z.; Lee, Y.; Park, J.; Craig, S. L.; Ko, H. Large-Area Cross-Aligned Silver Nanowire Electrodes for Flexible, Transparent, and Force-Sensitive Mechanochromic Touch Screens. *ACS Nano* **2017**, *11*, 4346-4357.

Appendix A: Supporting Information

Video S6.1: Demonstration of the dipole chaining process simulated in COMSOL. One dipole is placed at the center of the domain, whereas the second dipole is positioned at an orientation angle of 30° to the first one with respect to the y-axis (i.e., the direction of the magnetic field). The initial distance between the two dipoles is selected as the mean particle distance (L_m), calculated at the particle concentration of 25 mg/mL.

Video S6.2 – S6.5: Demonstration of the dipole chaining process, with orientation angles of zero, 45° , 60° , and 90° , respectively. The distance between the two dipoles is the same as in Video S2.

Video S6.6: Demonstration of particle migration toward the substrate under the influence of the magnetophoretic force. The particles were released at a vertical distance (L_m) away from the substrate.

Curriculum Vitae

Karam Nashwan Al-Milaji (Ph.D. Candidate)

Email: engineer.karam.2008@gmail.com

LinkedIn: www.linkedin.com/in/karamalmilaji

Education:

Ph.D. in Mechanical and Nuclear Engineering Virginia Commonwealth University, Richmond, VA	(2019 – 2016) GPA 4.0/4.0
Master of Science in Mechanical and Nuclear Engineering Virginia Commonwealth University, Richmond, VA	(2014 – 2016) GPA 3.85/4.0
Bachelor of Refrigeration and Air Conditioning Engineering Technical College of Mosul, Iraq	(2003 – 2007)

Publications:

- **Al-Milaji, K. N.**, Gupta, S., Pecharsky, V. K., Hadimani, R. and, Zhao, H., “Inkjet Printing of Magnetic Particles Toward Anisotropic Magnetic Properties”, *Scientific reports*, 2019. (under review)
- **Al-Milaji, K. N.** and Zhao, H., “New Perspective of Mitigating Coffee-ring Effect: Interfacial Assembly”, submitted to *The Journal of Physical Chemistry*, 2019, 123, 12029-12041.
- **Al-Milaji, K. N.** and Zhao, H., “Probing the Colloidal Particle Dynamics in Drying Sessile Droplets”, *Langmuir*, 2019, 35, 2209-2220.
- Li, Z; **Al-Milaji, K. N.**; Zhao, H; Chen, DR., “Electrohydrodynamic (EHD) jet printing with a circulating dual-channel nozzle”, *J. Micromech. Microeng.*, 2019, 29, 035013.
- Huang, Q; **Al-Milaji, K. N.**; Zhao, H, “Inkjet Printing of Silver Nanowires for Stretchable Heaters”, *ACS Applied Nano Materials*, 2018, 1, 4528-4536.
- **Al-Milaji, K. N.**, Vinod Radhakrishnan, Prajakta Kamerkar, and Zhao, H., “pH-Modulated Self-Assembly of Colloidal Nanoparticles in Dual-Droplet Inkjet Printing Process”, *Journal of Colloid and Interface Science*, 2018, 529, 234-242.
- Secondo, R., **Al-Milaji, K.N.**, Ng, T.N., Zhao, H, and Kinsey, N., “Numerical Characterization of Monolayer Ink-Jet Printed Polystyrene Lattice,” Conference proceeding on Lasers and Electro-Optics (CLEO), OSA Technical Digest (online) (Optical Society of America, 2018), paper JTh2A.80.

- **Al-Milaji, K. N.**, Secondo, R., Ng, T.N., Kinsey, N., and Zhao, H., “Interfacial Self-Assembly of Colloidal Nanoparticles in Dual-Droplet Inkjet Printing”, *Advanced Materials Interfaces*, 2018, 5, 1701561. **(Highlighted as inside cover)**
- **Al-Milaji, K. N.** and Zhao, H., “Mask-assisted Electro spray for Superoleophobic Surfaces: An Experimental and Numerical Study”, *Surface and Coatings Technology*, 2017, 316, 146-154.
- **Al-Milaji, K. N.** and Zhao, H., “Fabrication of Superoleophobic Surfaces by Mask-assisted Electro spray”, *Applied Surface Science*, 2017, 396, 955–964.

Conferences and workshops:

- **Al-Milaji, K. N.**, Gupta, S., Pecharsky, V. K., Hadimani, R. and, Zhao, H., “Inkjet Printing of Magnetic Particles Toward Anisotropic Magnetic Properties”, Virginia Soft Matter Workshop, Charlottesville, 2019.
- **Al-Milaji, K. N.**, Gupta, S., Pecharsky, V. K., Barua, R., Zhao, H., and Hadimani, R. L., “Differential Effect of Magnetic Alignment on Magnetocaloric Effect during Additive Manufacturing of Magnetocaloric Particles”, MMM, Las Vegas, Nevada, 2019. (Poster)
- **Al-Milaji, K. N.** and Zhao, H., “Probing the Colloidal Particle Dynamics in Drying Sessile Droplets”, 93rd ACS Colloid & Surface Science Symposium, Georgia Tech, Georgia, Atlanta, 2019.
- **Al-Milaji, K. N.** and Zhao, H., “Probing the Colloidal Particle Dynamics in Drying Sessile Droplets”, Virginia Soft Matter Workshop, Blacksburg, 2018.
- Huang, Q., **Al-Milaji, K.N.**, Zhao, H., Stretchable Silver Nanowire Micro-conductors by Direct Inkjet Printing, ASME's International Mechanical Engineering Congress and Exposition (IMECE), Pittsburgh, Pennsylvania, 2018.
- **Al-Milaji, K. N.** and Zhao, H., “pH-modulated self-assembly of colloidal nanoparticles in a dual-droplet inkjet printing process”, 92nd ACS Colloid & Surface Science Symposium, State College, Pennsylvania, 2018.
- **Al-Milaji, K. N.**, Harstad, S. M., Hadimani, R. L., H. Zhao, “Inkjet printing of magnetic particles towards anisotropic magnetic properties”, 92nd ACS Colloid & Surface Science Symposium, State College, Pennsylvania, 2018.
- **Al-Milaji, K. N.**, Secondo, R.R., Ng, T.N., Kinsey, N., and Zhao, H., “Interfacial Self-Assembly of Colloidal Nanoparticles in Dual-Droplet Inkjet Printing”, MRS Fall, Nov 2017.
- **Al-Milaji, K.N.**, Zhao, H., “Formation of Monolayer Nanoparticles through Self-Assembly in a Dual-Droplet Inkjet Printing”, 5th Virginia Soft Matter Workshop, James Madison University, Harrisonburg, Virginia, 2017.

- Harstad, S. M., **Al-Milaji, K. N.**, El-Gendy, A. A., Gupta, S., Pecharsky, V. K., H. Zhao, and Hadimani, R. L. “Additive manufacturing towards functionally graded nanomaterials”, MMM, Pittsburgh, 2017. (Poster)
- **Al-Milaji, K. N.**, Zhao, H, “Fabricating Superoleophobic and Superhydrophobic Surfaces with Multi-Roughness Using Airbrush and Electrospray”, Virginia Soft Matter Workshop, Richmond, 2016.
- **Al-Milaji, K. N.**, Zhao, H, “Fabricating Superoleophobic and Superhydrophobic Surfaces with Multi-Roughness Using Airbrush and Electrospray”, Virginia Soft Matter Workshop, Charlottesville, 2015.

Qualification/Technical Proficiencies:

- Analytical and creative thinking.
- Project planning and management.
- Solid engineering background.
- 8 years of experience in Refrigeration and Air Conditioning Engineering.
- Self-motivated and ability to multi-task, working under pressure to strict deadlines.
- Willing to travel and working independently.
- Ability to use MATLAB, AutoCAD, COMSOL, and Blender.

Language Skills: Fluent in Arabic and English.

Relevant Coursework: Thermodynamics, Heat and Mass Transfer, Fluid Mechanics, Refrigeration and Air Conditioning, Electrical and Electronic Engineering, Mechanical Design, Drawing of Refrigeration and Air Conditioning systems, Steam Engineering, Refrigeration Systems, Air Conditioning Systems, Renewable Energy, Control Circuits.

Research Experience:

- Electrospray of functional materials to fabricate super liquid repellent surfaces.
- Inkjet printing of functional materials for different applications.
- Electrohydrodynamic (EHD) printing of functional materials.
- Dual-droplet inkjet printing of colloidal suspensions for producing monolayer depositions.
- Computational analysis using COMSOL Multiphysics.

Relevant Experience: Good experience in SEM, AFM, LSM, Goniometer, Profilometer, and Rheometer.

Professional Experience:

Maintenance Engineer of Air Conditioning Systems at Oil Distribution Company. Nov 2010 – Dec 2013

- Installed and maintained domestic refrigeration and air conditioning

systems like split unit and window type air conditioners, water coolers, and refrigerators.

Maintenance Engineer of HVAC Systems at Midland Refineries Company (MRC). Feb 2008 – Nov 2010

- Installed and maintained all types of air conditioning like VRF systems, air and water Chillers, air handling units, package systems, split units, and window type units.

Achievements: Installation of two VRF units type FUJITSU for two distillation units in AL-Daura Refinery.

Awards:

- 2020-2019 Dissertation Assistantship Award Program
- 2018-2019 Outstanding Graduate Research Award
- 2009 Outstanding maintenance engineer at MRC.
- 2007 Academic excellence award.